Luminosity Performance Limitations Due to the Beam-Beam Interaction in the Large Hadron Collider

Matthew Paul Crouch

A thesis submitted to the University of Manchester for the degree of Doctor of Philosophy in the Faculty of Science and Engineering.

The University of Manchester

in the

SCHOOL OF PHYSICS AND ASTRONOMY

2018

CERN-THESIS-2017-420
//2017

Contents

List of Figures

List of Tables

"In the beginning the Universe was created. This has made a lot of people very angry and been widely regarded as a bad move."

Douglas Adams

THE UNIVERSITY OF MANCHESTER

Abstract

for the degree of Doctor of Philosophy

by Matthew Paul Crouch

Thesis title: Luminosity Performance Limitations Due To The Beam-Beam Interaction In The Large Hadron Collider

In the Large Hadron Collider (LHC), particle physics events are created by colliding high energy proton beams at a number of interaction points around the ring. One of the main performance indicating parameters of the LHC is the luminosity. The luminosity is limited by, amongst other things, the strength of the beam-beam interaction. In this thesis, the effect of the beam-beam interaction on the luminosity performance of the LHC and the proposed High Luminosity Large Hadron Collider (HL-LHC) is investigated. Results from a number of dedicated, long-range beam-beam machine studies are presented and analysed. In these studies, the minimum beam-beam separation for two different β^* optics are identified. This separation defines the minimum operational crossing angle in the LHC. The data from these studies are then compared to simulation of the dynamic aperture and the results are discussed. In addition to studies of the LHC, an analytical approach is derived in order to describe the hourglass effect, which may become a contributing factor in limiting the luminosity performance of the HL-LHC.

Word count: 52,058

Declaration of Authorship

I, Matthew Crouch, declare that this thesis titled, 'Luminosity performance limitations due to the Beam-Beam interaction in the Large Hadron Collider' and the work presented in it are my own. I confirm that:

- This work was done wholly or mainly while in candidature for a research degree at this University.
- Where any part of this thesis has previously been submitted for a degree or any other qualification at this University or any other institution, this has been clearly stated.
- Where I have consulted the published work of others, this is always clearly attributed.
- Where I have quoted from the work of others, the source is always given. With the exception of such quotations, this thesis is entirely my own work.
- I have acknowledged all main sources of help.
- Where the thesis is based on work done by myself jointly with others, I have made clear exactly what was done by others and what I have contributed myself.

Signed:

Date:

Copyright

- The author of this thesis (including any appendices and/or schedules to this thesis) owns certain copyright or related rights in it (the Copyright) and he has given The University of Manchester certain rights to use such Copyright, including for administrative purposes.

- Copies of this thesis, either in full or in extracts and whether in hard or electronic copy, may be made only in accordance with the Copyright, Designs and Patents Act 1988 (as amended) and regulations issued under it or, where appropriate, in accordance with licensing agreements which the University has from time to time. This page must form part of any such copies made.

- The ownership of certain Copyright, patents, designs, trade marks and other intellectual property (the Intellectual Property) and any reproductions of copyright works in the thesis, for example graphs and tables (Reproductions), which may be described in this thesis, may not be owned by the author and my be owned by third parties. Such Intellectual Property and Reproductions cannot and must not be made available for use without the prior written permission of the owner(s) of the relevant Intellectual Property and/or Reproductions.

- Further information on the conditions under which disclosure, publication and commercialisation of this thesis, the Copyright and any Intellectual Property and/or Reproductions described in it may take place is available in the University IP policy in any relevant Thesis restriction declarations deposited in the University Library, The University Library regulations and in The University's policy on presentation of Theses.

Acknowledgements

I would firstly like to acknowledge my supervisors who, without them, I would not have been offered this PhD. To Bruno Muratori, without your endless supply of coffee and enthusiasm for mathematics and physics, I would never have made it out of the first year. To Rob Appleby, thank you for all your support and advice when I needed it most, this thesis would most certainly not be possible without it. To Tatiana Pieloni, thank you for inviting me into the beam-beam group at CERN and the many discussions and advice you have provided me. This thesis would never have materialised without all of your help, so thank you for all of your support, advice, criticism, and encouragement when I needed it most.

Next, I have to thank all my friends and colleagues at CERN, Manchester and the Cockcroft Institute, who have been fortunate (or unfortunate) enough to share an office with me. To Jimmy, Sarah, Ewen, Lee, Sam, Nick, Emilia and others, who have made my transition during my LTA or Fellowship as painless as possible. You have had to suffer my endless complaining about this thesis for long enough, but at least now, it is finally over. I'd also like to extend a quick thank you to Alessio for helping me manage the various issues I encountered involving `Sixtrack`, without your help, my results may have taken even longer.

To my friends; Stuart, Steve, Mike, Alexei, Jeeves, Lindsay, Aaron, Dean, Mackinnon, and many others that I cannot possibly include here. Thank you for listening to my endless complaints that have accompanied this thesis and my PhD. I should also thank the Manchester Metros ice hockey team for providing a much needed break from research. You all reminded me that there is life outside of work, even if it did involve 12 am face-offs in Whitley Bay.

I must of course thank my parents for their endless love, advice and most importantly financial support. Without that I would have never been able to stay in education for as long as I have. Nothing I could write here would ever express my gratitude. I would also like to thank Simon, Jemma and Olivia. For no matter how stressed I am, a quick conversation with my niece always cheers me up.

Matthew Paul Crouch

To my Niece, Olivia

Chapter 1

Introduction

1.1 Outline and Motivation

In a colliding storage ring like the LHC, luminosity is a key measure of the overall machine performance. To ensure the maximum efficiency during collisions, losses due to various beam dynamics processes should be minimised, such that particles are only lost due to collisions with counter rotating bunches. One effect that is unavoidable in the LHC and is known to cause additional losses is the beam-beam interaction. At each collision point the bunches will experience the electric field of the counter rotating bunch. The interaction between two counter rotating beams can be strong and hence dictate the choice of operation parameters for the machine. Understanding the beam-beam interaction and its effects are vital to maximise the luminosity performance in the LHC and push the luminosity reach for future machines. The impact of the beam-beam interaction on the luminosity performance in the LHC is the topic of this thesis. A brief summary of the thesis is given in the following section.

1.2 Thesis Summary

This thesis contains research conducted throughout a 4 year period with 9 months of that spent on long-term attachment at CERN. It consists of three introductory chapters and three main research chapters, followed by a brief summary. The aim of this thesis was to identify and quantify the impact of beam-beam effects on the luminosity performance of the LHC. The luminosity is a key parameter which defines the performance of the machine. It is therefore important to understand these effects, and the impact they have on the luminosity. Chapters 2 and 3 introduce the general concepts of accelerator physics which are related to this thesis. Within these chapters, elements of beam dynamics, the beam-beam interaction and the CERN accelerator complex are introduced. The chapters following these introductions, contain research undertaken during this PhD and provides the main topic of this thesis, which is the performance limitations of the luminosity due to beam-beam effects. The work in this thesis can be summarised as follows;

- Chapter 4 contains work detailing an alternative method of obtaining analytical expressions for the electric field in the rest frame of the bunch, whilst including a non-Gaussian charge density distribution. In the HL-LHC, the particular choice of operational parameters such as β^*, will result in a coupling between the transverse bunch size to the longitudinal position. This is known as the hourglass effect. The hourglass effect can limit luminosity performance because the particles may not collide at the minimum β^*. In order to study the luminosity performance, accurate models of the hourglass effect are required. Currently no analytical formula exists to describe this effect. As a result, computationally expensive multi-particle simulations are required. This chapter provides a method of obtaining analytical solutions to describe the hourglass effect. The theory is used to re-derive

electric field for a fixed Gaussian distribution and is then applied to the case the hourglass effect is present. The derived expressions are discussed and compared to the known round bunch expression.

- Chapter 5 presents experimental work that was collected during the 2015 and 2016 LHC runs. This chapter details two long-range beam-beam machine studies. These studies were performed to determine the maximum luminosity reach as defined by the long-range beam-beam interactions in the LHC for two optic set ups. From these studies, the minimum crossing angle was identified for a $\beta^* = 0.8$ m and $\beta^* = 0.4$ m. The minimum operational crossing angle was identified at $\alpha = 260$ μrad during the 2016 study. For crossing angles smaller than this value, the long-range beam-beam interaction reduces the beam and luminosity lifetimes. Identifying the limit before additional beam losses occurred allowed the operational crossing angle to be reduced during luminosity production runs. The crossing angle was reduced to $\alpha = 280$ μrad. Operating at this reduced crossing angle will improve the luminosity performance of the LHC by approximately $10-15\%$.

- In chapter 6, the results from the 2016 long-range beam-beam machine study were compared to dynamic aperture simulations performed in `Sixtrack`. This chapter introduces and discusses the topic of dynamic aperture in accelerator physics and its relationship to the beam lifetimes. A method of calculating the dynamic aperture from measured intensity loss is discussed, before the measured data is compared to tracking simulations. The dynamic aperture is simulated for every crossing angle step during the long-range beam-beam machine study, as discussed in chapter 5. The impact of magnetic errors, linear coupling and the beam-beam interaction the dynamic aperture is evaluated. These studies show that the magnetic errors play a important role in defining the dynamic aperture and hence the choice of operational parameters for the LHC and future machines.

Finally, a summary chapter is provided overviewing the main findings of this thesis.

Chapter 2

Beam Dynamics

2.1 Single Particle Dynamics

Beam dynamics concerns the behaviour of charged particles in an accelerator. Providing an accurate description of the beam dynamics is a vital requirement of any machine to ensure that design, operation, machine performance, and protection goals are all achieved. Before collective effects can be considered a brief overview of single particle dynamics are introduced in this chapter. The transverse beam dynamics are primarily a concern in the LHC as the bunches are relativistic. These are discussed and reviewed in the following chapter.

2.1.1 Maxwell's Equations

The dynamics of charged particles moving within an electromagnetic field is described by Maxwell's equations [1, 2]. Maxwell's equations in differential form

are given by the following set of coupled partial differential equations;

$$\vec{\nabla} \cdot \vec{E} = \frac{\rho}{\epsilon_0}, \tag{2.1}$$

$$\vec{\nabla} \times \vec{E} = -\partial_t \vec{B}, \tag{2.2}$$

$$\vec{\nabla} \cdot \vec{B} = 0, \tag{2.3}$$

$$\vec{\nabla} \times \vec{B} = \mu_0 \vec{j} + \mu_0 \epsilon_0 \partial_t \vec{E}, \tag{2.4}$$

where μ_0 and ϵ_0 are the magnetic and electric permeability in free space, $\vec{E}$ and $\vec{B}$ are the electric and magnetic fields respectively, $\vec{j}$ is the current density and ρ is the charge density distribution.

Since Maxwell's equations are a system of coupled partial differential equations, analytic solutions can often be difficult to find and depend on the boundary conditions of the system. Maxwell's equations can be used to describe both the single particle behaviour as well as the collective behaviour of many particles. The behaviour of many particles in a bunch are difficult to model and would require extensive computational simulation in order to calculate the electric fields of all of the particles. The problem can be simplified by considering the bunch as an ensemble and transforming to the rest frame of the bunch. This reduces the number of equations that need to be solved, since the magnetic field can be set to zero under fixed time, $t = 0$. In this case, Maxwell's equations reduce to

$$\vec{\nabla} \cdot \vec{E} = \frac{\rho}{\epsilon_0}, \tag{2.5}$$

$$\vec{\nabla} \times \vec{E} = 0. \tag{2.6}$$

Written in terms of the scalar potential φ, where the charge density distribution ρ describes the distribution of the particles in the bunch results in Poisson's

equation,

$$\nabla^2\varphi = \frac{\rho}{\epsilon_0}. \tag{2.7}$$

From the scalar potential or the electric field of the bunch, the dynamics of the interaction with other particles can be calculated.

The understanding of a number of the key concepts of single particle dynamics in a colliding beam storage ring like the LHC will allow more complicated collective effects like the beam-beam interaction to be described.

2.1.2 Transverse Dynamics

In a colliding beam storage ring like the LHC, the beam dynamics are dominated by the transverse motion of particles, since the beam energy is sufficiently large, the bunches travel close to the speed of light. The transverse motion of a particle inside a bunch is complicated and can be non-linear in nature [3].

2.1.2.1 Linear Dynamics and Hill's Equations

An accelerator like the LHC contains different types of magnets which are arranged in such a way, as to ensure that a beam of charge particles will pass through, and survive for many turns. The particular layout of these magnets around the whole ring is known as a lattice. For periodic particle motion around an accelerator lattice, the transverse linearised equation of motion can be described in terms of the spatial components x, y and x', y', which represent the angle from the transverse spatial plane. The coordinate space (x, x', y, y') is known as *trace space*. Later in the chapter the concept of *phase space* will be introduced which is a coordinate space in (x, p_x, y, p_y). In phase space the coordinates $p_{x,y}$ are used and these are the momentum components in the x or y

plane. The coordinates x', y' and p_x, p_y are related through.

$$p_x = m_0 c \beta_r \gamma x', \tag{2.8}$$

with a similar expression in y. Here $\beta_r = \frac{v}{c}$, where v is the particle speed, γ is the relativistic factor, and m_0 is the rest mass of the particle. In the absence of any coupled motion Hill's equations [4] are given by

$$x'' + \kappa_x(s)x = 0, \tag{2.9}$$

$$y'' + \kappa_y(s)y = 0. \tag{2.10}$$

Where $\kappa_{x,y}$ is a an arbitrary function that depends on the longitudinal position s. These equations can be solved using the *ansatz* that includes an s-dependent amplitude and phase as given by [4, 5],

$$x(s) = \sqrt{\epsilon\beta(s)}\cos(\psi(s) + \psi_0), \tag{2.11}$$

where the phase advance through the lattice is $\psi(s)$, β is the β-function, and ϵ and ψ_0 are constants of integration. A similar equation will be given in terms of y. If the machine has a circumference of length L, the β-function in the x or y plane will have the periodic condition

$$\beta(s) = \beta(s + L).$$

Differentiating the *ansatz* given by equation 2.11 and requiring that the trigonometric terms vanish result in two conditions that must be satisfied. These conditions are

$$\frac{1}{2}\left(\beta\beta'' - \frac{\beta'^2}{2}\right) - \beta^2\psi'^2 + \beta^2\kappa = 0, \tag{2.12}$$

and

$$\beta^{'}\psi^{'} + \beta\psi^{''} = 0. \tag{2.13}$$

Integrating the second condition since

$$\beta^{'}\psi^{'} + \beta\psi^{''} = (\beta\psi^{'})'$$

shows that $\beta\psi^{'}$ must be constant. Hence the relationship between the phase advance $\psi(s)$ and the β-function is given by

$$\psi(s) = \oint_0^s \frac{1}{\beta(s)} ds. \tag{2.14}$$

In addition to the phase advance, the β-function can be related to the machine tune. The tune is defined as the total number of transverse particle oscillations around the reference trajectory per revolution. The tune is related to the β-function by

$$Q_{x,y} = \frac{1}{2\pi} \int \frac{1}{\beta(s)} ds. \tag{2.15}$$

Using the condition that the derivative of the β-function and the phase advance $(\beta\psi^{'})$ is constant and substituting back into equation 2.12, yields a new differential equation in β only. The equation is

$$\frac{1}{2}\beta\beta^{''} - \frac{1}{4}\beta^{'2} + \beta^2\kappa = 1. \tag{2.16}$$

Introducing $\alpha = -\frac{1}{2}\beta^{'}$ and $\gamma = \frac{(1+\alpha^2)}{\beta}$ gives

$$\beta^{''} + 2\kappa\beta - 2\gamma = 0, \tag{2.17}$$

which can be simplified to

$$\beta'' + 2\alpha' = 0. \tag{2.18}$$

These parameters α, γ and β and their relationship to the coordinate s yields the *Courant-Snyder* invariant [4, 5]. In the horizontal plane, the Courant-Synder invariant is

$$\gamma_x x^2 + 2\alpha_x x \cdot x' + \beta_x x'^2 = \epsilon_x. \tag{2.19}$$

The parameters α_x, γ_x and β_x have an important physical interpretation for accelerator physics; they correspond to particle motion and introduce the topic of betatron motion and the single particle emittance. The single particle emittance is related to the single particle action by

$$2J_{x,y} = \epsilon_{x,y}. \tag{2.20}$$

The invariant given by equation 2.19 describes how a single particle moving through trace space will travel along the contour of an ellipse [4]. The ellipse itself will rotate in the $x - x'$ plane but the area of the ellipse will remain constant. Liouville's theorem states that for a particle beam undergoing conservative forces, the particle density in phase space will remain conserved [4]. A schematic of the particle phase space ellipse is shown in figure 2.1. The Courant-Snyder parameters α, β and γ are dependent on the longitudinal position s. This dependence can be removed by transforming to the *Floquet* coordinates, Transforming the particle trajectories along the (x, x') plane from ellipses to circles [6]. The

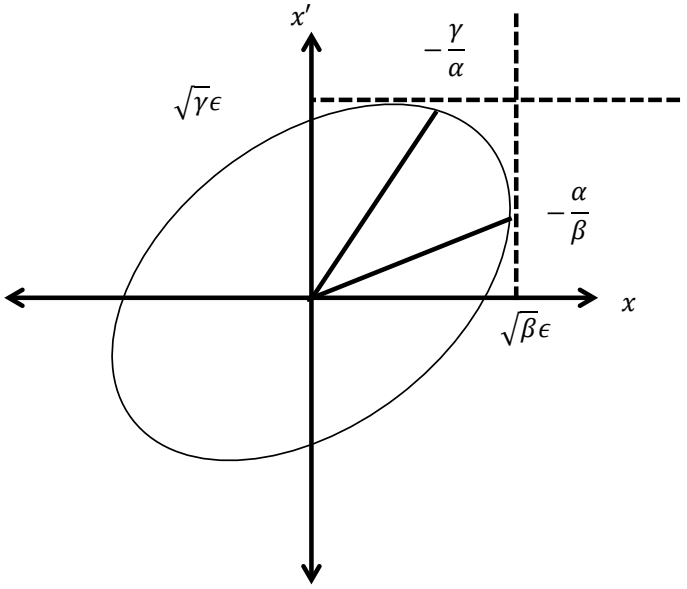

FIGURE 2.1: Particle ellipse along the x, x' axis showing the relationship between the Courant-Snyder parameters α, β, γ.

transform to the Floquet coordinates $\{\bar{x}, \bar{y}\}$ and $\{\bar{x}', \bar{y}'\}$ is given by

$$\begin{pmatrix} \{\bar{x}, \bar{y}\} \\ \{\bar{x}', \bar{y}'\} \end{pmatrix} = \begin{pmatrix} \sqrt{\beta_{x,y}(s)} & 0 \\ -\frac{\alpha_{x,y}(s)}{\sqrt{\beta_{x,y}(s)}} & \frac{1}{\sqrt{\beta_{x,y}(s)}} \end{pmatrix} \cdot \begin{pmatrix} \{x, y\} \\ \{x', y'\} \end{pmatrix}, \tag{2.21}$$

where $\cdot$ represents matrix multiplication. From the Floquet coordinates labelled $\mathcal{F}$, a one turn matrix can be derived that describes the particle phase space ellipse around a circular accelerator. A one turn matrix is defined as a mapping of one of the accelerator coordinates from one position in the ring to the same position after a complete turn. The normal form transformation can be written as

$$M_{turn} = \mathcal{F} R(\Phi) \mathcal{F}^{-1}, \tag{2.22}$$

where $R(\Phi)$ is the rotation matrix,

$$R(\Phi) = \begin{pmatrix} \cos\Phi & \sin\Phi \\ -\sin\Phi & \cos\Phi \end{pmatrix}, \tag{2.23}$$

and Φ is the angle of rotation.

To further develop the understanding and properties of the Courant-Snyder invariant, the evolution of the Courant-Synder ellipse during acceleration is considered.

As the particles in the machine are accelerated the Courant-Synder invariant ϵ_x will decrease. This is sometimes called "*Adiabatic Damping*". The shrinking of ϵ_x can be understood by considering the particle momentum $\mathbf{p}(x, z)$. The particle momentum before and after the acceleration in shown in figure 2.2. As the particle

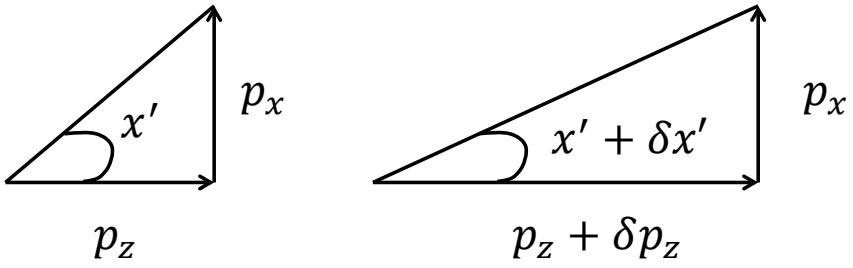

FIGURE 2.2: Evolution of momenta before a particle is accelerated (left) and after the particle has been accelerated (right).

is accelerated its momentum p_z along the longitudinal will increase by $p_z + \delta p_z$, however the transverse component p_x will not change. Since the longitudinal momentum component p_z has increased and the transverse component of the momentum p_x has not changed, x' must change. The angle between p_z and p_x must decrease and hence the length of the hypotenuse will increase by $x' + \delta x'$. This new value of the hypotenuse is given by

$$\delta x' = -x' \frac{\delta p}{p}. \tag{2.24}$$

This will reduce the Courant-Synder invariant ϵ_x. However if a beam of particles with the same ϵ_x but random phases φ are introduced as described in ref [7], then the emittance of the beam can be written in terms of an invariant, normalised emittance which decreases as a function of momentum. This normalised

emittance is written as

$$\epsilon_n = \beta_r \gamma \epsilon, \tag{2.25}$$

where $\beta_r = \frac{v}{c}$ is the particle speed v, over the speed of light c, γ is the relativistic boost factor, and ϵ is the physical emittance. This normalised emittance does not change during acceleration and hence does not violate Liouville's theorem. In the LHC the bunches can be considered to be Gaussian. For a Gaussian distribution the bunch size can be written in terms of σ as,

$$\sigma_{x,y} = \sqrt{\epsilon_{x,y}\beta_{x,y}}. \tag{2.26}$$

The discussion above is derived considering that the particles all move along the design momentum which is labelled p_0. In reality however, this will not be the case and particles will have a spread in momenta, this is typically denoted as δ, where

$$\delta = \frac{\Delta p}{p_0}. \tag{2.27}$$

Deviation from the reference momentum can introduce chromatic effects which will impact the particle dynamics [3, 4, 8, 9]. One chromatic effect that arises in dipoles due to momentum deviation is called *dispersion*. Particles in a bunch will have a momentum spread and this momentum spread will result in particles following a different trajectory through the magnetic elements. This in turn will lead to particles following different orbits around the accelerator lattice. The impact on the particle momentum due to dispersion is given in terms of the dispersion function [8, 9] as

$$\Delta\{x, y\} = D_{x,y}\delta. \tag{2.28}$$

Dispersion effects are just one result of a monochromatic beam in an accelerator. In the next section other chromatic effects and coupled betatron motion are considered along with the Hamiltonian formalism of a particle moving in an accelerator. The Hamiltonian formalisation is often more suitable to describe these effects than Hill's equations.

2.1.3 The Accelerator Hamiltonian

The Hamiltonian $\mathcal{H}$, of a physical system corresponds to the total energy within that system in terms of a set of canonical variables. Similarly the Lagrangian, L, corresponds to the dynamics of a particular system and is the difference between the kinetic energy, E_k and the potential energy, E_p. The Lagrangian of a system is given by equation 2.29

$$\mathcal{L} = E_k - E_p. \tag{2.29}$$

The Hamiltonian of a system is written in terms of the position and momentum of that particle as given by equation 2.30,

$$\mathcal{H} = E_k + E_p. \tag{2.30}$$

These two formalisations have many important uses in physics [10]. The Hamiltonian and Lagrangian of a system are related to one another by a Legendre transformation [11], namely

$$\mathcal{H}(q_k, p_k; t) = \sum_i \dot{q}_i p_i - L(q_k, \dot{q}_k; t), \tag{2.31}$$

where the position and momentum are denoted by q and p respectively, $\dot{q}$ corresponds to the time differential of the position (i.e the velocity), with t representing

the time. The time component is often considered as the independent variable, so that the total energy of the system is considered to be conserved. If the Hamiltonian of a system is known, the time evolution of that system will be defined by Hamilton's equations [12],

$$d_t p = \partial_q \mathcal{H}, \tag{2.32}$$

$$d_t q = -\partial_p \mathcal{H}. \tag{2.33}$$

If the Hamiltonian of a system does not contain any coupling terms, then Hamilton's equations can be applied easily. If, however, the components p and q can not be separated, then Hamilton's equations will become non-trivial and may be difficult to solve. A simple application of the accelerator Hamiltonian is to consider a magnetic field within the thin lens approximation [4], where this approximation treats the magnetic element as having a small length compared to the focal length. The magnetic field for a multipole of any order is given by

$$B_y(x, y, s) + iB_x(x, y, s) = (B_n(s) + iA_n)\,(x + iy)^{n-1}, \tag{2.34}$$

where the normal and skew coefficients are A_n and B_n respectively. The variable n is the multipole of interest, i.e $n = 1$ corresponds to a dipole, $n = 2$ is a quadruple etc. Thus the linear Hamiltonian $\mathcal{H}_0$ for a quadrupole can be written in terms of some focussing function $\kappa_{x,y}$ as,

$$\mathcal{H}_0 = \frac{1}{2}\left(p_x^2 + p_y^2 + \kappa(s)x^2 - \kappa(s)y^2\right), \tag{2.35}$$

where $p_{x,y}$ are the momentum components and x, y are the position components. The contribution from the real magnetic field to n^{th} order can hence be written

as,

$$\mathcal{H}_n = \frac{q}{p}\Re\left[n^{-1}\left(B_n(s) + iA_n\right)(x+iy)^{n-1}\right]. \tag{2.36}$$

From equation 2.36, the momentum change with s can then be calculated from Hamilton's equation as

$$d_s p_{\{x,y\}} = -d_{\{x,y\}}\mathcal{H}. \tag{2.37}$$

For some higher-order multipoles, such as sextupoles ($n = 2$) and octupoles $n = 3$, this will introduce an amplitude dependent detuning along with other non-linear effects. These higher-order magnets are all found in the LHC and can affect the particle dynamics [3, 13]. Some of the non-linear effects that arise from sextupoles and octupoles will be reviewed in the following section.

2.1.4 Non-Linear Dynamics

As discussed previously, the tune $Q_{x,y}$ of a machine is the number of betatron oscillations of a particle around the reference trajectory. Much like a harmonic oscillator, resonances exist that can cause the betatron oscillations to become driven [14]. This can lead to particle motion becoming unstable, with unstable motion leading to particle loss from the machine if the oscillation is not damped by a correcting magnet or some other physical process. Resonance behaviour in an accelerator arises due to non-linearities in the lattice. For example magnetic errors can excite resonance as well as higher-order multipoles or beam-beam interactions. The resonance condition is given by [3, 4] as

$$aQ_x + bQ_y = c, \qquad a, b, c \in Z \tag{2.38}$$

where the order of the resonance (n), is given by

$$|a| + |b| = n. \tag{2.39}$$

The resonance diagram for c values up to 5 is shown in figure 2.3. In figure 2.3

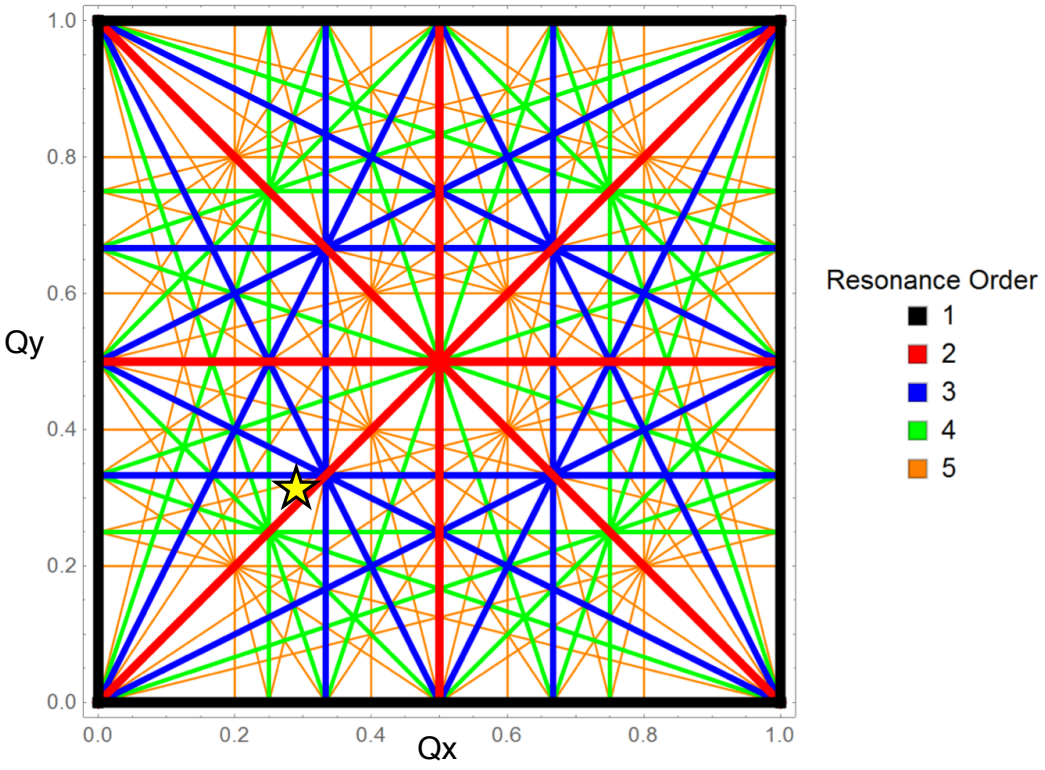

FIGURE 2.3: Non-integer resonance diagram up to 5^{th} order between 0 and 1 in the horizontal (Q_x) and vertical planes (Q_y) with the LHC fractional working point identified at $Q_x = 0.31$ and $Q_y = 0.32$ at collision [15].

it can be seen that the resonance lines are not all the same thickness. Resonant behaviour does not just occur at the non-integer resonance but at some finite region around that resonance. This is known as the stop band width and is discussed in detail in reference [4]. For hadron machines like the LHC, the higher-order resonances could have a significant impact on beam stability which may lead to particle losses.

2.1.4.1 Chromaticity

Energy dependent effects such as dispersion arise from difference between the particle momentum and the reference particle momentum p_0. Additionally, off-reference momentum particles will experience a variation of tune which is dependent on the deviation from the reference momentum; this is called *chromaticity*. For example, particles travelling through a quadrupole with momenta that lies off-reference will experience a different quadrupole field to that of the ideal particle. As a result each particle will have a different focal point after the quadrupole. A schematic of chromaticity is shown in figure 2.4. Considering the tune variation

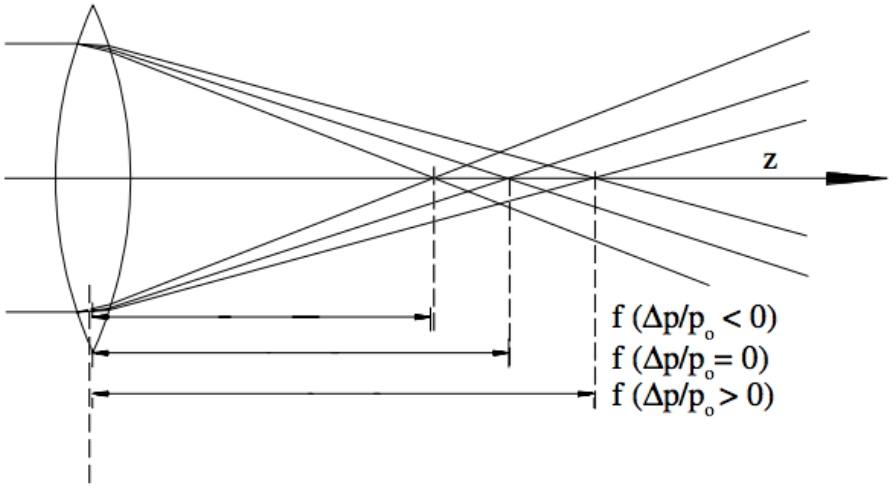

FIGURE 2.4: Schematic showing chromatic effects due to a quadrupole for different off-reference momentum particles [4].

with momentum deviation

$$\delta = \frac{p_1 - p_0}{p_0},$$

then the linear and non-linear chromatic terms can be written from the Taylor expansion of the tune as,

$$Q_{x,y}\left(\bar{p}\right) = Q_{x_0,y_0} + \partial_{\bar{p}} Q_{x,y} \cdot \bar{p} + \frac{\partial^2_{\bar{p}} Q_{x,y}}{2} \cdot \bar{p}^2 + ... + \frac{\partial^n_{\bar{p}} Q_{x,y}}{n!} \cdot \bar{p}^n. \tag{2.40}$$

The differential $\partial_{\vec{p}}^{n} Q_{x,y}$ is often denoted in the literature as Q', where Q' is called the chromaticity and higher-order primed terms are often referred to as the non-linear chromaticity [4]. Higher-order magnets such as quadrupoles and sextupoles introduce chromaticity which can impact a particle's trajectory through the field. In the LHC, these higher-order terms can all have an impact on the beam dynamics [13].

In addition to chromaticity, non-linear and collective effects such as the beam-beam interaction can also introduce a detuning with amplitude. The detuning with amplitude is defined as the tune variation as a function of the particle action. Similarly to the chromaticity the detuning with amplitude can be derived using a Taylor expansion about the unperturbed tune as a function of particle emittance $\epsilon_{x,y}$. Expanding the tune around the particle emittance in the horizontal and vertical planes gives

$$\begin{aligned} Q_{x,y}(\epsilon_x, \epsilon_y) = Q_{x_0,y_0} + \partial_{\epsilon_x} Q_{x,y} \epsilon_x + \partial_{\epsilon_y} Q_{x,y} \epsilon_y + \\ + \frac{1}{2} \left(\partial^2_{\epsilon_x} Q_{x,y} \epsilon_x^2 + \partial^2_{\epsilon_y} Q_{x,y} \epsilon_y^2 + 2 \partial_{\epsilon_x \epsilon_y} Q_{x,y} \epsilon_x \epsilon_y \right) + \dots \, . \end{aligned} \tag{2.41}$$

The amplitude detuning arising due to non-linearities in the magnetic and electric fields can cause particles to diffuse to large amplitudes, or be pushed onto resonances. It should however be noted that amplitude detuning is not the only mechanism capable of causing particles to move onto resonant tunes. Additional mechanisms include the effect of changing chromaticity for particles with non-zero $\delta p/p$, power ripple in the magnets, and linear coupling. The concept of linear coupling will be introduced in the following section. Amplitude dependent detuning can however be beneficial and can minimise coherent motion of the bunch. In the LHC, a common source of amplitude detuning arises due Landau damping produced by the octupole magnets and the beam-beam interaction [16]. The beam-beam interaction and Landau damping will also be discussed in more

detail later in section 2.2 and 2.1.6.

In addition, another mechanism which is often confused with Landau damping is called beam decoherence. Decoherence occurs when a beam is excited by a single kick. This kick excites betatron oscillations and these oscillations combined with amplitude detuning and chromaticity cause the particles in the bunch to oscillate out of phase with one another and the beam is said to have decohered. Unlike Landau damping, decoherence will lead to an emittance growth.

2.1.5 Linear Coupling

In the previous sections only uncoupled motion has been considered, however in a real machine coupled motion between the x and y plane can arise due to some magnetic components in the lattice. Linear coupling can have a significant impact on the particle dynamics and can lead to resonant motion and dynamic aperture reduction. The topic of dynamic aperture will be introduced in more detail in chapter 6 but the impact of linear coupling on the particle motion is described briefly. Linear betatron coupling can arise from a number of magnetic elements in a machine. Solenoid and skew-quadrupole fields are such examples of magnetic elements which can lead to coupled motion [8]. To include coupled motion due to a skew quadrupole, a simple derivation from Hill's equations 2.9 can be considered. Hill's equations when coupled are no longer a function of one coordinate and instead will lead to two coupled differential equations in the transverse planes. These equations are

$$x'' + k_x x + \bar{\kappa}_x y = 0, \tag{2.42}$$

$$y'' - k_y y + \bar{\kappa}_y x = 0, \tag{2.43}$$

where the function $\bar{\kappa}_{x,y}$ is the focussing strength of the skew quadrupole and is given by

$$\bar{\kappa} = \frac{\varphi^2}{z^2}. \tag{2.44}$$

Following the approach by Wiedermann [4] the *ansatz* is chosen of the form

$$x = a_1 \cos\varphi + \frac{b_1}{\sqrt{\bar{\kappa}}} \sin\varphi + c_1 \cosh\varphi + \frac{d_1}{\sqrt{\bar{\kappa}}} \sinh\varphi, \tag{2.45}$$

$$y = a_2 \cos\varphi + \frac{b_2}{\sqrt{\bar{\kappa}}} \sin\varphi + c_2 \cosh\varphi + \frac{d_2}{\sqrt{\bar{\kappa}}} \sinh\varphi, \tag{2.46}$$

where φ varies from 0 to length L of the quadrupole and the constants $a_{1,2}, b_{1,2}, c_{1,2}$ and $d_{1,2}$ account for the focussing and defocussing components of the skew quadrupole in both planes. These constants must be related to each other and hence at the beginning of the quadrupole when $z = 0$ the constants relate to one another through

$$x_0 = a_1 + c_1, \quad y_0 = a_2 + c_2, \tag{2.47}$$

$$x_0' = b_1 + d_1, \quad y_0' = b_2 + d_2. \tag{2.48}$$

Since the motion is coupled, the position dependent coefficients must be related to one another. Similarly the momentum dependent coefficients will also be related. This leads to

$$a_1 = a_2, \quad b_1 = b_2, \quad c_1 = -c_2, \quad d_1 = -d_2. \tag{2.49}$$

Now the coefficients have been constrained, the transformation matrix can be derived for a skew quadrupole and is given as in ref [4]. The matrix $\mathcal{M}_{skew}$ will transform the original coordinates x_0, x_0', y_0, y_0' to the new coordinates x, x', y, y',

as a particle travels through the skew quadrupole. This matrix is given by

$$\mathcal{M}_{skew} = \begin{pmatrix} \mathcal{C}^{+} & \frac{1}{\sqrt{\bar{\kappa}}}\mathcal{S}^{+} & \mathcal{C}^{-} & \frac{1}{\sqrt{\bar{\kappa}}}\mathcal{S}^{-} \\ -\sqrt{\bar{\kappa}}\mathcal{S}^{-} & \mathcal{C}^{+} & -\sqrt{\bar{\kappa}}\mathcal{S}^{+} & \mathcal{C}^{-} \\ \mathcal{C}^{-} & \frac{1}{\sqrt{\bar{\kappa}}}\mathcal{S}^{-} & \mathcal{C}^{+} & \frac{1}{\sqrt{\bar{\kappa}}}\mathcal{S}^{+} \\ -\sqrt{\bar{\kappa}}\mathcal{S}^{+} & \mathcal{C}^{-} & -\sqrt{\bar{\kappa}}\mathcal{S}^{-} & \mathcal{C}^{+} \end{pmatrix}, \tag{2.50}$$

where $\mathcal{C}^{\pm} = \cos\varphi \pm \cosh\varphi$ and $\mathcal{S}^{\pm} = \sin\varphi \pm \sinh\varphi$. The terms $|\mathcal{C}^{+}|$ and $|\mathcal{C}^{-}|$ can generally be considered as the direction of the tune shift due to the linear coupling. In the LHC, due to the choice of working point, the $|\mathcal{C}^{-}|$ coupling is generally more of a concern as this tune shift can cause particles to move closer to the third order resonance.

2.1.6 Landau Damping

As a bunch travels through the elements of an accelerator lattice, wake fields can excite coherent waves which can displace the bunch centroid from its equilibrium position [14, 17]. The wake fields will act on all of the particles in the bunch, importantly however, there is a frequency spread meaning that all particles will have slightly different frequencies. As a result each individual particle will have a different response to the coherent wave. This frequency spread means that some particles will gain energy from other particles whilst others will loose energy from surrounding particles. This exchange of energy between the particles in the bunch will damp the coherent motion of the bunch centroid and act in a way to stabilise the coherent oscillation. An in-depth discussion along with a mathematical description can be found in ref [14, 17, 18].

This concludes the single particle dynamic part of the introduction. In the next section, the dynamics of the beam-beam interaction will be discussed.

2.2 The Beam-Beam Interaction

For a colliding beam storage ring like the LHC, the main objective is to generate luminosity by colliding two proton beams at dedicated interaction points (IPs) around the machine. The resulting interaction between beams produce particle collisions that are of interest to the high-energy physics community. The collisions between the bunches result in the interaction of the electromagnetic fields of the two beams. This interaction is known as the beam-beam interaction and cannot be avoided in the LHC. These effects can be strong and non-linear and can impede machine performance. In the following section, luminosity and the beam-beam interaction are introduced. The concept of luminosity is discussed along with a number of simple calculations corresponding to operational scenarios which may impact luminosity performance. Then the beam-beam force is derived and the effects that arise from this force are reviewed.

2.2.1 Luminosity

The luminosity is a key machine performance indicator for the LHC. Luminosity is generated through head-on collisions between bunches in counter rotating beams. In a standard operational physics fill in the LHC, the bunches will collide at 4 IPs around the ring. IP1 and IP5 house the two low β experiments, ATLAS and CMS. These detectors were responsible for detecting the Higgs boson and require tightly squeezed beams with small β^*. This generates high luminosity in order to study rare physics events. The experiment ALICE is located at IP2. This experiment investigates heavy ion collisions between lead ions. Finally LHCb, located at IP8 investigates physics involving the bottom quark. There are a total of seven experiments located around the LHC ring all requiring different operational requirements from the machine in order to study different particle

physics processes. This provides a number of operational challenges for the machine that must be addressed. Firstly the concept of luminosity in a colliding beam storage ring like the LHC will be discussed.

The luminosity is defined as the ratio of the number of events detected over a specified time period to the interaction cross section. The luminosity can hence be written as

$$d_t R = \mathcal{L} \cdot \sigma_{cross}, \tag{2.51}$$

where R is the number of collisions, $\mathcal{L}$ is the luminosity, and σ_{cross} is the cross section for a given interaction rate. Luminosity in the LHC is generated by colliding bunches and is dependent on the colliding bunch distributions. The instantaneous luminosity can be calculated following the procedure in [16] from

$$\mathcal{L} \propto \kappa \int_{-\infty}^{\infty} \rho_1(x, y, z; z_0) \cdot \rho_2(x, y, z; z_0) \mathrm{d}\mathbf{r}^4, \tag{2.52}$$

where $\mathbf{r} = (x, y, z, z_0)$ and z_0 is the time-like component, ρ_i is the charge density distribution with the subscripts $1, 2$ denoting which beam, and κ is the kinematic relativistic factor,

$$\kappa = \sqrt{(\bar{v_1} - \bar{v_2})^2 - \frac{(\bar{v_1} \times \bar{v_2})^2}{c^2}}.$$

Since the bunches in the LHC can be considered to have a Gaussian charge density distribution with equal bunch sizes in the transverse planes, then the integral 2.52 is re-written as

$$\mathcal{L} = \kappa N_1 N_2 f_{rev} N_b \int_{-\infty}^{\infty} \int_{-\infty}^{\infty} \int_{-\infty}^{\infty} \exp\left[-\frac{x^2}{\sigma_x^2} - \frac{y^2}{\sigma_y^2} - \frac{z^2}{2\sigma_z^2} - \frac{z_0^2}{2\sigma_z^2}\right] \mathrm{d}x\mathrm{d}y\mathrm{d}z\mathrm{d}z_0, \tag{2.53}$$

where $\kappa = 2$, since $\bar{v}_1 = -\bar{v}_2$ and the collisions are in the absence of any crossing angle ($\alpha = 0$). The parameters $N_{1,2}$ correspond to the bunch population, f_{rev} is the frequency of revolution around the machine, and N_b is the number of bunches in the beam assuming all of the bunches have the same population. The transverse bunch size at the IP is

$$\sigma_{x,y} = \sqrt{\epsilon_{x,y}\beta^*_{x,y}}, \tag{2.54}$$

where $\beta^*_{x,y}$ is the β-function at the IP. Excluding any coupling between the planes and using the identity

$$\int_{-\infty}^{\infty} e^{-at^2} dt = \sqrt{\frac{\pi}{a}}, \tag{2.55}$$

and integrating equation 2.53, leaves

$$\mathcal{L} = \frac{N_1 N_2 f_{rev} N_b}{4\pi\sigma_x\sigma_y}. \tag{2.56}$$

Equation 2.56 gives the instantaneous luminosity for a round bunch. Extending the equation to include elliptical bunches can be performed by considering equal bunch lengths $\sigma_{1,z} = \sigma_{2,z}$ but unequal bunch sizes $\sigma_{1,x} \neq \sigma_{2,x}$ and $\sigma_{1,y} \neq \sigma_{2,y}$. This will give the luminosity formula for an elliptical bunch as

$$\mathcal{L} = \frac{N_1 N_2 f_{rev} N_b}{2\pi\sqrt{\sigma^2_{1,x} + \sigma^2_{2,x}}\sqrt{\sigma^2_{1,y} + \sigma^2_{2,y}}}. \tag{2.57}$$

The approach detailed in [16] is easily extendable to include more realistic collision scenarios such as in the presence of a crossing angle and transverse offset. Including these effects will be discussed in the next section.

2.2.1.1 Luminosity with Crossing Angle and Transverse Offsets

The result obtained in equation 2.56 is an ideal case in which there is no transverse offset between the two beams and no crossing angle. To provide a more realistic interpretation of luminosity in a colliding beam storage ring, the additional effects from crossing angle and offset are included. Following the method in [19], an adjusted coordinate system is introduced and the schematic of these coordinates is shown in figure 2.5. The adjusted coordinates include the crossing angle α and the transverse offset $\delta_{1,2}$ with respect to the reference orbit. The subscripts $1, 2$ denote which beam. The transformation between Cartesian and the modified

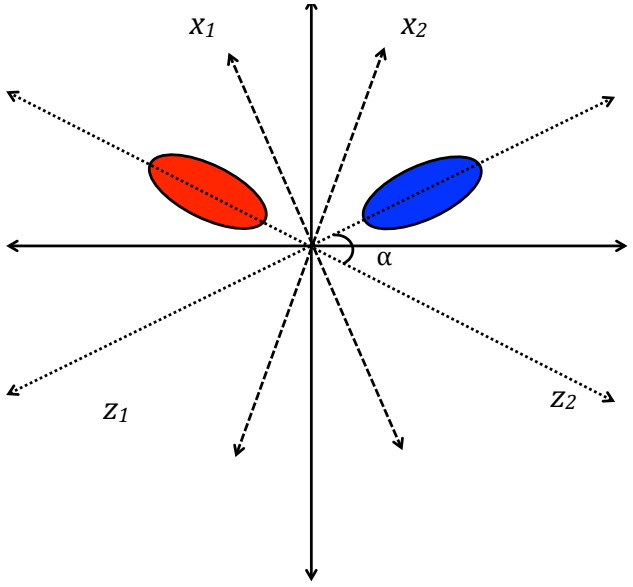

FIGURE 2.5: Schematic of the coordinate system of two bunches colliding with an offset and a crossing angle α.

Cartesian coordinates is given by

$$x_1 = \delta_1 + x\cos\alpha - z\sin\alpha, \qquad z_1 = z\cos\alpha + x\sin\alpha,$$

$$x_2 = \delta_2 + x\cos\alpha + z\sin\alpha, \qquad z_2 = z\cos\alpha - x\sin\alpha.$$

Starting from equation 2.52 and transforming to the modified coordinate system gives

$$\mathcal{L} = \kappa N_1 N_2 f_{rev} N_b \int_{-\infty}^{\infty} \rho_{1,x}(x_1)\rho_{1,y}(y_1)\rho_{1,z}(z_1 - z_0) \cdot \rho_{2,x}(x_2)\rho_{2,y}(y_2)\rho_{2,z}(z_2 + z_0)\mathrm{d}\hat{\mathbf{r}}^4, \tag{2.58}$$

where κ is the kinematic factor and $\hat{\mathbf{r}} = (x_{1,2}, y_{1,2}, z_{1,2}, z_0)$. To initially treat this problem, the offset in the horizontal and vertical plane will be set to zero ($\delta_{1,2} = 0$) and the crossing angle will be assumed to be in the horizontal plane only. Then for a 3-dimensional Gaussian charge density distribution, the y and z_0 integrals can be be evaluated using the identity

$$\int_{-\infty}^{\infty} e^{-(at^2+bt+c)}\mathrm{d}t = \sqrt{\frac{\pi}{a}} e^{\frac{b^2-ac}{a}}.$$

This gives the luminosity with only the x and z integrals to be performed. With the offset set to zero, substituting the coordinate transform, $x_{1,2}$ and $z_{1,2}$ into the x and z Gaussian charge density distribution gives,

$$\mathcal{L} = \frac{N_1 N_2 f_{rev} N_b}{8\pi^2 \sigma_z \sigma_x^2 \sigma_y} \kappa \iint e^{-\frac{x^2\cos^2\alpha + z^2\sin^2\alpha}{\sigma_x^2}} e^{-\frac{x^2\sin^2\alpha + z^2\cos^2\alpha}{\sigma_z^2}} \mathrm{d}x\mathrm{d}z. \tag{2.59}$$

For small values of x and α the paraxial approximation can be used. The paraxial approximation gives $\sin\alpha \approx \tan\alpha \approx \alpha$. The resulting equation is comparable to the expression 2.56 , but includes an additional reduction factor. Hence, the luminosity varies with crossing angle α as,

$$\mathcal{L} = \frac{N_1 N_2 f_{rev} N_b}{4\pi\sigma_x\sigma_y} \cdot F_{red}(\alpha), \tag{2.60}$$

where the approximation $\sigma_z \gg \sigma_{x,y}$ can be used since in the LHC at IP1, $\sigma_x \approx 16\ \mu$m and $\sigma_z = 7.5$ cm, then the reduction factor $F_{red}(\alpha)$ is expressed as,

$$F_{red}(\alpha) = \frac{1}{\sqrt{1 + \left(\frac{\sigma_z}{\sigma_x}\tan\alpha\right)^2}}. \tag{2.61}$$

For LHC-like bunches, the function $F_{red}(\alpha)$ will improve as the crossing angle is reduced. The dependence with crossing angle for bunch lengths of $\sigma_z = 7.5$ cm and various operational β^*s are shown in figure 2.6. The reduction factor

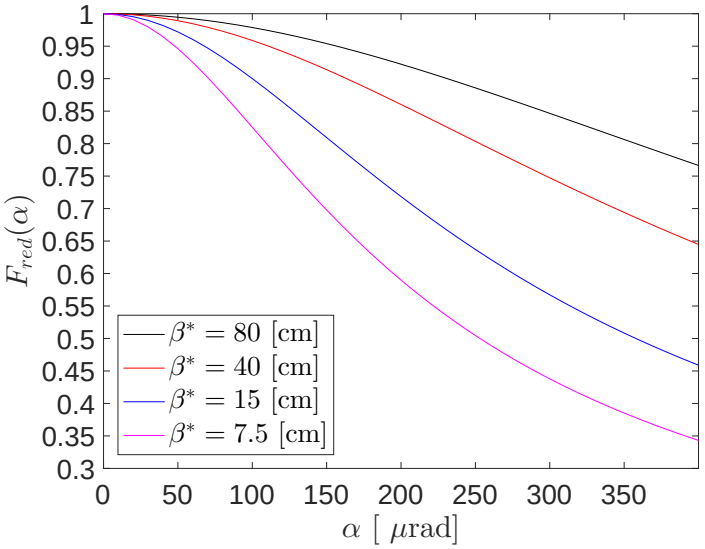

FIGURE 2.6: Variation of $F_{red}(\alpha)$ with full crossing angle α for various different β^* options in the LHC and HL-LHC

calculated above only includes a crossing angle; in reality the bunches may also collide with an offset. Following the same method but for a non-zero δ_x, and assuming the crossing angle and offset is in the horizontal plane yields, after the y and z integration,

$$\mathcal{L} = \frac{N_1 N_2 f_{rev} N_b}{8\pi^2 \sigma_z \sigma_x^2 \sigma_y} \kappa \iint e^{-\frac{x^2\cos^2\alpha + z^2\sin^2\alpha}{\sigma_x^2}} e^{-\frac{x^2\sin^2\alpha + z^2\cos^2\alpha}{\sigma_z^2}} \times e^{-\frac{\delta_{1,x}^2 + \delta_{2,x}^2 + 2(\delta_{1,x}+\delta_{2,x})x\cos\alpha - 2(\delta_{2,x}-\delta_{1,x})z\sin\alpha}{2\sigma_x^2}} dx dz. \tag{2.62}$$

Performing the integration over the x variable first and introducing additional variables A, B, and W from [16],

$$A = \frac{\sin^2\alpha}{\sigma_x^2} + \frac{\cos^2\alpha}{\sigma_z^2}, \qquad B = \frac{(\delta_2 - \delta_1)\sin\alpha}{2\sigma_x^2}, \qquad W = e^{-\frac{(\delta_2-\delta_1)^2}{4\sigma_x^2}}, \tag{2.63}$$

leaves the luminosity integral in the form,

$$\mathcal{L} = \frac{N_1 N_2 f_{rev} N_b}{8\pi^{3/2}\sigma_z}\kappa \int_{-\infty}^{\infty} W \frac{e^{-(Az^2+2Bs)}}{\sigma_x\sigma_y}\mathrm{d}z. \tag{2.64}$$

This can be written in terms of equation 2.56, again with additional reduction terms cast in terms of W, $\exp\frac{B^2}{A}$ and F_α. The luminosity including these reduction factors is written in equation 2.65,

$$\mathcal{L} = \frac{N_1 N_2 f_{rev} N_{bunch}}{4\pi\sigma_x\sigma_y} \cdot W \cdot e^{\frac{B^2}{A}} \cdot F_\alpha. \tag{2.65}$$

Equation 2.65 enables the instantaneous luminosity to be calculated whilst also including crossing angle and an offset. Figure 2.7 shows the luminosity as a function of different offsets and crossing angles. The luminosity can be considered as

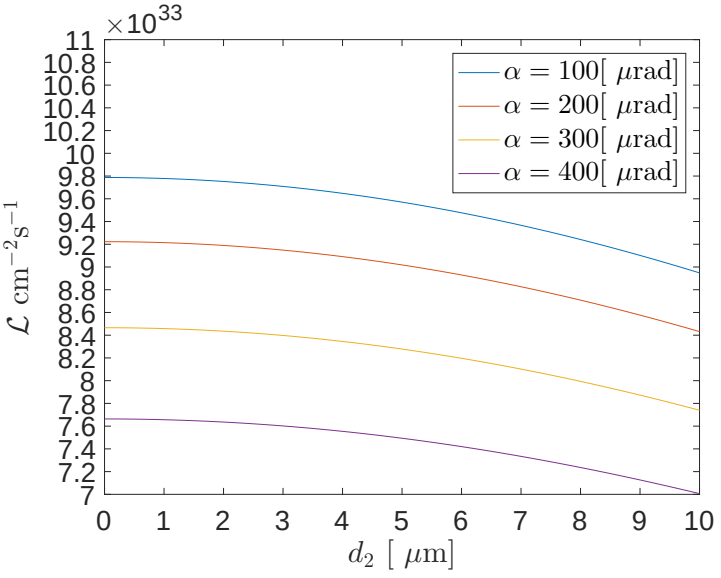

FIGURE 2.7: Luminosity variation as a function of offset and crossing angle

the product of the round beam head-on colliding case and the reduction factors.

The reduction factors are sometimes collectively labeled as the luminosity reduction factor F_{loss}. In a machine like the LHC, the luminosity reduction factor is approximately of the order of $F_{loss} \sim 0.8$, with the largest luminosity reduction factor arising due to the crossing angle α.

2.2.1.2 Integrated Luminosity

In addition to the instantaneous luminosity, the integrated luminosity is another useful parameter for determining the luminosity performance of a machine over an extended period of time. The instantaneous luminosity will define the luminosity at a given moment in time, i.e between two colliding bunches or two colliding beams. The integrated luminosity on the other hand, defines the luminosity over a given period of time and will include operational aspects such as turn-around time between fills [16]. The integrated luminosity is expressed as

$$\mathcal{L}_{int} = \int_0^{\tau} \mathcal{L}(\tau) \mathrm{d}\tau. \tag{2.66}$$

Figure 2.8 shows the integrated luminosity and the luminosity performance of the LHC from the 2011 to 2016 runs. Throughout the operational runs, the luminosity performance has increased, exceeding expectations significantly. One contributing factor to the high luminosity performance is due to tight controls on the long-range beam-beam interaction, the suppression of instabilities and operational experience from previous runs of the LHC [20]. The interaction between the two colliding beams will also impact the particle dynamics over the duration of a fill. In the next section, the beam-beam force is introduced.

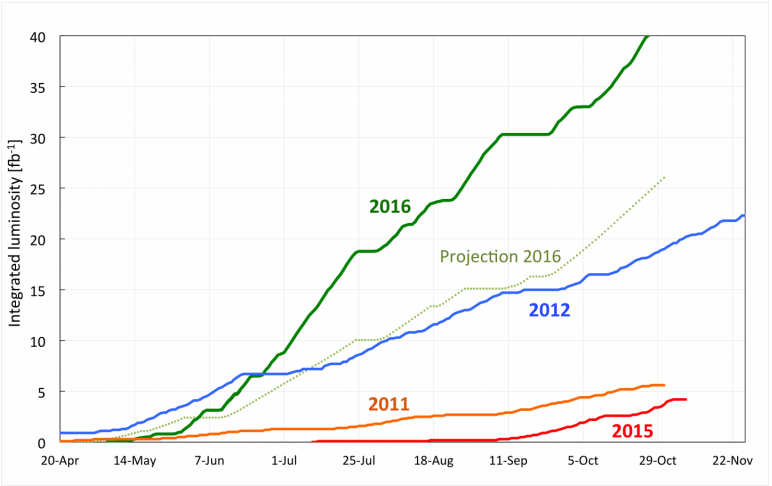

FIGURE 2.8: Integrated luminosity in the LHC [21].

2.2.2 The Beam-Beam Force

The beam-beam force can be computed by considering the charge density distribution of a bunch and calculating the electric field that a counter rotating test particle will experience, as it traverses the bunch. From this, the change in momentum imparted to that test particle can be obtained. There are a number of possible approaches that allow the electric field of a charge distribution to be calculated. Traditionally, as in the literature, Poisson's equation is solved [16, 22, 23], although an alternative approach from Maxwell's equations is proposed and outlined in Chapter 4. Poisson's equation is a second order, inhomogeneous partial differential equation given by

$$\nabla^2 \varphi = \frac{\rho}{\epsilon_0}, \tag{2.67}$$

where the Laplace operator is given by $\nabla^2 = \partial^2_{x_i} + \partial^2_{x_{i+1}} + ... + \partial^2_{x_n}$, φ is the electric scalar potential, ϵ_0 is the permittivity of free space. and ρ is the charge density distribution. This equation can be solved by applying the superposition principle through a convolution of a Green's function with the charge density

distribution [24]. The electric potential is calculated using

$$\varphi(x,y,z) = \frac{1}{\epsilon_0}\iiint \mathcal{G}(x,y,z,x',y',z')\rho(x',y',z')\mathrm{d}x'\mathrm{d}y'\mathrm{d}z', \tag{2.68}$$

where $\mathcal{G}$ is the Green's function [1, 24] and the primed coordinates represent the integral over the charge density distribution, and the unprimed coordinates are the integral over the potential. Following the method in [16, 25], this can be expressed using the δ-function in the 3-dimensions as,

$$\mathcal{G}(x,y,z,x',y',z') = \frac{1}{4\pi^{3/2}}\int_0^\infty \frac{1}{q^{3/2}} e^{-\frac{|x-x'|^2-|y-y'|^2-|z-z'|^2}{q}}\mathrm{d}q. \tag{2.69}$$

Taking the Green's function and substituting a Gaussian charge density distribution into equation 2.68 gives the integral to be evaluated as

$$\varphi(x,y,z) = \frac{1}{\epsilon_0}\frac{1}{4\pi^{3/2}}\iiiint \frac{1}{q^{3/2}} e^{-\frac{|x-x'|^2-|y-y'|^2-|z-z'|^2}{q}} e^{-\frac{x'^2}{2\sigma_x^2}-\frac{y'^2}{2\sigma_y^2}-\frac{z'^2}{2\sigma_z^2}}\mathrm{d}x'\mathrm{d}y'\mathrm{d}z'\mathrm{d}q. \tag{2.70}$$

For a simple Gaussian charge density distribution, the integrals can be written separately in terms of x', y' or z', and can be solved individually. The x' integration can be solved using the identity 2.71,

$$\int_{-\infty}^{\infty} \frac{1}{\sqrt{2\pi}\sigma_x^2} e^{-\frac{x'^2}{2\sigma_x^2}} \frac{1}{\sqrt{q}} e^{-\frac{|x-x'|^2}{q}}\mathrm{d}x' = \frac{e^{-\frac{x^2}{2\sigma_x^2+q}}}{\sqrt{2\sigma_x^2+q}}. \tag{2.71}$$

Applying this integral identity to the remaining variables, the 3-dimensional potential can be expressed with just the integral over q to be performed. The integral is often left in the form given by [16, 22, 25],

$$\varphi(x,y,z) = \frac{nq}{4\pi\epsilon_0}\frac{1}{\sqrt{\pi}}\int_0^\infty \frac{e^{-\frac{x^2}{q_x}-\frac{y^2}{q_y}-\frac{z^2}{q_z}}}{\sqrt{q_x q_y q_z}}\mathrm{d}q, \tag{2.72}$$

where n is the number of particles in the bunch and the $q_{x,y,z}$ terms are,

$$q_x = 2\sigma_x^2 + q, \qquad q_y = 2\sigma_y^2 + q, \qquad q_z = 2\sigma_z^2 + q.$$

For simplicity and brevity, the 2-dimensional round bunch case is considered here, with the elliptical beam case shown in [22]. The round bunch potential can be calculated by setting $z = 0$ and transforming to cylindrical coordinates through $x = r\cos\vartheta, y = r\sin\vartheta$. This gives the round bunch potential as

$$\varphi(r) = \frac{nq}{4\pi\epsilon_0}\int_0^\infty \frac{e^{-\frac{r^2}{q_r}}}{\sqrt{q_r}}\mathrm{d}q, \tag{2.73}$$

where $q_r = 2\sigma_r^2 + q$. This potential is related to the electric field of the bunch by the gradient of the scalar potential. Hence using

$$E = -\nabla\varphi, \tag{2.74}$$

the electric field in the rest frame of the bunch is

$$E(\mathbf{r}) = -\frac{nq}{4\pi\epsilon_0}\frac{1}{r}\left[1 - e^{-\frac{r^2}{2\sigma_r^2}}\right]. \tag{2.75}$$

To calculate the force experienced by a counter rotating test particle traversing the Gaussian bunch, the force generated by the electric fields must be computed. To achieve this, the electric field is boosted into the collision frame. A schematic of the electric field before and after the boost in the two reference frames is shown in figure 2.9. In the rest frame of the bunch the electric field lines propagate out in all directions. After the boost, the field lines are confined almost entirely to the transverse planes, orthogonal to the direction of the boost. A longitudinal component of the electric field will however be introduced for non-zero crossing angles. The Lorentz boost of the electromagnetic field tensor to the collision

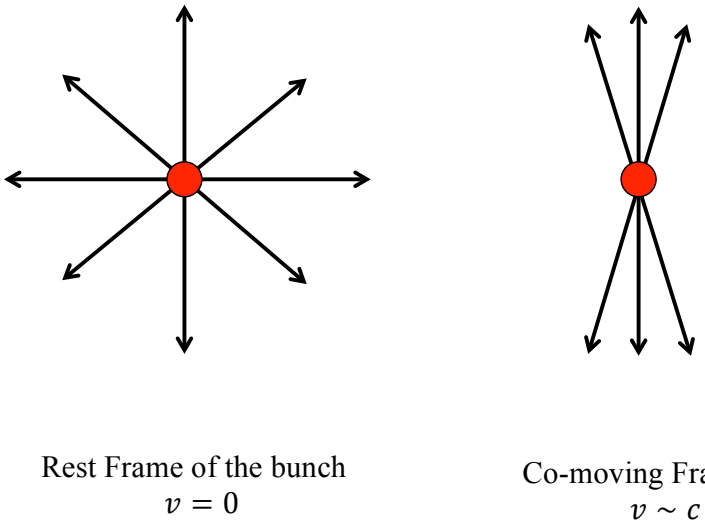

FIGURE 2.9: Schematic of the electric field lines in the rest frame and after the boost. The opening angle of the field line varies with $1/\gamma$.

frame is given by

$$F'_{\mu\nu} = L^{\rho}_{\mu} F_{\rho\sigma} L^{T\sigma}_{\nu}, \tag{2.76}$$

where $F_{p\sigma}$ is the electromagnetic field tensor and L^{p}_{μ} is the boost matrix [26]. Requiring that the boost acts in the z direction yields the following transformation of the electric fields,

$$\mathbf{E} = \begin{pmatrix} \gamma(\bar{E}_x + v_r \bar{B}_y) \\ \gamma(\bar{E}_y - v_r \bar{B}_x) \\ \bar{E}_z, \end{pmatrix}, \tag{2.77}$$

$$\mathbf{B} = \begin{pmatrix} \gamma(\bar{B}_x - v_r \frac{\bar{E}_y}{c^2}) \\ \gamma(\bar{B}_y + v_r \frac{\bar{E}_x}{c^2}) \\ \bar{B}_z, \end{pmatrix}, \tag{2.78}$$

where v_r is the velocity and barred terms $(\bar{E}, \bar{B})$ represent the electric and magnetic fields in the rest frame. Hence the Lorentz force in the collision frame of

the bunch acting on a counter rotating test particle with charge q is given by

$$\begin{pmatrix} F_x \\ F_y \\ F_z \end{pmatrix} = q \begin{pmatrix} \gamma_r E_x \left(1 - u_z v_r / c^2\right) \\ \gamma_r E_y \left(1 - u_z v_r / c^2\right) \\ E_z + \gamma_r v_r (E_x u_x + E_y u_y)/c^2 \end{pmatrix}. \tag{2.79}$$

Now these expressions have been obtained, the round bunch electric field obtained in equation 2.75 can be used to calculate the force. If the particles in the bunch are at rest with respect to one another, the problem can be considered electrostatic and hence the magnetic field can be set to $\bar{\mathbf{B}}$=0 in the rest frame. Using the expressions for the electric and magnetic field, 2.77 and 2.78 respectively, and boosting along the z axis gives the electric and magnetic fields in the collision frame as

$$E_r = -\frac{\gamma n q}{4\pi\epsilon_0}\frac{1}{r}\left[1 - e^{-\frac{r^2}{2\sigma_r^2}}\right], \qquad B_\vartheta = -\frac{n q \beta_r c \mu_0}{4\pi}\frac{1}{r}\left[1 - e^{-\frac{r^2}{2\sigma_r^2}}\right],$$

with the beam-beam force given by

$$F_{bb} = -\frac{n q^2 (1 + \beta_r^2)}{2\pi\epsilon_0}\frac{1}{r}\left[1 - e^{-\frac{r^2}{2\sigma_r^2}}\right]. \tag{2.80}$$

Equation 2.80 gives the beam-beam force that a counter rotating test particle will experience. The beam-beam force is shown in figure 2.10 and can be seen to be non-linear towards larger test particle amplitudes. Hence, due to the non-linearity of the beam-beam force, the distance of a test particle from a Gaussian bunch will have an important impact on the bunch dynamics. Particles with small radial amplitude experience a linear beam-beam force and this applies to short range interactions and is known as the *head-on* beam-beam interaction. The maximum and minimum of the force is located at 1.59 σ and this numerical result is a consequence of the Gaussian distribution. Large amplitude particles observe a non-linear force acting over large distances, this is known as the *long-range*

beam-beam force. The details of the two types of interactions will be discussed in detail in the next section. In order to consider the impact of the long-range

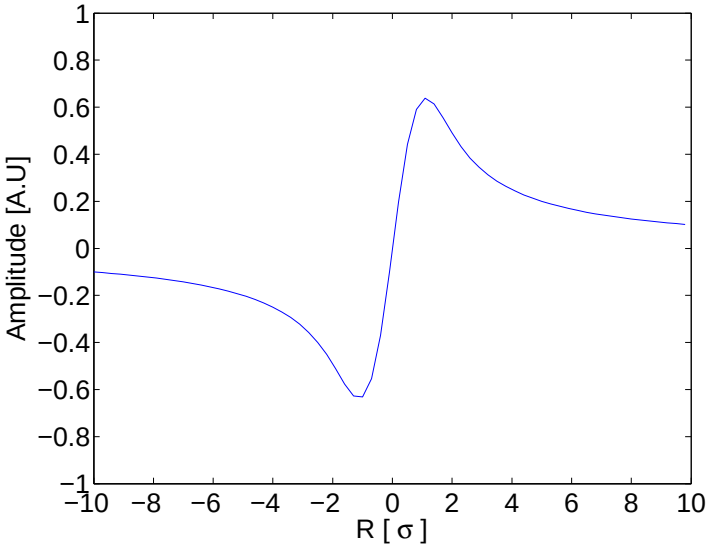

FIGURE 2.10: The beam-beam force in arbitrary units for a radial symmetric bunch versus the radial coordinate R in units of bunch sigma. The maximum and minimum of the beam-beam force is located at $R = \pm 1.59\ \sigma$.

and head-on beam-beam force on the particle dynamics, the momentum kick to the particle should be derived. The momentum kick imparted by the bunch onto the counter rotating test particle can be calculated easily by integrating the beam-beam force over the time taken for the test particle to move through the length of the bunch. Introducing the time-like variable $z = s - ct$, then the kick is calculated from the integral

$$\Delta r' = \frac{\Delta P}{P} = \int_{-\infty}^{\infty} F_{bb}(r,t)dt, \tag{2.81}$$

which when evaluated, yields in Cartesian coordinates,

$$\Delta x' = -\frac{2r_0 N}{\gamma_r}\frac{x}{r^2}\left(1 - e^{-\frac{r^2}{2\sigma_r^2}}\right), \tag{2.82}$$

where the classical particle radius r_0 is introduced and given by

$$r_0 = \frac{1}{4\pi\epsilon_0}\frac{q^2}{m_e c^2}. \tag{2.83}$$

From the momentum change or kick due to the beam-beam force described above, the impact of the head-on and long-range beam-beam interaction on particle dynamics is discussed in the next section.

2.2.3 Head-On Beam-Beam Effects

The head-on (HO) beam-beam interaction occurs when two counter rotating bunches collide at the IP and generate luminosity. A schematic of the head-on beam-beam interaction is shown in figure 2.11. The head-on beam-beam interaction is characterised by the linear part of the beam-beam force, since this applies to small amplitude particles as shown in figure 2.10. To determine the behaviour of particles at small amplitude the impact on the tune will be considered.

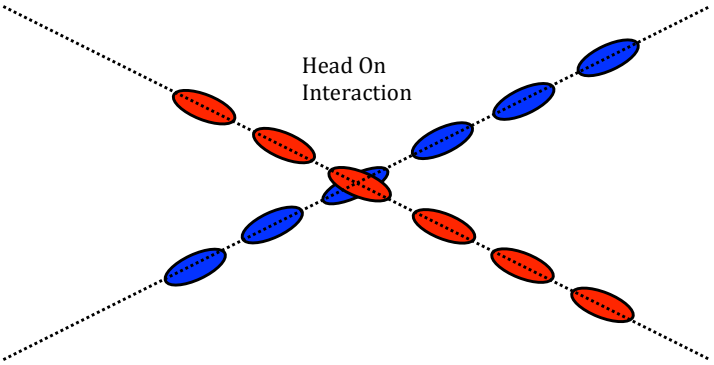

FIGURE 2.11: A schematic of the head-on beam-beam interaction between two colliding beams.

Particle tracking simulations can allow the tune footprint to be calculated. The tune footprint can be calculated by tracking particles of various amplitudes in phase space through the elements of a machine over several turns. Details of

particle tracking will be discussed later in chapter 6. From the resulting tracking simulations, a Fourier transformation can be performed over the particle oscillation as a function of turn number to obtain the frequency data. Using the frequency data, the tune shift (non-linear detuning) due to the beam-beam force can be calculated. The non-linear detuning with the particle amplitude R_J can be obtained using the derivation given in ref [16], and is given as

$$\Delta Q(R_J) = \frac{2\xi_{bb}}{R_J}\left(1 - I_0\left(\frac{R_J}{2}\right)e^{-\frac{R_J}{2}}\right), \tag{2.84}$$

where I_0 is the modified Bessel function, ξ_{bb} is the beam-beam parameter which will be introduced later, and $R_J = \frac{\epsilon\beta}{2\sigma^2}$, where ϵ in this case represents the single particle emittance. Restricting ourselves to the 2-dimensional case, to a particle with tune shifts $\Delta Q_{x,y}$ and amplitudes x, y, the detuning can be calculated and mapped from amplitudes x, y to tune space $Q_{x,y}$. An example of the tune footprint for a head-on colliding bunch is shown in figure 2.12. In this figure 2.12,

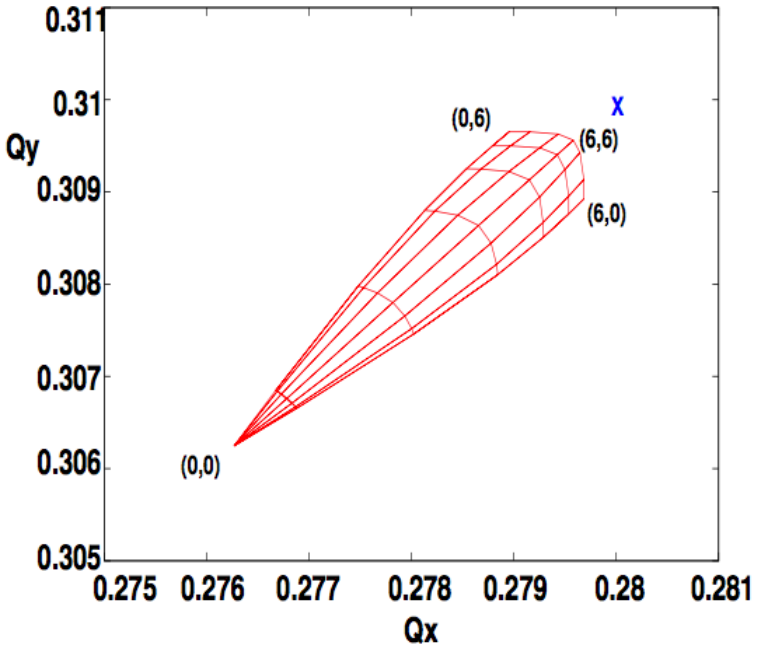

FIGURE 2.12: The tune footprint for a single head-on beam-beam interaction at injection tunes $Q_x = 0.28$ and $Q_y = 0.31$ from ref [16].

each intersection point of the lines represents a pair of amplitudes denoted by

the coordinates (x, y). These amplitudes are mapped to the tune space Q_x, Q_y and show the detuning due to the head-on beam-beam interaction. The head-on beam-beam interaction is stronger than the long-range interaction and hence provides the largest tune shift to a counter rotating particle. This is because the maximum change in momentum of the the beam-beam force, which can be calculated by differentiating the beam-beam force, is located at $r = 0$ [16]. Particles that have the smallest radial amplitudes will have the largest tune shift and hence will be shifted further away from the unperturbed tune. The unperturbed fractional tune in figure 2.12 corresponds to the LHC tunes at injection with $Q_{x,y} = 0.31/0.32$. For particles at large amplitudes and no long-range beam-beam interaction, the tune shift will tend towards the unperturbed tune. The value of this tune shift given within the asymptotic limit is

$$\Delta Q_{\mathrm{HO}} = \pm \frac{N r_0 \beta^*}{4\pi \sigma_x \sigma_y}, \tag{2.85}$$

where the sign of the tune shift depends on the relative beams' charges. When far from resonances and dynamic beta effects [16], this tune shift is approximately equal to the beam-beam parameter $\xi_{bb} \times n_p$, where n_p is the number of interaction points. This is a useful parameter for characterising the strength of the beam-beam interaction in colliding beam storage rings. The linear beam-beam parameter can be calculated by taking asymptotic limit of equation 2.82. For a round bunch in polar coordinates, the linear beam-beam parameter for small amplitudes r is

$$\xi_{bb} = \pm \frac{N r_0 \beta^*}{4\pi \gamma \sigma^2}. \tag{2.86}$$

Table 2.1 shows the beam-beam parameter for various colliding beam storage rings for comparison. From table 2.1 it can be seen that for the various machines the beam-beam parameters are the same order of magnitude with the exception

Machine	ξ_{bb} per IP
LHC [p-p]	0.0034
RHIC [Au-Au]	0.0015
LEP [e-e]	0.07
FCC [h-h]	0.005

TABLE 2.1: Beam-Beam parameters quantifying the strength of the beam-beam interaction in various previous and future colliding beam storage rings.

of at LEP. The beam-beam parameter in LEP is larger than the LHC. This arises due to the smaller vertical beam emittances which are achievable from radiation damping and almost no problems with resonances [27]. For LEP the damping time was approximately 20 turns together with strong detuning.

Now that the head-on beam-beam interaction has been characterised, the long-range beam-beam interaction can be discussed in the next section.

2.2.4 Long-Range Beam-Beam Effects

The long-range beam-beam interaction occurs when bunches in the two beams experience the electromagnetic field from a counter rotating bunch at a distance. A schematic of the long-range beam-beam interaction is shown in figure 2.13. The long-range beam-beam interaction is characterised by the non-linear part

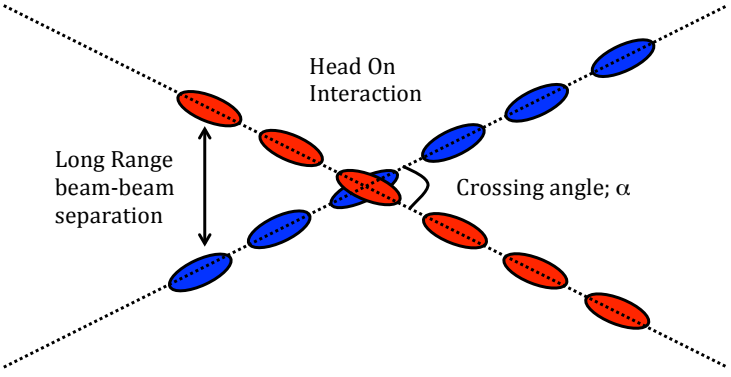

FIGURE 2.13: A schematic of the long-range beam-beam interaction between two colliding beams.

of the beam-beam force shown in figure 2.14. The non-linear force provides

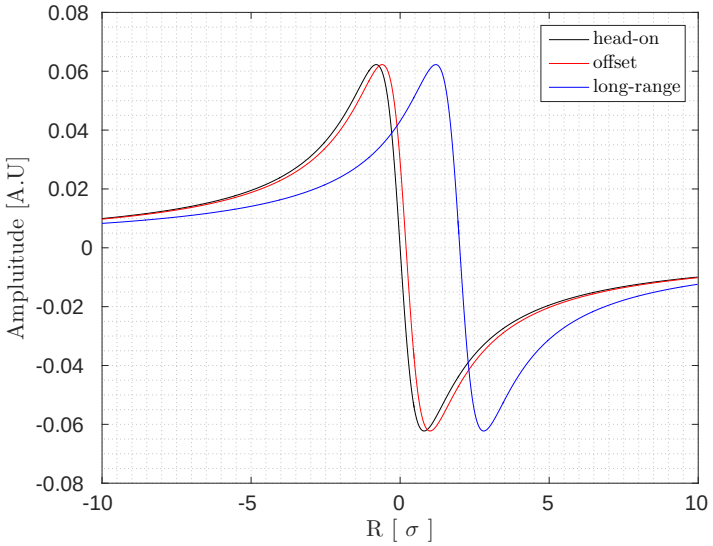

FIGURE 2.14: The force diagram for the beam-beam interaction with different values of d_{sep}.

an amplitude dependent tune shift to the particles [16]. Unlike the head-on beam-beam force, the beam-beam distance will vary from the inner triplet to the collision point, the inner triplet will be introduced in chapter 3. Normally the beam-beam separation is calculated as the distance between the bunches at the first long-range beam-beam encounter.

The tune shift due to the long-range beam-beam interaction at large separations can be determined by considering the beam-beam force as seen in equation 2.80. For large separations the exponential term will become small, $e^{-\frac{r^2}{2\sigma_r^2}} \ll 1$ and hence the tune shift from the long-range interaction to first order, will vary with the inverse square of the beam-beam separation distance d_{sep} as

$$\Delta Q_{\mathrm{LR}} = -\frac{N r_0 \beta^*}{2\pi\gamma (d_{sep})^2}. \tag{2.87}$$

For small separations however, the exponential term will no longer be small and will provide an amplitude dependent tune shift. The amplitude dependent tune shift will affect the tune footprint in a different way to that of the head-on interaction. Figure 2.15 shows the long-range beam-beam tune footprint. The

long-range tune shift causes the tails of the footprint to extend and potentially cross resonances, which may lead to emittance growth and particle losses. The tails of the bunch in this case refer to particles found at amplitudes larger than $\sim 3\ \sigma$. This extension of the tails is further exacerbated with the number of long-range collisions. In addition, the long-range beam-beam tune shift can have a different sign compared to the head-on tune shift as seen in equation 2.87. The change in sign compared to head-on interactions arises due to the opposite gradient of the beam-beam kick found at larger amplitudes ($r > 2\ \sigma$). The strength

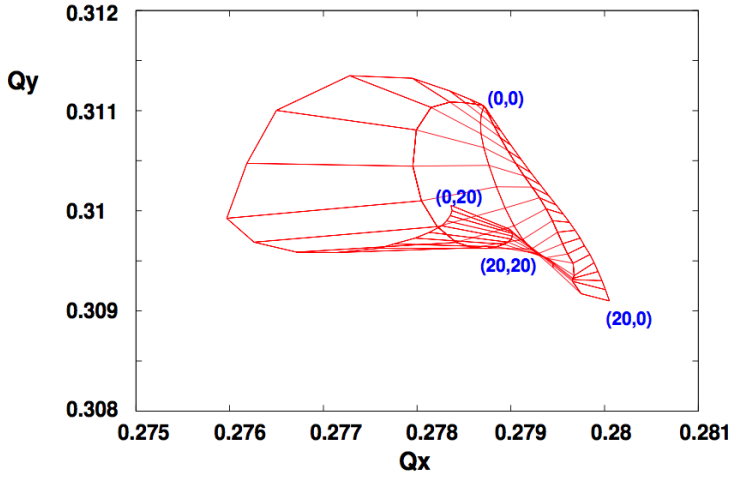

FIGURE 2.15: Example of the tune footprint for only long-range beam-beam interactions for a vertical separation and amplitude between 0 and 20 σ [16].

of the long-range beam-beam interaction depends on the collision configuration for the machine and is closely related to the β-function (β^*) at the IP and the emittance (ϵ_n) of the beam. For a colliding beam storage ring like the LHC, the beam-beam separation is one of the factors that define the luminosity performance of the machine. The impact of the long-range beam-beam interaction on the LHC luminosity performance is discussed in detail in chapter 5.

2.2.5 Coherent Beam-Beam Effects

Two colliding beams will not only exert a single particle kick but also a coherent kick to the bunch itself. If the colliding bunches have a slight offset with respect

to the other, or there is an asymmetry between the particle distributions of the two bunches, coherent oscillations can be introduced which may lead to unstable motion and closed orbit effects [8, 16]. The strength and effect of the coherent oscillations depend on a number of factors. One factor which affects the nature of the oscillations is the phase advance between the colliding bunches. Coherent beam-beam effects can drive different types of motion and these are normally described as coherent modes. The dipolar and quadrupolar are two examples of coherent modes that are described schematically in figure 2.16. The dipole modes arise when the bunches meet every turn either in or out of phase with one another. If the bunches arrive in phase with one another the distance between the bunches does not change from turn to turn, hence there is no net force that drives the oscillation. Since there is no coherent kick in this case, the mode is called the Σ-mode and is found at the unperturbed tune. In the LHC at collision, this is located at a fractional tune of $Q_{x_0,y_0} = 0.31/0.32$. The unperturbed tune is denoted using Q_0. The second dipole mode is known as the π-mode. This mode arises when the bunches meet out of phase with one another each turn and there is a force difference between the two bunches. This leads to a driven oscillation that can cause significant beam stability issues, if not controlled and damped. The coherent tune shift is denoted by ΔQ_π and the direction of the tune shift depends on whether there is a focussing or defocussing effect between the colliding bunches. In the LHC, the π-mode is defocussing as the colliding bunches both have positive charges. The coherent tune shift calculation is non-trivial and can be difficult to calculate. An exact derivation will be strongly dependent on the charge density distribution of the colliding bunches. For a simple calculation the LHC bunches can be considered to have a Gaussian transverse bunch distribution, in this case the tune shift characterised by the π-mode can be calculated when bunches arrive out of phase with one another. The tune shift for the π-mode is

given by [28]

$$Q_\pi = Q_0 + \beta^* \frac{1}{2\pi} \partial_x \Delta x'_{\text{coherent}}(x_0, y_0). \tag{2.88}$$

where x_0, y_0 are the coordinates of the closed orbit, β^* is the β-function at the IP, and $\partial_x \Delta x'_{\text{coherent}}$ is the derivative of the beam-beam kick. The derivative of the kick $\partial_x \Delta x'_{\text{coherent}}$ is given by the expression 2.89 and is calculated as

$$\partial_x \Delta x'_{\text{coherent}}(x, y) = -\frac{2Nr_0}{\gamma_r} \left[\left(\frac{1}{r^2} - \frac{x^2}{r^4} \right) \left(1 - e^{-\frac{r^2}{4\sigma_r^2}} \right) + \frac{x^2}{2r^2\sigma^2} e^{-\frac{r^2}{4\sigma^2}} \right]. \tag{2.89}$$

The tune change for the rigid bunch model is hence just the quadrupolar component of the beam-beam kick. However this does not take into account the additional non-linear terms of the beam-beam kick. To account for the non-linear terms the π-mode tune shift is often quoted in terms of a factor Y. If the bunches collide head-on then the π-mode including the factor Y is

$$Q_\pi = Q_0 + Y\xi_{bb}. \tag{2.90}$$

This factor Y is called the Yokoya factor and has a values between $Y = 1.21 - 1.33$ for round $\sigma_x = \sigma_y$ and flat ($\sigma_x \gg \sigma_y$) beams [8, 29]. For a simple calculation shown in equation 2.89, the rigid bunch model underestimates the Yokoya factor. This occurs due to the assumption that the bunch distribution does not change throughout the interaction with a counter rotating beam. In fact, the beam distribution will change and hence in order to obtain a more realistic, but still analytical calculation, higher-order moments of the bunch distribution should be considered. The impact of the higher order moments can be calculated through an expansion as described by Yokoya [30] or through numerical particle in cell methods [31].

Taking a Fourier transform of the bunch oscillation enables the Σ and π-modes

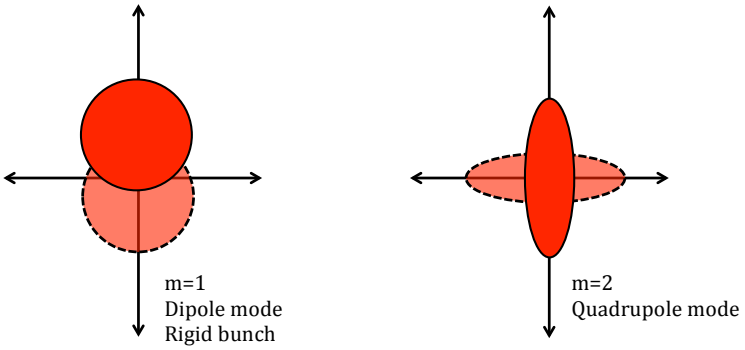

FIGURE 2.16: Schematic of the beam motion during dipole and quadrupole coherent oscillations.

to be located. The result of this Fourier transform is shown in figure 2.17 and was calculated using the strong-strong simulation code `combi` [32]. The coherent

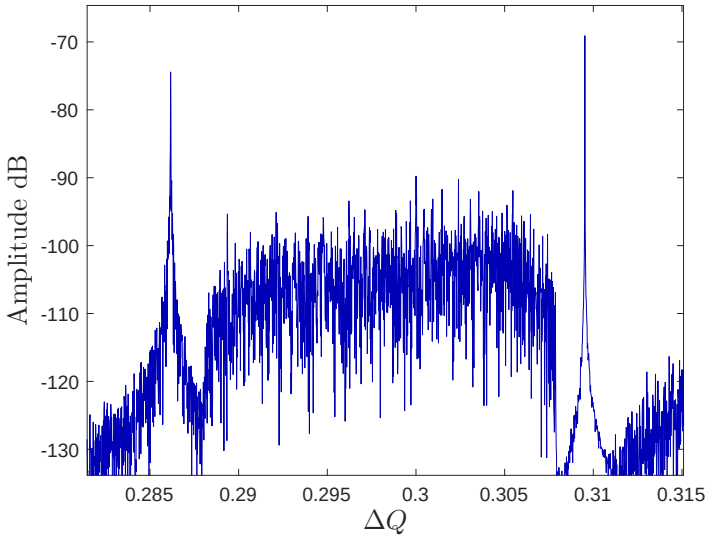

FIGURE 2.17: The tunes of the dipolar coherent modes generated using a strong-strong simulation code. The Σ-mode can be clearly identified at the unperturbed machine tune $Q = 0.31$. The undamped π-mode lies outside of the incoherent spectrum at $Q = 0.286$.

modes shown in figure 2.17 shows the spectrum for HL-LHC bunch parameters. The π and Σ modes can be seen clearly and are separated by the incoherent spectrum. The size of the incoherent spectrum is given by ξ_{bb} and defines the spectrum of frequencies in which particles will be Landau damped. The peak on the left hand side of the figure shows the π-mode at approximately $\Delta Q = 0.286$ whilst the peak on the right corresponds to the Σ-mode at $\Delta Q = 0.31$ at the

unperturbed tune. The incoherent spectrum is found between these two modes and arises due to the tune spread created by detuning. Particles with frequencies that lie within the incoherent spectrum will no longer oscillate coherently with one another and are stabilised by Landau damping [16]. The frequency width in which the particles are Landau damped is approximately equal to the linear beam-beam parameter ξ_{bb}. The collision configuration shown in figure 2.17 corresponds to two collisions at IP1 and IP5 with an asymmetric phase advance between collision points. The beam-beam parameter for a HL-LHC-like bunch is $\xi_{bb} = 0.0125$ per IP, which is approximately a factor of 3 larger than the LHC.

2.3 Discussion

This chapter has provided a brief overview of the key topics of collider physics. The simple linear and non-linear dynamics that a charged particle experiences as it travels around a machine lattice has been reviewed and the general equations of motion were introduced. This included the concept of the invariant emittance, phase advance and betatron motion. Following this, the Hamiltonian formalism was discussed. This formalisation was used to describe dispersive effects that arise due to off-momentum particles in a bunch as well as the dynamics of a particle moving through an n^{th} order magnetic multipole. Non-linear effects such as linear coupling and higher order chromaticity are also briefly introduced and discussed.

Following this, the topic of this thesis, the beam-beam interaction was introduced. The beam-beam interaction is first described by introducing the concept of luminosity, which is a key parameter that can be used to determine the performance of a colliding beam storage ring like the LHC. Firstly, the luminosity is derived for the simplest possible collision configuration, that is, the collision between two

round, Gaussian bunches colliding head-on and without offset. Following this, additional effects which arise in a real in the LHC are also introduced. The impact of crossing angle and transverse offset on the luminosity are quantified. These effects are usually categorised into reduction factors, which reduce the instantaneous luminosity between two head-on colliding bunches and can limit luminosity performance. In addition to the luminosity, the beam-beam interaction exerts a force on the counter rotating beam. This kick is calculated, firstly by considering the electric field of a Gaussian bunch. The electric field is calculated by finding the scalar potential in the rest frame of the bunch and then performing a Lorentz boost along the z-direction. From this the kick can be derived. The kick will result in a tune shift and this is shown for both the long-range and the head-on beam-beam interactions. The concept of a tune footprint is also introduced here and analysed with regard to both the long-range and head-on interactions. Finally this chapter concludes by considering coherent motion between two colliding bunches.

The effects and beam dynamic processes in this chapter are found in many different types of accelerators that generate luminosity through collisions with counter propagating beams. In the next chapter, specifics of the Large Hadron Collider at CERN will be presented.

Chapter 3

The Large Hadron Collider

3.1 Outline

This chapter briefly discusses the LHC injection chain and introduces LHC in more detail. The LHC injection chain consists of one linear accelerator and three circular machines that accelerate protons and inject them into the LHC. The accelerators in the injector chain are discussed along with the relevant energies from injection to extraction. In the following section, the LHC is introduced. Firstly the machine layout and typical procedures during standard operation are presented along with some of the nominal beam parameters. The relevant beam instrumentation that is used throughout this thesis is introduced. The methods and equipment used to analyse the intensity, emittance and luminosity data are presented. A closer review of the interaction point is also discussed; at these locations beam-beam interactions occur. Additionally, beam-beam effects that are observed in the LHC are discussed. Finally, one of the proposed future machines at the LHC are introduced. The HL-LHC is discussed along with the luminosity performance. In particular a number of luminosity levelling scenarios are reviewed.

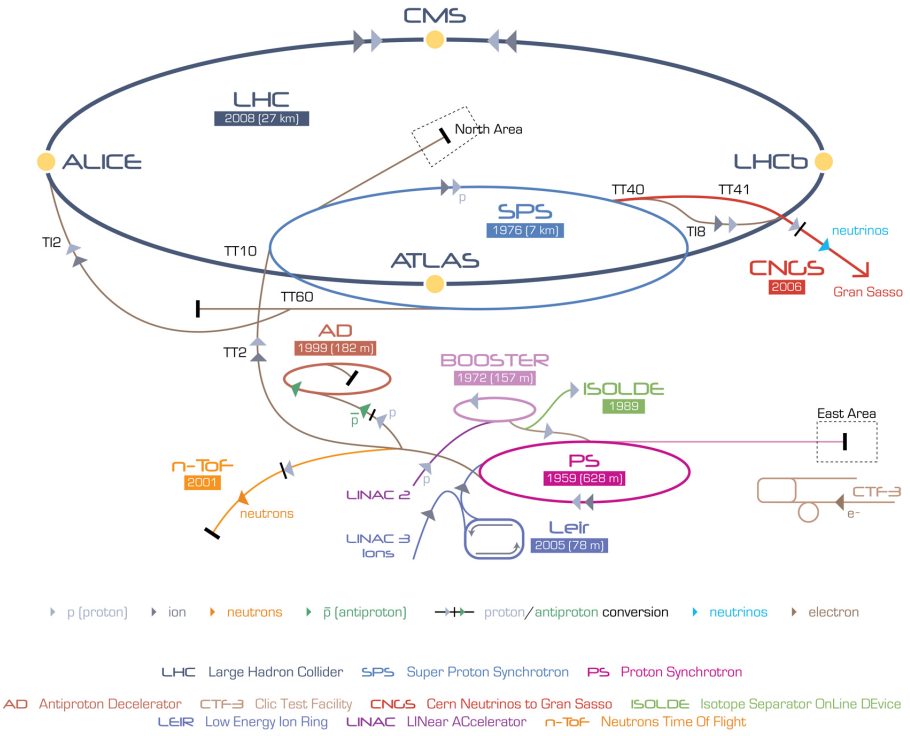

FIGURE 3.1: The accelerator facilities at CERN and the injection process into the LHC [33]

3.2 The CERN accelerator complex

The Large Hadron Collider (LHC) is the largest of the particle accelerators based at the CERN laboratory. The CERN laboratory contains multiple particle accelerators, with many providing protons for the LHC. In addition to the current working machines, CERN and others also research and develop new state of the art particle accelerators [33]. A schematic of the complex is shown in figure 3.1. The protons start in LINAC2 and are accelerated to a kinetic energy of 50 MeV before being injected into the Proton Synchrotron Booster (PSB). Here they are accelerated up to 1.4 GeV, before being injected into the Proton Synchrotron (PS). The PS accelerates the protons to 25 GeV and injects them into the Super Proton Synchrotron (SPS). Finally the protons are injected into the LHC at an injection energy of 450 GeV.

3.3 The LHC

The LHC is a 26.6 km twin ring colliding beam storage synchrotron that produces luminosity to study the physics of the Standard Model, as well as potential physics beyond the Standard Model [34]. The LHC first became operational in 2008 and, as of 2017, is currently the largest particle accelerator in the world. The LHC is the successor to the Large Electron-Positron Collider [35] that ceased operation in 2000.

3.3.1 Machine Layout

The LHC is split into 8 octants with 8 Insertion Regions (IRs). Each IR performs some principle function, whether it be beam cleaning or collisions. The particle physics experiments are located in IR 1, IR 2, IR 5, and IR 8. ATLAS and CMS are located in IR 1 and IR 5; these experiments require high luminosity to study rare physics by colliding tightly squeezed beams with a low β-function at the IP [36, 37]. The ALICE experiment is located at IR 2 and does not operate with tightly squeezed beams during proton physics runs ($\beta^* = 3$m) [38]. The β-function at the IP is however, reduced during ion (Pb-Pb) and proton-ion runs (p-Pb). The LHCb experiment is located at IR 8 and similarly to the Alice experiment does not require tightly squeezed beams with $\beta^* = 8$ m [39].

To obtain the small β^* at IP1/5 the beams must be focussed. This is achieved by using a triplet configuration of quadrupoles in the IR that increases the β-function in the surrounding elements before focussing to the required β^* at the IP. The particular magnet configuration and arrangement is discussed later in section 3.4.1. The β-function variation for beam 1 and beam 2 as a function of longitudinal position along the beam pipe is shown in figure 3.2. The remaining IRs contain LHC diagnostic, beam quality, injection and extraction systems. IR

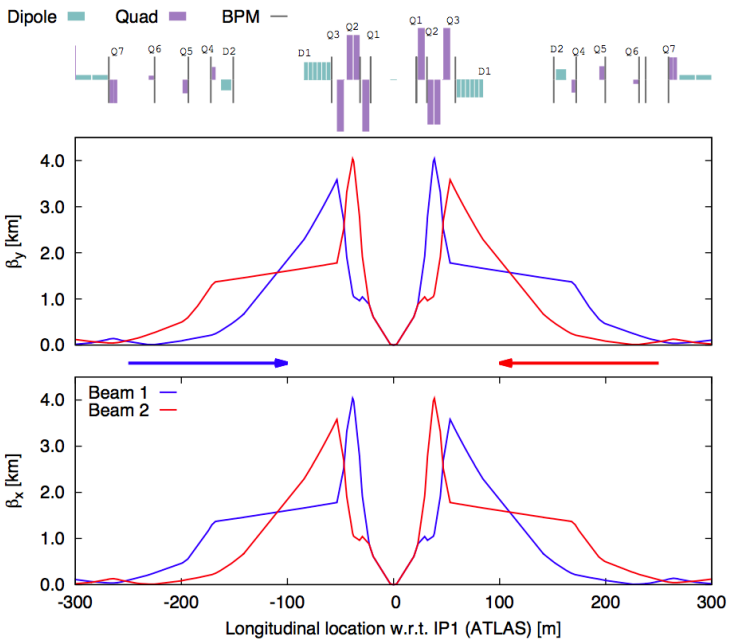

FIGURE 3.2: β-function through IP1 where the ATLAS experiment is located, with a $\beta^* = 0.6m$ for both beams in horizontal and vertical planes [13].

3 and IR 7 are reserved for momentum cleaning and betatron cleaning respectively. The momentum cleaning section cleans off-momentum particles from the bunches, whereas the betatron cleaning section cleans high amplitude particles. The machine Radio-Frequency (RF) instrumentation is located at IR 4 and the LHC beam dump is located at IR 6. The systems are all designed to monitor and control the bunches as the beams circulate round the machine. This helps to ensure that the machine is not damaged by the high energy beams and that performance is optimised. The design parameters for the LHC are given in table 3.1.

3.3.2 Operational Configuration

Whilst operating during the proton physics run (p-p), the bunch intensities are of the order of $n_p \approx 10^{11}$ compared to the $n_p \approx 10^7$ during the ion physics run. The smaller bunch intensities during the ion runs lead to significantly weaker beam-beam effects (since the beam-beam parameter is proportional to intensity,

LHC parameter	Value
Beam Momentum at Injection [GeV/c]	450
Beam Momentum at Collision [GeV/c]	6500
Peak Dipole Magnetic Field [T]	8.33
Bunch Intensity [ppb]	1.15×10^{11}
Number of Bunches per beam	2808
Bunch Spacing [ns]	25
Peak Luminosity [$\mathrm{cm}^{-2}\ s^{-1}$]	10^{34}
Total Crossing Angle [μrad]	280
Tunes [Q_H/Q_V]	64.31/59.32
Emittance ϵ_n [μm]	2.5
β-function at the IP1/5 [m]	0.40
β-function at the IP2/8 [m]	3/8

TABLE 3.1: Typical operational parameters for the LHC during the 2015-2016 run.

see chapter 2). Hence the proton physics collisions are of particular interest to this thesis. Each beam in the LHC, during a nominal luminosity production fill consists of 2808 bunches separated by 25 ns. The beams are further split into sets (or trains) of bunches that need to be spaced appropriately, such that bunches collide at the correct IPs around the ring. In addition to this, the size of the spacing between the trains are required to ensure that there is a large enough abort gap to dump the beam in the event of equipment failure. To avoid any damage to the machine due to the high energy beam, an abort gap spacing of 3 μs is required. This spacing allows for the rise time of the extraction kicker magnets. There are two types of beam extraction methods in the LHC. The first type of dump is called the synchronous beam dump and occurs during normal operation. In this type of extraction, the kicker magnets will execute at the same time and will be fired in synchronisation with the 3 μs abort gap [40]. Secondly, there is an asynchronous beam dump. This occurs with all kicker magnets firing out of synchronisation with the LHC abort gap [40]. This can lead to a large number of bunches hitting the collimators and potentially causing damage to the collimators themselves.

3.3.3 LHC Operational Cycle

During a standard luminosity production fill, the beam undergoes the standard operation cycle. This standard operational cycle is described by five different beam flags; Injection, Ramp, Squeeze, Adjust and Stable beams. These processes are highlighted in figure 3.3 along with the corresponding main dipole and octupole powering. In addition to dipoles and octupoles, many different multipoles exist in the LHC [41]. Quadrupoles are used around the ring to focus or defocus the beam in the arcs or at the IP. Sextupoles and other higher order magnets are used in the lattice to correct chromaticity and errors from the dipoles and other non-linearities of the machine. During the injection and ramp operational stages, the optics are set to maximise the aperture and hence, as a result, the β-function at the IP is large and will remain so throughout the ramp [42]. Once the beams have been ramped up to a flat top energy of 6.5 TeV, the β-function at the IP is reduced with the crossing angle remaining fixed in IP1 and IP5, in preparation for luminosity production. This reduces the beam size down, however the beams are still not in collision. The next stage is the adjust operational procedure. During this stage, the parallel separation orbit bumps are collapsed at IP1 and IP5. This brings the bunches into collision and begins to produce luminosity. Once the beams have been adjusted and the bunches are colliding, the operational flag will be set to stable beams. Throughout the stable beams flags, the luminosity will be optimised to ensure that the bunches are colliding without an offset until finally, the beams are dumped at the end of the fill.

3.3.4 Beam Instrumentation

There are a number of different systems and instruments in the LHC that enable the beam quality and losses to be observed. These are vital to determine the efficiency of the machine by analysing the the beam data obtained from dedicated

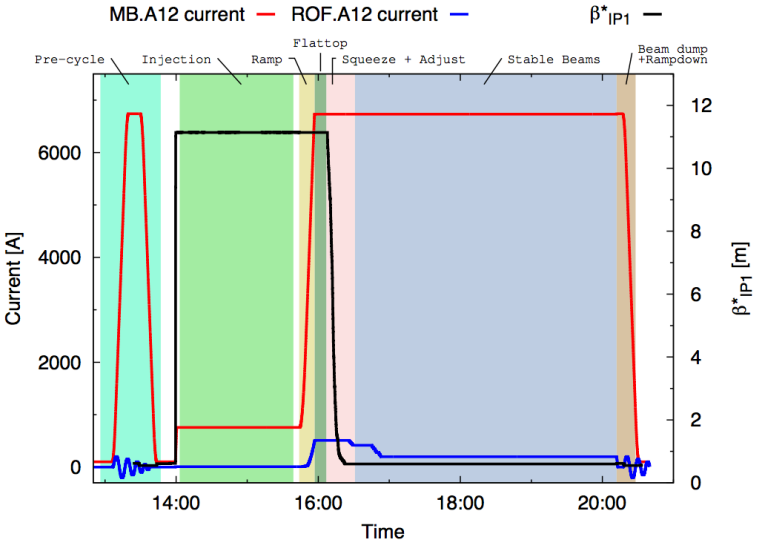

FIGURE 3.3: The standard operational cycle for the LHC during a normal luminosity production fill in 2012 [13]. The β^* at the IP is shown in black along with the powering of the main dipoles and the octupoles.

machine studies and during luminosity production runs. The individual bunch intensity can be measured using the Fast Beam Current Transformer (FBCT). This instrument measures the intensity of every bunch in the beam every second, to a high degree of accuracy and has an error smaller than $< 1\%$ [42]. The FBCT measures the bunch intensity by detecting the change in magnetic field as a bunch moves close to a magnetic torus. This in turn generates a current in the secondary coil of a transformer, which has a known number of turns. This measured current in the coil can hence be used to calculate the bunch intensity. A schematic of the FBCT is shown in figure 3.4.

In addition to the bunch intensity it is also possible to measure the single bunch emittance. The emittance can be calculated using the Beam Synchrotron Radiation Telescope (BSRT). This device does not have the accuracy of the FBCT but is capable of making measurements with an accuracy of $\sim 10\%$ [44]. The BSRT is useful mostly for relative measurements with the bunch size obtained on a bunch by bunch basis. A schematic of how the synchrotron light from a bunch in the LHC is used to calculate the emittance is shown in figure 3.5. Each

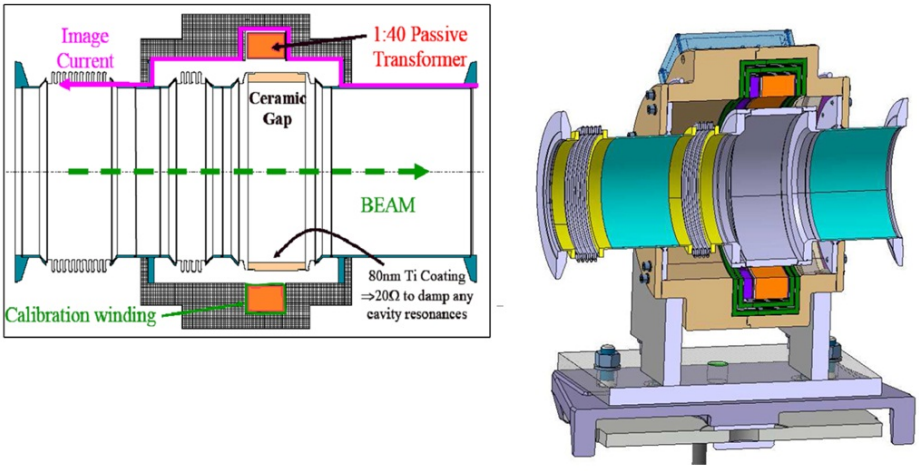

FIGURE 3.4: Schematic of the Fast Beam Current Transformers (FBCT) that are used to analyse the beam and bunch current [43].

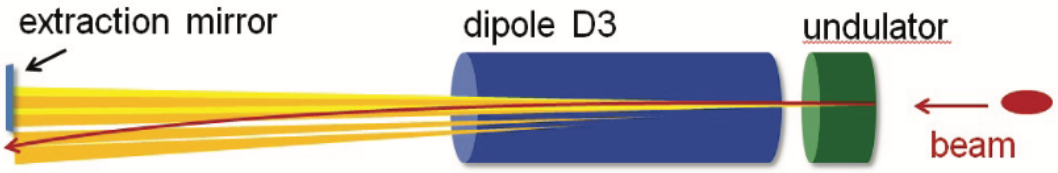

FIGURE 3.5: Schematic of how the synchrotron light from a proton bunch is obtained [45].

beam of the LHC will travel through a small, superconducting undulator close to the edge of a dipole magnet. This will cause synchrotron light to be emitted by the bunch and to be extracted through a viewport to the BSRT. The BSRT will observe the synchrotron light and calculate the transverse bunch profiles over some integration time. From the transverse bunch profiles the emittance of the bunch can be calculated.

As discussed in chapter 2, the tune $Q_{x,y}$ is another useful parameter that can be measured. The machine tune can be measured using the base band tune (BBQ) system. This piece of equipment allows the passive monitoring and measurement of the beam tune as well as linear coupling [46, 47]. The BBQ system calculates and measures the beam tune using two specific beam position monitors (BPMs). These BPMs are located with other beam instrumentation at IR4. The difference

signal between the two BPMs is measured and used to calculate the betatron modulation of the beam position.

3.4 The Interaction Points

There are 8 interaction regions around the LHC and 4 IPs where the beams collide. At these points, a number of high energy physics experiments exist to study various particle physics processes [36–39].

3.4.1 The Inner Triplet and Surrounding Region

The low β experiments are located at IP1 and IP5. Here the beams are squeezed down to approximately $\sigma_r \approx 16\mu$m. To achieve such a small beam size, a system of very strong quadrupoles are used to blow the β-functions of the beams up so that they can be squeezed down at the IP. Since the beam size is inversely proportional to the luminosity, reducing the beam σ to a size as small as possible will maximise the luminosity production rate. Figure 3.6 shows a schematic and arrangement of the inner triplet. The separation dipoles are labelled as D_1 and

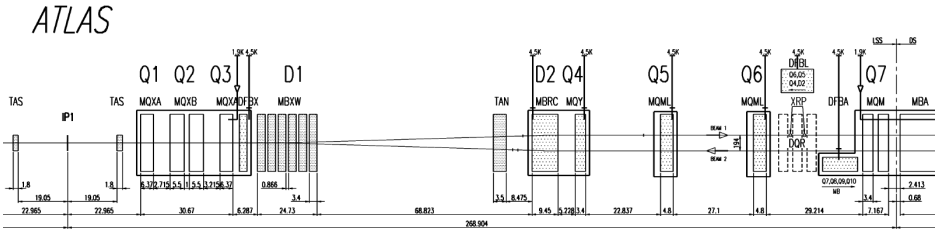

FIGURE 3.6: Schematic and arrangement of magnets to the right of IP1 where the ATLAS experiment is located [48].

D_2 and these dipoles enable the two beams to be moved in and out of collision at the IR. The inner triplet quadrupoles are responsible for blowing up the β-function and focussing the beam sizes at the IP. These quadrupoles are labelled

$Q_{1,2,3}$. Finally the additional $Q_{4,5,6,7}$ labels indicate matching quadrupoles, which ensure that beam parameters at each end of the IR match the connecting arcs.

3.4.2 Collimation in the LHC

The LHC was designed to collide two beams at 7 TeV. This corresponds to a beam energy of 360 MJ making the beams capable of significantly damaging the LHC, if not controlled properly. In addition to the destructive capabilities of the beams, the superconducting magnets that control the beam are sensitive to beam losses and will quench if a relatively small number of protons collide with the superconducting magnetic cores [49, 50]. To prevent magnetic quenching, beam cleaning using a collimation system is used. The collimation system is split into three parts, with the primary, secondary and tertiary collimation components shown schematically in figure 3.7. The collimation system is designed with a

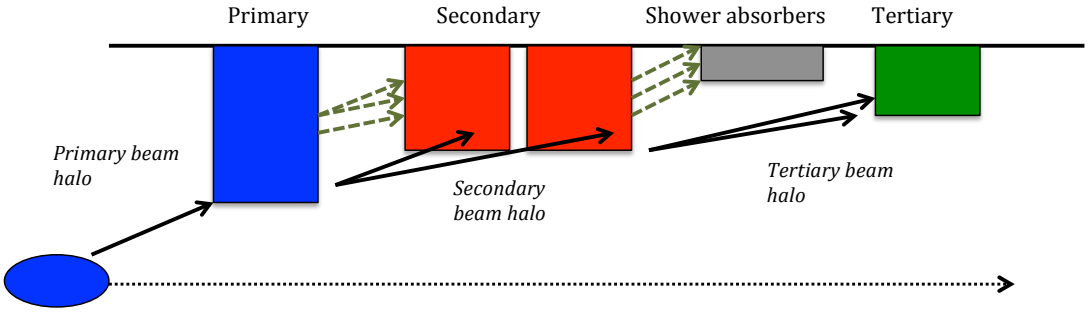

FIGURE 3.7: Schematic of the primary, secondary and tertiary collimation system in the LHC.

number of aims in mind. Firstly, the collimation system must protect the superconducting magnets and sensitive equipment. This is achieved by cleaning the beam halo (particles at large amplitudes) during LHC operation. The beam halo will continually be filled by various beam dynamic processes throughout the duration of a fill. Many different beam dynamic processes can cause particles to diffuse to higher amplitudes; beam-beam effects and magnetic errors are two examples. Removing the beam halo will also improve the particle physics data by

minimising any halo induced background at the experiments [49]. Secondly, the collimator system must protect the machine aperture itself from any additional, unexpected, abnormal particle losses. If a significant number of losses are detected by the beam loss monitors located at the collimators, a beam abort trigger will be executed to protect the machine. Additionally the collimation system is required to perform abort gap cleaning.

Beam cleaning by the collimators occurs in a number of stages as seen in the schematic shown in figure 3.7. The beam cleaning process is executed by three different types of collimators, each with different principle design goals. The primary collimators are required to remove the high energy protons from the beam and generate a secondary proton halo [49]. This secondary proton halo will be removed by the secondary collimators and any leakage from these are absorbed by the tertiary collimators. Tertiary collimators are usually located at specific points around the ring in order to remove halo that arises due to aperture bottlenecks at the triplets [49].

In addition to the requirements mentioned above, separate cleaning systems are located at IR3 and IR7 to provide optimised beam cleaning. In IR3, the collimation system is optimised to perform beam cleaning for off-momentum protons. In IR7, the collimation system is designed to clean protons that have large betatron amplitudes [49].

3.5 Beam-Beam interactions in the Large Hadron Collider

The beams collide at 4 IPs around the ring and at these points the bunches will experience the electromagnetic field of bunches in the counter rotating beam. The number of interactions and strength of these interactions will depend on a

number of different factors. Factors that affect the strength and number of the beam-beam interactions include: the bunch spacing, the number of bunches in the train, intensity, emittance, and the crossing angle. An example of a typical filling scheme during a normal luminosity production fill is shown in figure 3.8. In the 2015-2016 machine configuration, a train of 48 bunches with 25 ns bunch

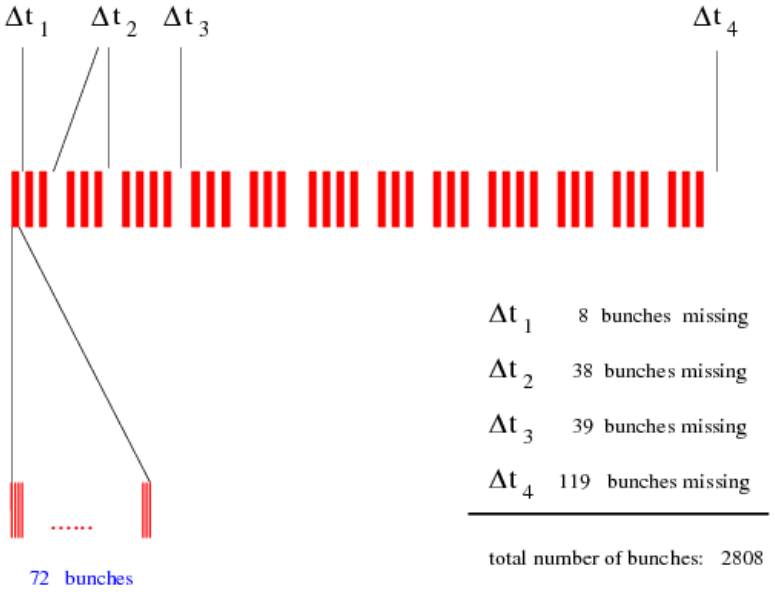

FIGURE 3.8: Example of a typical bunch filling scheme during a normal luminosity production fill from [51].

spacing will experience a varying number of long-range and head-on beam-beam interactions. During luminosity operation, the bunches in the centre of the train, called the nominal bunches, will experience a maximum of 34 long-range interactions per IP and up to 4 head-on interactions. Bunches at the front of the train will experience less long-range interactions with a minimum of 17 interactions. Bunches which do not experience the maximum number of long-range beam-beam interactions are known as Pacman bunches. The number of head-on and long-range interactions for a typical luminosity production fill is shown in figure 3.9. The variation of the number of long-range interactions depending on the position in the train is shown in figure 3.10. This section summarises some aspects of the LHC as in current operation. However, the accelerator physics community always seeks to push machine performance and build more powerful machines. A

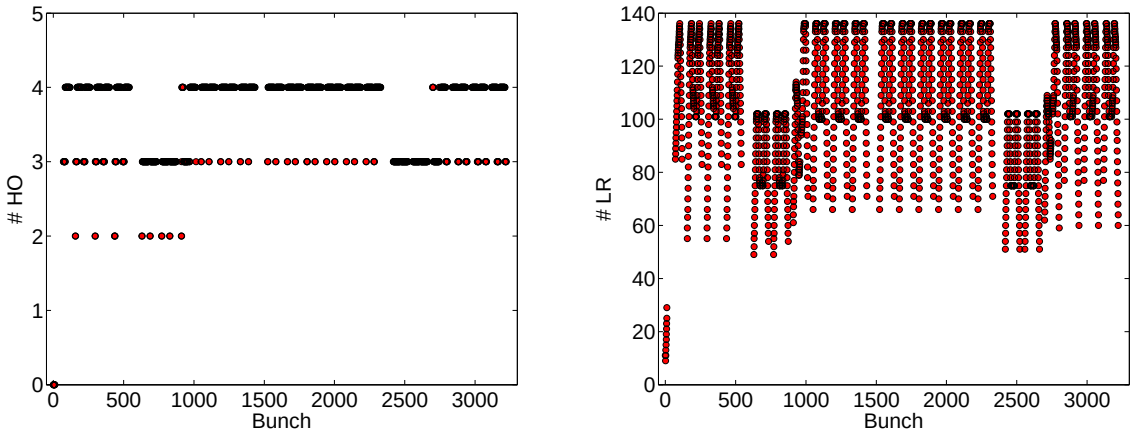

(a) (b)

FIGURE 3.9: Number of head-on (figure(a)) and long-range (figure(b)) interactions for each bunch for a typical luminosity production fill during the 2015/6 run, with a bunch spacing of 25ns.

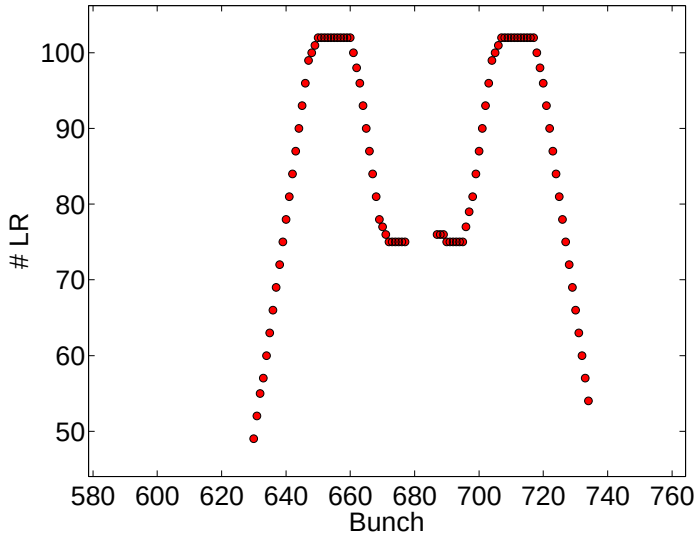

FIGURE 3.10: Variation of the number of long-range beam-beam interactions for bunches in a single train depending on the position in the train.

number of upgraded machines have been proposed to push the energy range and the luminosity performance. In the next section, one of those machines is briefly discussed.

3.6 Future machines at CERN

After the LHC, a number of machines have been proposed to push the luminosity reach and the energy performance. The next planned update for the LHC is the HL-LHC [52].

3.6.1 HL-LHC

The High Luminosity Large Hadron Collider (HL-LHC) is a proposed upgrade for the LHC to increase the luminosity performance [52]. A comparison between the beam parameters in the LHC and HL-LHC are shown in 3.2. Aside from the

Parameter	LHC	HL-LHC
Bunch Intensity [ppb]	1.15×10^{11}	2.2×10^{11}
Number of Bunches per beam	2808	2748
Peak Luminosity [cm^{-2} s^{-1}]	1×10^{34}	5×10^{34}
Total Crossing Angle [μrad]	$375 \rightarrow 280$	590
$\xi_{beam-beam}$ with Crab Cavities	3.8×10^{-3}	1.1×10^{-2}
Emittance ϵ_n [μm]	3.75	2.5
β-function at IP1/5 [m]	0.55	0.15

TABLE 3.2: Comparison of the beam parameters between the nominal LHC and the HL-LHC. The value for the HL-LHC assumes levelled luminosity.

increase of the bunch population and reduction in emittance, a number of methods of increasing the peak and integrated luminosity have been suggested [53]. One method of increasing the luminosity is to include crab cavities [54]. These cavities provide a kick to the head and the tail of the bunch, changing the angle between the bunches and maximising the head-on beam-beam collision. The crab cavities and an increase in the emittance and bunch intensity will increase the strength of the beam-beam interaction. This could lead to emittance growth and an increase in particle losses. These effects could have a negative impact on the luminosity and bunch lifetimes, causing a large decay at the beginning of the fill. Instead, luminosity levelling has been proposed to counteract the effects

of a quickly decaying luminosity [52, 53]. The luminosity will instead be held constant throughout the duration of a fill by using luminosity levelling. Some of the luminosity levelling options are discussed in the next section.

Luminosity levelling is likely to play an important role in the machine performance. In order for the luminosity levelling to be effective it should not impact beam stability and performance. Several luminosity levelling scenarios are discussed along with the performance implications.

3.6.1.1 Luminosity Levelling in the HL-LHC

As discussed in Chapter 2, the maximum luminosity can be achieved by minimising the reduction factor F_{loss}. Luminosity levelling proposes to provide constant luminosity production throughout the duration of a fill, whilst making small corrections to the parameters in equation 2.65. Some options for luminosity levelling are presented next.

One possible luminosity levelling option is to use crab cavities [55]. RF crab cavities are due to be installed in the HL-LHC and these could be used to level the luminosity. Crab cavities could be used to adjust the crossing angle over the duration of a fill [56]. A schematic of crab cavity crossing is shown in figure 3.11. The crab cavities provide a kick to the head and tail of the bunch and tilt the bunches towards the IP, hence reducing the geometric loss factor and providing a head-on collision. Crab cavities can be used to level the luminosity by changing the tilt of the bunches and hence the geometric loss factor. Increasing the tilt will reduce the overlap between the two bunches and reduce the luminosity. Crab cavity levelling would be used to reduce the tilt throughout operation as the bunch intensity decays and hence keep the luminosity fixed throughout a luminosity production fill.

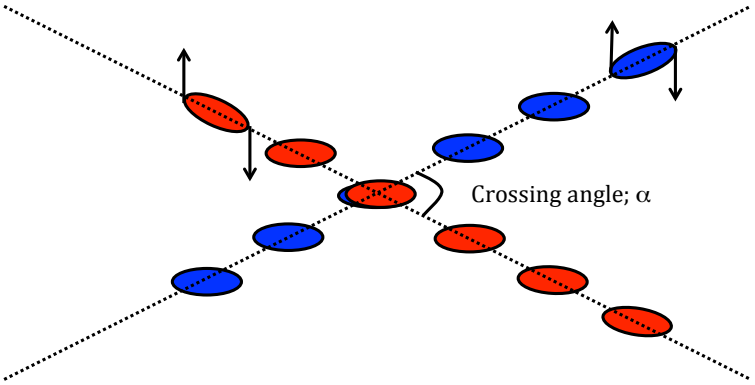

FIGURE 3.11: Schematic of crab cavity crossing.

Crab cavities have been used successfully at the KEKB electron collider [57], however they are yet to be tested in a hadron collider. Introducing and using crab cavities in the LHC will change the beam-beam effects and could potentially induce a number of issues. One of the main advantages of using the crab cavities is that the cavities will be located at each IP. With a crab cavity located at each IP, bunches can be crabbed at all IPs independently of one another by simply varying the voltage across each cavity [56]. At present however, there are several significant limiting factors which can cause issues for the detectors and from the perspective of the beam dynamics. Firstly, the longitudinal vertex density will vary with the crossing angle as shown in figure 3.12. The longitudinal vertex density is defined by the number of collisions along the length of the bunch. Varying the longitudinal density distribution during a luminosity production fill

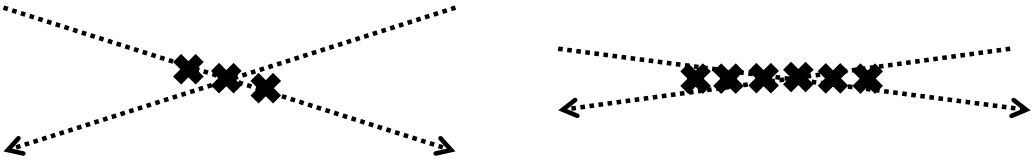

FIGURE 3.12: Schematic of the longitudinal vertex density variation with crossing angle. Here the arrows indicate the direction of the bunches. Reducing the crossing angle increases the longitudinal vertex density meaning that collisions occur along the entire length of the bunch, instead of a large number of collisions occurring in a very small area.

can introduce calibration issues for the detectors. If the crossing angle is large,

then the longitudinal vertex density will be small. This can make it difficult for the detector to discern the number of collision events. The changing crossing angle over the duration of the fill will also result in the tunes changing at each levelling step. This could provide issues operationally as the constantly changing tune would have to be corrected during operation. Additionally, the crab cavities themselves could impart noise to the bunches as well as introducing phase jitter, which is caused by a transverse offset mismatch [56, 58]. These effects could all provide issues with stability and may reduce the maximum achievable beam-beam tune spread ξ_{bb} and affect the luminosity production.

An alternative option for levelling in the HL-LHC is called β^*-levelling. A schematic of β^*-levelling is shown in figure 3.13 with the different β^* at each step. This levelling scenario is performed by reducing the β-function at the IP over the duration of the fill and squeezing the beam as the bunch intensity decays. One of the benefits of this process is that it is adiabatic and hence does not change the bunch emittance. This means that as the particle spatial component x decreases, the momentum component x' increases, meaning that the emittance remains constant through each change in β^*. Luminosity levelling through β^* variation is currently the most likely method of levelling for the low β experiments [55]. During β^*-levelling, the longitudinal vertex density will remain fixed as desired by the experiments. Additionally reducing the β^* keeps the tune fixed at each levelling step and the head-on beam-beam tune spread remains constant, as this is not dependent on β^* for the round bunch optic ($\sigma_x = \sigma_y$). For the flat bunch optic ($\sigma_x \neq \sigma_y$) however, changing the β^* at each levelling step will change the coherent tunes. This could cause operational issues and needs to be controlled during operation to ensure that the π-mode is damped. One of the drawbacks of β^*-levelling is the variation of the closed orbit at each levelling step. This will need to be tightly controlled operationally to ensure that the beams do not drift substantially, in order to avoid driving coherent oscillations and creating

a transverse offset between the two colliding bunches. The coherent modes for two different levelling steps are shown in figure 3.14 for a round and flat bunch optic. In the round bunch option shown in figures 3.14(a) and 3.14(b), the coher-

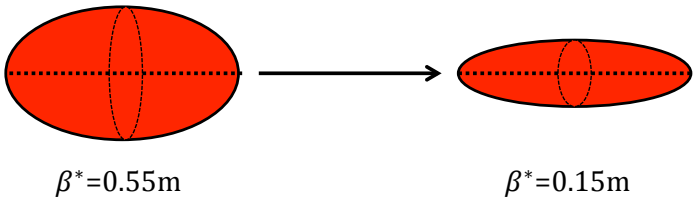

FIGURE 3.13: Schematic of β^*-levelling at the IP.

ent tunes in the horizontal and vertical planes do not change with the levelling step. For the flat bunch option this is not the case. In the horizontal plane the beam-beam tune shift $\xi_{bb,x}$ increases, whereas in the plane in which the β^* is held constant the beam-beam parameter $\xi_{bb,y}$ will decrease. The coherent tune shifts for the flat and round optics are shown in figure 3.14 using the method described in [59]. The different ξ_{bb} in each plane could impact particle stability. There has also been some experience operationally using β^*-levelling during normal operation in IP2 and IP8. This makes β^*-levelling an appealing method of obtaining constant luminosity throughout the duration of a fill.

Levelling with offset is the simplest option proposed for the HL-LHC [56]. Due to the nature and goal of the experiments located at the IPs, different luminosity performance targets are required. The experiments located at IP2 and IP8 have much lower luminosity tolerances than at IP1 and IP5 and hence luminosity levelling by offset is already implemented at these points [60]. Similarly to crab cavities, offset levelling can be applied independently at all IPs through a local orbit bump. The individual orbit bump can also be implemented easily, providing a simple method of changing between offsets. Crucially, levelling with offset keeps the longitudinal vertex density fixed throughout the levelling steps. The main issues with this levelling option concern the beam-beam interaction and stability.

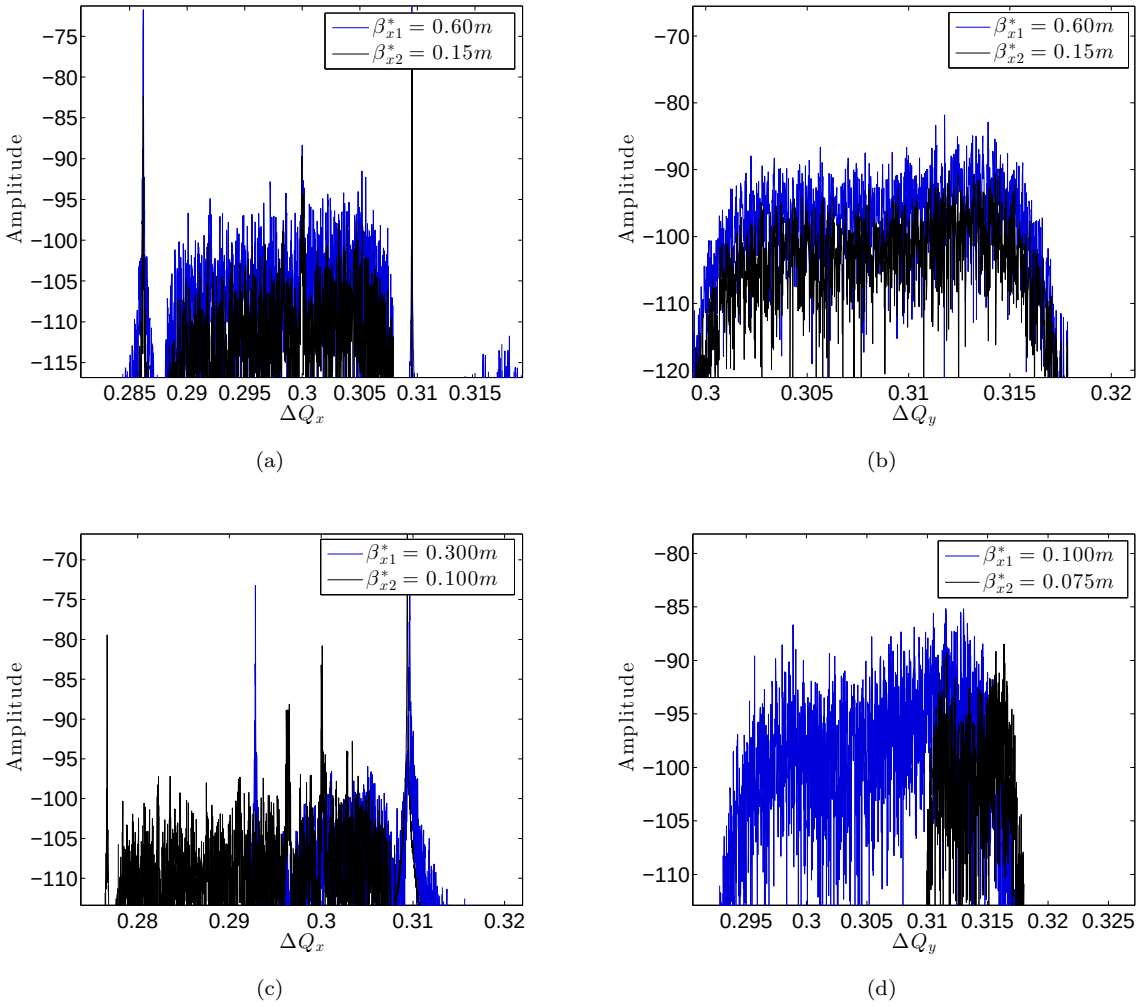

FIGURE 3.14: The coherent modes from simulations in *combi* during β^*-levelling. The coherent modes for the round bunch are shown in 3.14(a) and 3.14(b) and the flat bunch coherent modes are shown in 3.14(c) and 3.14(d).

Levelling with offset changes the strength of the beam-beam interaction with every step. Different beam-beam separations can have a significant impact on beam dynamic processes in the beam and can induce losses and emittance growth. The tune spread during the levelling will also vary appreciably as the radial offset changes. This can once again impact stability and lead to losses as was observed in the 2012 operation [60]. The stability issue was cured by ensuring bunches underwent a head-on collision at IP1 and IP5. This provided the required Landau damping to stabilise the bunches as discussed in section 2.1.6. This suggests that

offset levelling would not be a viable option for levelling at the low β^* experiments.

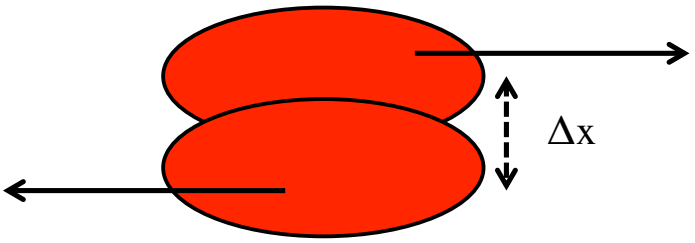

FIGURE 3.15: Schematic of offset levelling at the IP.

3.7 Summary

In this chapter, the LHC layout and the injectors that provide protons to the LHC have been introduced. Firstly, the purpose of the main IRs are discussed, along with the basic operational cycle and the various beam flags which are used during normal luminosity production runs. Following the section concerning the layout of the LHC, key beam instrumentation such as the FBCTs, the BBQ and the BSRTs are introduced along with a basic explanation of how the equipment works. In the section following the LHC and the CERN accelerator complex, the performance parameters of the proposed upgrade of the LHC to the HL-LHC and the impact on the beam-beam effects and luminosity is considered. The HL-LHC will aim to provide an even larger luminosity performance reach. To achieve the increase in luminosity, the bunch emittance is reduced to $\epsilon_n = 2.5$ μm compared to 3.75 μm in the nominal LHC, whilst the bunch population is increased to $n_p = 2.2 \times 10^{11}$ ppb. These bunch parameters have a direct impact on the strength of the head-on interaction, leading to a much larger beam-beam parameter. Strong beam-beam interactions can decreases the bunch lifetime and limit the integrated luminosity, if the luminosity decay is large. To prevent a fast decay in luminosity

and to provide constant luminosity production throughout the duration of a fill, luminosity levelling was proposed. The concept of luminosity levelling along with three methods in which levelling can be implemented are discussed and reviewed briefly. The advantages and disadvantages of the the three proposed methods are evaluated. The impact on the coherent modes is also assessed for β^*-levelling with a simple collision scenario.

Chapter 4

Analytical Expressions for the Beam-Beam Interaction

4.1 Introduction

The luminosity performance in a colliding storage ring like the LHC is dependent on a number of factors such as bunch population, emittance and geometric loss factors arising from transverse offset and crossing angle [61]. The impact of typical bunch parameters and operational scenarios are discussed in chapter 2. In addition to the transverse bunch parameters, bunch length effects can also further limit the luminosity performance [62]. One example of an effect that can limit the luminosity performance is the hourglass effect; the impact of this effect will be discussed in detail later in the chapter. In the first section of this chapter, the preliminary mathematics required to understand the later sections are developed. These preliminaries are then applied to derive a new method of obtaining analytical solutions to Poisson's equation. This method derived is based on using the general complex solutions to the Laplace equation. An *ansatz* is chosen with a number of unknown functions to be constrained and found. Some

of these functions are holomorphic and analytic, and are shown to satisfy the Cauchy-Riemann and Laplace equations. These functions are then used to constrain Maxwell's equations including a source charge term. This yields a system of equations which can be solved in the most general, n dimensional case. These equations are then projected down to 2 and 3 dimensions, where the method is applied to a number of different charge density distributions. This allows analytical expressions to be obtained for the electric field. These expressions are then compared to literature where possible.

In order to obtain the luminosity requirements for future machines like the HL-LHC, beam parameters such as the β^*, emittance must be reduced and the beam intensity increased. The reduced β^* can impact the luminosity performance if this parameter becomes comparable to the length of the bunch. Within this regime, the hourglass effect can prevent particles colliding at the minimum β^*. One proposed option for the HL-LHC is the flat bunch option [52]. This used in combination with β^*-levelling could result in a bunch length comparable to the β-function at the IP. The hourglass effect will introduce a coupling between the transverse bunch size and the longitudinal position, causing a parabolic variation towards the IP. Until now, no analytic method is available to describe this effect. The method presented in this chapter is used to describe the hourglass effect and an analytic expression for the electric field is obtained and compared to the standard Gaussian distribution.

4.2 Outline

The beam-beam force is traditionally derived by solving Poisson's equation where the source charge ρ is given by a fixed Gaussian charge density distribution. Analytically it is possible to obtain solutions to Poisson's equation for a 2 dimensional

Gaussian bunch. This approximation is usually suitable for most high energy colliders as the longitudinal electric field will be confined to the transverse planes, since the bunches travel close to the speed of light within the ultra-relativistic limit [16, 63, 64]. However in a real collider, coupling between the bunch planes is possible and the non-zero crossing angle can introduce longitudinal effects that may no longer be negligible [62]. Some symplectic methods have been derived so far but are only approximate and do not calculate the exact electric fields [65]. To obtain an exact electric field calculation the full 3 dimensional case should be considered.

The chapter is laid out in the following way; firstly the general derivation in n dimensions is described. Here all the preliminaries are outlined, along with the mathematical framework that will allow analytical solutions involving the beam-beam interaction to be obtained. A brief introduction to the Cauchy-Riemann equations and the Laplace equation are provided, initially from the well known 2 dimensional and then later extended to the general n dimensional case based on *hypercomplex coordinates*. The hypercomplex coordinates are shown to solve the n dimensional Cauchy-Riemann equations and the Laplace equation by introducing two separate arbitrary functions, g and h, that depend only on one of the hypercomplex coordinates. From this, a general complex coordinate transform is described that can then be applied when one of the Cauchy-Riemann equations are no longer homogenous and instead depends on some term ρ. A general *ansatz* is introduced with functions that need to be constrained. One of the functions can be shown to correspond to the particular solution, when $\rho \neq 0$. A system of equations are obtained from substituting the *ansatz* into the modified Cauchy-Riemann equations and these equations are solved. A relationship between the particular solution and the Cauchy-Riemann equations is found through the method of characteristics. This is used to solve one final equation relating the homogenous general solution to the particular solution.

In the section following the general outline, the method of unconstrained functions is applied to the two dimensional transverse Maxwell's equations in the presence of various source charge terms. Firstly, setting the source charge ρ to take the form of a Gaussian charge density distribution allows the well known round bunch derivation for the electric field to be obtained. This provides proof of principle for the method. Following this, alternative, non-linear but simple distributions are used to find the electric fields and are once again compared to results from literature.

Using the mathematical framework of the method of unconstrained functions, the electric field for a 3 dimensional Gaussian charge density distribution is obtained without requiring the complex coordinate transformation. Finally, a preliminary approach to obtaining analytical expressions including the hourglass is discussed. The charge density distribution including the coupling is included into the framework of the method of unconstrained functions and an expression is obtained and discussed.

Finally the chapter is summarised and discussed with regard to further work.

4.3 General Complex Formalism

Here, the general mathematical framework is outlined for the method of unconstrained functions. This framework is an extension of the method by B. Muratori *et. al*, which was used to find analytical expression for fringe field magnets [66]. Unlike the fringe field case however, Maxwell's equations must be considered in the presence of a source charge term ρ. This requires Poisson's equation to be solved, as opposed to the Laplace equation. Poisson's equation is an inhomogeneous linear second order partial differential equation and analytical solutions

are often difficult to obtain. Instead, an approach solving a system of equations from Maxwell's equations is proposed in a similar method to [66].

The Cauchy-Riemann equations form the cornerstone of complex analysis and determine whether a function is *analytic* and *holomorphic* [67]. An analytic function is defined as a function that is infinitely differentiable [68]. Additionally, a function that is also analytic in the complex plane is said to be holomorphic and these have found a multitude of applications in physics and applied mathematics [69]. The Cauchy-Riemann equations in 2 dimensions are written as

$$\partial_x f_p - \partial_y f_q = 0, \tag{4.1}$$

$$\partial_x f_p + \partial_y f_q = 0. \tag{4.2}$$

Cross differentiating these equations allows the Laplace equation to be obtained

$$\nabla^2 f = 0, \tag{4.3}$$

where the Laplace operator is defined as $\nabla^2 = \partial_x^2 + \partial_y^2$. The Laplace equation occurs throughout the theory of electromagnetism, heat theory and gravitational theory [70]. A general solution to the Laplace equation in 2 dimensions can be found by introducing the complex variables u and v, which are written as

$$u = x + iy, \qquad v = x - iy. \tag{4.4}$$

Transforming equations 4.1 and 4.2 to the complex coordinates yields a general solution in terms of holomorphic functions that satisfy the Laplace equation 4.3. The coordinate transformation of the Laplace equation yields

$$\partial_{uv}^2 f = 0,$$

and the general solution to equation 4.3 is given by

$$f = g(u) + h(v), \tag{4.5}$$

where g and h are arbitrary functions of u and v only. This approach can be further extended to n dimensions by introducing *hypercomplex* coordinates [71–73]. These hypercomplex coordinates in n dimensions are written as

$$w = \sum_{j=1}^{n} \alpha_j x_j, \qquad \tilde{w} = \sum_{j=1}^{n} \bar{\alpha}_j x_j, \tag{4.6}$$

where α_j and $\bar{\alpha_j}$ may be complex constants, n is the number of dimensions and x_j is the real coordinate. Considering the n dimensional Laplace equation, namely

$$\nabla_n^2 f = 0,$$

and for simplicity considering that f is a function of one hypercomplex coordinate w only, transforming to the new coordinate using the chain rule gives

$$\partial_{x_j} f = \partial_{x_j} w f',$$
$$\partial_{x_j}^2 f = \partial_{x_j}^2 w f' + (\partial_{x_j} w)^2 f'',$$

where the prime denotes differentiation with respect to the argument. Substituting these results into the n dimensional Laplace equation gives,

$$\nabla^2 f = \sum_{j=1}^{n} \left[\partial_{x_j}^2 w f' + \left(\partial_{x_j} w\right)^2 f'' \right] = 0.$$

This yields the same result as ref [71–73]. Furthermore this gives two conditions that need to be satisfied to ensure that f satisfies the Laplace equation. These

conditions are,

$$\sum_{j=1}^{n} \partial_{x_j}^2 w = 0, \qquad \sum_{j=1}^{n} (\partial_{x_j} w)^2 = 0. \tag{4.7}$$

The first condition states that w must be a particular solution of the Laplace equation. The second condition states that the square of the sum of the coefficients α_j must be equal to zero. This method of solving the Laplace equation using the hypercomplex coordinates can also be applied to solve the homogeneous wave equation. The wave equation is similar to the Laplace equation in terms of structure, but has positive spatial dimensions and a negative time-like dimension giving a Lorentzian signature $(+,+,+,-)$, whereas the Laplace equation including time has both positive space and time components giving a Euclidean signature $(+,+,+,+)$ [74]. These two equations can be related to one another through the Wick rotation [75] by introducing an imaginary transformation of the time component $t = -i\tau$. If the 4 dimensional wave equation is considered

$$\Box\varphi = 0,$$

where $\Box$ is the D'Alembertian operator $\Box = \partial_x^2 + \partial_y^2 + \partial_z^2 - \frac{1}{c^2}\partial_t^2$, then this equation can be solved using the hypercomplex coordinate

$$w = \delta t + i\alpha x + i\beta y + i\gamma z. \tag{4.8}$$

Then from equation 4.7, the constants must satisfy

$$\delta^2 - \alpha^2 - \beta^2 - \gamma^2 = 0. \tag{4.9}$$

The solutions to either the Laplace or wave equation can hence be transformed to one another by a Wick rotation of the hypercomplex coordinates, w and $\tilde{w}$ [75]. This changes the signature from Lorentzian to Euclidean.

The higher-dimensional approach to obtaining holomorphic functions to the Laplace and homogenous wave equations have long been known and have been studied in depth over the years [76]. Whittaker and others developed a real n dimensional general integral solution to the Laplace equation [77–79], of which Penrose later re-derived a more mathematically sophisticated complex contour integral [80]. The contour integral derived by Penrose has a geometrical interpretation. This geometrical interpretation was used to found *twistor* theory. This theory was originally developed in order to provide a framework for quantum gravity [81–83], but was later extended to describe twistor string theory [84]. Unfortunately twistor theory has been unable to provide a framework to describe quantum gravity, but the theory has had a significant impact on the field of mathematics, especially in the areas of differential equations and integrable systems, as well as in some areas of physics such as fluid dynamics [85, 86]. The real Whittaker integral in 3 dimensions is written

$$f = \int F\left(\alpha z + i\beta x\cos\vartheta + i\gamma y\sin\vartheta, \vartheta\right)\mathrm{d}\vartheta, \tag{4.10}$$

where α, β, γ and ϑ are arbitrary constants [87]. The Penrose integral takes the form shown in ref [81–83] and is given by

$$f = \int g(w, \lambda)\mathrm{d}\lambda,$$

where the function $\lambda = e^{i\vartheta}$ is the spinor coordinate and is closely related to the ϑ constant in the Whittaker integral. The Laplace equation is often found in the theory of electromagnetism. In the next section, the general complex contour integral solution to the Laplace equation and its relationship to Maxwell's equations are investigated.

4.4 Application to Maxwell's Equations

Maxwell's equations containing only the electric field components can be written in 2 dimensions, without any source term as

$$\partial_x E_y - \partial_y E_x = 0,$$
$$\partial_x E_x + \partial_y E_y = 0,$$

where $E_{x,y}$ is the electric field. These equations are comparable to the Cauchy-Riemann equations shown in equation 4.1 and 4.2. It is possible to use the general solutions of the Laplace equation to seek solutions of Maxwell's equations. A general n dimensional approach is derived in the following section. This framework will then be applied to describe the beam-beam interaction with an arbitrary charge density distribution. Consider the following modified Cauchy-Riemann equations in n dimensions as from ref [88],

$$\sum_{p,q}^{n} \epsilon^{ab,\ldots,pq} \partial_p E_q = 0, \tag{4.11}$$

$$\sum_{p,q}^{n} \partial^p E_p = \rho, \tag{4.12}$$

where $\epsilon^{ab,\ldots,pq}$ is the Levi-Civita symbol [89] written as

$$\epsilon_{ab,\ldots,pq} = \begin{cases} +1 & \text{if } (a,b,\ldots,p,q) \text{ is an even permutation of } (1,2,3,\ldots,n) \\ -1 & \text{if } (a,b,\ldots,p,q) \text{ is an odd permutation of } (1,2,3,\ldots,n) \\ 0 & \text{otherwise.} \end{cases} \tag{4.13}$$

If the inhomogeneous term ρ is set to zero, these equations reduce to the Cauchy-Riemann equations in n dimensions and can be solved using traditional methods.

If however $\rho \neq 0$, then in 2 or 3 dimensions these equations are comparable to Maxwell's equations with a non-zero source charge term. The regime in which this source charge term is non-zero is of particular interest to problems involving the beam-beam interaction, in which the counter rotating beam needs to be considered. Solutions of E are sought by making an n dimensional *ansatz* with a number of unconstrained functions. The *ansatz* takes the form

$$E_\alpha(x_j, ..., x_n) = f_j(x_j, ..., x_n)\left[1 - \mathcal{H}(x_j, ..., x_n)\right], \tag{4.14}$$

where $\alpha = \{x_1, x_2, ..., x_j\}$, f_j are unconstrained functions that need to be found and $\mathcal{H}$ is a function that relates to the particular solution for a non-zero charge density distribution $\rho \neq 0$. The function $\mathcal{H}$ is set to $\mathcal{H} = e^H$ for the initial derivation, since the beam-beam interaction is considered here. Introducing the functional form of the particular solution that is comparable to a Gaussian distribution may further reduce the degrees of freedom and help to constrain the system of equations. Non-Gaussian distributions are also considered later in the chapter. Substituting the *ansatz* in equation 4.14 into equations 4.11 and 4.12 and collecting terms containing the function $\mathcal{H}$ gives two sets of equations to be solved. These equations are

e^0 :

$$\sum_{p,q}^{n} \epsilon^{ab,...,pq} \partial_p f_q = 0, \tag{4.15}$$

$$\sum_{p,q}^{n} \partial^p f_p = 0, \tag{4.16}$$

e^H :

$$\sum_{p,q}^{n} \epsilon^{ab,...,pq} f_p \partial_q H = 0, \tag{4.17}$$

$$\sum_{p,q}^{n} f_p \partial^p H = -\rho e^{-H}, \tag{4.18}$$

where, once again, $\epsilon^{ab,...,pq}$ is the Levi-Civita symbol [89], $a, b, ..., p, q$ take values between $0, 1, 2, ..., n$, and n represents the number of dimensions. Tensor notation is used here to express the curl operator such that when p and q take values from 1 to 2, equations 4.15 and 4.16 will reduce to the 2 dimensional Cauchy-Riemann equations,

$$\partial_x f_p - \partial_y f_q = 0,$$

$$\partial_x f_p + \partial_y f_q = 0.$$

Hence, it can be seen that the first set of equations with the e^0 terms are the Cauchy-Riemann equations in n dimensions and upon cross differentiation and substitution can be shown to give the n dimensional Laplace equation. The n dimensional Laplace equation is given as

$$\sum_{j=1}^{q} \nabla_n^2 f_j = 0. \tag{4.19}$$

The functions $f_1, ..., f_n$ will satisfy the Laplace equation and can be solved by introducing the hypercomplex coordinate

$$w = \sigma + i\xi, \qquad \tilde{w} = \sigma - i\xi, \tag{4.20}$$

where σ and ξ take the form $\sigma = \alpha_n x_n$ and $\xi = \sum_j^{n-1} \alpha_j x_j$. Thus the general solution for each of the functions f_j can be written as,

$$f_j = g_j(w) + h_j(\tilde{w}), \tag{4.21}$$

under the condition that,

$$a_n^2 + \sum_{j=1}^{n-1} i^2 \alpha_j^2 = 0. \tag{4.22}$$

Substituting these functions back into the homogenous Cauchy-Riemann equations allows transformations between all the functions f_j to be found. All the functions f_j, can be expressed in terms of just one function, labelled f_1. The transformation between the functions are given by a linear combination of the complex constants α_j and $\bar{\alpha_j}$. The general solution to f_1 is hence written as,

$$f_1 = c_1 g(w) + c_1 h(\tilde{w}), \tag{4.23}$$

with the remaining functions f_j given by,

$$f_j = c_j g(w) + c_j h(\tilde{w}), \tag{4.24}$$

where $c_{1,2,..,j}$ are linear functions of α_j obtained from the hypercomplex coordinates 4.20. The first set of e^0 equations have been solved and yield solutions to the Laplace equation that in turn can be used to further constrain the equations in the e^H set. The homogenous equation in the e^H set of equations can be solved through the method of characteristics [90], if the Jacobian of the system is defined. The Jacobian can be written as

$$\mathbf{J} = \begin{vmatrix} \partial_\sigma w & \partial_\xi w \\ \partial_\sigma \tilde{w} & \partial_\xi \tilde{w} \end{vmatrix} \neq \{0, \infty\}. \tag{4.25}$$

This can be seen to be true in general by using the hypercomplex coordinate 4.20. Substituting the hypercomplex coordinates 4.20, gives the Jacobian as

$$\mathbf{J} \equiv -2i. \tag{4.26}$$

Transforming equation 4.17 to the complex coordinates $(w, \tilde{w})$, substituting all the functions f_j in terms of just one function f_1, and applying the method of characteristics allows the relationship between H and the functions f_j to be found. For a full description and discussion of the method of characteristics see appendix A. Applying the method of characteristics yields a system of ordinary differential equations to be solved, namely

$$\sum_{p,q}^{n} f_p \mathrm{d}_p + f_q \mathrm{d}_q = 0, \tag{4.27}$$

when $p \neq q$. This gives the functional form of H in terms of the general solutions to the Laplace equation

$$H = H\left(\int g \mathrm{d}w + \int h \mathrm{d}\tilde{w}\right). \tag{4.28}$$

The method of characteristics used here also introduces a geometric relation between the functions H, g and h. This states that functions f_j must lie orthogonal to the characteristic surface H.

Equation 4.28 gives the relationship between the general solutions to the Laplace equation, denoted by the functions f and g, and the particular solution H. However, in order to find the particular solution, equation 4.18 must be solved. Transforming equation 4.12 to hypercomplex coordinates and substituting all the functions f_j in terms of f_1, yields after simplification,

$$\left(e^H\right)' = -\frac{\mu\rho}{g_k(w)h_k(\tilde{w})}, \tag{4.29}$$

where μ is a combination of the constants α_i and ρ is the source charge term. This can be further split into integrals using the functional form of H,

$$\partial_w H = gH',$$
$$\partial_{\tilde{w}} H = hH'.$$

This gives the two separate integral equations as

$$\int \partial_w H e^H = -\int \frac{\mu\rho}{h(\tilde{w})} \mathrm{d}w, \tag{4.30}$$
$$\int \partial_{\tilde{w}} H e^H = -\int \frac{\mu\rho}{g(w)} \mathrm{d}\tilde{w}. \tag{4.31}$$

This is as far as the system of equations can be reduced without introducing the source charge term ρ and the functions g and h. The functions g and h can be expressed in a general form as contour integral solutions that satisfy the Laplace equation [77–79, 81–83], namely,

$$g = \int \hat{g}(w, \lambda)\mathrm{d}\lambda, \qquad h = \int \hat{h}(\tilde{w}, \lambda)\mathrm{d}\lambda. \tag{4.32}$$

Equations 4.30 and 4.31 can be solved independently of one another. Importantly, these equations establish a relationship between the solutions to the Laplace equation and the inhomogeneous term ρ, in terms of a complex contour integral. In 3 or more dimensions this contour integral gives the particular solution over a complex surface.

In summary, the set of equations 4.15 to 4.18 have been solved with the aim of keeping the expressions and conditions as general as possible before introducing a specific form of ρ. The first set of equations are the Cauchy-Riemann equations and therefore Laplace equations can be derived from these. The Laplace equations can be solved by introducing the functions g and h, which are contour

integral functions of the hypercomplex coordinates w and $\tilde{w}$, respectively. Since these functions also satisfy the Cauchy-Riemann equations they are analytic and holomorphic. The second set of equations relate the general Laplace equations to the particular solution H. The homogenous equation in this set of equations was re-written in terms of the hypercomplex coordinates and solved using the method of characteristics. This allows the functional form of H to be obtained. Finally the inhomogeneous equation is expressed in terms of the hypercomplex coordinates and the functions g and h are related to the function H and the source charge term ρ. The full system of equations have been left with just the inhomogeneous equation to be solved in terms of the ρ, g and h.

In the next section, the method described above is applied to the 2 dimensional transverse Gaussian bunch and the well known round bunch electric field is re-derived based on the new method. The framework is then applied to alternative, non-exponential, non-linear charge density distributions and the electric fields are compared to the literature.

4.5 2 Dimensional Gaussian Bunch

To ensure that the method derived in section 4.3 is valid, the mathematical method was used to derive the standard round Gaussian bunch electric field [16].

Initially considering the hypercomplex coordinate given by expression 4.20 and setting $n = 2$ gives

$$w = \alpha_1 x + i\alpha_2 y, \qquad \tilde{w} = \alpha_1 x - i\alpha_2 y,$$

where the constants must satisfy condition 4.22, hence

$$\alpha_1^2 - \alpha_2^2 = 0. \tag{4.33}$$

From inspection it can be seen that $\alpha_1 = 1$ and $\alpha_2 = 1$. The hypercomplex coordinates become the standard complex coordinates,

$$w = x + iy, , \qquad \tilde{w} = x - iy. \tag{4.34}$$

Working in the rest frame of the bunch to negate any magnetic fields yields an electrostatic problem. Within this limit, equations 4.15 and 4.16 in 2 dimensions reduce to

e^0 :

$$\partial_x f_2 - \partial_y f_1 = 0, \tag{4.35}$$

$$\partial_x f_1 + \partial_y f_2 = 0. \tag{4.36}$$

e^H :

$$f_1 \partial_y H - f_2 \partial_x H = 0, \tag{4.37}$$

$$f_1 \partial_x H + f_2 \partial_y H = -\rho e^{-H}. \tag{4.38}$$

The e^0 set of equations are the Cauchy-Riemann conditions and show that f_1 and f_2 must be holomorphic and analytic. Cross differentiating equations 4.35 and 4.36 yields two Laplace equations in terms of f_1 and f_2.

$$\nabla^2 f_1 = 0, \qquad \nabla^2 f_2 = 0.$$

Equations 4.5 can be satisfied using the general solution to the Laplace equation, which can be written in terms of two separable functions $g_{1,2}$ and $h_{1,2}$. The functions $g_{1,2}$ contain the complex coordinate w only and $h_{1,2}$ contains $\tilde{w}$ only. The Laplace equations for $f_{1,2}$ are solved in the form

$$f_1 = g_1(w) + h_1(\tilde{w}), \tag{4.39}$$

$$f_2 = g_2(w) + h_2(\tilde{w}). \tag{4.40}$$

Substituting 4.39 and 4.40 into equations 4.35 and 4.36, results in a complex linear transformation relating the functions f_1 and f_2. The function f_1 is related to f_2 through

$$f_1 = g + h, \tag{4.41}$$

$$f_2 = ig - ih, \tag{4.42}$$

where the subscript is now dropped such that $g_1 = g$ and $h_1 = h$. This solves the Cauchy-Riemann equations in $f_{1,2}$. Considering next, the homogenous equation in the e^H set. Equation 4.37 can be solved via the method of characteristics. This gives

$$\frac{\mathrm{d}x}{f_2} = \frac{\mathrm{d}y}{f_1} = \frac{\mathrm{d}H}{0}, \tag{4.43}$$

which yields the ordinary differential equation

$$f_1 \mathrm{d}x + f_2 \mathrm{d}y = 0. \tag{4.44}$$

Transforming to the new coordinates and substituting the expressions for f_1 and f_2 in terms of g and h, gives the functional form for H as

$$H = H\left(\int g\mathrm{d}w + \int h\mathrm{d}\tilde{w}\right). \tag{4.45}$$

This leaves the inhomogeneous equation to be solved. Transforming to complex coordinates and substituting $f_{1,2}$ into equation 4.38 gives

$$g\partial_{\tilde{w}}H + h\partial_w H = -\frac{\rho e^{-H}}{\sqrt{2}}. \tag{4.46}$$

Using the functional form of H and differentiating, allows the expressions for $\partial_w H$ and $\partial_{\tilde{w}}H$ to be used. These expressions are

$$\partial_w H = H'g, \qquad \partial_{\tilde{w}}H = H'h,$$

which results in the final inhomogeneous equation, which can be simplified to,

$$\left(e^H\right)' = -\frac{1}{2\sqrt{2}}\frac{\rho}{g(w)h(\tilde{w})}. \tag{4.47}$$

This equation can be separated into two integrals that can be solved independently of one another. These equations are

$$e^H = -\frac{1}{2\sqrt{2}}\frac{1}{h(\tilde{w})}\int \rho\mathrm{d}w,$$
$$e^H = -\frac{1}{2\sqrt{2}}\frac{1}{g(w)}\int \rho\mathrm{d}\tilde{w}.$$

The equations can be simplified no further without the functions g and h. These functions are general solutions to the Laplace equation and can hence be obtained through either the Penrose or Whittaker integral. The integral over the complex

coordinate can be solved to give

$$f_1 = \frac{x}{r^2}, \qquad f_2 = \frac{y}{r^2}, \tag{4.48}$$

where $r = \sqrt{x^2 + y^2}$. Substituting complex coordinates for x and y, and simplifying yields

$$f_1 = \frac{1}{w} + \frac{1}{\tilde{w}}. \tag{4.49}$$

Thus from inspection, the functions g and h are

$$g = \frac{1}{w}, \qquad h = \frac{1}{\tilde{w}}. \tag{4.50}$$

Now that both g and h have been obtained, the inhomogeneous equation can be solved. The inhomogeneous equation given by equation 4.47 relates these functions g and h to the particular solution of Poisson's equation, H. The integral to evaluate is

$$e^H = -\frac{1}{2\sqrt{2}}\tilde{w} \int e^{-4w\tilde{w}} \mathrm{d}w.$$

This integral can be evaluated trivially and gives H as

$$H = -\frac{1}{2}r^2, \tag{4.51}$$

where $r = \sqrt{x^2 + y^2}$. The complete system of equations has now been solved and the functions f_1, f_2 and H have been constrained in terms of the charge density distribution ρ. Substituting the functions $f_{1,2}$ and H back into the original *ansatz*

for the electric field gives the well known function form, as shown in [16] as

$$E_x = \frac{x}{r^2}\left[1 - e^{-\frac{x^2}{2}-\frac{y^2}{2}}\right], \tag{4.52}$$

$$E_y = \frac{y}{r^2}\left[1 - e^{-\frac{x^2}{2}-\frac{y^2}{2}}\right]. \tag{4.53}$$

This method has provided an alternative approach to deriving the electric fields in the rest frame of the bunch. Using analytic expressions from the Laplace equation and the relationship of these functions to the source charge term allows the complete system of equations to be constrained allowing the electric field to be derived in a compact and concise manner. To obtain the beam-beam kick a Lorentz boost is applied in the direction of movement and the force applied to a counter rotating test particle is calculated. Since the method was derived for an arbitrary charge density distribution and the hypercomplex coordinates can be written in n dimensions, the method can easily be extended to include higher dimensions and can include complicated coupling in the charge density distribution. These aspects will be discussed in the following sections.

4.5.1 Non-Linear Distributions

The method of unconstrained functions described above is not necessarily limited to studying beam-beam effects and can also be applied to space charge. Space charge occurs when particles within a bunch exhibit an electric field on themselves [91]. This electric field can be calculated in the same way as the beam-beam interaction, by solving Poisson's equation. Beam-beam effects in the LHC occur at a flat top energy of 6.5 TeV and the electric fields are almost entirely confined to the transverse planes, since the bunches are within the ultra-relativistic limit. Space charge effects at flat top energy in the LHC can be considered to be negligible. However, in machines operating at lower energies, space charge effects will

impact performance. Space charge effects, much like the beam-beam interaction can lead to emittance growth, which can limit machine performance and bunch lifetimes [17]. Much like the LHC, understanding and accurately modelling such effects is vital to assess machine performance and identify possible issues during operation. In this section, the electric fields generated by non-linear distributions prevalent in the space charge literature are re-derived using the method of unconstrained functions.

The Kapchinskij-Vladimirskij (KV), waterbag, and parabolic distributions are distributions that have been studied with regard to space charge [92]. The dynamics of non-linear bunches with space charge has been considered extensively [91, 93]. The method of unconstrained functions will be used to derive the electric field for non-linear distributions of the form

$$\rho = \frac{m}{\pi\sigma_x\sigma_y}\left[1 - \frac{x^2}{\sigma_x^2} - \frac{y^2}{\sigma_y^2}\right]^{m-1}, \tag{4.54}$$

where depending on the value of m, this distribution yields a number of non-linear distributions [92]. When $m = 1$, expression 4.54 takes the form of the KV distribution, for $m = 2$, this distribution is called the Waterbag distribution, and finally, when $m = 3$, the distribution is parabolic.

As an example, the parabolic distribution is considered. For a 2 dimensional round bunch of the form 4.54, with $m = 3$, gives the charge density distribution as,

$$\rho_{pb}(x, y) = \frac{3N}{\pi\sigma^2}\left(1 - x^2 - y^2\right)^2, \tag{4.55}$$

where the term outside the bracket represents the line density and x and y are in number of sigma. Normalising to the line density, transforming to the complex

coordinates,

$$x = w + \tilde{w}, \qquad y = i(w - \tilde{w}),$$

gives

$$\rho_{pb}(w, \tilde{w}) = (1 - 4w\tilde{w})^2. \tag{4.56}$$

The inhomogeneous equation in 2 dimensions is given by equation 4.47 and replacing the exponent e^H with the general function $\mathcal{H}$ yields the two separable modified equations,

$$\mathcal{H} = -\mu \int \tilde{w}\rho \mathrm{d}w, \tag{4.57}$$

$$\mathcal{H} = -\mu \int w\rho \mathrm{d}\tilde{w}. \tag{4.58}$$

As a 2 dimensional bunch is being considered, then the result from section 4.5 can be exploited and the functional form of $\mathcal{H}$ relating the Laplace solutions to the particular solution can be used. Using expression 4.45 and choosing the integration over w (although the choice of integration does not vary the resulting form) and substituting the charge density distribution gives

$$\mathcal{H} = -\frac{\tilde{w}}{2\sqrt{2}} \int (1 - 4w\tilde{w})^2 \mathrm{d}w. \tag{4.59}$$

Performing the integration over w gives $\mathcal{H}$ in the form of equation 4.60,

$$\mathcal{H} = -\frac{1}{2\sqrt{2}} \frac{(1 - 4w\tilde{w})^3}{12}. \tag{4.60}$$

Transforming back to real Cartesian coordinates, substituting $f_{1,2}$ from the 2 dimensional solution to the Laplace equation, and $\mathcal{H}$ into the adjusted *ansatz*,

written as,

$$E_\alpha(x,y) = f_\alpha(x,y)\left[1-\mathcal{H}\right],$$

yields the electric field in the x and y plane as,

$$E_x = \frac{x}{r^2}\left[1-\frac{1}{2\sqrt{2}}\frac{(1-r^2)^3}{12}\right], \tag{4.61}$$

$$E_y = \frac{y}{r^2}\left[1-\frac{1}{2\sqrt{2}}\frac{(1-r^2)^3}{12}\right]. \tag{4.62}$$

This gives the same functional form as seen in ref [92], when $x^2+y^2 \leq \sigma^2$ and is within some constant scaling factor. Note, that the choice of the constants α_1 and α_2 is arbitrary, however these must satisfy condition 4.22. The method of unconstrained functions can also be applied to higher dimensional cases. In the next section, the method of unconstrained functions will be applied to find the electric field of a 3 dimensional Gaussian charge density distribution. The results will be compared to the literature.

4.6 3 Dimensional Gaussian Bunch

One of the benefits of the method of unconstrained functions is that the framework is based on the hypercomplex coordinates and can be extended to any number of dimensions. The method of unconstrained functions can be applied to higher dimensional problems, in which solutions to the Laplace equation via the Green's function method may become challenging. Extending to an n dimensional space does however present difficulties when considering odd dimensional complex surfaces, such as the case for 3 dimensions [94]. To effectively describe a 3 dimensional complex surface an additional geometrical interpretation must be considered [81, 82, 94]. This geometrical interpretation, although interesting, can

be avoided by not relying on the hypercomplex coordinates to solve the system of equations given by 4.15 to 4.18. Instead, if a solution to the Laplace equation can be generated through the Whittaker solution or the Penrose integral, this can be used to constrain the entire system of equations and still find solutions in the presence of a charge density distribution, without requiring that the functions g and h are completely separable. For a 3 dimensional electric field in the rest frame of the bunch Maxwell's equations take the form,

$$\partial_y E_z - \partial_z E_y = 0, \tag{4.63}$$

$$\partial_x E_z - \partial_z E_x = 0, \tag{4.64}$$

$$\partial_x E_y - \partial_y E_x = 0, \tag{4.65}$$

$$\partial_x E_x + \partial_y E_y + \partial_z E_z = \rho(x, y, z). \tag{4.66}$$

The *ansatz* given by expression 4.14 can be written as

$$E_\alpha(x, y, z; t) = f_j(x, y, z; t) \left[1 - e^{H(x,y,z;t)}\right], \tag{4.67}$$

for $j = 1, 2, 3$ and $\alpha = \{x, y, z\}$. Using the 3 dimensional *ansatz* will result in the system of equations given by 4.15 to 4.18 for $n = 3$ becoming

$\underline{e^0}$

$$\partial_y f_3 - \partial_z f_2 = 0, \tag{4.68}$$

$$\partial_x f_3 - \partial_z f_1 = 0, \tag{4.69}$$

$$\partial_x f_2 - \partial_y f_1 = 0, \tag{4.70}$$

$$\partial_x f_1 + \partial_y f_2 + \partial_z f_3 = 0. \tag{4.71}$$

$\underline{e^H}$

$$f_2\partial_z H - f_3\partial_y H = 0, \tag{4.72}$$

$$f_1\partial_z H - f_3\partial_x H = 0, \tag{4.73}$$

$$f_1\partial_y H - f_2\partial_x H = 0, \tag{4.74}$$

$$f_1\partial_x H + f_2\partial_y H + f_3\partial_z H = -\rho e^{-H}. \tag{4.75}$$

The first set of equations in e^0 are the Cauchy-Riemann equations in 3 dimensions and hence Laplace equations. The 3 dimensional solution to the Laplace equation can be obtained using [95] and is given as

$$f_1 = \frac{x}{r^3}, \quad f_2 = \frac{y}{r^3}, \quad f_3 = \frac{z}{r^3}, \tag{4.76}$$

where $r = \sqrt{x^2 + y^2 + z^2}$. This provides solutions to the first e^0 set of equations without requiring a transformation to the hypercomplex coordinates and a separation of the coordinates. Substituting the solutions given in 4.76 into equations 4.72, 4.73 and 4.74 gives equations 4.77 to 4.79,

$$y\partial_z H - z\partial_y H = 0, \tag{4.77}$$

$$x\partial_z H - z\partial_x H = 0, \tag{4.78}$$

$$y\partial_x H - x\partial_y H = 0. \tag{4.79}$$

Since the r term has cancelled, these equations can be solved using the method of characteristics allowing the functional form of H in terms of $f_{1,2,3}$ to be determined. This gives H as

$$H = H\left(\int x dx + \int y dy + \int z dz\right) \rightarrow$$
$$H = H\left(\frac{1}{2}x^2 + \frac{1}{2}y^2 + \frac{1}{2}z^2\right). \tag{4.80}$$

The Laplace solutions given by 4.76 have fixed the relationship to the characteristic surface H. Finally, to obtain the exact form of H, the inhomogeneous equation in terms of the charge density distribution ρ must be solved. Substituting $f_{1\rightarrow 3}$ into equation 4.75 gives

$$H'\left(\frac{x}{r^3}x + \frac{y}{r^3}y + \frac{z}{r^3}z\right) = -\rho e^{-H}; \tag{4.81}$$

collecting terms and simplifying yields

$$\left(e^H\right)' = -re^{-\frac{1}{2}r^2}.$$

This leaves one integration over r to be evaluated. Integrating equation 4.6 over r, yields a direct relationship between r and H, which is given by,

$$e^H = e^{-\frac{1}{2}r^2}. \tag{4.82}$$

This gives the form for e^H which can be substituted into the *ansatz*. Hence, the electric field written in component form is

$$E_x = \frac{x}{r^3}\left[1 - e^{-\frac{1}{2}r^2}\right], \tag{4.83}$$
$$E_y = \frac{y}{r^3}\left[1 - e^{-\frac{1}{2}r^2}\right], \tag{4.84}$$
$$E_z = \frac{z}{r^3}\left[1 - e^{-\frac{1}{2}r^2}\right]. \tag{4.85}$$

These expressions derived here can be compared directly to the alternative derivation through Poisson's equation detailed in Ref [25]; this is shown in figure 4.1. The functional form of the electric field is equivalent to [25] for a particle with no transverse offset and restricted to $E_z(0, 0, z)$. The solutions are equivalent in the absence of any coupling between the planes. The method of unconstrained func-

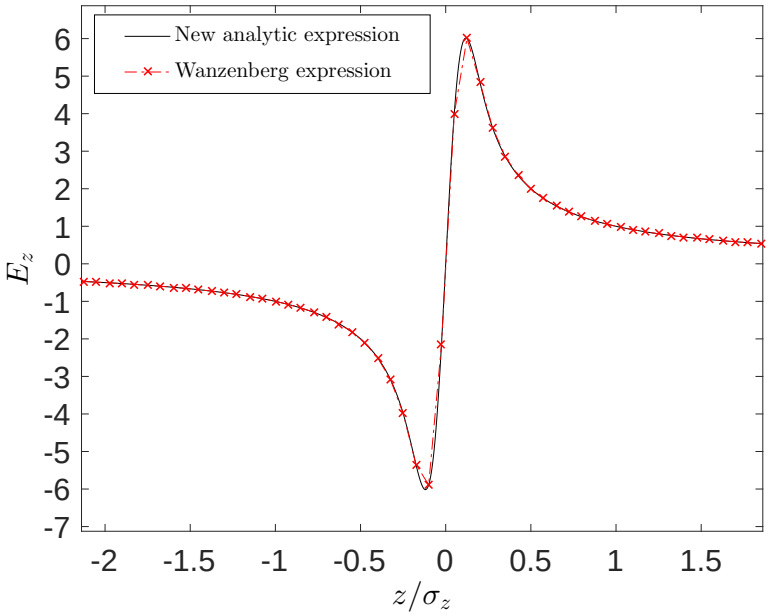

FIGURE 4.1: Comparison between the expressions obtained for the longitudinal electric field between the new analytic method and traditional method of solving Poisson's equation.

tions as detailed earlier in the chapter has been applied to a 3 dimensional charge density distribution without requiring a complex coordinate transformation. Instead the system of equations were constrained by obtaining the 3 dimensional solutions to the Laplace equation through the general solution provided by Whittaker/Penrose integral. The solution to the Laplace equation has allowed the system to be constrained in a similar way to the 2 dimensional derivation. The Laplace solutions constrain the relationship to the particular solution of Poisson's equation, allowing the functional form of the particular solution to be obtained through the method of characteristics. Finally, the functional form of H and the Laplace solutions were used to solve the inhomogeneous equation containing the

charge density distribution ρ, allowing the electric field in the rest frame of the bunch to be obtained. This method has so far been applied to simple distributions without any coupling. In the final section of this chapter, a first attempt approach of describing the hourglass effect using the method of unconstrained functions is discussed along with analysis and discussion.

4.7 The Hourglass Effect: A First Approach

The beam-beam interaction is a strong dynamic effect in which the electric and magnetic fields produced by the proton bunch will cause the charge density distribution of the counter rotating bunch to vary throughout the interaction. For most cases in the LHC, the standard fixed Gaussian charge density distribution provides an accurate description of the beam-beam interaction, as the bunches can be considered to be ultra-relativistic and with negligible coupling between the planes. However as the high energy community demands for more luminosity increases, the machine performance must be pushed. To obtain more luminosity, the strength of the beam-beam interaction and its impact on performance is likely to increase. To produce more luminosity the bunches must be squeezed more at the IP or the bunch population must be increased. Squeezing the bunch more can lead to bunch length and coupling effects which can no longer be ignored [62]. These effects can cause a drop in luminosity at the IP since the bunches may not collide at the minimum β-function. The luminosity for a head-on colliding bunch including offset and crossing angle is discussed in detail in chapter 2. From the discussion presented there, the luminosity can be written as

$$\mathcal{L} = \frac{N_1 N_2 f_{rev} N_{bunch}}{4\pi\sigma_x\sigma_y} F(\vartheta, \sigma_z),$$

where the function $F(\vartheta, \sigma_z)$ is the geometric loss factor. The loss factor in the LHC during normal operation is about $F(\vartheta, \sigma_z) = 0.80$ [61]. The components required to calculate this factor are usually obtained during machine operations and dedicated experiments, or through numerical computation. The luminosity reduction due to the hourglass effect can be included in this loss factor. The hourglass effect is not well understood analytically and often requires computationally expensive calculations. An analytical expression describing the hourglass effect could significantly improve computation speed of the beam-beam effect in simulation. An analytical expression including the hourglass effect could greatly benefit computational speed for both tracking codes such as `Sixtrack` and multi-bunch and particle strong-strong simulation codes such as `combi`. Particle in cell methods for strong-strong simulations can be time consuming, especially when trying to simulate many bunches [32].

The method of unconstrained functions can be applied to the problem of the hourglass effect to find analytical expressions for the electric fields, in the presence of a complicated charge density distribution. The hourglass effect causes a parabolic behaviour in the transverse bunch size. This parabolic effect arises due to the change of β-function with the distance from the collision point and couples the transverse bunch size to the longitudinal position [16]. The hourglass effect arises when the transverse bunch size becomes comparable to the length of the bunch $\sigma_r \sim \sigma_z$. The β-function will vary over the interaction length and depend on the longitudinal position. The β variation about the IP can be written as

$$\beta(z) = \beta^* \left(1 + \frac{z^2}{\beta^{*2}}\right). \tag{4.86}$$

This will cause the transverse bunch size to vary though the IP as

$$\sigma_r = \sqrt{\epsilon_r \beta^* \left(1 + \frac{z^2}{\beta^{*2}}\right)}. \tag{4.87}$$

Figure 4.2 shows the variation of the transverse bunch size (σ_r) as a function of the longitudinal position towards the collision point at $z = 0$. The bunch size varies parabolically away from the IP. For smaller values of β^*, the larger the variation of the bunch size with longitudinal position. One possible optics option for the HL-LHC is to use a flat bunch. If this choice of optics is chosen and luminosity levelling is performed by reducing β^* in steps, the final step of the luminosity levelling will have $\beta^*_{x,y} = 0.150/0.075$m. The final step leaves the β^* in the vertical plane comparable to the length of the bunch, resulting in the vertical plane varying following equation 4.87. In this scenario, the bunch length effects will no longer be negligible and could impede luminosity performance. In order to understand the impact from the perspective of the beam dynamics, this effect needs to be understood. The variation around the IP will result in a different electric field, since the bunch will not remain a fixed Gaussian throughout the interaction. The charge density distribution including the parabolic variation

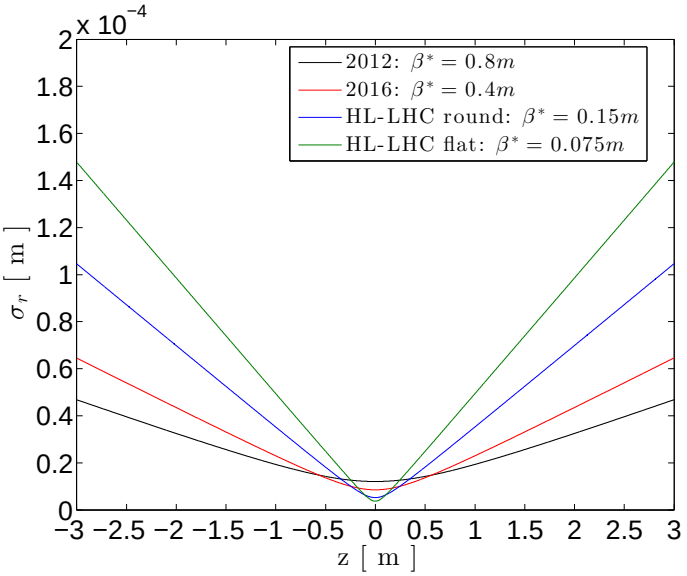

FIGURE 4.2: Variation of the transverse beam sizes for various LHC and HL-LHC optics.

around the IP is shown in figure 4.3. Particles with a small radial amplitude will observe an approximately Gaussian charge density distribution and hence the electric fields these particles experience will be largely unchanged. For particles

at larger amplitudes, the charge density distribution deviates significantly from the standard Gaussian distribution and behaves comparatively like a bi-Gaussian distribution. The electric fields that these particles experience may no longer be well described by the fixed Gaussian distribution from the literature [16]. The

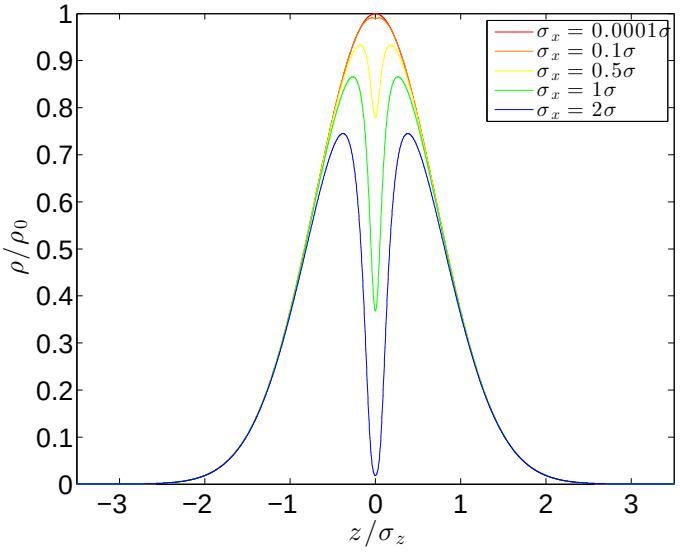

FIGURE 4.3: Gaussian charge density distribution including the coupling due to the hourglass effect in the rest frame of the bunch for particles of different radial amplitudes.

charge density distribution including the transverse bunch size coupling to the longitudinal position in Cartesian coordinates can be written as

$$\rho(x,y,z) = \rho_n \exp\left[-\frac{x^2}{2\sigma_x^2(1+\frac{z^2}{\beta^{2*}})} - \frac{y^2}{2\sigma_y^2(1+\frac{z^2}{\beta^{2*}})} - \frac{z^2}{2\sigma_z^2}\right]. \tag{4.88}$$

For an axially symmetric round bunch, polar coordinates can be introduced and will transform the charge density distribution to,

$$\rho(r,z) = \rho_n \exp\left[-\frac{r^2}{2\sigma_r^2(1+\frac{z^2}{\beta^{2*}})} - \frac{z^2}{2\sigma_z^2}\right]. \tag{4.89}$$

Following this, the hypercomplex coordinates w and $\tilde{w}$ can also be recast in terms of the polar coordinates. The Cartesian coordinates in terms of the hypercomplex

coordinates are

$$x = \alpha_1(w + \tilde{w}), \quad y = \alpha_2(w + \tilde{w}), \quad z = \alpha_3(w - \tilde{w}),$$

where the complex constants are $\alpha_1 = \frac{1}{\sqrt{2}}, \alpha_2 = \frac{1}{\sqrt{2}}$ and $\alpha_3 = i$. The polar coordinate transformation to complex coordinates will be given by,

$$r = \sqrt{(w + \tilde{w})^2}, \quad z = i(w - \tilde{w}). \tag{4.90}$$

The charge density distribution including the hourglass effect is given by equation 4.89 and hence the method of unconstrained functions can be used to obtain an analytical expression of the electric field in the rest frame of the bunch. Whether the charge density distribution can be obtained in closed form depends on the integration of the source charge term. Since the derivation is in 2 dimensions, the initial steps detailed in section 4.5 can be applied. Starting from the 2 dimensional inhomogeneous equation,

$$\left(e^H\right)' = -\frac{1}{2\sqrt{2}} \frac{\rho_{hg}}{g(w)h(\tilde{w})}, \tag{4.91}$$

then the integrals can be separated using

$$H' = \frac{1}{g}\partial_w H,$$
$$H' = \frac{1}{h}\partial_{\tilde{w}} H.$$

Substituting the equation 4.89 into the inhomogeneous equation 4.91, gives the following two integrals

$$e^H = -\frac{\tilde{w}}{2\sqrt{2}} \int \exp\left[-\frac{(w+\tilde{w})^2}{2\sigma_r^2\left(1-\frac{(w-\tilde{w})^2}{\beta^{2*}}\right)} + \frac{(w-\tilde{w})^2}{2\sigma_z^2} \right] dw, \tag{4.92}$$

$$e^H = -\frac{w}{2\sqrt{2}} \int \exp\left[-\frac{(w+\tilde{w})^2}{2\sigma_r^2\left(1-\frac{(w-\tilde{w})^2}{\beta^{2*}}\right)} + \frac{(w-\tilde{w})^2}{2\sigma_z^2} \right] d\tilde{w}. \tag{4.93}$$

Note that the choice of integral is arbitrary and both will yield the same functional form of e^H. The two integrals in fact correspond to different hemispheres of the Riemann sphere; however this is beyond the scope of this thesis. More details can be found in [81, 82, 94]. Either one of these integrals will provide the function e^H. The charge density distribution including the hourglass effect can be re-written in the form

$$\rho_{hg} = \rho_n \exp\left[(w^2+\tilde{w}^2)\left(1-\frac{1}{\sigma(w,\tilde{w})}\right) - 2w\tilde{w}\left(1+\frac{1}{\sigma(w,\tilde{w})}\right) \right], \tag{4.94}$$

where $\sigma = \left(1-\frac{(w-\tilde{w})^2}{\beta^{2*}}\right)$ and the complex coordinates are in units of the bunch sigma. If $\sigma(w,\tilde{w}) = 1$, then there is no coupling between the bunch planes and the Gaussian bunch expression in complex coordinates is re-obtained as in section 4.5. Unfortunately, this integral is not trivial and it is unlikely that a closed form expression can be found. There are two possible options to proceed; initially an expansion to a required order can be made around small values of the complex coordinates w and $\tilde{w}$. This will provide a good approximation for small values of w and $\tilde{w}$. Realistically, only small order terms can be evaluated as each higher order term will require multiple integration by parts. Small order terms will however likely contain the most dominant terms from the charge density distribution. This will allow the model to be evaluated to some degree. The second option is to evaluate the integral numerically providing an exact solution to the integral. Both approaches will be attempted and the two results compared.

Firstly, the expansion of the exponential function is discussed. Selecting equation 4.92 and expanding around the complex coordinates w provides an area in complex space in which the analyticity of the function will be preserved. However, H will not be analytic throughout all of w and $\tilde{w}$ and will be limited to when the complex coordinates are small. The Taylor expansion of the exponential function can be written as

$$e^{-\mu\psi} = \sum_{n=0}^{\infty} \frac{(-\mu\psi)^n}{n!},$$
$$e^{-\mu\psi} \approx 1 - \mu\psi + \frac{\mu^2}{2}\psi^2 - \frac{\mu^3}{6}\psi^3 + \frac{\mu^4}{24}\psi^4 + \mathcal{O}(\psi^5),$$

where ψ is the argument of the exponential shown in equation 4.94 and μ is a constant coefficient of ψ. Substituting the expansion into equation 4.92 yields

$$e^H = -\frac{\tilde{w}}{2\sqrt{2}} \int \left(1 - \mu\psi + \frac{\mu^2}{2}\psi^2 - \frac{\mu^3}{6}\psi^3 + \frac{\mu^4}{24}\psi^4 + \mathcal{O}(\psi^5)\right) \mathrm{d}w. \tag{4.95}$$

These integrals can then be treated by splitting into separate integrals labelled $\mathcal{I}_0, \mathcal{I}_1, \mathcal{I}_2$ respectively, with the subscripts denoting the polynomial order of the function. Considering integrals up to second order gives the following integrals to evaluate,

$$\mathcal{I}_0 = -\frac{\tilde{w}}{2\sqrt{2}} \int 1 dw, \quad \mathcal{I}_1 = \frac{\tilde{w}}{2\sqrt{2}} \int \mu\psi dw, \quad \mathcal{I}_2 = -\frac{\tilde{w}}{2\sqrt{2}} \int (\mu\psi)^2 dw.$$

The first integral, $\mathcal{I}_0$ is trivial is

$$\mathcal{I}_0 = -\frac{w\tilde{w}}{2\sqrt{2}}. \tag{4.96}$$

This is the same result as when there is no coupling present, or when $\sigma = 1$. The effect of the coupling will be retained in the higher order moments of the distribution. The remaining integrals $\mathcal{I}_1$ and $\mathcal{I}_2$ are not trivial and require integration

by parts. Consider the integral $\mathcal{I}_1$ first leaving the $\frac{\tilde{w}}{2\sqrt{2}}$ outside and integrating gives

$$\mathcal{I}_1 = \left(\frac{w^3}{3} + \tilde{w}^2 w\right)\left(1 - \frac{1}{\sigma}\right) + \int \left(\frac{w^3}{3} + \tilde{w}^2 w\right) \cdot \partial_w \left(\sigma^{-1}\right) dw... \\ -w^2\tilde{w}\left(1 + \frac{1}{\sigma}\right) + \int w^2\tilde{w} \cdot \partial_w(\sigma^{-1}) dw. \tag{4.97}$$

From the integration by parts it can be seen that the integral cannot be evaluated in closed form. Upon each iteration of the integration, additional integrals arise, which in turn need to be evaluated by parts. Evaluating the most dominant terms up to second order allows the electric field including the coupling in the charge density distribution to be analysed. Taking the expression for H and substituting into the *ansatz* in equation 4.14 gives

$$E_r = \frac{r}{r^2 + z^2}\left[1 - \left(-\mathcal{I}_0(r,z) + \mathcal{I}_1(r,z) - ...\right)\right], \tag{4.98}$$

$$E_z = \frac{z}{r^2 + z^2}\left[1 - \left(-\mathcal{I}_0(r,z) + \mathcal{I}_1(r,z) - ...\right)\right]. \tag{4.99}$$

The radial electric field in the rest frame of the bunch including the additional coupling in the charge density distribution is shown in figure 4.4. In figure 4.4, the radial electric field is shown for particles along various longitudinal positions in the bunch. Particles with a large value of z have a smaller radial electric field profile compared to particles with a small longitudinal displacement which have a short, sharp radial electric field profile.

From figure 4.4, the radial electric field profile for a particle at σ_{z_1} corresponding to a small z undergoes a large electric field around $r = 0$. However the radial electric field tends to zero quickly towards larger amplitudes. For a particle located at σ_{z_4}, which corresponds to a large value of z, the electric field is much more sustained between $-1 \leq r \leq 1$, although the total magnitude of the field is much smaller than the σ_{z_1} case. Similarly to the previously mentioned case,

the electric field falls to zero quickly towards larger radial amplitudes. For radial

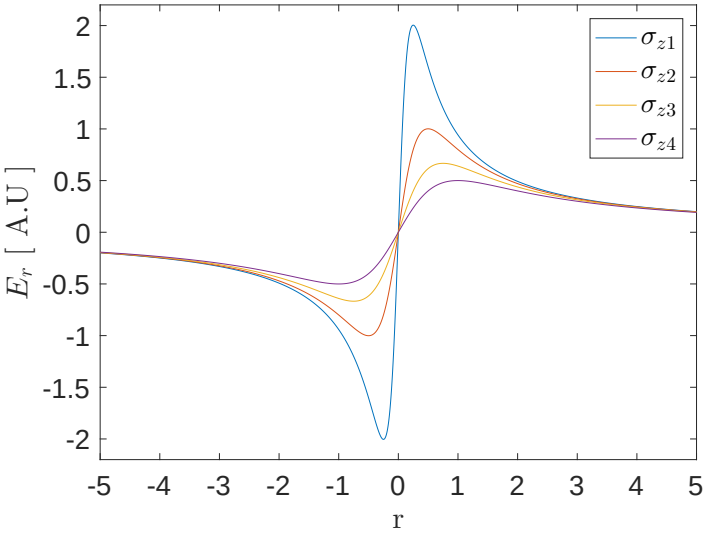

FIGURE 4.4: The radial electric field including a coupling due to the hourglass effect in the charge density distribution.

amplitudes that are considerably larger, the electric field will diverge as the Taylor expansion of the hourglass function diverges. Qualitatively, the electric field behaves in a similar way as the standard fixed Gaussian distribution. There is however an imaginary component to the field. On closer inspection the magnitude of the imaginary part of the field is of the order of 10^{-21} and can hence be negated. Initial investigation of the distribution does not appear to show any significant deviation of the functional form from the fixed Gaussian model. The comparison between the Gaussian distribution and the hourglass distribution will be considered later. To determine the impact of the higher order terms on the distribution, the integral is also evaluated numerically and compared to the expansion. This will signify how well the expansion represents the integral.

4.7.0.1 Numerical Integration of the Hourglass Exponential

As previously shown, the integral cannot be evaluated in closed form. Instead the integral was evaluated numerically using global adaptive quadrature to determine

an approximate value of the integration [96, 97]. The integral has a defined range in the complex planes $w, \tilde{w}$ between $0 \rightarrow 1$ as shown in figure 4.5. Values outside of this range $0 \geq \{w, \tilde{w}\} \leq 1$, diverge and tend to infinity. Using this

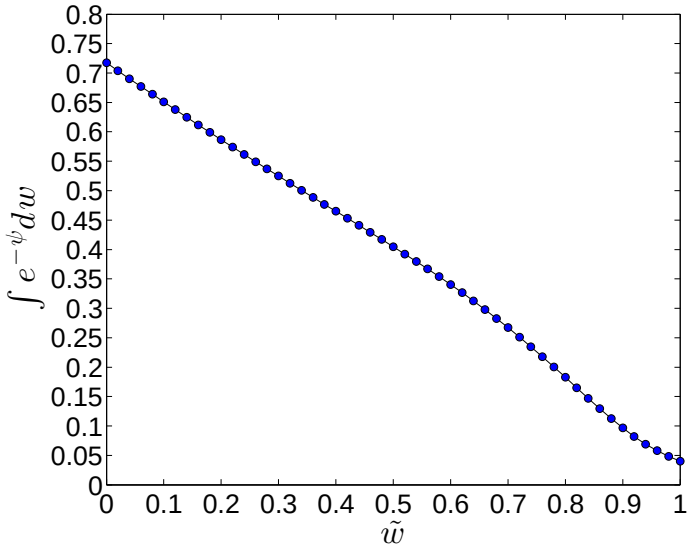

FIGURE 4.5: The value of the numerical integral as a function of $\tilde{w}$ from $0 \rightarrow 1$ with the integration over w from $0 \rightarrow 1$.

numerical integration and substitution in place of e^H allows the accuracy of the Taylor expansion used in the previous section to be evaluated. A comparison between the numerical integration and the expansion is shown in figure 4.6. The difference between the two curves is approximately 4% with the higher order terms reducing the electric field profile with respect to the expansion towards larger radial amplitudes. The difference accounts for the higher order terms that are neglected from the expansion. The higher order terms reduce the value the electric field as $r \rightarrow \infty$. At small values of r however the agreement is very good as these terms are well accounted for during the expansion. To determine the impact of the hourglass effect on the electric field, a direct comparison between the fixed Gaussian distribution and the distribution including the hourglass effect is discussed in the next section.

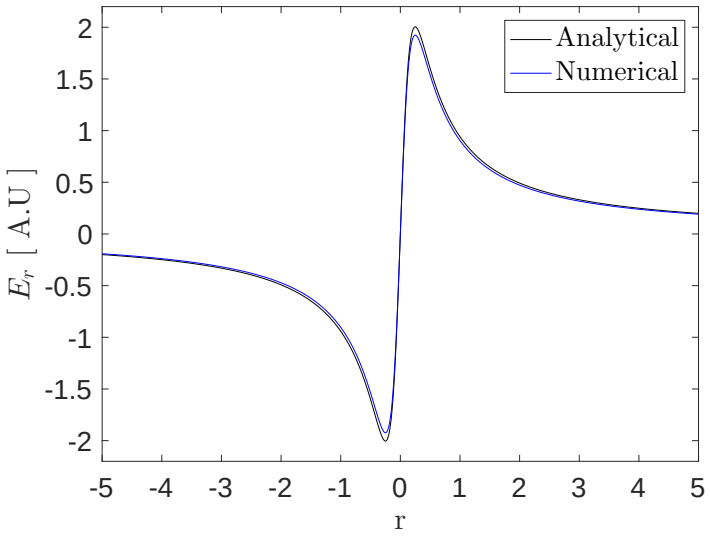

FIGURE 4.6: The transverse electric field calculated from the numerical integration compared to the expansion of the exponential.

4.7.0.2 Comparison to the Fixed Gaussian Model

In order to determine the impact of the coupled charge density distribution on the electric field profile, the analytical expansion of the electric field including the hourglass coupling in the charge density distribution is directly compared to the fixed Gaussian expression. The radial and longitudinal electric field profiles for the two charge density distributions are shown in figure 4.7 and figure 4.8. The radial electric fields shown in figure 4.7 compares well towards larger radial amplitudes as the field tends to zero at ∞. At smaller radial amplitudes however, there is some difference between the two field profiles. The coupling between the planes in the charge density distribution appears to have an effect on the small amplitude particles. For these particles, the linear part of the field is stronger in comparison to the electric field caused by the fixed Gaussian charge density distribution. The linear part of the electric field also acts over a smaller region of r. This implies that more particles in the bunch at a particular longitudinal position will experience a non-linear electric field. For particles at radial amplitudes $r > 3\sigma$, the long-range effect of both electric fields are almost identical and

will tend to zero at ∞.

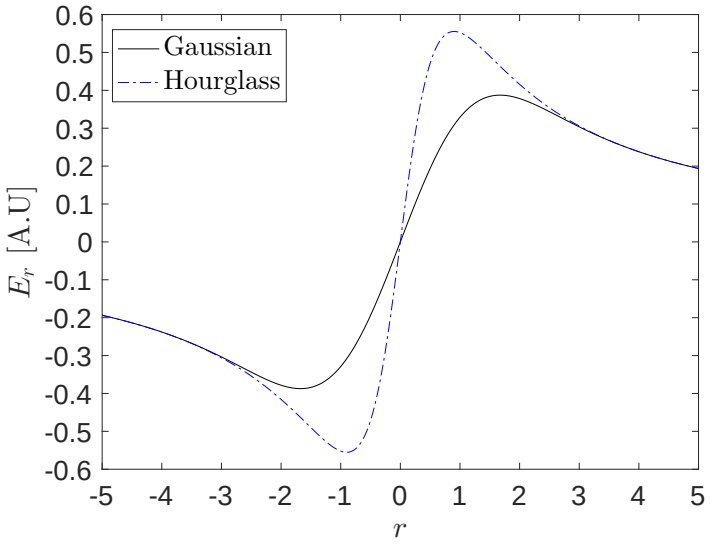

FIGURE 4.7: Comparison between the radial electric field profile for the coupled charge density distribution and the fixed Gaussian charge density distribution.

The longitudinal electric fields from the two different models are compared to one another in figure 4.8. There is no difference between the longitudinal electric fields.

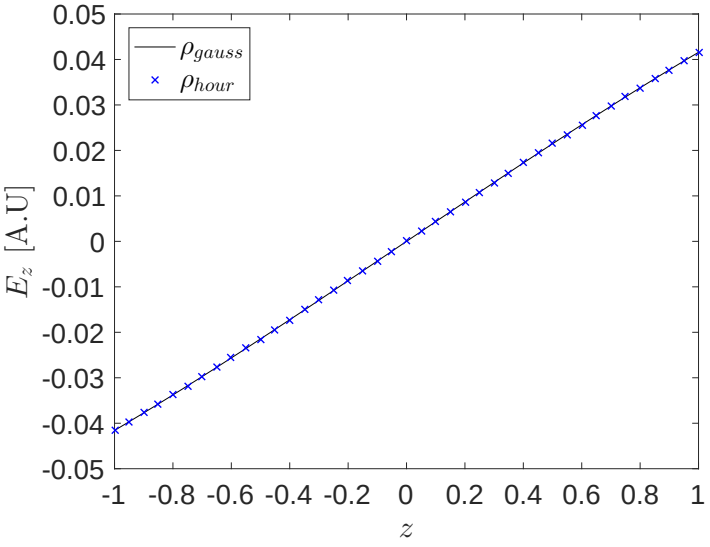

FIGURE 4.8: Comparison between the longitudinal electric field profile for the coupled charge density distribution and the fixed Gaussian charge density distribution.

4.8 Discussion

The purpose of this chapter was to address the difficulties in deriving analytical solutions when the charge density distribution is coupled. As the LHC and HL-LHC strives to push luminosity performance, effects such as the hourglass effect will become more significant. Therefore in order to evaluate the impact on the dynamics, numerical evaluation is often required. This will require large computational resources in order to evaluate the effect, since an analytical expression is not available. Throughout this chapter, a mathematical framework for obtaining analytical expressions based on complex coordinate transforms and contour integrals has been derived. The first section introduces the required fundamentals of complex analysis in order to derive the mathematical framework. Initially the 2 dimensional Cauchy-Riemann equations are stated and from these the Laplace equation is derived. The Laplace equation is shown to be solved analytically through a complex coordinate transformation, with the general solution to the Laplace equation shown in 2 dimensions, expressed as two arbitrary functions g and h. The solution to the Laplace equation is further generalised to n dimensions by introducing the hypercomplex coordinates given by equation 4.20, along with the corresponding conditions 4.22. Not only this, but a connection between the hypercomplex coordinates satisfying the Laplace equation and the wave equation can be made through a Wick rotation. The Wick transformation is not used for the work in this thesis as the derivations of the electric field are performed in the rest frame of the bunch, however, this connection maybe useful for other problems. These generalised hypercomplex coordinates are then applied to the scenario when one of the Cauchy-Riemann equations is no longer homogeneous.

A solution to the modified Cauchy-Riemann equations with an inhomogeneous term ρ can be found by introducing the *ansatz* given by expression 4.14. This *ansatz* contains a number of unknown functions labelled $f_{1,\ldots,n}$ and a function H

that corresponds to the particular solution of Poisson's equation. Substituting the *ansatz* into the n dimensional modified Cauchy-Riemann equations allows a system of equations to be obtained. The first set of equations contain only f_j and are the standard Cauchy-Riemann equations. From these expressions the n dimensional Laplace equation can be derived. The functions $f_{1,\ldots,n}$ are transformed to new hypercomplex coordinates and are shown to be holomorphic functions that satisfy the Laplace equation. This provides solutions for the first set of equations. In the second set of equations the homogeneous equation is approached first. This can be solved through the method of characteristics and relates the general solution of the Laplace equation to the particular solution of Poisson's equation. From the method of characteristics, the functional form of H is calculated and contains the holomorphic functions $f_{1,\ldots,n}$. Finally, only the equation that contains the inhomogeneous term ρ remains. Transforming this final equation to the new hypercomplex coordinates and substituting the functions $f_{1,\ldots,n}$, allows two independent equations to be obtained which need to be solved. Simplifying this equation yields a direct relationship between the general solution to the Laplace equation and the particular solution to Poisson's equation.

This provides the general mathematical framework that can allow analytical solutions for a general charge density distribution to be obtained. The method is then applied for a few different charge density distributions and the electric fields were calculated. The electric fields recovered using this method agree with results in the literature.

Finally the method was applied to a charge density distribution that included the hourglass effect, which is characterised by a coupling of the transverse bunch size to the longitudinal position. The electric field was obtained and evaluated both numerically and through an expansion and the results compared. The new

electric field expression was then compared to the standard fixed Gaussian case and discussed.

This chapter concludes the theoretical investigation of the luminosity performance in the LHC and its future upgrade the HL-LHC. In the following section, experimental and simulation research is conducted with regard to the long-range beam-beam interaction.

Chapter 5

The Long Range Beam-Beam Limit in the LHC

5.1 Introduction

The long-range beam-beam interaction is one effect that will dictate luminosity performance and the choice of operational parameters for the LHC [98]. This chapter will discuss some of the relevant findings from two dedicated machine studies that took place during the 2015 and 2016 proton physics run. In the first section, a review of the long-range beam-beam effects and the impact of these effects during luminosity production runs in the LHC is provided. Then in the following section, luminosity observations during the 2012 LHC run are discussed, which provides the motivation for the study. Since this chapter discusses the luminosity decay, a number of the different luminosity decay models are discussed. Then the results from two dedicated machine studies, which took place in 2015 and 2016, are introduced. The machine study procedures will be discussed in chronological order with the 2015 study results presented first. The intensity,

luminosity, and emittance during the study is analysed and the long-range beam-beam limit is determined. The impact of the long-range beam-beam interaction as a function of crossing angle and collision pattern is discussed and analysed. In the 2015 machine study, the impact of chromaticity and Landau octupole strength on the lifetimes are also reviewed.

The procedure and analysis from the 2016 machine study is then discussed in the following section. The difference in optics and collision schemes between the 2015 and 2016 machine studies is highlighted. Again, the bunch by bunch intensity and luminosity data is reviewed, as well as the emittances. The analysis is summarised and the long-range beam-beam limit is identified. This provided evidence and justification that the crossing angle in the LHC could be reduced during normal operation without interference from the long-range beam-beam interaction. Initial results from early fills at the reduced crossing angle are discussed and reviewed.

5.2 The Long Range Beam-Beam Limit in the LHC

Summarising the discussion of beam-beam effects in chapter 2 and 3, the strength of the long-range beam-beam interaction will be dependent on the normalised beam separation in the drift space at the IP. The normalised beam separation depends on the β-function at the IP (denoted by β^*) the normalised emittance ϵ_n, the crossing angle α and the relativistic factor γ. The beam-beam separation for small crossing angles within the paraxial limit ($\tan\vartheta \approx \vartheta$) can be written as

$$d_{sep} \approx \sqrt{\frac{\beta^*\gamma}{\epsilon_n}}\alpha. \tag{5.1}$$

The strength of the long-range beam-beam interactions can be varied using the parameters in equation 5.1. During long-range beam-beam machine studies, the strength of the long-range beam-beam interaction is increased by reducing the crossing angle α. This reduces the beam-beam separation, d_{sep}, which is measured in units of the RMS beam size and calculated using equation 5.1 [99]. To provide a comparison to different configurations and for consistency, a normalised separation in the drift space is used throughout this chapter.

Bunches in the LHC form trains that undergo combinations of head-on and long-range beam-beam interactions, as discussed earlier in chapter 1 and 3. A schematic of the collision configuration is shown in figure 5.1. All bunches in the train will undergo head-on collisions, however bunches do experience differing numbers of long-range interactions depending on their position in the train. The number of long-range interactions will depend on the filling scheme during that particular time of operation. During the 2016 luminosity production run, bunches in the train had 17 to 34 long-range beam-beam interactions per IP. This means that the beam-beam effects will vary depending on the bunch position in the train. The bunches not in the centre of the train, that have less than 34 long-range beam-beam interactions, are often called Pacman bunches. Pacman bunches will exhibit different lifetime behaviour to those bunches in the centre of the train. Pacman bunches at the front and end of the train had the smallest number of collisions with 17 interactions. The number of long-range beam-beam interactions increases for bunches towards the centre of the train up to 33 interactions per IP. The bunches in the centre of the train with the most number of head-on and long-range beam-beam interactions are called nominal bunches, and these bunches experience 34 interactions per IP. The number of head-on and long-range interactions for a bunch during a typical luminosity production fill is shown in figure 5.2, with the long-range pattern for a single train isolated and shown in figure 5.3. In figure 5.3, the long-range pattern can be observed clearly,

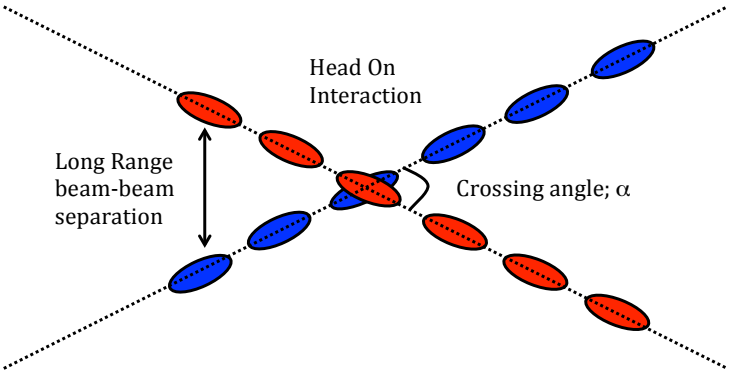

FIGURE 5.1: Beam-beam interactions in the LHC.

with nominal bunches having the largest number of collisions over one turn in the machine. The aim of this chapter is to describe how the long-range beam-

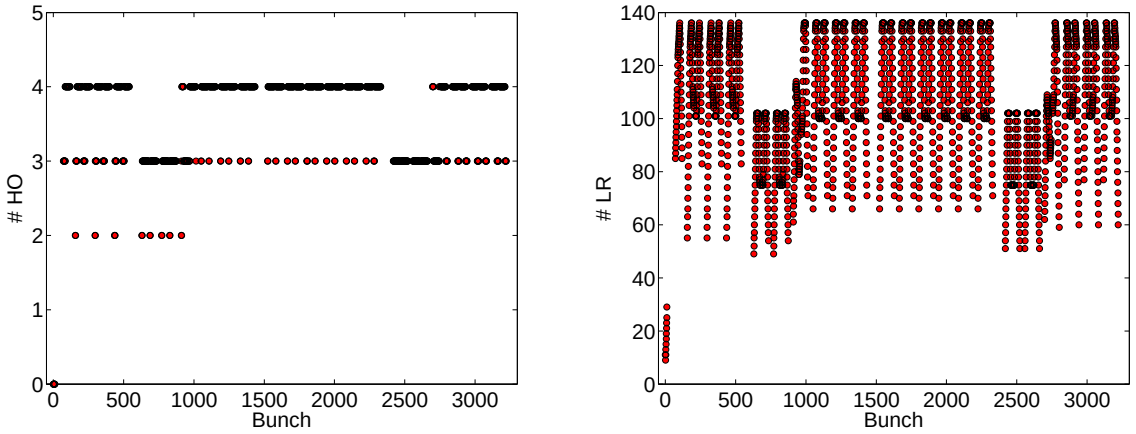

(a) (b)

FIGURE 5.2: Number of long-range and head-on interactions for each bunch for a typical luminosity production fill during the 2015/6 run, with a bunch spacing of 25 *n*s.

beam effects depend on the beam separation, d_{sep}, which will allow the necessary margins to be defined in terms of separation and parameter choices for the LHC. The motivation for this chapter is reviewed in the next section.

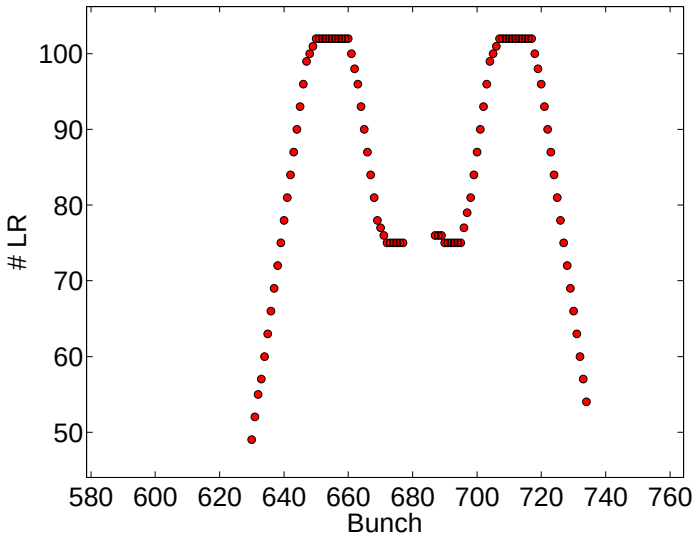

FIGURE 5.3: Single train from a luminosity production fill and the total number and pattern of the long-range beam-beam interactions.

5.2.1 Motivation

During the 2012 LHC run, the optics, operational parameters and relatively small beam-beam separations of 9.5 σ to 12.5 σ lead to strong beam-beam interactions. This was characterised by a large beam-beam parameter of approximately $\xi_{bb} = 0.007$ per IP. This coupled with high Landau octupole and chromaticity settings, resulted in beam-beam effects that had a significant impact on the beam and luminosity lifetimes. This dependence was most strongly observed in the first hour of luminosity production fills during 2012 operations. This can be seen clearly in figure 5.4, which shows the luminosity decay rate, $\lambda = \frac{1}{\tau}$ as a function of the bunch position along the train, where there is a sensitivity to the tune spread at IP2 and IP8 during the first hour of the fill. In order to retain long fill lengths and reduce losses, the beam-beam separations were increased at IP2 and IP8 [100].

FIGURE 5.4: Luminosity decay rate (λ) dependence on the long-range beam-beam interaction during the 2012 LHC run [100]. The lifetimes of the bunches depend strongly on the bunch position (or slot number) in the train and the luminosity decay rates are the largest in the first two hours of the fill.

A number of machine experiments were proposed with the aim of identifying the minimum crossing angle achievable in the LHC for a defined optics [101–103]. Reducing the crossing angle in steps increases the strength of the long-range beam-beam interaction. With the beam-beam separation reduced, the impact on the intensity and luminosity lifetimes can be observed and the operational tolerances can be defined. Unlike the previous long-range beam-beam studies undertaken at the LHC to determine luminosity reach, the lifetimes were observed for 10-15 minutes at each crossing angle step during the 2015 and 2016 machine studies. This allows the intensity losses to stabilise, resulting in the decay rates over a period of time to recover to some converged value at each crossing angle step. The long-range beam-beam interaction would eventually limit the recovery of the decay rates measured at the previous crossing angle step. This could be explained by the non-linearity of the long-range beam-beam interaction reducing the dynamic aperture. This can cause particles to undergo chaotic and irregular motion. It can also result in particles in the core of the bunch diffusing to the tails where the particles can then be scraped off by the collimators. The non-linearities of the long-range beam-beam interaction can cause these tails to be replenished with particles from the core. Operationally it is beneficial from the perspective of luminosity production to operate at the smallest possible crossing angle. This will increase the geometric loss factor from crossing angle given by

$$S = \frac{1}{\sqrt{1 + \left(\frac{\sigma_s}{\sigma_x}\tan\frac{\alpha}{2}\right)^2}}. \tag{5.2}$$

The geometric factor increases with crossing angle as shown in figure 5.5. Operating the machine at a smaller crossing angle does impact the strength of the beam-beam interaction. As shown previously from equation 5.1, a smaller crossing angle results in stronger long-range beam-beam effects, which in turn can induce particle losses. To maximise luminosity production, the machine should

be operated at the smallest possible crossing angle before additional losses are observed due to the long-range beam-beam interaction. This defines the long-range beam-beam limit and the minimum beam-beam separation.

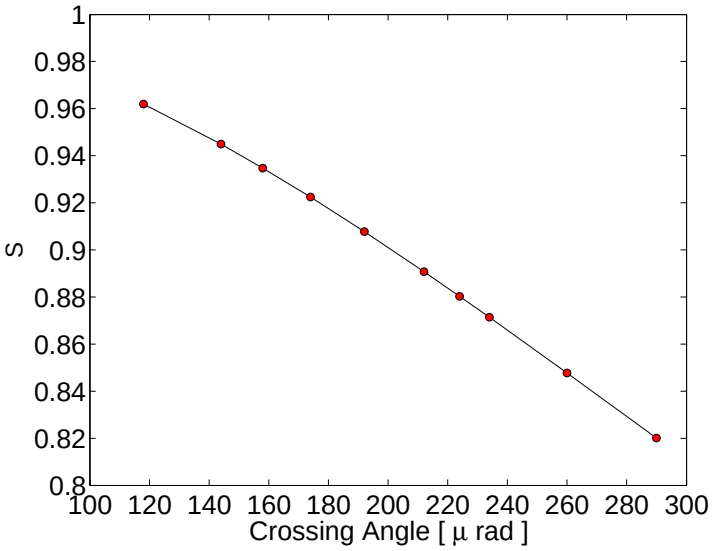

FIGURE 5.5: Geometric loss factor variation with crossing angle.

Discussed in the next section is a review of some of the luminosity decay models that have been used for previous studies and at other accelerators.

5.2.2 Decay Models

A number of different models are available to describe luminosity and intensity decay rates, some of these are described and summarised in [104] and references therein. Here a few of the key models are reviewed and discussed to provide an overview of the literature and previous attempts to model luminosity evolution in colliding storage rings.

5.2.2.1 Simple Exponential Decay

An effective method of fitting the decay of some function with time, i.e intensity or luminosity, is the simple exponential model. The model provides a lot of freedom in the fitting parameters with more complicated models often just variations of this model. The simple exponential decay model is written as

$$N = N_0 e^{-\lambda \cdot t} + c(t), \tag{5.3}$$

where N is the parameter being studied i.e, intensity or luminosity, λ is the decay rate, which corresponds to the inverse of the lifetime τ, t is the time, and c is a non-zero constant that accounts for the fact that the bunch intensity does not decay completely to zero. The constant in this case will tend to zero as the decay time tends to infinity. An example of the fitting using the simple exponential decay model applied to a single bunch is shown in Figure 5.6. The fitting describes the decay well and is calculated using a least squares method [105, 106].

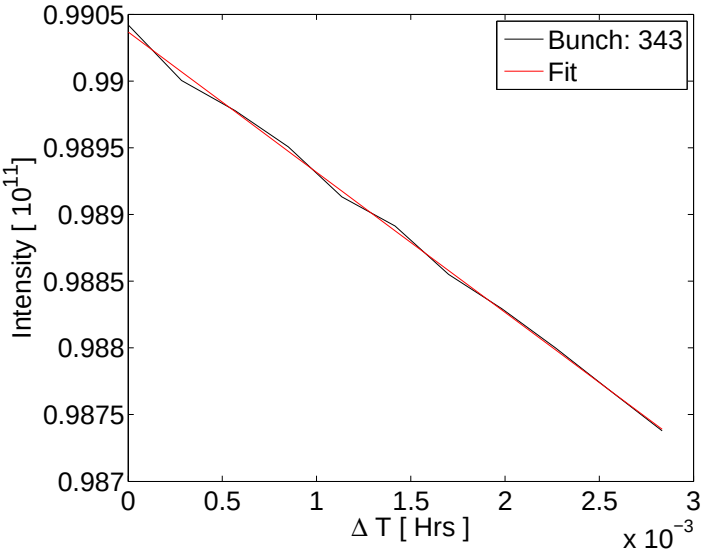

FIGURE 5.6: Example fit of the simple exponential decay model to the intensity data. From this the intensity decay rate λ can be calculated.

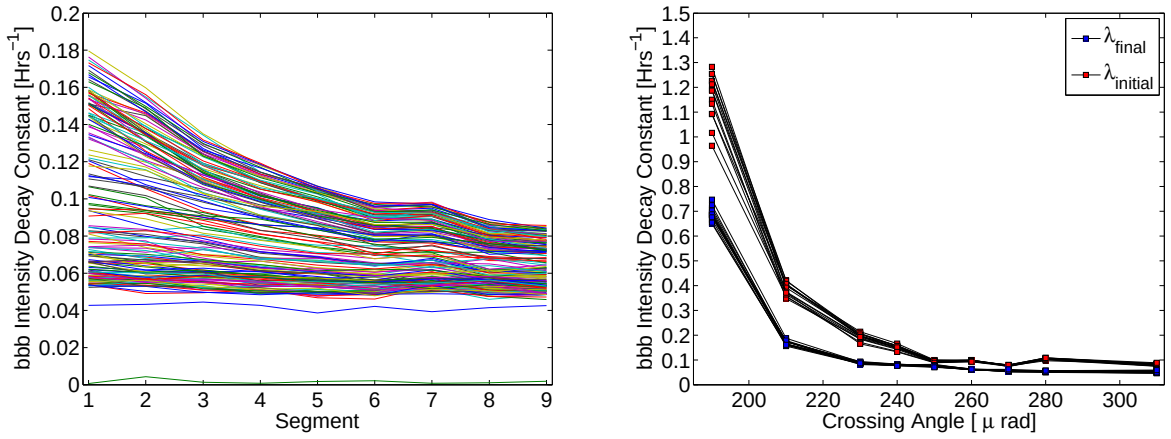

(a) (b)

FIGURE 5.7: The left hand plot fig 5.27(a), shows the calculated bunch by bunch (bbb) decay rate λ convergence over the duration of a crossing angle step. The right hand plot fig 5.27(b) shows the decay rate variation over crossing angle when calculated at the beginning of the crossing angle step compared to the end of the crossing angle step.

The simple c variable exponential decay model used in this chapter was found to describe the intensity and luminosity decays well, during the long-range machine studies and throughout luminosity production fills.

For the 2016 machine study, the fitting method was further refined to account for the variation in calculated lifetime throughout each crossing angle step. The decay rates were calculated using a similar method as in the previous machine study by fitting equation 5.3 to the intensity or luminosity data; however unlike the previous analysis, each crossing angle step was further divided into smaller steps called segments. The decay model was fitted over each segment and the value of λ could be obtained as it varied throughout the crossing angle step. The additional fitting would allow possible decay regimes to be identified throughout each crossing angle. The variation of the decay rate λ as a function of segment is shown in figure 5.7. The first segment corresponds to the first initial minutes of the crossing angle step, whilst the last segment corresponds to the last few minutes of the crossing angle step, with each crossing angle step lasting approximately $10 - 15$ minutes. The decay rate can be seen to converge to some

final value. The decay rates quoted for the 2016 machine study and the 2016 luminosity production fills are the final converged values of λ.

5.2.2.2 Tevatron Model

One particular luminosity model that has had success is the Tevatron model [107]. This model was developed with the aim of characterising the luminosity decay over long fill lengths, specifically with the aim of determining how the antiproton intensity reduction impacted the "luminosity burn-off" . Three models were derived and include a time dependency in the decay rate λ. The first two models are essentially extensions to the simple exponential decay model, including a time dependancy of various forms in λ. The second model allows a polynomial dependence on the time dependence. The third and final variation of the model is different to the simple exponential decay and includes a linear function of time. The three models are given by

$$\mathcal{L}(t) = \mathcal{L}_0 e^{-\frac{t}{\tau}}, \tag{5.4}$$

$$\mathcal{L}(t) = \mathcal{L}_0 e^{-\frac{t}{\mathcal{T}(t)}}, \tag{5.5}$$

$$\mathcal{L}(t) = \mathcal{L}_0 \times \left(1 + \frac{t}{\tau_0 C_3}\right)^{-x(t)}. \tag{5.6}$$

In the second variation of the model $\mathcal{T}(t) = \mathcal{T}_0 + C_1 \times t^{c_2}$ and the four fitting parameters $\mathcal{L}(0)$, $\mathcal{T}_0$, C_1 and C_2 are free variables. In the final model of the luminosity, the function $x(t)$ is written

$$x(t) = C_3 + C_4 t, \tag{5.7}$$

where once again, C_3 and C_4 are free variables. These models provide a number of different options that could potentially describe the luminosity evolution in the Tevatron. Out of the three models given by equations 5.4, 5.5, and 5.6, the

luminosity stores in the Tevatron were best described by equation 5.5. Further details of these models can be found in [104, 107] and the references therein.

5.2.2.3 Brightness Model

Similarly to the Tevatron model, the brightness model developed by X. Buffat also includes a variation of the decay rate with time [104]. The decay rate variation with time in this model is dependent on the brightness, which is closely related to the luminosity of the bunch. The brightness of the bunches can be written as

$$\mathcal{B} = \frac{n_i n_j}{8\pi^2 \epsilon_i \epsilon_j}, \tag{5.8}$$

where $n_{i,j}$ is the number of particles in the bunch, i, j corresponds to beam 1 and beam 2 respectively and $\epsilon_{i,j}$ is the emittance of bunch. The decay model can then be separated into two distinct regimes given by

$$\mathcal{B}(t) = \begin{cases} \mathcal{B}_c \left[\frac{\tau_1}{\tau_1+\tau_2} + \left(1 - \frac{\tau_1}{\tau_1+\tau_2}\right) e^{(t_c-t)\frac{\tau_1+\tau_2}{\tau_1\tau_2}} \right], & t < t_c, \\ \mathcal{B}_c e^{-\frac{t-t_c}{\tau_1}}, & t > t_c, \end{cases} \tag{5.9}$$

where $\tau_{1,2}$ correspond to the two lifetimes of the processes, t_c is the critical time at which the decay rate changes from one regime to another, and $\mathcal{B}_c$ corresponds to the brightness at the point of the regime change, $\mathcal{B} = \mathcal{B}(t_c)$. At $t = t_c$ the transition from one decay regime to another is assumed to be instantaneous and continuous such that there is no impact on the brightness from the transition alone. The brightness of the bunch can be affected by a number of different processes that act over different time scales. For example, a slow process such as intra-beam scattering will act over a lifetime τ_1, whereas a fast process, such as emittance growth due to close proximity of a resonance will have a significantly smaller lifetime, τ_2. The brightness is also closely related to the luminosity,

allowing luminosity lifetimes to be obtained. The bunch luminosity is related to the bunch brightness following $\mathcal{L} \propto \mathcal{B}^2$.

The simple exponential model is used throughout the analysis here for simplicity and speed of calculation. This model provides an accurate fit and calculation of the decay rate, as shown in figure 5.6. Including the additional sub-fitting as used in the 2016 machine study further refined the calculation, allowing the decay rate variation over the duration of crossing angle step to be quantified, avoiding the complexities involved with using the Tevatron or brightness models.

In the next section, the decay rates calculated by the simple exponential model is applied to measured data from two dedicated long-range beam-beam machine studies.

5.3 Results

In this section, the analysis from two dedicated long-range beam-beam machine studies are presented and discussed. The impact with regard to luminosity production and performance in the LHC is highlighted.

5.3.1 LHC 2012 Run: Long-Range Beam-Beam Effects In Stable Beams

Throughout luminosity production fills during the 2012 LHC run, the lifetimes depended strongly on the number of long-range beam-beam interactions. An example fill from the 2012 LHC run was selected and analysed in ref [104], with the worst lifetimes observed during the first hour of stable beams. This is shown in figure 5.4. In order to observe which bunches had the worst lifetimes, the bunch by bunch luminosity decay rate as a function of bunch number was investigated,

as seen in figure 5.8. Figure 5.9 shows the luminosity lifetime dependency of two

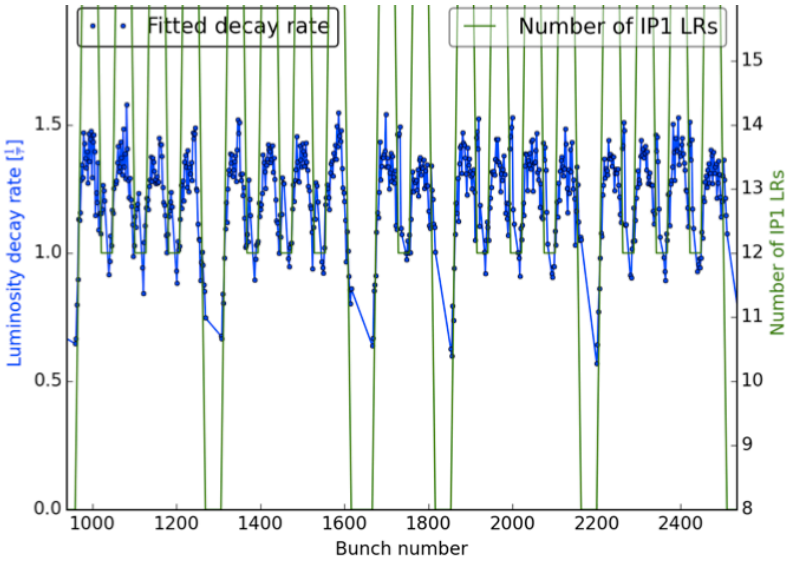

FIGURE 5.8: Decay rate dependence for a luminosity production fill during the 2012 LHC run, showing a clear dependence on the number of long-range beam-beam interactions [104].

different bunch trains, with collisions at different IPs. Figure 5.9(a), shows a bunch train with only collisions at IP1 and IP5. Here the lifetimes do not vary strongly with the number of long-range beam-beam interactions. Figure 5.9(b) shows the lifetimes for a train with additional collisions at IP2 and IP8. Here there is a strong dependency on the long-range beam-beam interaction which causes the lifetimes to reduce below 10 hours. The beam-beam contribution from IP2 and IP8 are causing additional losses and effecting the luminosity lifetime. The beam-beam separation during this fill at IP2 and IP8 was 10 σ and 12 σ respectively. In order to make IP2 and IP8 transparent from the perspective of the beam-beam interaction, the beam-beam separation was increased to $> 26\ \sigma$ at IP2 and IP8, by increasing the crossing angle [100]. This crossing angle increase and an emittance reduction from $\epsilon_n = 3.75\ \mu$m to $\epsilon_n = 2.5\ \mu$m, mitigated the lifetime dependency on the long-range beam-beam interaction.

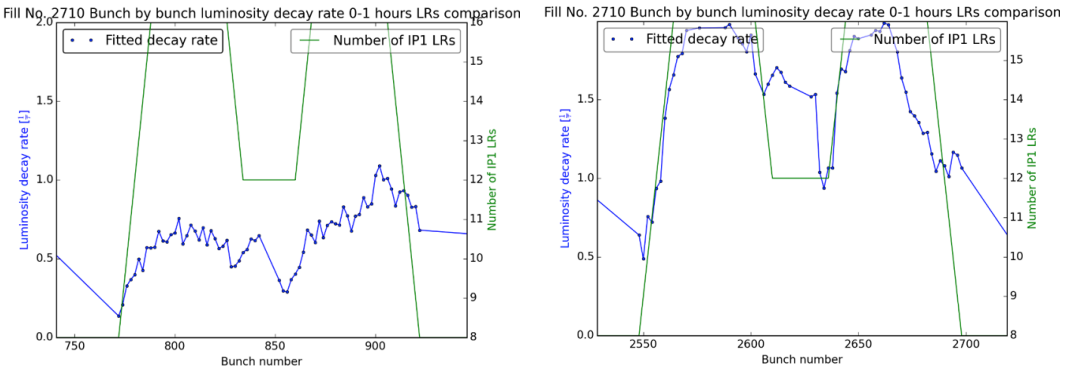

(a) (b)

FIGURE 5.9: Zoom of specific bunch trains and the long-range dependence for during the first hour of fill 2710 detailed in reference [104]. Figure 5.9(a) shows a train with no collisions at IP2 and IP8 and figure 5.9(b) shows a train with collisions at IP2 and IP8.

During the 2015/6 run of the LHC, the lifetimes were well controlled and instabilities were suppressed. A dedicated long-range beam-beam study was proposed towards the end of the 2016 run, in order to identify the minimum beam-beam separation at IP1 and IP5 and push the luminosity performance. This is discussed in the next section.

5.3.2 Machine Study 1: LHC 2015

To identify the long-range beam-beam limit and the luminosity reach with the 80 cm β^* optics, a dedicated machine study was performed with a train of 48 bunches per beam (fill 4368). These trains were injected and ramped up through the standard physics operational cycle and collided at 6.5 TeV at IP1 and IP5 only. The single train of 48 bunches was used to reflect nominal operation for luminosity production in 2015. The first two bunches in the train were reference bunches, with the first bunch only undergoing head on collisions and the second bunch a non-colliding witness bunch. The rest of the bunches in the train experience a combination of head-on and long-range beam-beam interactions depending on

the position along the bunch train. The nominal bunches in the centre of the train underwent 34 long-range collisions per IP as seen in figure 5.10.

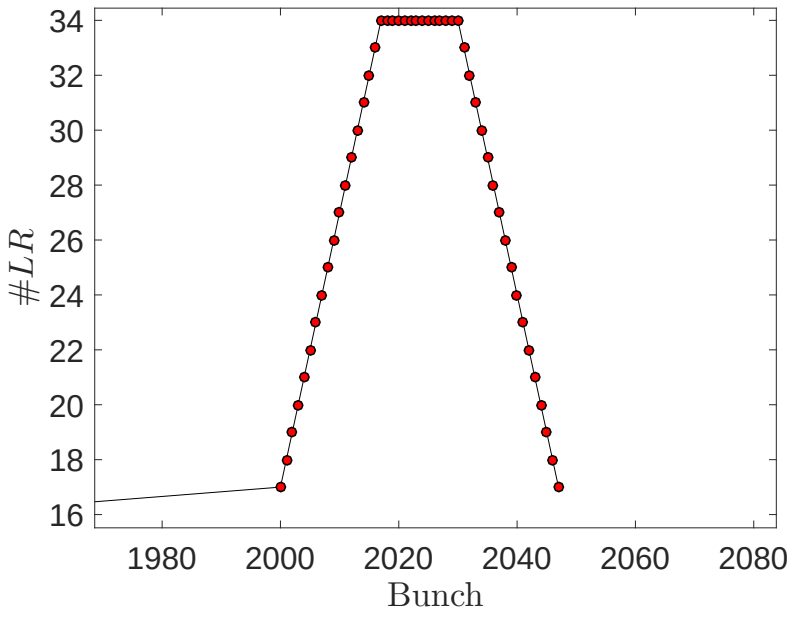

FIGURE 5.10: Number of long-range beam-beam for a train of bunches during the 2015 machine study.

The crossing angle at IP1 and IP5 was then reduced simultaneously in steps. Unlike previous machine studies machine studies of the luminosity reach through crossing angle scan, during these machine studies the crossing angle steps were fixed for 10−15 minutes. This enabled extended and more accurate measurements of the bunch lifetimes to be made. The crossing angle steps were:

$$290 \rightarrow 260 \rightarrow 234 \rightarrow 224 \rightarrow 212 \rightarrow 192 \rightarrow 174 \rightarrow 158 \rightarrow 144 \rightarrow 118 \quad [\mu\text{rad}]. \tag{5.10}$$

This corresponded to a reduction in the normalised beam-beam separation of

$$13.2\ \sigma \rightarrow 5.5\ \sigma,$$

for an emittance $\epsilon = 2.5$ μm and $\beta^* = 0.8$ m. At each crossing angle step, the decay rates of the luminosity and intensity were monitored and observed. In addition to the crossing angle scan, at the end of this machine study and at the smallest crossing angle, the impact of chromaticity and Landau octupoles on the decay rates was also investigated. At the minimum crossing angle of 118 μrad, the chromaticity was reduced from 15 units to 2 units in one step and the impact on the decay rates were observed. At this value of chromaticity and crossing angle, the Landau octupole strength was $k_{oct} = 16.27$ Tm^{-3} and the current was reduced from 476 A down to 0 A, and once again the impact on the beam intensity and luminosity decay rates were observed. A full description of the procedure is found in references [108, 109].

5.3.2.1 Bunch by Bunch Intensity

The bunch by bunch intensity data allows the impact of the crossing angle scan on individual bunches to be observed, as well as characterising how the bunch position can affect particle losses. The bunch by bunch intensity data was fitted with equation 5.3 and the decay rate was calculated and plotted for each bunch as a function of crossing angle. This is shown in Figure 5.11.

Figure 5.11(a) shows that as the crossing angle is reduced, no significant increase in decay rate is observed between the angles of $\alpha = 280$ μrad to $\alpha \approx 190$ μrad. At crossing angles smaller than $\alpha = 190$ μrad, the impact on the decay rates varies depending on the bunch, with some bunches suffering more than others. The smallest crossing angle of $\alpha = 118$ μrad, corresponds to lifetimes below $\tau < 10$ hours for some bunches. Bunches in beam 2, shown in Figure 5.11(b) exhibit a similar trend as beam 1, however the impact on the decay rate for crossing angles smaller than $\alpha = 190$ μrad is much larger, with the majority of bunches reducing to lifetimes of approximately $\tau = 6$ hours and some bunches experiencing lifetimes

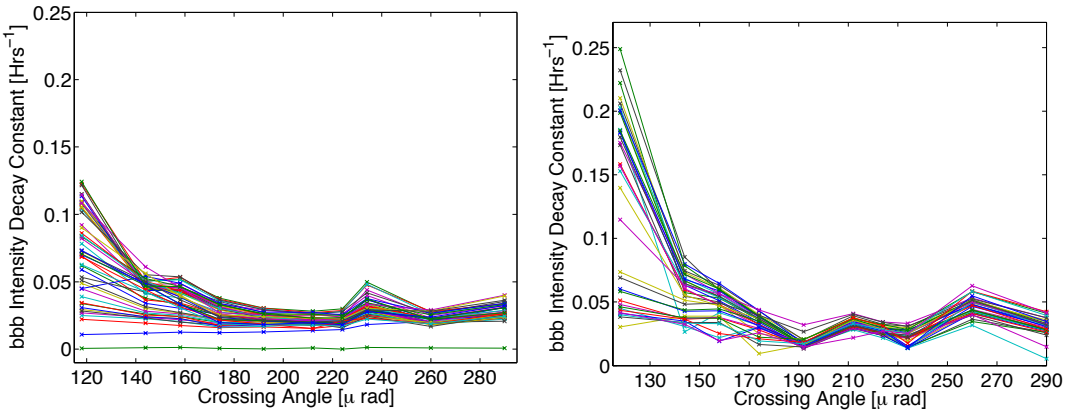

(a) Beam 1 (b) Beam 2

FIGURE 5.11: Bunch by bunch intensity decay rate as a function of crossing angle for beam 1 and beam 2.

as small as $\tau \approx 4$ hours. From these figures it can be seen that not all bunches are affected by the reduction in crossing angle equally and the position of the bunch in the train may play a significant role.

The bunch decay rate as a function of position in the train and the number of long-range beam-beam interactions, is shown in Figures 5.12 and 5.13. Figure 5.12 shows clearly a strong dependence of the decay rates on the number of long-range beam-beam interactions and the size of the crossing angle. Nominal bunches in the centre of the train suffer more than the bunches at the head or tail of the train. The dependence of the decay rates on the long-range beam-beam pattern arises more clearly with reducing crossing angle. For nominal bunches in the centre of the train, lifetimes drop below $\tau = 10$ hours at a crossing angle of $\alpha = 118$ μrad. This crossing angle corresponds to a small beam-beam separation of $d_{sep} = 5.5$ σ. Figure 5.13 shows a similar trend as seen in beam 1, with nominal bunches experiencing the largest decay rate. The intensity data retrieved for beam 2 did however suffer from measurement issues, providing spurious calculations of the intensity. This resulted in some of the bunch intensity data being excluded.

In beam 1 (fig 5.12), it can also been seen that there is some asymmetry between the head and tail of the train. There are a number of possible explanations

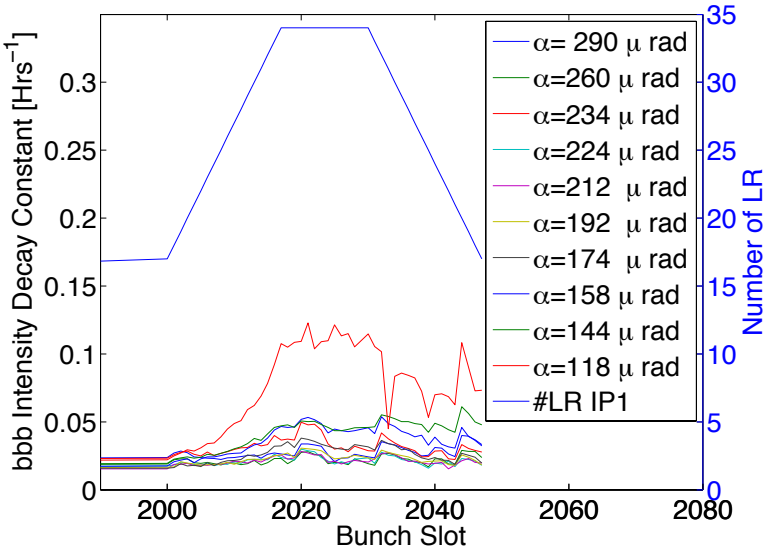

FIGURE 5.12: Beam 1: bunch by bunch decay rates as a function of bunchslot and the number of long-range interactions

for this. Electron cloud effects act along the bunch train and could cause the asymmetry. The cumulative effect of electron cloud could be impacting bunches towards the end of the train, causing these bunches to experience larger losses. An alternative explanation is the closed orbit drift caused by the increased strength of the long-range beam-beam interaction. The long-range beam-beam interaction provides a kick to each bunch that will change its orbit around the LHC. This may also introduce a transverse offset between the bunches which will further affect the lifetimes.

Figure 5.14 highlights the strong dependency of the decay rate with increasing number of long-range beam-beam interactions. The bunch at the front of the train has 17 long-range beam-beam interactions per IP and the impact from the crossing angle reduction is small to negligible. For this bunch, the decay rates remain approximately fixed throughout the crossing angle variation. The value of the decay rates correspond to lifetimes around 50 hours. Alternatively, the nominal bunches in the centre of the train, undergo a significant increase in decay rate resulting in lifetimes reducing to below 10 hours.

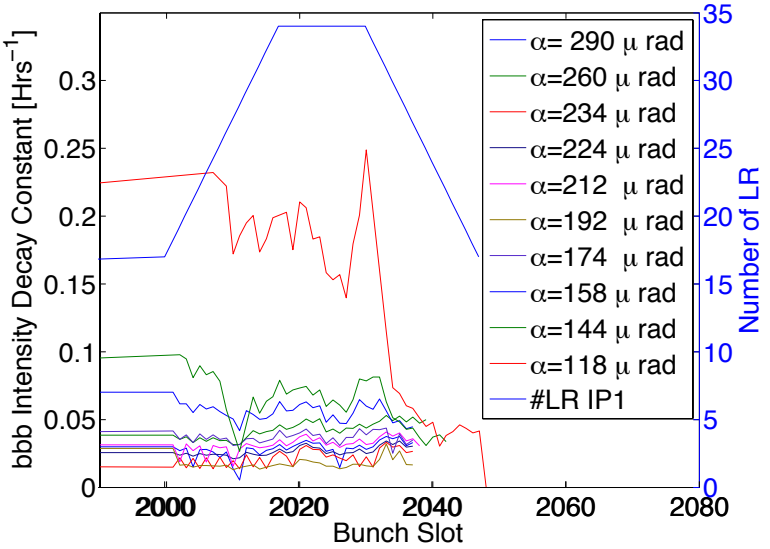

FIGURE 5.13: Beam 2: bunch by bunch decay rates as a function of bunchslot and the number of long-range interactions

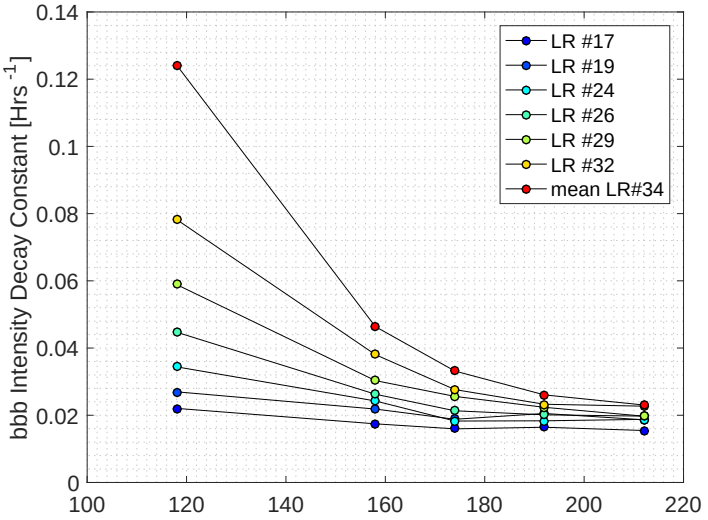

FIGURE 5.14: Beam 1: Decay rate dependence on the number of long-range comparison between nominal bunches and PACMAN bunches.

A similarly important figure indicating the decay rate as a function of the number of long-range beam-beam interactions at various crossing angles, is figure 5.15. The points corresponding to bunches with less than 20 long-range beam-beam interactions per IP remain approximately fixed as the crossing angle is reduced, with almost negligible variations. For long-range beam-beam interactions larger than 20 the crossing angle reduction begins to have an impact on decay rates.

At the smallest crossing angle $\alpha = 118$ μrad, a non-linear dependence of the decay rates on the number of long-range interactions can be observed as seen in figure 5.15. In order to confirm that the behaviour is indeed non-linear, the polynomial best fit of the measured intensity decay rates is calculated and shown in figure 5.16. The difference between the measured decay rates and the decay rates calculated by a polynomial line of best fit and a linear line of best fit is shown in figure 5.17. The polynomial fit agrees well with the measured decay

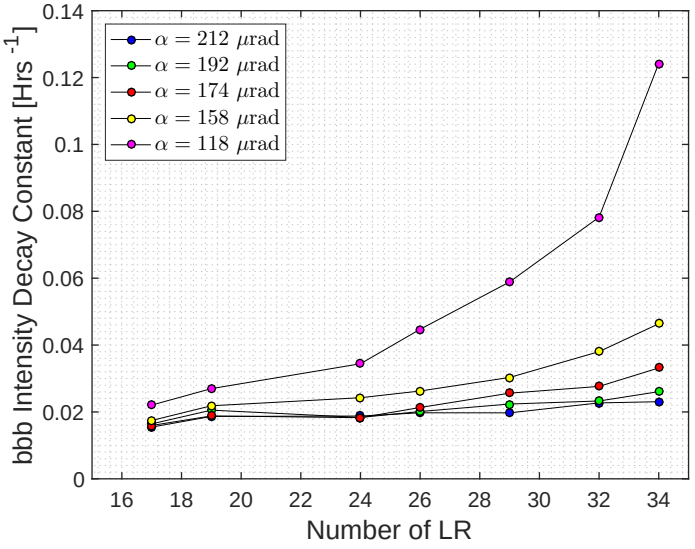

FIGURE 5.15: Beam 1: Decay rate dependence on the number of long-range beam-beam interactions at different crossing angles.

rates and the difference between the polynomial line of best fit and the data is smaller than 0.5% and gives $\chi^2 = 6.65 \times 10^{-5}$. The linear fit is accurate to within approximately 3% of the measured decay rates, giving $\chi^2 = 1.4 \times 10^{-3}$. This confirms that the behaviour of the decay rates with the number of long-range beam-beam interactions is indeed linear for small crossing angles, when the beam-beam separation is small.

There is a clear correspondence between the strength of the long-range beam-beam interaction and the intensity decay rates and losses that the bunches experience. The nominal bunches in the centre of the train clearly suffer more than the Pacman bunches as the crossing angle is reduced. However all bunches retain

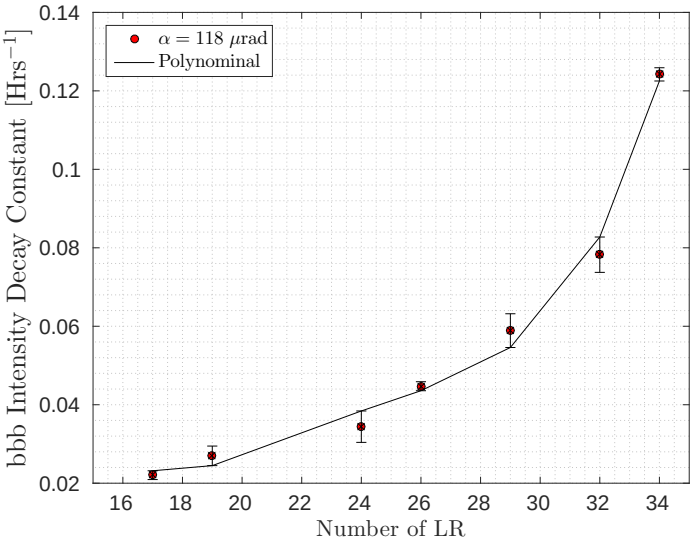

FIGURE 5.16: Polynomial line of best fit of the measured bunch by bunch intensity decay rates for the nominal bunches at the smallest crossing angle of the 2015 long-range beam-beam machine study.

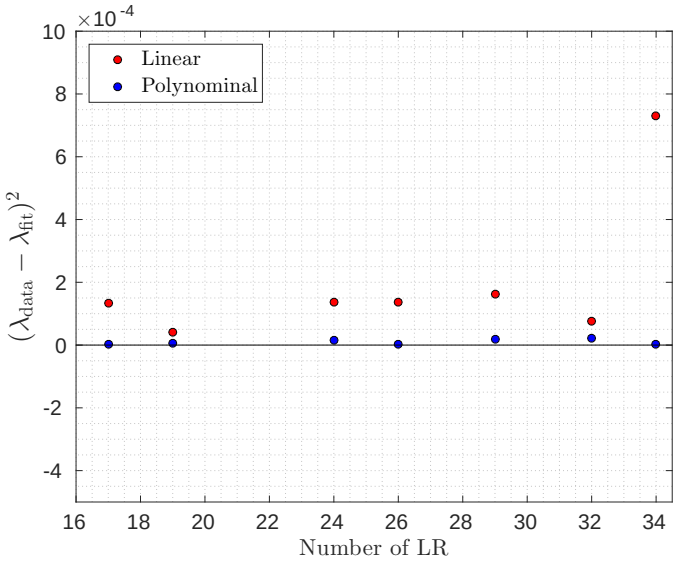

FIGURE 5.17: Difference square comparison of the measured decay rates at $\alpha = 118$ μrad to the polynomial and linear lines of best fit. The polynomial fit provides a more accurate fit and better describes the non-linear behaviour of the intensity decay rates with the number of long-range beam-beam interactions.

good lifetimes and undergo no significant effect from the crossing angle reduction, until a crossing angle of $\alpha = 190$ μrad is reached. Above crossing angles of $\alpha = 190$ μrad, the lifetimes remain above 10 hours. From the intensity data alone, this suggests that the crossing angle and hence the beam-beam separation

can be reduced without introducing any significant impact on the intensity decay rates. The analysis of the bunch by bunch intensities suggest that the beam-beam limit is at approximately $\alpha = 190$ μrad, which corresponds to a beam-beam separation of 7.5 σ. Before the luminosity lifetimes are investigated, it is important to investigate the emittance and cause an emittance growth. Since the long-range beam-beam interaction can affect both particle losses and emittance growth, the principle reason for any drop in luminosity lifetimes should be considered. In the next section, the emittance data will be considered.

5.3.2.2 Emittances

The bunch emittances were calculated using data obtained from the BSRT. The nominal and head-on only colliding bunches are shown in Figures 5.18(a), 5.18(b), 5.18(c) and 5.18(d). From figure 5.18(a), 5.18(b), 5.18(c) and 5.18(d), a noticeable asymmetry in the bunch planes can be observed, most apparently in the beam 2 data. In the beam 2 data, the horizontal plane emittance is $\epsilon_x = 3.5 - 4.0$ μm during the crossing angle scan. In the vertical plane, the emittance remains approximately fixed throughout the crossing angle scan just below $\epsilon_y = 3$ μm. In beam 1, the asymmetry between the bunch planes is not as pronounced, with emittances between $\epsilon_{x,y} = 2.4 - 3$ μm. The asymmetry between the emittance planes could have an impact on the long-range beam-beam interaction and affect the loss mechanism. If the bunch emittance is large in one plane, then long-range beam-beam interactions in this plane could have a smaller beam-beam separation and hence experience a stronger long-range beam-beam interaction.

The emittances do not remain constant throughout this long-range beam-beam machine study, with the most significant changes observed in the larger plane. In the horizontal plane, the bunch remains approximately constant until a crossing angle of $\alpha = 190$ μrad is reached. This crossing angle corresponds to the location

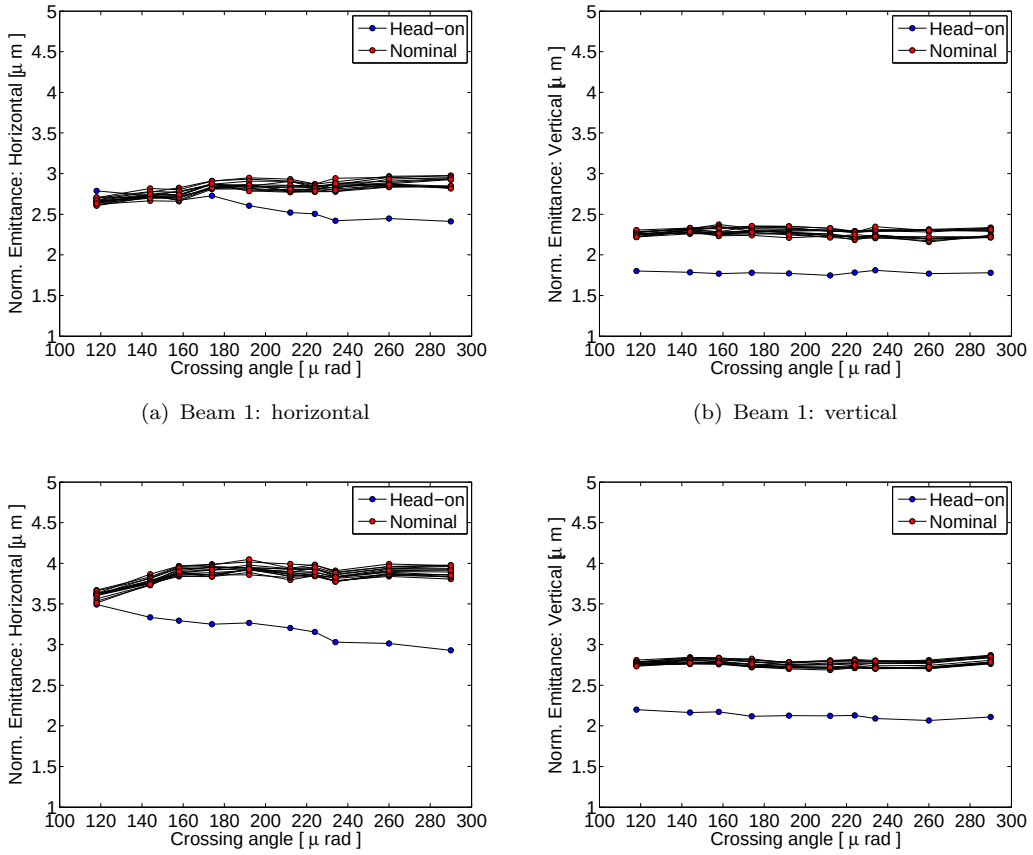

(a) Beam 1: horizontal

(b) Beam 1: vertical

(c) Beam 2: horizontal

(d) Beam 2: vertical

FIGURE 5.18: Mean beam emittance as a function of crossing angle in each plane for the nominal bunches and the head on only.

of the long-range beam-beam limit, with a separation of 7.5 σ. Below this beam-beam separation, the nominal bunches emittance in beam 1 and beam 2 undergo an apparent emittance reduction. A similar observation was obtained in the high brightness head-on beam-beam limit machine study [110]. The emittance reduction implies that the long-range beam-beam interaction behaves in a similar way to a collimator, cutting into the core of the bunch. The long-range beam-beam interaction at small crossing angles provides a strong non-linear beam-beam kick to the particles. This causes particles in the core ($r < 2\,\sigma$) to diffuse to larger amplitudes where they will then be lost. In the horizontal beam planes, the head-on bunch undergoes an emittance increase of approximately $\delta\epsilon_x \approx 16\%$ in beam 1 and $\delta\epsilon_x \approx 14\%$ in beam 2. The vertical emittance for this bunch remains

approximately constant throughout the machine study. Much like the head-on bunch, the emittances in the vertical plane for the nominal bunches remain stable throughout the machine study and do not change significantly.

Next, the luminosity lifetimes are considered in order to determine whether it is the geometrical emittance change or the intensity loss which determines the luminosity performance..

5.3.2.3 Bunch By Bunch Luminosity

The bunch by bunch luminosity data was obtained from ATLAS at IP1 and the decay rates for the nominal bunches was plotted against the crossing angle as shown in Figure 5.19. The nominal bunches show the same trend as found in the bunch by bunch intensity data, with decay rates and lifetimes corresponding well to what was previously observed in the intensity data. The luminosity throughout the machine study suffered from significant orbit drifts, which will impact the quality of the luminosity data [108, 109]. The luminosity is dependent on intensity, emittance, and the geometrical overlap between the two beams. Many different mechanisms in the LHC exist which can impact any one of these parameters and deteriorate the luminosity. This introduces an uncertainty in the luminosity data which hence impacts the decay rate calculation. One example of such an effect is a transverse offset caused by an orbit drift at the IP between the two beams. A transverse offset will lead to a reduction in luminosity. When the data was fitted to calculate the decay rate, any sudden reduction in luminosity was removed to prevent spurious decay rate calculations. The sudden drops in luminosity data often arise due to the re-optimisation of the luminosity. To re-optimise the luminosity, the bunches are brought in and out of collision until the maximum luminosity is found. It is also difficult to actually determine whether the bunches do or do not collide with an offset without performing these

luminosity scans. The luminosity is optimised regularly to ensure that the transverse offset between the bunches is minimised. Even with the possible transverse offsets, the same trend is observed in the luminosity data as in the intensity data. There is no significant variation in the decay rate above a crossing angle of $\alpha = 190$ μrad, for beam-beam separations > 7.5 σ. However, below this beam-beam separation, the decay rates begin to increase and correspond to a reduction in lifetime. The lifetimes calculated from the decay rate are similar to those obtained in the intensity data, with the minimum lifetime observed calculated to be approximately of the order of 4 hours, which corresponds to lifetimes measured in the beam 2 data. Hence the luminosity lifetimes appear to be dominated by the intensity losses and not by the changes in emittances.

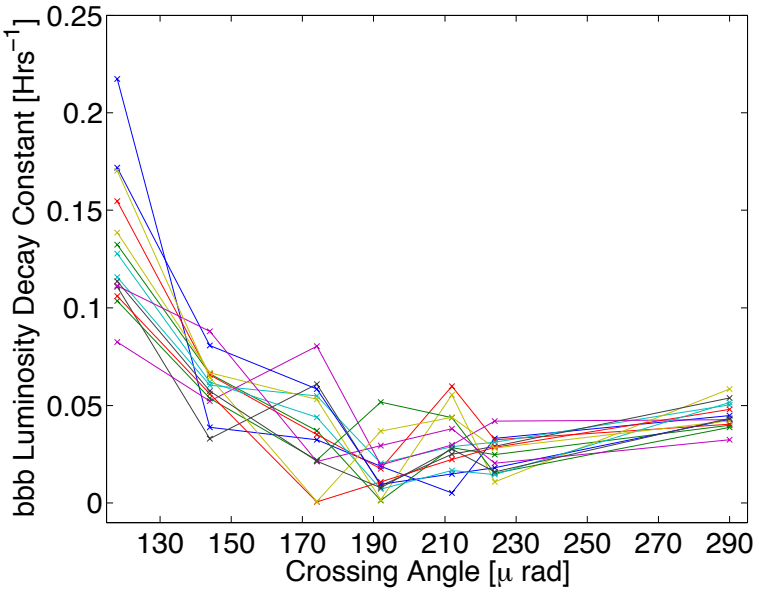

FIGURE 5.19: Bunch by bunch luminosity for the nominal bunches in the train.

5.3.2.4 Impact of Chromaticity and Landau Octupoles on Decay Rates

At the final and minimum crossing angle of $\alpha = 118$ μrad, corresponding to a beam-beam separation of approximately 5.5 σ, the impact of chromaticity and Landau octupoles on the decay rate was characterised in two experimental steps.

In the first step, the chromaticity was reduced from $Q' = 15$ units to $Q' = 2$ units and the decay rates were once again observed. The chromaticity is quoted in terms of units as in ref [111]. In the subsequent experimental step and after a small tune trim to beam 2, the strength of the Landau octupole were reduced. The chromaticity remained at $Q' = 2$ units as the Landau octupole strength was reduced from $k_{oct} = 16.27$ Tm^{-3} to $k_{oct} = 0$ Tm^{-3}. Again, the decay rates were monitored for a period of time. The length of this experimental step was limited as the non-colliding bunch became unstable, as expected since the octupoles are the source of Landau damping for this bunch.

Figures 5.20 and 5.21 shows the decay rates including the final experimental steps in which the Landau octupole and chromaticity were varied. The reduction of the chromaticity and strengths of the Landau octupoles results in a significant lifetime recovery for the nominal bunches in both beam 1 and beam 2. At reduced chromaticity and Landau octupole strength, the decay rates completely recover to lifetimes that were previously observed at the initial crossing angle $\alpha = 290$ μrad. The lifetimes improve from below 10 hours back to above 30 hours. The colliding bunches remain stable even with Landau octupole strength and chromaticity reduced, with only the non-colliding bunch becoming unstable.

Figure 5.22 shows the improvement of the decay rates as a function bunch position in the train. When the chromaticity is reduced to $Q' = 2$ units, the decay rates improve for the nominal bunches in the centre of the train by approximately $\sim 50\%$. In the following experimental step, when the strength of the Landau octupole is reduced, the decay rates fully recovered to the values found at the largest crossing angle $\alpha = 290$ μrad. From the analysis of this machine study, the colliding bunches remain stable, even with chromaticity and Landau octupole strength significantly reduced and at a small crossing angle. This suggests that the LHC could be operated at a smaller crossing angle if the chromaticity and strength of the Landau octupoles were decreased. However the reduction of the

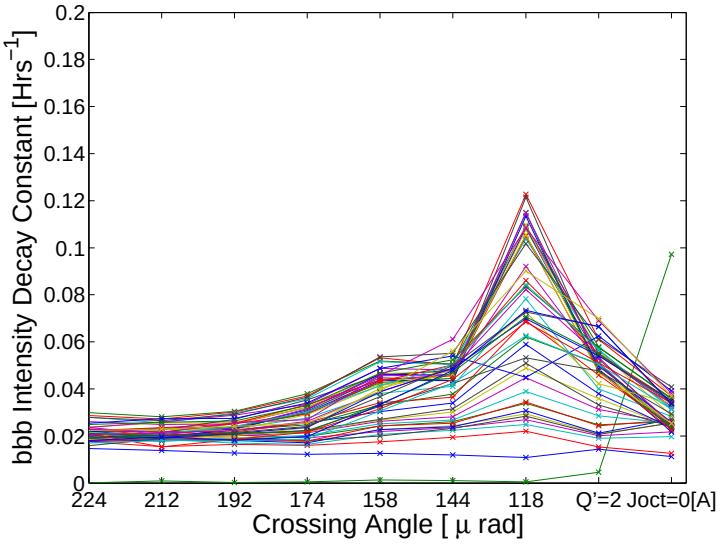

FIGURE 5.20: Beam 1: Decay rate improvement with reduced chromaticity and Landau octupole strength as a function of crossing angle.

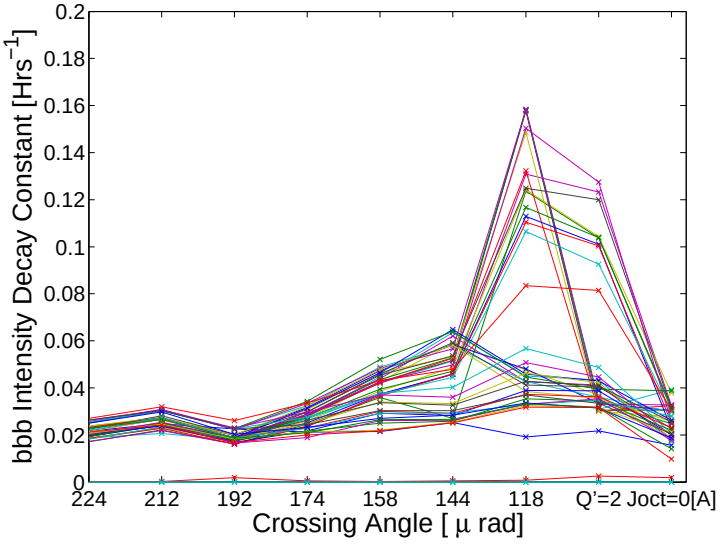

FIGURE 5.21: Beam 2: Decay rate improvement with reduced chromaticity and Landau octupole strength as a function of crossing angle.

chromaticity and strength of the Landau octupoles on the head-on and non-colliding bunches may impact stability. This is discussed in the next section.

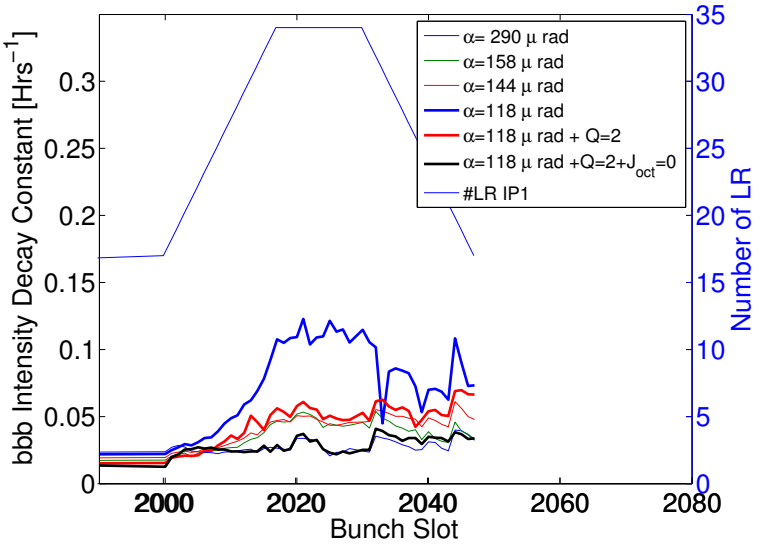

FIGURE 5.22: Beam 1: Decay rate improvement with reduced chromaticity and Landau octupole strength as a function of bunchslot.

5.3.3 Head-On Only and Non-Colliding Bunches

In this machine study, a non-colliding and a head-on only colliding bunch were also included by leaving a suitable number of bunch slots free between the colliding trains. These bunches can be used as reference bunches to analyse the effect of crossing angle reduction on the decay rates when there is no long-range beam-beam interaction present and also when there is no beam-beam interaction at all. Figure 5.23 shows the measured intensity decay rate as a function of crossing angle for both the non-colliding and head-on only colliding bunch. The non-colliding bunch has consistently small decay rates throughout the machine study and undergoes a negligible amount of particle losses. As expected the decay rate does not have any dependence on the reducing crossing angle. The head-on only colliding bunch does have some dependence on the crossing angle with decay rates improving towards smaller crossing angles. The lifetimes for the head-on only colliding bunch improves from $\tau > 30$ hours to $\tau = 100$ hours. As the crossing angle is reduced, the tune spread from the head-on beam-beam interaction increases. This provides a larger area for Landau damping and hence

improves the lifetimes. In addition to this, any longitudinal effects arising from synchro-betatron modes may be suppressed [112].

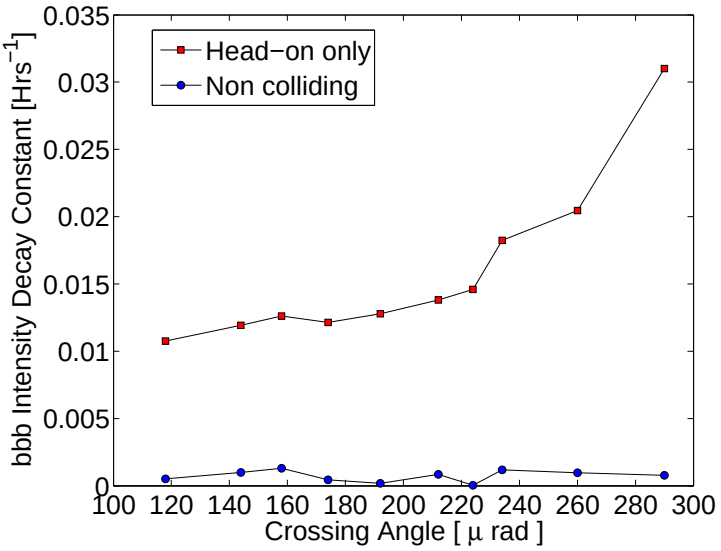

FIGURE 5.23: Head on and non colliding bunch decay rate variation with crossing angle.

Figure 5.24 shows the RMS emittance for both the head-on and non-colliding bunch in beam 1 throughout the crossing angle scan. The non-colliding bunch, much like the decay rates, show no significant variation with crossing angle. The head-on only bunch undergoes a small emittance growth for crossing angles smaller than $\alpha = 240$ μrad. The emittance increase for the head-on bunch from a crossing angle of $\alpha = 290$ μrad to the final crossing angle of $\alpha = 190$ μrad is of the order of about $\delta\epsilon_{rms} = 14\%$.

As the chromaticity and Landau octupole current is reduced the colliding bunches remain stable and see an improvement in lifetime after a small tune trim to beam 2. The only bunch that experiences a reduction in lifetime is the non-colliding bunch as seen in Figure 5.25. The chromaticity reduction does not appear to have a significant impact on the decay rate for the non-colliding bunch with only a small increase in decay rate with lifetimes remaining above 10 hours. As the Landau octupole current is reduced the decay rate increases significantly for the

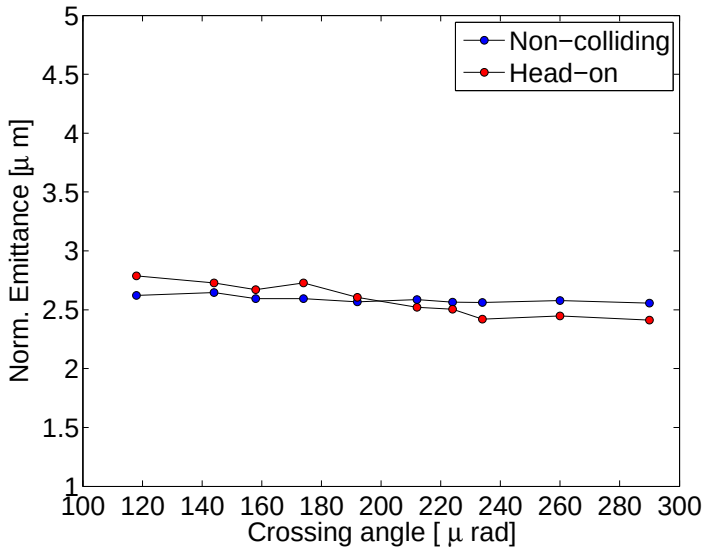

FIGURE 5.24: Emittance variation for the beam 1 head-on and non-colliding bunches as the crossing angle is reduced.

non-colliding bunch, resulting in a lifetime below 10 hours. The Landau octupoles provide a source of Landau damping for the non-colliding bunch which keeps the bunch table. When the octupole current is reduced there is no mechanism like the beam-beam interaction to provide the required damping, hence the bunch becomes unstable. The high chromaticity and Landau octupole operation

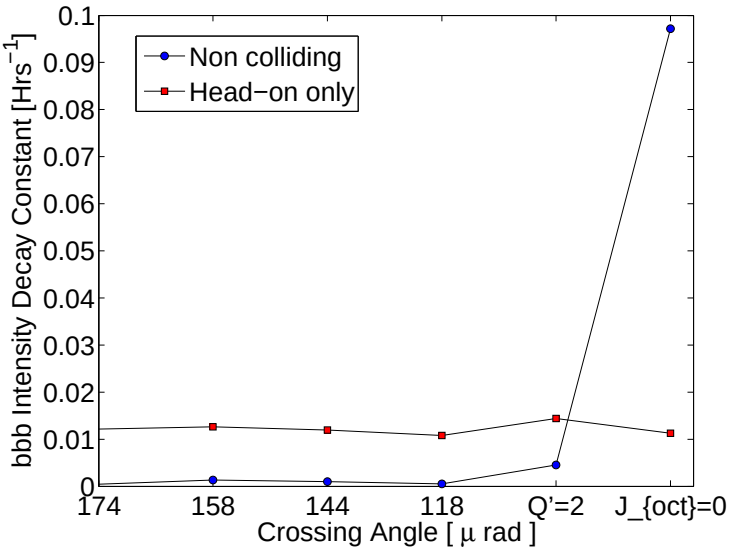

FIGURE 5.25: Beam 1: decay rate with crossing angle and reduction of chromaticity and Landau octupole current

clearly limits the crossing angle at which the LHC can operate. However, high chromaticity and octupole operation is required to prevent instabilities [113].

The analysis from the 2015 long-range beam-beam machine study has identified the minimum operational beam-beam separation for a β^* of 0.8 m. The minimum beam-beam separation is found at approximately 7.5 σ. This beam-beam separation corresponds to a crossing angle $\alpha = 190$ μrad. For crossing angles and separations smaller than this, the long-range beam-beam interaction begins to dictate particle losses and reduce the lifetimes. The chromaticity and strength of the Landau octupole current also has a significant impact on the lifetimes and prevents the beam-beam separation being reduced further. However, this high chromaticity and octupole settings are required in order to prevent instabilities during the squeeze.

5.3.4 Machine Study 2: LHC 2016

In the 2016 run of the LHC, the long-range beam-beam machine study was repeated, with the aim to once again determine the long-range beam-beam limit for the LHC whilst operating at a β^* of 0.4 m. This experiment was categorised into two separate fills (5136 and 5137), the first fill was a repeat of the 2015 machine study, with a single train of 48 bunches, with one head-on only colliding bunch and one non-colliding bunch with collisions at IP1 and IP5 only. The second fill investigated the additional impact on the intensity and luminosity lifetimes, with additional collisions at IP2 and IP8, as is typical for nominal operational fills. The second fill consisted of three trains of 48 bunches, with the first train colliding at IP1/2 and 5, the second train colliding at IP1/5 and 8, and finally the last train colliding at all 4 IPs. The additional IPs are not expected to contribute to the reduction in lifetimes as the beams are separated by > 10 σ, with the β-function at these IP2 and IP8, 3m and 11m, respectively.

Unfortunately, the first fill did not reach the long-range beam-beam limit, as discussed in ref [114], so only the second fill of the experiment is discussed here.

The crossing angle was reduced simultaneously in both IP1 and IP5, in the same way as the 2015 machine study. The crossing angle steps during the second fill are given by

$$310 \rightarrow 280 \rightarrow 270 \rightarrow 260 \rightarrow 250 \rightarrow 240 \rightarrow 230 \rightarrow 210 \rightarrow 190 \quad [\mu\text{rad}]. \tag{5.11}$$

These crossing angles correspond to a beam-beam separation for a fixed emittance $\epsilon = 2.5$ μm and $\beta^* = 0.4$m at flat top energy of

$$10.65 \rightarrow 9.32 \rightarrow 8.99 \rightarrow 8.65 \rightarrow 8.32 \rightarrow 7.99 \rightarrow 7.65 \rightarrow 6.99 \rightarrow 6.32 \quad [\sigma]. \tag{5.12}$$

Once again, the lifetimes were observed for 10-15 minutes at each crossing angle step. At a crossing angle of $\alpha = 210$ μrad, the Landau octupole current was reduced from operational settings of $J_{oct} = 476$ A down to $J_{oct} = 188$ A, corresponding to $k_{oct} = 16.26$ Tm$^{-3} \rightarrow k_{oct} = 6.43$ Tm^{-3}, and the impact on the lifetimes was observed. At the same chromaticity and Landau octupole powering, the crossing angle was reduced again, down to $\alpha = 190$ μrad.

The tune footprint calculated for a nominal bunch as the crossing angle is reduced is shown in figure 5.26. As the crossing angle is reduced, the size of the tune footprint becomes larger as the strength of the beam-beam interaction increases. As the crossing angle is reduced, the impact from the long-range beam-beam interaction increases, causing the footprint tails to spread out. This can cause the particles to cross many resonance lines. This can impact particle stability and lead to losses [16].

Figure 5.27 shows the total beam intensity as a function of time as well as the orbit corrector magnet current over the duration of the fill. The corrector magnet

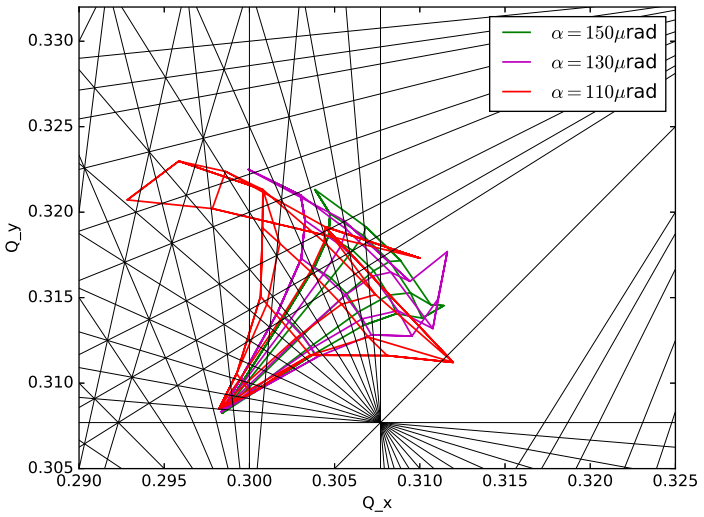

FIGURE 5.26: Tune footprint variation as a function reducing the crossing angle for a bunch undergoing head-on and long-range beam-beam interactions.

currents indicate when the crossing angle change was applied by the machine operators. The corrector magnet strengths were then used as a guide to determine over what time interval the fitting windows need to be applied.

In the following sections, the bunch by bunch intensity, luminosity and emittance data obtained from the long-range beam-beam machine study are discussed and the long-range beam-beam limit is identified.

5.3.4.1 Bunch By Bunch Intensity

The bunch by bunch intensity decay rate for all bunches in beam 1 and beam 2 at different crossing angles is shown in figure 5.28. In beam 1, there is no real effect of the reduction in crossing angle until approximately $\alpha = 260$ μrad. For angles below $\alpha = 260$ μrad the decay rates decrease non-linearly and depends strongly on the crossing angle, with some bunches undergoing significant losses at the smallest crossing angle of $\alpha = 190$ μrad, even with the reduced Landau octupole strength at the smallest crossing angle. Alternatively beam 2 does not

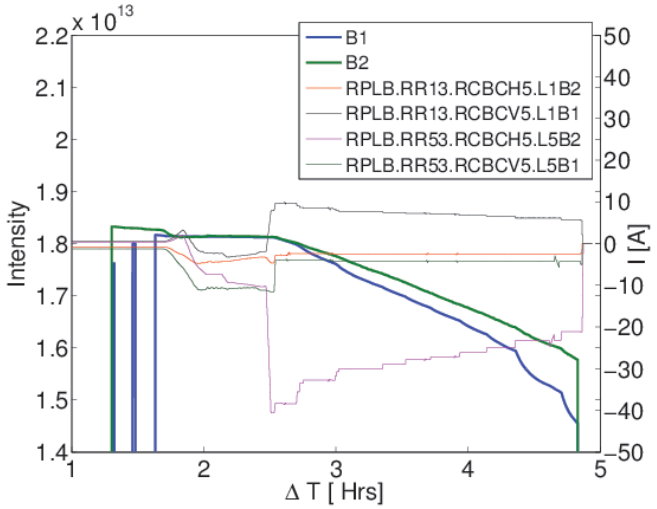

(a)

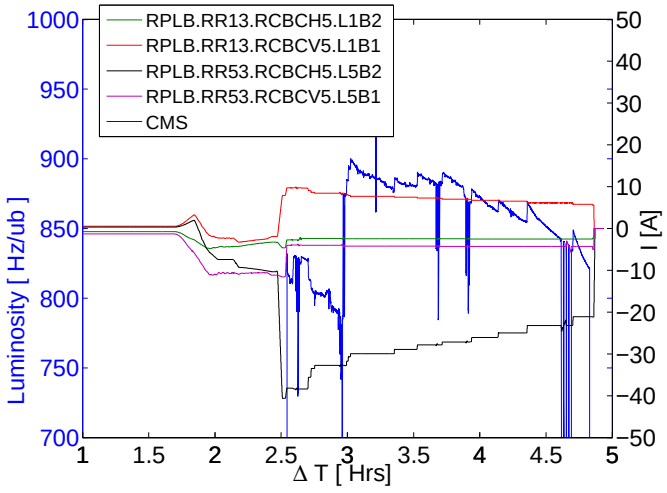

(b)

FIGURE 5.27: Total intensity and luminosity variation over the duration of the second fill: 5137 with the crossing angle steps indicated by the horizontal and vertical corrector powering labelled *RPLB*.

appear to have such a strong dependence on the crossing angle. During this long-range beam-beam machine study, beam 2 appears to be unaffected until the final crossing angle of $\alpha = 190$ μrad. At the final crossing angle the lifetimes finally drop below 10 hours for a large proportion of the bunches.

An isolation of some of the Pacman and the nominal bunches is depicted in figure 5.29, showing the same trend as previously observed during the 2015 machine study. The decay rates observed during the 2016 machine study were considerably

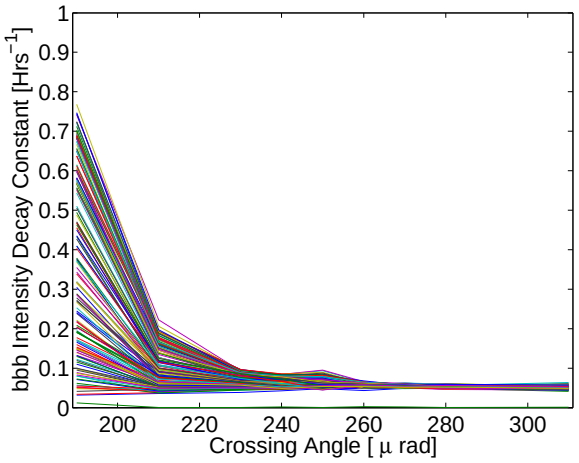

(a) Beam 1

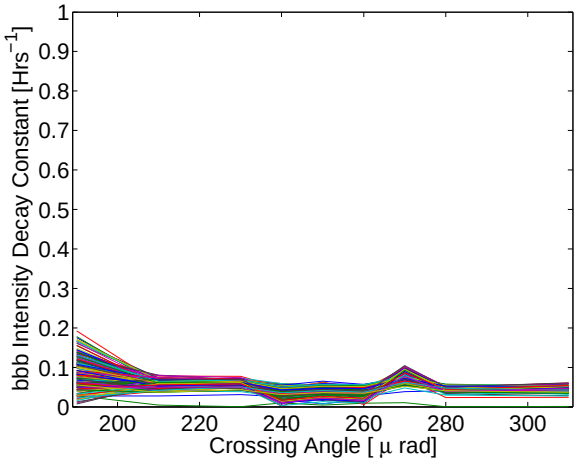

(b) Beam 2

FIGURE 5.28: Bunch by bunch intensity decay rate as a function of crossing angle.

larger than those observed at a smaller crossing angle during the 2015 machine study. This behaviour is expected due to the different machine optics. In the 2016 machine optics the $\beta^* = 0.40$m, whereas in the 2015 machine study the $\beta^* = 0.80$m. A smaller β^* will result in a smaller beam-beam separation and hence a stronger long-range beam-beam interaction. In these plots, the mean decay rate of the nominal bunches is plotted with error bars given by the standard deviation over all of the nominal bunches. Figure 5.29 shows the dependence of the decay rates on the crossing angle for the different bunch trains in the fill.

Each train underwent a different collision pattern, in order to determine the impact of the additional collisions at IP2 and IP8. In beam 1, no real effect on the decay rates was observed until a crossing angle of $\alpha = 260$ μrad is reached. This corresponds to a beam-beam separation of 8.5 σ. Below this crossing angle, the decay rates in beam 1 deteriorate significantly with each crossing angle step. As expected bunches with a large number of long-range beam-beam interactions suffered the worst decay rates, shown in figure 5.29. Pacman bunches in beam 1 with less than 20 long-range interactions do not really experience a significant increase in decay rates and the lifetimes τ remain above 10 hours. This is consistent with what was previously observed in the 2015 machine study. Beam 2, does not show any significant effect from the crossing angle reduction with decay rates remaining acceptable throughout. This is until the final crossing angle of $\alpha = 190$ μrad is reached. At the final crossing angle, bunches in beam 2 with more than 20 long-range interactions also experience lifetimes $\tau < 10$ hours; however these bunches do not suffer the same small lifetimes as bunches in beam 1.

The decay rate for the Pacman bunches as a function of crossing angle and the number of long-range interactions is shown in figure 5.30. The relationship between the number of long-range and the decay rate is non-linear in beam 1, with the decay rates suffering considerably for a crossing angle of $\alpha = 210$ μrad or less. Beam 2 shows some dependence of the decay rates with the number of long-range but it clearly does not follow the same non-linear trend observed in beam 1. However even at the smallest crossing angle of $\alpha = 190$ μrad, bunches with more than 24 long-range interactions suffer decay rates that correspond to less than $\tau = 10$hours. Comparing the decay rate as a function of bunch slot, crossing angle, and the number of long-range beam-beam interactions as seen in figure 5.31, shows a strong long-range pattern in beam 1. In this case, the nominal bunch decay rates reduce significantly below $\tau = 10$ hours in all trains.

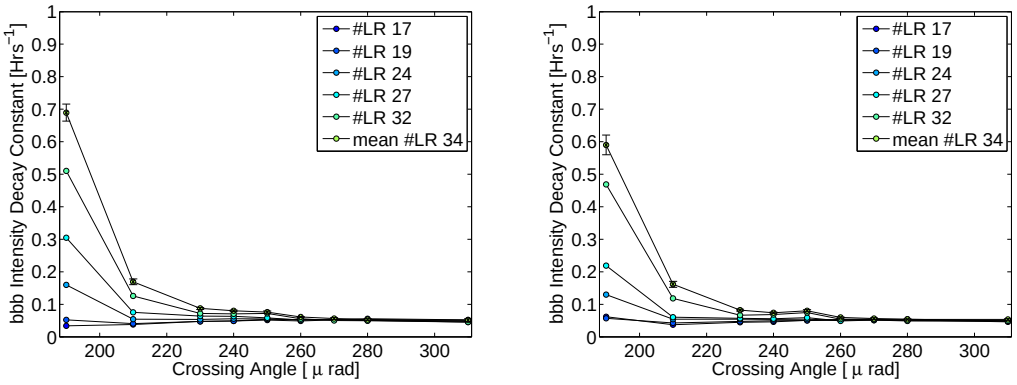

(a) Beam 1: train 1

(b) Beam 1: train 2

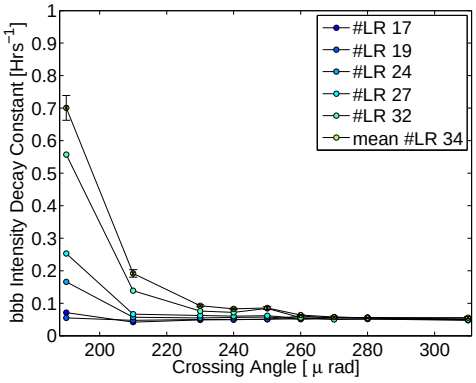

(c) Beam 1: train 3

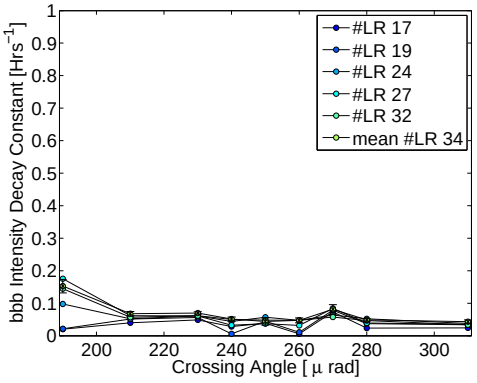

(d) Beam 2: train 1

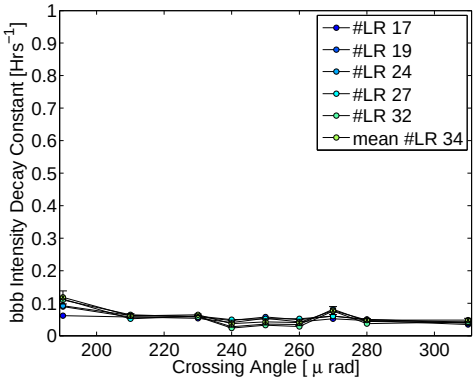

(e) Beam 2: train 2

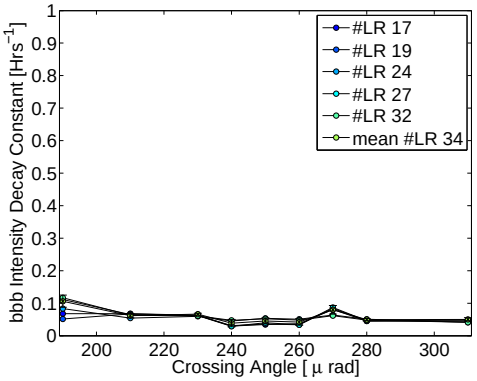

(f) Beam 2: train 3

FIGURE 5.29: Variation of the decay rate λ for the pacman and nominal bunches as a function of crossing angle for both beam 1 and beam 2.

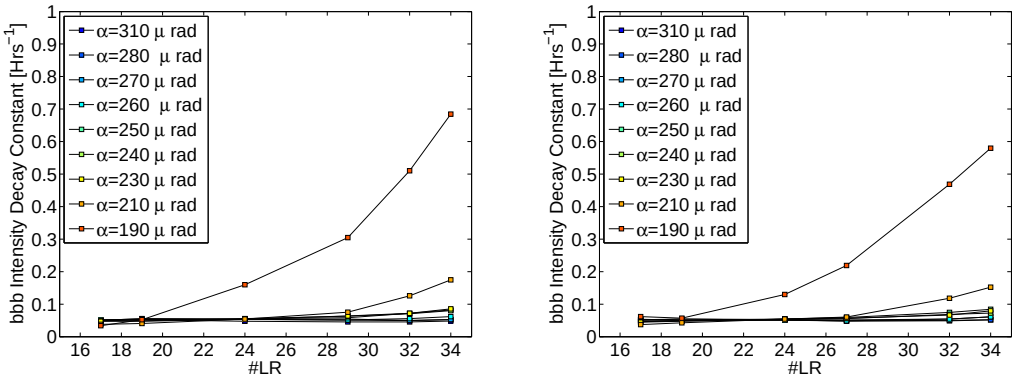

(a) Beam 1: train 1

(b) Beam 1: train 2

(c) Beam 1: train 3

(d) Beam 2: train 1

(e) Beam 2: train 2

(f) Beam 2: train 3

FIGURE 5.30: Bunch by bunch intensity decay rate for the pacman bunches as a function of crossing angle for beam 1 and beam 2. Bunches in beam 1 with the 34 long-range beam-beam interactions have the largest decay rates which corresponds to a small intensity lifetime.

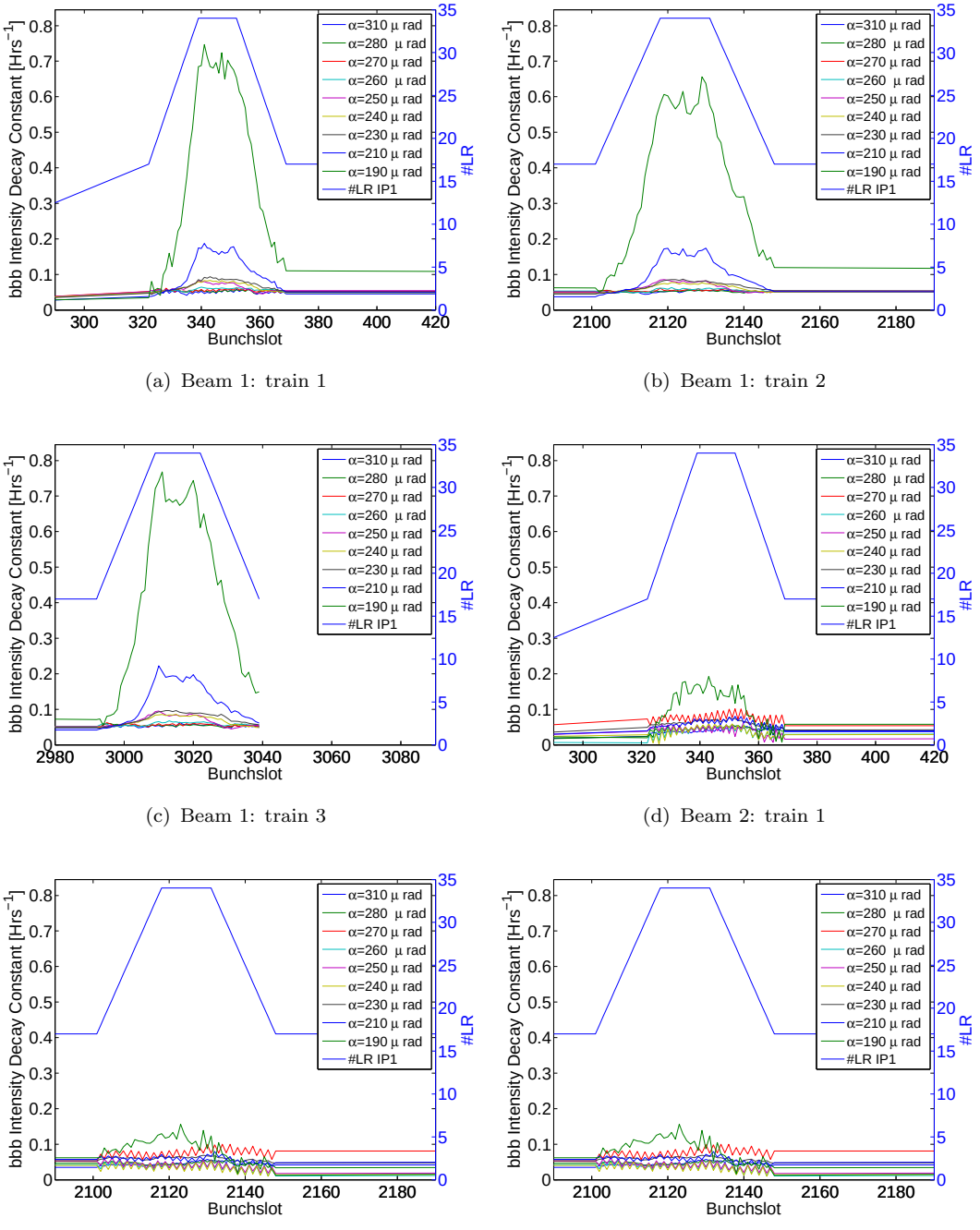

(a) Beam 1: train 1

(b) Beam 1: train 2

(c) Beam 1: train 3

(d) Beam 2: train 1

(e) Beam 2: train 2

(f) Beam 2: train 3

FIGURE 5.31: Bunch by bunch intensity decay rate as a function of bunchslot, crossing angle and the number of long-range beam-beam interactions for beam 1 and beam 2. The decay rates in beam 1 follow closely the long-range beam-beam pattern

5.3.4.2 Emittances

The RMS mean emittance for the bunches in trains 1,2, and 3, were plotted as a function of crossing angle in figure 5.32, where the RMS emittance is defined by

$$\epsilon_{n,\mathrm{rms}} = \sqrt{\epsilon_{n,x}^2 + \epsilon_{n,y}^2}. \tag{5.13}$$

A number of interesting observations can be seen in the emittance data. Firstly the RMS emittance appears to show a reduction in emittance for all colliding bunches during the crossing angle scan. This similarly was observed in the 2015 machine study, as well as in the head-on beam-beam limit study [110]. This is most strongly observed in beam 1, with the RMS emittance reducing by approximately 18% in train1, 22% in train 2 and 18% in train 3. Some emittance reduction is also observed in beam 2, corresponding to 7%, 10% and 10% in train 1, 2, and 3 respectively. The head-on bunch remains approximately fixed throughout the crossing angle scan. In addition to the reduction in emittance observed throughout beam 1 and beam 2, there is some emittance split between the bunches in the train. With bunches grouping into families of slightly smaller or larger emittances depending on the injection pattern of machines earlier on in the injection chain. The bunches are normalised with respect to their initial emittance to remove the dependency.

Figures 5.33 and 5.34 show the normalised change in emittance in the horizontal and vertical, with the injection pattern from the PS removed. The change in emittance is plotted as a function of bunch slot at each crossing angle. Figure 5.33 shows a reduction in emittance for bunches in beam 1 which appears to follow the long-range beam-beam pattern. Bunches in the centre of the train, which are most sensitive to the strength of the long-range beam-beam interaction, undergo the largest change in emittance, with emittance loss increasing with reducing crossing angle. The horizontal plane suffers larger variations of emittance than

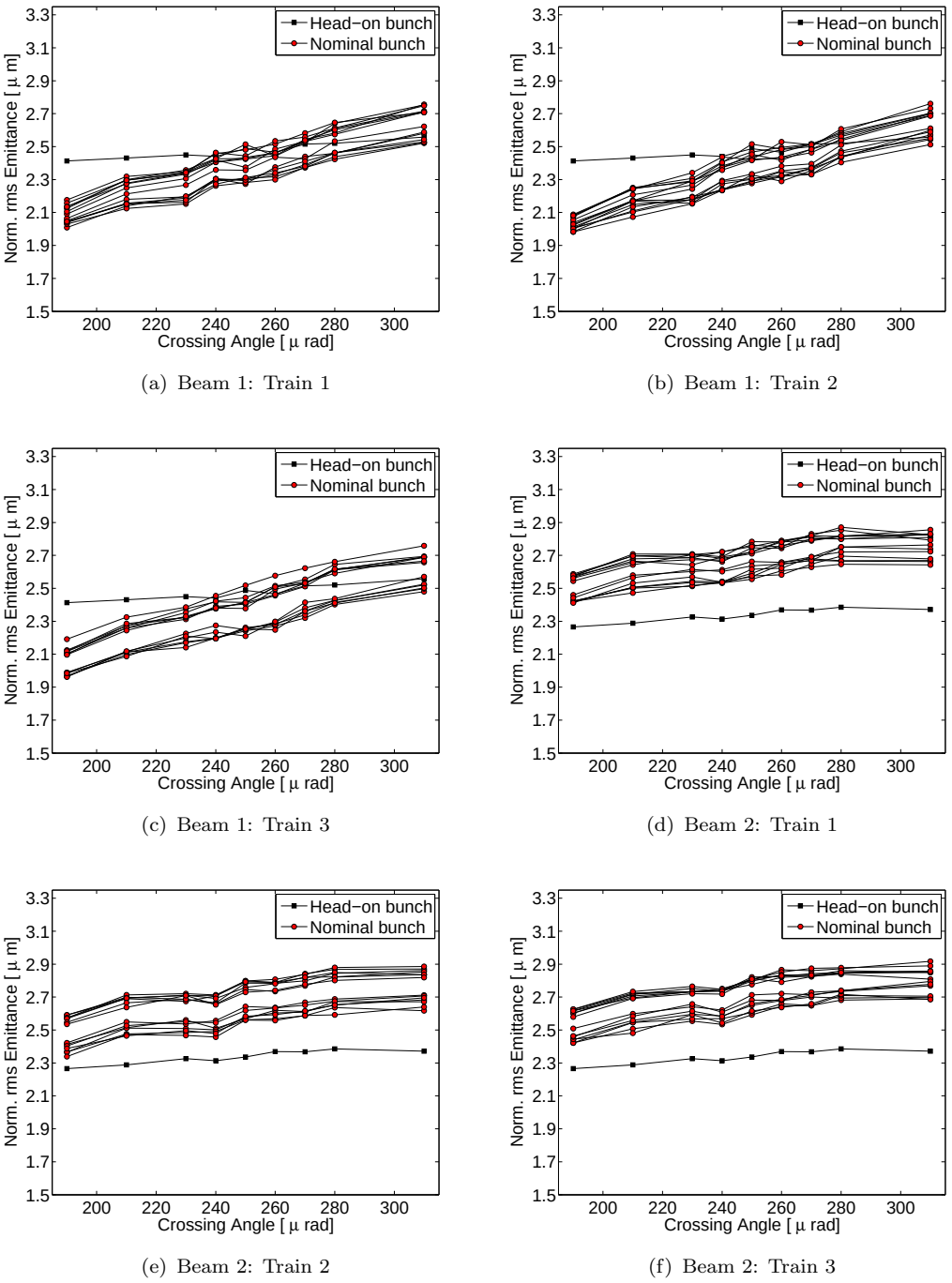

(a) Beam 1: Train 1

(b) Beam 1: Train 2

(c) Beam 1: Train 3

(d) Beam 2: Train 1

(e) Beam 2: Train 2

(f) Beam 2: Train 3

FIGURE 5.32: RMS beam 1 and 2 mean emittance as a function of crossing angle.

compared to the vertical plane. Figure 5.34 shows the emittance change in the horizontal and vertical planes for beam 2. For bunches in the second beam, no long-range beam-beam pattern is observed, although an emittance change with each crossing angle step is present. Similarly to the 2015 study, the long-range

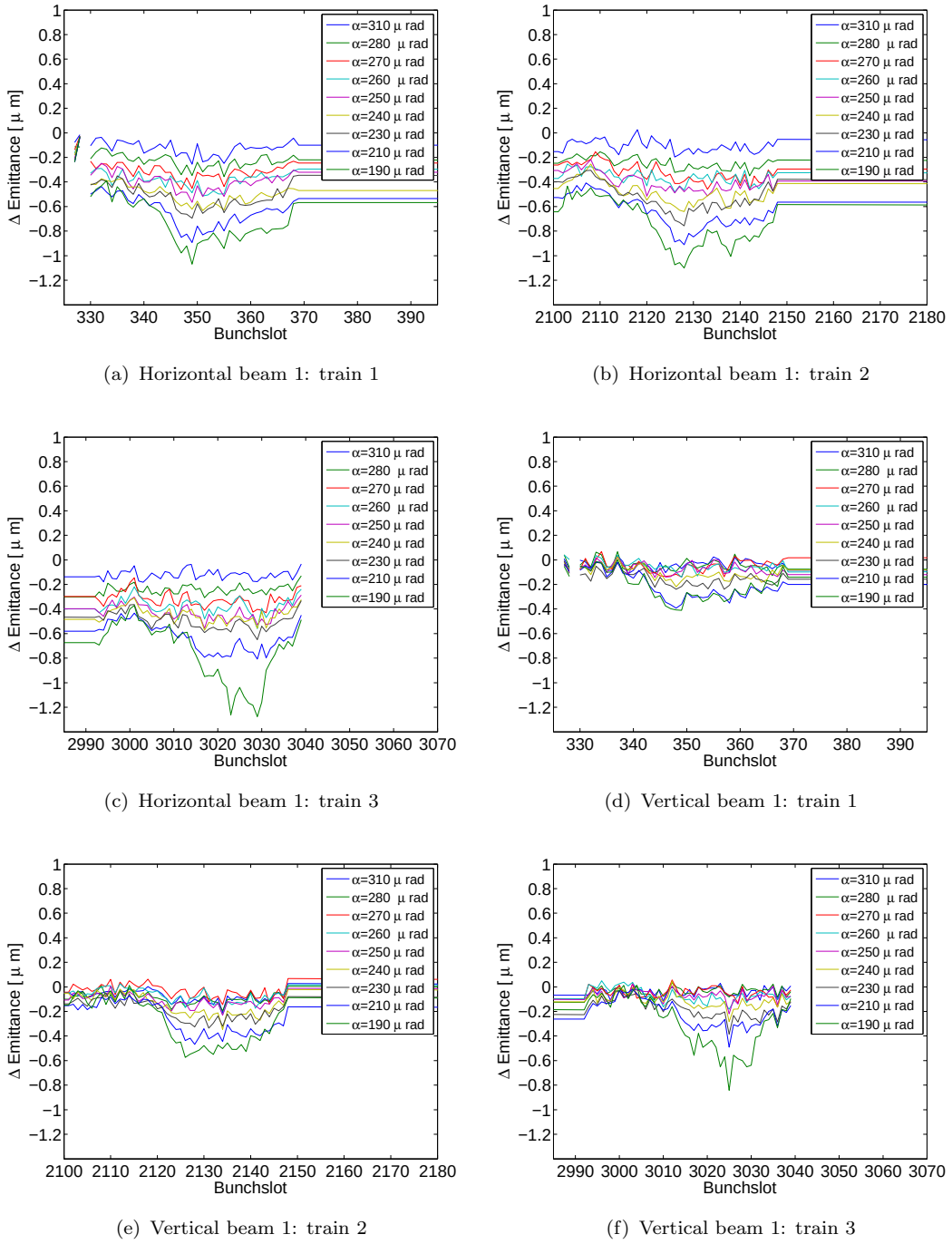

(a) Horizontal beam 1: train 1

(b) Horizontal beam 1: train 2

(c) Horizontal beam 1: train 3

(d) Vertical beam 1: train 1

(e) Vertical beam 1: train 2

(f) Vertical beam 1: train 3

FIGURE 5.33: Beam 1 emittance change normalised to the initial bunch emittances as a function of bunchslot and crossing angle.

beam-beam interaction with beam-beam separations $< 8.5\ \sigma$, behaves in a way comparable to that of a collimator which is cutting into the core of the bunch.

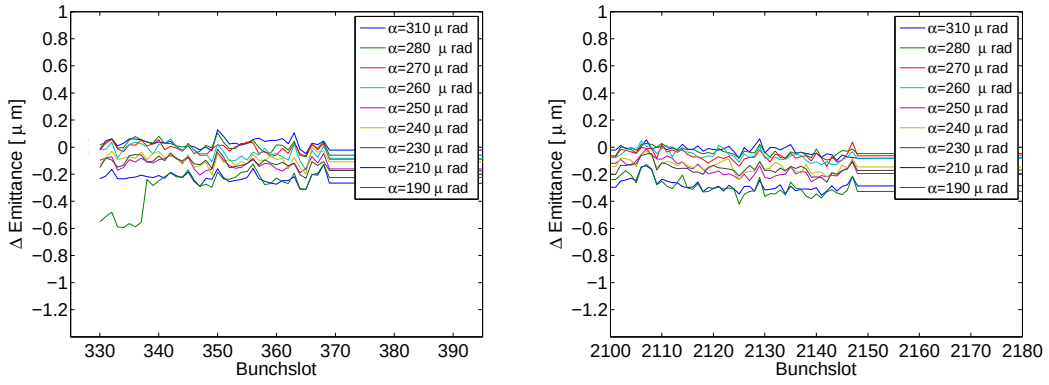

(a) Horizontal beam 2: train 1

(b) Horizontal beam 2: train 2

(c) Horizontal beam 2: train 3

(d) Vertical beam 2: train 1

(e) Vertical beam 2: train 2

(f) Vertical beam 2: train 3

FIGURE 5.34: Beam 2 emittance change normalised to the initial bunch emittances as a function of bunchslot and crossing angle.

5.3.4.3 Bunch by Bunch Luminosity

Unlike the 2015 machine study, the 2016 machine study also obtained bunch by bunch luminosity data from the CMS detector to record. The CMS detector tends to publish luminosity data with a better time resolution than the ATLAS detector, which in turn will lead to a more accurate fitting of the decay model. Much like the intensity data, a long-range beam-beam pattern is observed in the bunch by bunch luminosity data, as shown in figure 5.35. However the impact is only really observed at the last crossing angle. The decay rates calculated here will depend on the intensities of the colliding bunches in both beams as well as the emittance and transverse offset. Since beam 2 did not really observe a significant impact from the crossing angle reduction, it is likely that this impacts the calculation of decay rate. In addition to this the luminosity data will also be affected by transverse offset and emittance effects. These effects can all impact the calculated value of luminosity decay rate. In the next section, the impact of

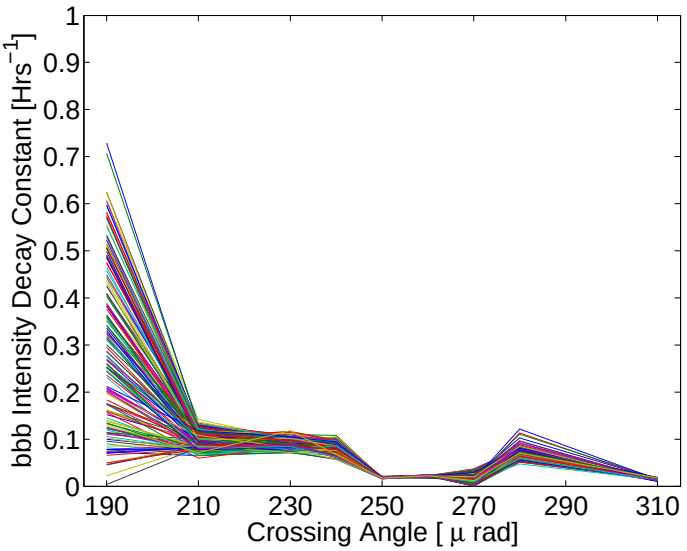

FIGURE 5.35: Bunch by bunch decay rate as a function of crossing angle obtained from luminosity data provided by the CMS detector.

the additional collisions at IP2 and IP8 are discussed.

5.3.4.4 Impact of Additional Collisions at IP2 and IP8.

The strength of the long-range beam-beam interaction is dependent on the beam-beam separation as defined by equation 5.1 and is dependent on the crossing angle, the emittance, and the β-function at the IP. In the 2012 LHC run, the additional long-range beam-beam effects from IP2 and IP8 had a significant effect on the lifetimes [104]. To mitigate the long-range effect from IP2 and IP8, the beam-beam separation was increased. The beam-beam separation during the 2012 LHC run in IP2 and IP8 was approximately 12σ and 10σ respectively, however in the 2015 and 2016 run this separation was increased to approximately 26σ.

The impact from additional collisions at IP2 and IP8 are expected to be minimal during the machine experiment. This is partly due to the small bunch emittances, $\epsilon = 2.5$ μm and larger β^* values at IP2 ($\beta^* = 10$m) and at IP8 ($\beta^* = 3$m). Since the β^* value at IP8 is smaller, collisions at this IP are expected to have a marginally larger effect on the lifetimes than that at IP2. The comparison between the Pacman bunches at the front of all three of the different trains is shown in Figure 5.36 at the smallest crossing angle. As it can be seen in Figure 5.36, the effect on the decay rates from the additional collisions at IP2 and IP8 are small. Collisions at IP8 do as expected have a slightly larger contribution to the decay rates, however it is not large and there is approximately a 20% difference between the decay rates for nominal bunches that collide at IP1,2 and 5 compared to bunches that collide at IP1,2,5 and 8.

5.3.4.5 Head-On and Non-Colliding Bunches

As in the 2015 machine study, the head-on and non-colliding bunches were analysed separately to determine their dependence on the crossing angle. Figure 5.37

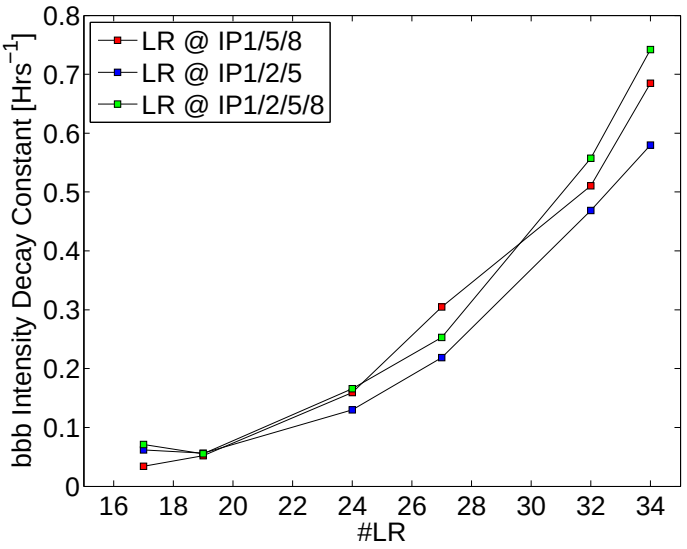

FIGURE 5.36: Comparison of the decay rates for pacman bunches at the front of all three of the bunch trains of beam 1 at a crossing angle of $\alpha = 190$ μrad.

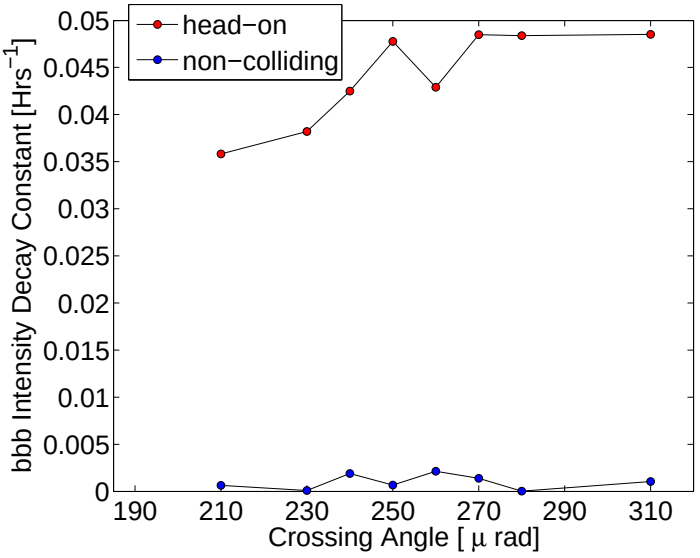

FIGURE 5.37: Decay rate as a function of crossing angle for the head on and non colliding bunches.

shows the decay rate as a function of crossing angle for both the head-on only and non-colliding bunch in beam 1. A comparable trend is observed for the head-on colliding bunch as seen in the 2015 machine study at a $\beta^* = 0.8$ m. The decay rate for the head-on only bunch improves as the crossing angle is reduced.There is no apparent effect on the non-colliding bunch from the crossing angle reduction as expected and agrees with the 2015 machine study.

5.3.5 LHC 2015/2016: Stable Beams

In the 2015/2016 LHC nominal luminosity fills, the long-range beam-beam effects were mitigated during stable beams by increasing the crossing angle at IP2 and IP8 and increasing the beam-beam separation at these IPs. Figure 5.38 shows the reduced impact of the long-range beam-beam effects on the decay rates with a reduced crossing angle at IP1 and IP5, with the beam-beam separations at IP2 and IP8 kept sufficiently large at $d_{sep} > 26\ \sigma$. Due to the success of the 2015/6 machine run and the two dedicated long-range beam-beam machine studies, it was decided to push the luminosity reach for the LHC towards the end of the 2016 proton-proton run. Pushing the luminosity reach by reducing the crossing angle will improve luminosity performance as well as providing a better understanding of the machine for the 2017 run.

Analysis of the dedicated machine studies show that the LHC can operate at a smaller beam-beam separation of 8.5 σ at IP1 and IP5, without lifetimes deteriorating due to long-range beam-beam interactions. Figure 5.38 shows an example nominal fill after a crossing angle reduction from $\alpha = 370\ \mu$rad to $\alpha = 280\ \mu$rad. The first hour from a luminosity production fill from the 2016 run is selected and analysed as shown in figure 5.38. The first hour was selected as it is this time in the fill that the long-range beam-beam interaction is the most prevalent. From figure 5.38 some apparent long-range beam-beam pattern can be observed for the different bunch trains. The decay rates do however remain within acceptable values above 10 hours. The worst lifetimes obtained correspond to bunch intensity lifetime of $\tau = 16.6$ hours. Similarly to the 2016 long-range beam-beam machine study, beam 1 is more sensitive to the crossing angle reduction, whereas beam 2 remains almost unaffected.

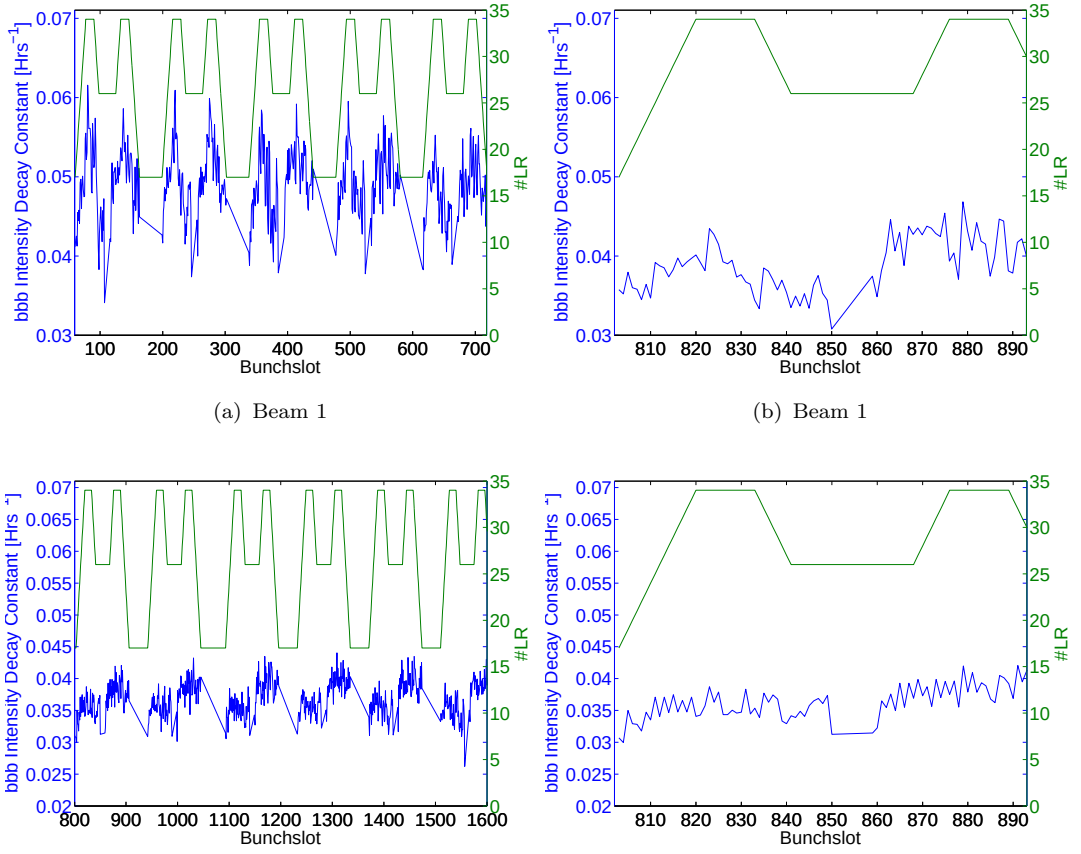

(a) Beam 1

(b) Beam 1

(c) Beam 2

(d) Beam 2

FIGURE 5.38: Decay rate dependence on the number of long-range beam-beam interactions after the crossing angle reduction to $\alpha = 280$ μrad.

5.4 Discussion

In this chapter, the long-range beam-beam limit in the LHC has been identified by characterising the decay rates for two different operational configurations, during two dedicated machine experiments. The analysis from the 2016 machine determined that the crossing angle could be reduced during normal operational fills. The lifetimes for a recent 2016 luminosity production fill, whilst operating at the new crossing angle is briefly discussed, along with the impact of the long-range beam-beam interaction on the fill.

In the 2015 machine study, collisions occurred at IP1 and IP5 only with a $\beta^* = 0.80$ m. The crossing angle was reduced in steps and the lifetimes were

measured. As the crossing angle is reduced, the beam-beam separation is reduced and the lifetimes correspond closely to the number of long-range beam-beam interactions each bunch experiences. The strength and number of the long-range beam-beam interaction is shown to have a significant impact on the lifetimes. For beam-beam separations smaller than 7.5 σ, the long-range beam-beam interaction began to dominate and cause particle losses. This separation corresponds to a crossing angle of $\alpha = 190$ μrad. At a minimum crossing angle of $\alpha = 118$ μrad, the lifetimes in the bunch by bunch intensity and luminosity data falls below 10 hours with beam 2 suffering more. A minimum bunch lifetime in beam 2 measured at approximately 4 hours. A crossing angle of $\alpha = 118$ μrad corresponds to a beam-beam separation of 5.5 σ. These lifetimes were observed whilst using the standard luminosity production operational settings of high chromaticity and Landau octupole current. In this study, it was found that reducing the chromaticity from $Q' = 15$ units to $Q' = 2$ units and the Landau octupole strength from $k_{oct} = 16.27$ Tm^{-3} to $k_{oct} = 0$ Tm^{-3}, resulted in an improvement in lifetimes, without compromising beam stability for the colliding bunches. Lifetimes improved for the nominal bunches, increasing from $\tau < 10$ hours, to values observed at the initial crossing angle of $\tau \geq 30$ hours. The high chromaticity and Landau octupole operation prevents the crossing angle being reduced below $\alpha = 190$ μrad. Operating at a smaller crossing angle would be beneficial from the perspective of luminosity production, however these settings are required in order to suppress instabilities during the squeeze.

The second machine study took place in 2016 and was split into two fills. The first fill was a repeat of the first machine study, colliding two trains of bunches but at a smaller β^* of 0.4 m. During this fill the long-range beam-beam limit was not reached due to an unexpected beam dump and time restraints prevented a repeat. The second fill of the machine study contained three trains of bunches which were collided at IP1 and IP5. Additionally each train had combinations of collisions

at IP2 and IP8. The long-range beam-beam limit was reached during this fill for a beam-beam separation of 8.5 σ. This corresponds to a crossing angle of approximately $\alpha = 260$ μrad in beam 1. The long-range beam-beam limit was not reached for the second beam until the smallest crossing angle $\alpha = 190$ μrad. For crossing angles above 260 μrad there was no noticeable impact from reducing the crossing angle on either beams and the decay rates and bunch lifetimes remained acceptable, above 10 hours. For beam-beam separations smaller than 8.5 σ, the decay rates begin to deteriorate. This resulted in lifetimes much less than $\tau = 10$ hours being obtained. Once again there was no obvious impact on beam 2, except for the smallest crossing angle $\alpha = 190$ μrad. The reason for the beam asymmetry is as of yet still unknown. In beam 2, only bunches with 24 long-range collisions or more experienced lifetimes smaller than $\tau = 10$ hours. From this machine study, the analysis suggests that it is possible to reduce the crossing angle operationally in the LHC without inducing additional losses. The crossing angle can be reduced from $\alpha = 370$ μrad to $\alpha = 280$ μrad with the current operational configuration, without encountering the long-range beam-beam limit and inducing unnecessary losses.

The crossing angle was reduced for nominal luminosity production runs at the beginning of October 2016. The crossing angle was reduced from 370 μrad to $\alpha = 280$ μrad, outside of the long-range beam-beam dominated region. The beam-beam separation was sufficiently large at ~ 9.3 σ, that good lifetimes were retained, enabling long fill lengths. In addition to the crossing angle reduction, the emittance was also reduced from $\epsilon_n = 3.75$ μm to $\epsilon_n = 2.5$ μm. The emittance reduction in combination with the crossing angle reduction, results in an increase in luminosity of approximately $15 - 17\%$, for a bunch intensity of $n_b = 1.25e^{11}$ protons per bunch.

In this chapter, the experiment results obtained during the two long-range machine studies have been discussed and analysed. In order to understand the diffusive processes that particles in the bunches experience, the experimental data will be compared to dynamic aperture simulations. The results and analysis will be discussed in chapter 6.

Chapter 6

Dynamic Aperture and the Long-Range Beam-Beam Interaction

6.1 Introduction

The analysis of the long-range beam-beam machine studies presented in chapter 5 show small beam and luminosity lifetimes for small crossing angles and beam-beam separations [108, 109, 115, 116]. The results from those studies enabled the minimum operational crossing angle in the LHC to be defined for that particular optics configuration and provided an understanding of the relation between intensity losses and the long-range beam-beam effect. The particle losses due to the long-range beam-beam effect arise due to a reduction of the dynamic aperture with crossing angle. It is important to quantify the impact of the long-range beam-beam interaction and the non-linearities of the machine on the dynamic aperture. This allows comparisons to be made between the expectations from

models and data obtained during the 2016 machine study. Providing this comparison allows the processes which limit dynamic aperture and affect luminosity performance in the machine to be understood.

6.2 Overview

In this chapter, results and analysis of dynamic aperture studies of the 2016 long-range beam-beam machine experiment are presented with the aim of characterising the dynamic aperture as a function of crossing angle. The measured dynamic aperture is calculated from intensity loss and compared to weak-strong long-term tracking simulations.

6.3 Dynamic Aperture

Dynamic aperture in a machine like the LHC is closely related to the onset of chaotic particle motion [13]. The dynamic aperture after an infinite number of turns is defined as the boundary in phase space for which particle motion inside that boundary is stable and outside that boundary is chaotic [117, 118]. This parameter is often denoted as $\mathcal{D}_\infty$ as given in ref [119]. Particles that lie outside this boundary and have chaotic motion can have amplitudes that grow significantly, resulting in particles being lost from the accelerator. For particles confined inside the dynamic aperture boundary in phase space, the particle trajectories should remain stable [120]. In reality however, even particles inside the dynamic aperture can be lost due to the phenomenon of *Arnol'd diffusion* [121]. Arnol'd diffusion can cause particle amplitudes to increase arbitrarily, which may result in the particle hitting the physical aperture of the machine, however the

time scale of Arnol'd diffusion may be so long that it is not relevant for physical applications.

For accelerator physics however, the concept of survivability or dynamic aperture after a finite number of turns is more practical. The dynamic aperture as a function of turn number is given by the inverse of the logarithm and is observed to have the form,

$$\mathcal{D}(N) = \mathcal{D}_{\infty}\left[1 + \frac{b}{(\log N)^{\kappa}}\right], \tag{6.1}$$

as given by ref [122, 123], and is based on the analysis of data from numerical simulations. In equation 6.1, $\mathcal{D}(N)$ is the dynamic aperture as a function of turn number N and $\mathcal{D}_{\infty}$ is the asymptotic value of the amplitude of the stability domain. The fitting variables b and κ are additional free fitting parameters as in [119]. The fitting parameters $(\mathcal{D}_{\infty}, b, \kappa)$ can take positive or negative values, with the sign of these values dependent on the system being studied. In order to understand the proposed model [119] and the sign of the fitting parameters, the KAM and Nekhoroshev theories are introduced briefly.

6.3.1 Kolmogorov-Arnol'd-Moser Theorem

Kolmogorov-Arnol'd-Moser (KAM) theory describes the behaviour of a system under the influence of a small non-linear perturbation. Under such a perturbation, solutions to the nearly integrable Hamiltonian system can still be found with the phase space motion remaining quasi-periodic i.e, stable, and confined to a KAM surface [124]. The KAM surface is hence defined as an invariant torus (doughnut-shaped surface) in which the particle's trajectory in phase space is confined [125]. If a particle's phase space amplitude trajectory lies on the KAM surface then the trajectory of that particle is likely to be confined within the bunch and will

remain stable, in the absence of Arnol'd diffusion. For the parameters given in equation 6.1, this interpretation of the model corresponds to the case when the fitting parameters b, κ and $\mathcal{D}_\infty$ are all positive $\mathbb{R}_{>0} = \{x \in \mathbb{R} \,|x \geq 0\}$. If the fitting parameters are all positive, then the KAM surface corresponds to the phase space region of the bunch in which the particle amplitude $r < \mathcal{D}_\infty$.

6.3.2 Arnol'd Diffusion

Arnol'd diffusion is closely related to KAM theory and determines the nature of some solutions that lie close to the unperturbed solutions of the Hamiltonian. In KAM theory, some solutions of the perturbed Hamiltonian will remain close to the unperturbed system, however this is not the case for all perturbed solutions. This means that perturbed solutions to the system can still exhibit an arbitrary amplitude growth [121]. As a result a given particle Hamiltonian that lies close to the unperturbed Hamiltonian may still experience diffusion to a higher amplitude and be lost. Hence even particles within the "stable" region of the bunch as described by figure 6.1 may still experience an arbitrary amplitude growth. Formally for a non-linear Hamiltonian there is no stable dynamic aperture and diffusion can occur from arbitrary small amplitudes [125].

6.3.3 Nekhoroshev Theorem

Particles outside of the dynamic aperture boundary in phase space will be governed by a Nekhoroshev-like escape to infinity. Particles will escape to infinity following

$$N(r) = N_0 \exp\left[\left(\frac{r_*}{r}\right)^{\kappa^{-1}}\right], \tag{6.2}$$

where $N(r)$ is the number of stable turns that have an initial particle amplitude that is smaller than r [119, 126–128]. Particles which have trajectories in phase space outside the stable core of the bunch $r > \mathcal{D}_\infty$, will undergo chaotic motion and diffuse to infinity following the Nekhoroshev-like escape. Eventually these particles will reach an amplitude where they are intercepted by the collimation system.

These fitting parameters under some conditions have a physical representation based on the above mentioned theories. In a 4-dimensional model, the fitting parameters; $\mathcal{D}_\infty$, b_0 and κ will all be positive and correspond to a partitioning of the phase space into stable and unstable regions. A schematic of this partitioning is shown figure 6.1, along with the dynamic aperture variation with the fitting parameters as shown in figure 6.2. Under this regime, the parameter b_0

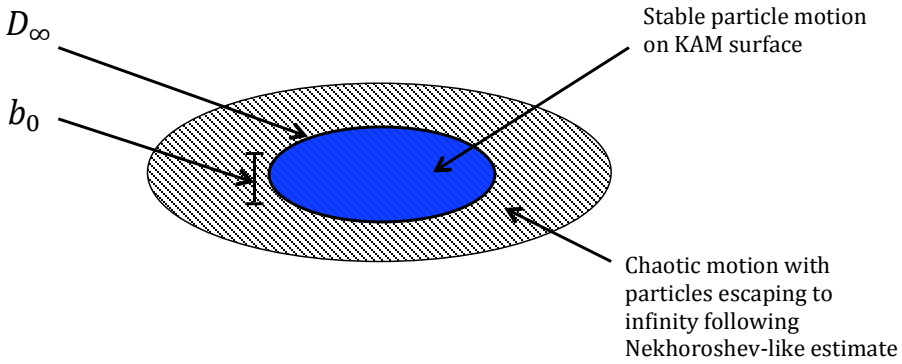

FIGURE 6.1: The partitioning of the bunch phase space for the positive valued fitting parameters $\mathcal{D}_\infty$, b_0 and κ as discussed in Ref [119].

corresponds to the size of the amplitude interval at which the diffusive mechanism occurs, and κ determines the rate of diffusion. The dynamic aperture varies significantly with more negative values of b_0 causing a larger reduction in dynamic aperture after 10×10^6 turns. The κ function on the other hand varies the slope of the inverse logarithmic function, with more negative values resulting in a steeper gradient. However the final dynamic aperture at 10×10^6 turns is within 0.25% for the different values of κ.The dynamics in a real machine will

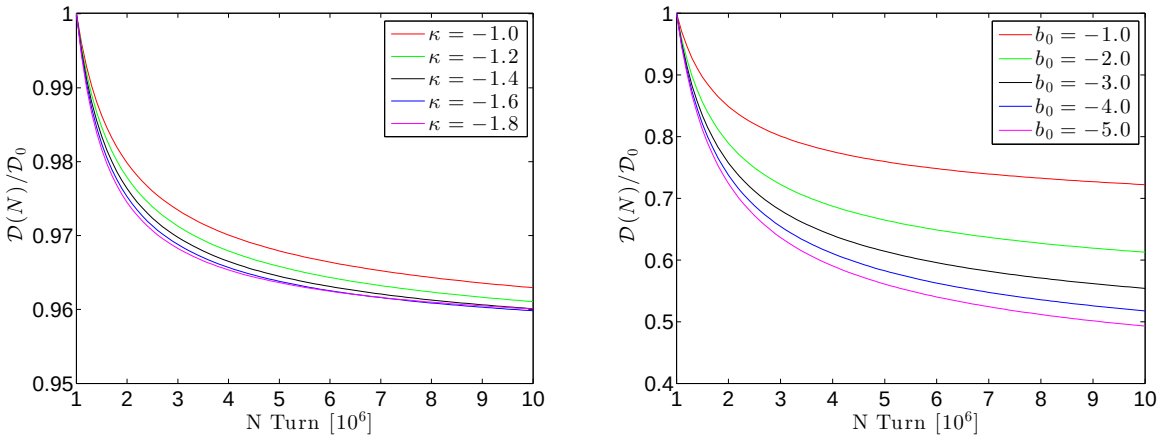

(a) (b)

FIGURE 6.2: The relative dynamic aperture evolution over time compared to the initial dynamic aperture $\mathcal{D}_0$, for different values of the free parameters κ and b_0.

however be a 6-dimensional system and hence non-positive values of the fitting parameters should be considered. This regime allows for negative values of the fitting parameters; $\mathcal{D}_\infty$, b_0 and κ [123]. If the fitting parameters are permitted to be negative, this will give two further possibilities,

$$\mathcal{D}_\infty > 0, \quad \kappa < 0, \quad b_0 < 0, \tag{6.3}$$

$$\mathcal{D}_\infty \leq 0, \quad \kappa > 0, \quad b_0 > 0. \tag{6.4}$$

Case 6.3 is indicative of a scenario with global chaoticity. In a system with global chaoticity, no stable KAM region is present and hence all particles will eventually after some finite time, escape to infinity. However the escape rate to infinity in a real machine could be considerably larger than the length of a fill [129]. The second case (6.4) goes beyond the physics of the model. Within this regime, the asymptotic value of the dynamic aperture is negative. If the parameter $\mathcal{D}_\infty < 0$ then this does not correspond to any physical scenario. Hence in this case, the KAM area reduces to zero and the escape time to infinity will follow the Nekhorohev-like estimate. These theories all provide the basis of the

method discussed by ref [119] and references therein, that allow the dynamic aperture from intensity loss to be calculated. The relationship between dynamic aperture and intensity loss is discussed in the following section.

6.3.4 Dynamic Aperture from Intensity Loss

A relationship between the dynamic aperture and the intensity loss as a function of turn number can be established following the method by M. Giovannozzi [119]. The particle intensity as a function of turn can be obtained directly from the FBCT data, in which the lost particles lie outside the boundary of stability at some turn N. The relationship between intensity loss and dynamic aperture is given by the integral

$$\frac{I(N)}{I_0} = 1 - \int_{\mathcal{D}(N)}^{\infty} \rho(\bar{\mathbf{x}}) d\bar{\mathbf{x}}, \tag{6.5}$$

where I is the intensity at some turn number N, I_0 is the initial intensity, and $\bar{\mathbf{x}}$ corresponds to the particle position. If the losses are assumed to only occur in the transverse planes, then $\bar{\mathbf{x}}$ corresponds to the transverse coordinates. Hence, for a round bunch with a Gaussian distribution, the integral becomes,

$$\frac{I(N)}{I_0} = 1 - \int_{\mathcal{D}(N)}^{\infty} e^{-\frac{r^2}{2}} r dr.$$

This yields the exponential relationship between the measured intensity and the dynamic aperture as

$$\frac{I(N)}{I_0} = 1 - e^{-\frac{\mathcal{D}^2(N)}{2}}, \tag{6.6}$$

where $\mathcal{D}(N)$ is in units of the bunch sigma. Equation 6.6 is comparable to the simple exponential model used in chapter 5, equation 5.3. Rearranging equation 6.6 and introducing the fractional intensity loss ($\Delta I = 1 - \frac{I}{I_0}$) gives the dynamic aperture as a function of turn number as,

$$\mathcal{D}(N) = \sqrt{-2\log(\Delta I)}. \tag{6.7}$$

Using expression 6.7, the dynamic aperture as a function of turn number can be calculated directly from the intensity loss. The behaviour of equation 6.7 follows an inverse logarithmic reduction of dynamic aperture with turn and is shown in figure 6.3. The behaviour close to $N = 0$ becomes numerically unstable, due to

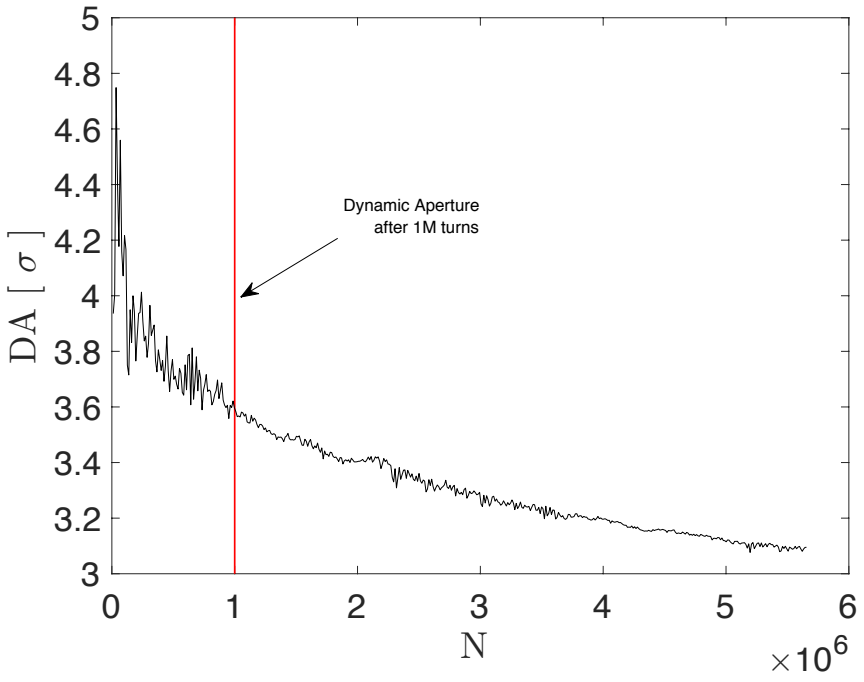

FIGURE 6.3: The inverse logarithmic decay of measured dynamic aperture as a function of the number of turns calculated. The dynamic aperture after 1×10^6 turns is highlighted by the red line.

the nature of the logarithmic function. Ideally N after a large number of turns ($N \geq 1 \times 10^6$) is preferred, however for tracking simulations the number of turns can significantly impact the computational time. Hence, for these simulations and for measured intensity data, the dynamic aperture calculated at 1×10^6

turns was used. In the next section, the computational method of calculating the dynamic aperture is introduced by using `Sixtrack`.

6.4 Sixtrack

Tracking codes such as `Sixtrack` are often used for dynamic aperture studies [130–132]. `Sixtrack` uses pairs of particles and tracks the pairs over various amplitudes in the $x-y$ plane. The particles are tracked in pairs in order to determine at which point in phase space chaotic motion occurs. `Sixtrack` uses lattice files generated by `MadX` [133]. The elements in the accelerator lattice are transformed from thick to thin lens, with the lattice used for these simulations given by LHC V6.503. The thin lens model used here enables the symplectic tracking of particles through the lattice and provides a good approximation for the LHC, since the particles remain close to the nominal design orbit and the deviation from the closed orbit is small around the ring. In addition to this the symplectic tracking is less computationally expensive than tracking through a thick lens lattice. This lattice was set up to have the same operational configuration as the real machine during the long-range beam-beam machine study. This lattice included beam-beam interactions with a $\beta^* = 0.4$ m at IP1 and IP5. During the machine studies discussed in chapter 5, additional collisions took place at IP2 and IP8 with a β^* of 10 m and 3 m, respectively. In that chapter, the collisions at IP2 and IP8 were shown to have a negligible impact on the beam lifetimes, since the beam-beam separation was significantly large, above 26 σ. Hence in order to reduce computational time, beam-beam interactions at IP2 and IP8 were not included in the tracking simulations.

The dynamic aperture itself is calculated in `Sixtrack` using a number of different methods. The chaoticity of a system is often calculated using the *Lyapunov*

exponent [134]. The Lyapunov exponent determines the onset of chaotic particle motion for two particles located close to one another in phase space [117, 118]. For two particle trajectories in phase space initially separated by δz_0, then the particles will diverge following

$$|\delta z(t)| \approx e^{\lambda t}|\delta z_0|, \tag{6.8}$$

where λ is the Lyapunov exponent [135]. If the Lyapunov exponent is positive ($\lambda > 0$), this indicates chaotic motion since the phase space separation between the two particles will continue to increase. When $\lambda < 0$, the particle trajectory is phase space will remain contained in a stable motion, since the particle separation in phase space will remain small. The Lyapunov exponent or computational alternatives are calculated in `Sixtrack` using the *distance* and *slope* methods. The distance and slope methods are two viable and efficient alternatives to calculate the Lyapunov exponent. The distance method determines the *certain* chaotic boundary by analysing the final separation of two initially close particles. One of the draw backs of this method is that the dynamic aperture may be overestimated [136]. Particles that undergo weak, irregular and chaotic behaviour may not be sufficiently separated after some period of time. An alternative, more pessimistic computational method is the slope method. This method examines the evolution of the distance in phase space and calculates the *strict* chaotic boundary. Once again, this can also lead to a misleading calculation of the dynamic aperture by underestimating the true value. If a pair of particles have a large, but regular motion, they may be falsely identified as chaotic particles. The preferred method here used for LHC type studies is the phase space averaged dynamic aperture and this is calculated using the post-processing tools available in the `sixdb` library [137, 138]. The dynamic aperture from the post-processing is used in the following section to analyse the results from the 2016 long-range beam-beam tracking study.

6.4.1 Magnetic errors

Particle motion in an accelerator is sensitive to a number of factors. Small manufacturing errors in the magnets or even the ground motion itself can impact the stability of a particle moving around the lattice [139]. In a real machine, the magnets will not be perfect and will sometimes be misaligned or have design manufacturing errors. The errors from the magnets can be categorised as systematic and random. The systematic errors can be corrected during operation. The random errors are more difficult to account for and arise due to imperfections in the magnets or due to magnetic misalignments, which can introduce additional unwanted multipoles. These can all affect the beam dynamics and lead to unwanted particle losses [140, 141]. To account for this, the errors in a number of the magnets were measured to provide realistic calculations in tracking simulations [142]. To determine the impact and severity of the magnet design errors, a number of measurements were made for the real LHC magnets. The magnet components were measured at hot and cold temperatures, as well as at high and low voltage. From this a linear model was constructed between the two regimes [140]. Due to the large number of magnets in the LHC, the rest of the magnets were measured at warm temperatures, with the cold magnet errors calculated using the linear model. Since not all of the magnets could be measured, 60 realisations of the lattice, sometimes known as seeds, are used in order to gain a 95% certainty in the dynamic aperture calculation [143].

Simulating 60 realisations of the lattice allow the range of dynamic aperture to be defined. The minimum dynamic aperture as a function of angle compared over two individual seeds versus the 60 seed case is shown in figure 6.4. A single seed used during tracking simulations, in the presence of magnetic errors can result in the minimum dynamic aperture being missed. Using 60 realisations of the lattice results in a dynamic aperture difference of about $1 - 2\ \sigma$ for some angles in the

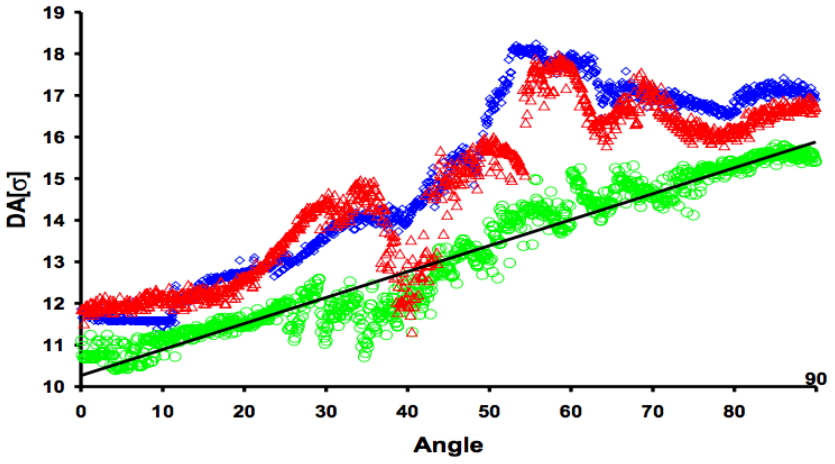

FIGURE 6.4: The minimum dynamic aperture for two different seeds (red and blue points) compared to the minimum dynamic aperture obtained from 60 realisations of the LHC lattice (green) [144].

$x-y$ plane compared to the single seed case for the bare machine lattice without beam-beam.

6.4.2 The Symplectic Beam-Beam Map

In addition to the magnetic errors of the lattice, how the beam-beam effect is modelled in `Sixtrack` should be considered. `Sixtrack` uses the thin lens approximation to study particles travelling around a lattice. In order to study the beam-beam interaction using `Sixtrack`, the beam-beam interaction must be described as a symplectic map within the thin lens approximation. To derive the beam-beam map in `Sixtrack`, it must be expressed in terms of the weak-strong approximation. The weak-strong approximation states that a moving test particle receives a kick from a counter rotating bunch, but the bunch distribution will remain unaffected by the test particle. In the ultra-relativistic limit, for a head-on collision without crossing angle, the electric field is almost entirely contained to the transverse planes, with the magnetic field component arising due to the Lorentz boost as detailed in [145]. In this limit, the bunch can be divided into slices, with the intensity of each slice following a Gaussian distribution

along the longitudinal direction. However in the LHC, the bunches collide with a crossing angle and coupling between the planes may be present. The impact of these operational scenarios need to be considered in the tracking simulations. The 6-dimensional scalar potential for each slice is given by

$$\varphi(x,y;\Sigma_{11},\Sigma_{33};\vartheta) = -\frac{r_p}{\gamma}\int_0^\infty \frac{\exp\left[-\frac{x^2}{2\Sigma_{11}+q}-\frac{y^2}{2\Sigma_{33}+q}\right]}{\sqrt{2\Sigma_{11}+q}\sqrt{2\Sigma_{33}+q}}\mathrm{d}q, \tag{6.9}$$

from [65], where q is the integration variable and Σ_{ij} corresponds to the 6×6 phase space envelope matrix of the strong bunch, given by

$$\Sigma_{ij} = < R_i R_j > - < R_i >< R_j > . \tag{6.10}$$

Here i,j are integer values from $1,...,6$, with the transverse 6-dimensional coordinates of the strong bunch denoted R. The coordinates of the strong bunch can be expressed as

$$R = \begin{pmatrix} X \\ P_X \\ Y \\ P_Y \\ Z \\ P_Z \end{pmatrix}. \tag{6.11}$$

Hirata developed a symplectic map based on this sliced potential. This symplectic map allowed bunch length effects to be approximated [65]. The impact of bunch length effects were shown to be no longer negligible under certain conditions, such as when bunch sizes vary significantly around the IP [62]. This symplectic mapping was implemented into `Sixtrack` and is known as the Synchro-Betatron Mapping (SBM). The mapping of the coordinates throughout the interaction is

given by

$$
\begin{aligned}
x^* &\to x^* + Sn^*F_x^*, \\
p_x^* &\to p_x^* - n^*F_x^*, \\
y^* &\to y^* + Sn^*F_y^*, \\
p_y^* &\to p_y^* - n^*F_y^*, \\
p_z^* &\to p_z^* - n^*F_z^* - \frac{1}{2}\left[n^*F_x^*(p_x^* - \frac{1}{2}n^*F_x^*) + n^*F_y^*(p_y^* - \frac{1}{2}n^*F_y^*)\right].
\end{aligned}
$$

In this notation, the $*$ represents parameters at the collision point, S is the slice number, n^* is the bunch population, and the functions $F_{x,y,z}$ represent the electric field in the x, y, z dimensions. The electric field is given by,

$$
F_\alpha^* = \partial_\alpha \varphi(\bar{x}^*, \bar{y}^*; \Sigma_{11}(\vartheta), \Sigma_{33}(\vartheta), \vartheta), \tag{6.12}
$$

where $\alpha = \{x^*, y^*, z^*\}$. In order to calculate the electric field of each slice, F_α^* must be calculated for every slice. This can be computationally expensive, especially in the strong-strong regime for multiple collision points. However, as far as the author is aware, there is no analytical alternative that can be implemented in `Sixtrack`. This provides some of the motivation for the theoretical approach detailed in chapter 4. The SBM includes coupling and was implemented into `Sixtrack` using a Lorentz boost Λ, including a longitudinal tilt. The Lorentz boost as shown in figure 6.5 between the weak and strong bunch is given by Leunissen, *et. al* [145], and takes the form,

$$
\Lambda = \begin{bmatrix}
\frac{1}{\cos\vartheta} & -\cos\alpha\sin\vartheta & -\tan\vartheta\sin\vartheta & -\sin\alpha\sin\vartheta \\
-\cos\alpha\tan\vartheta & 1 & \cos\alpha\tan\vartheta & 0 \\
0 & -\cos\alpha\sin\vartheta & \cos\vartheta & -\sin\alpha\sin\vartheta \\
-\sin\alpha\tan\vartheta & 0 & \sin\alpha\tan\vartheta & 1
\end{bmatrix}, \tag{6.13}
$$

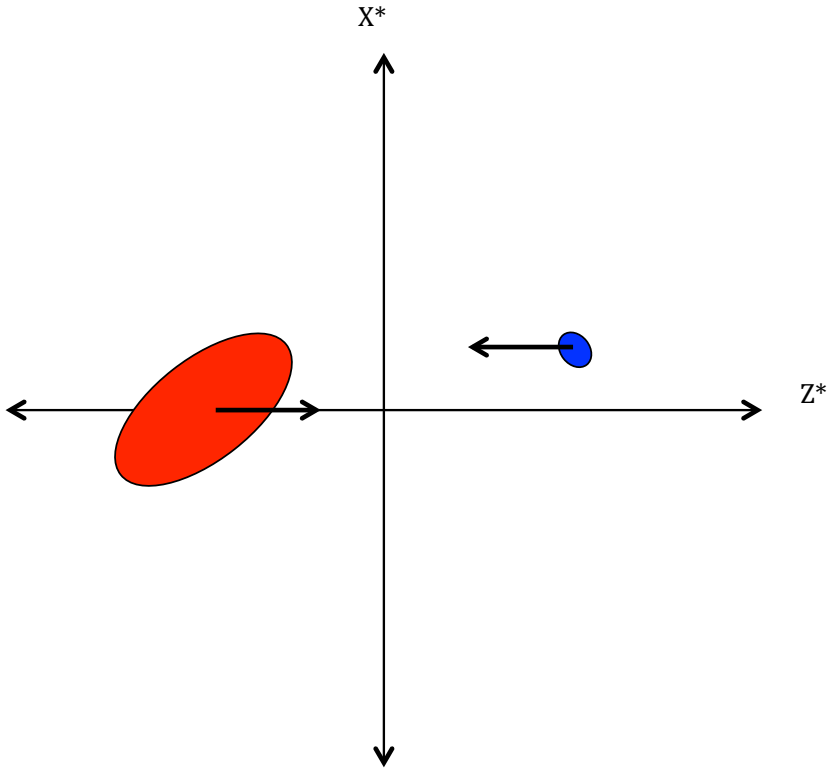

FIGURE 6.5: The Lorentz boost with a longitudinal tilt in the strong bunch to ensure a head-on collision with the test particle

where the crossing plane angle is denoted by α and 2ϑ is the full crossing angle. The SBM provides the basis for the beam-beam lens implemented in `Sixtrack`. Throughout these dynamic aperture studies, a number of the machine and bunch properties were varied such as crossing angle, emittance, intensity and coupling. To obtain the most realistic possible simulations bunch length effects were also included in the simulations using the SBM described above.

6.5 Results from Simulations

In this section, the results of tracking simulations using `Sixtrack` are presented and compared to measured dynamic aperture. Firstly, a crossing angle scan is performed in order to identify the impact of the beam-beam interaction on the dynamic aperture at different crossing angles. The dynamic aperture obtained

from these tracking simulations are then compared to measured dynamic aperture using the formula proposed by M. Giovannozzi [119], described in equation 6.7. In the following sections, the simulation setup is described along with some of the systematic and measured errors which could impact the results.

6.5.1 Simulation Setup

The pairs of particles in `Sixtrack` are tracked over a number of angles in the $x-y$ plane defined by the variable $k_{\max}$. The $k_{\max}$ can be converted to degrees following ref [144]:

$$\theta = \frac{90}{k_{\max}+1}. \tag{6.14}$$

To ensure that an accurate value of the minimum dynamic aperture was obtained from the tracking simulations, a reasonable number for $k_{\max}$ must be chosen to ensure that the computation time is small and the error on the dynamic aperture is minimised. The minimum dynamic aperture obtained as a function of $k_{\max}$ is shown in figure 6.6. The dependency on $k_{\max}$ is significant when determining the minimum dynamic aperture. When only 5 angles are scanned there is a large probability that the minimum dynamic aperture will be missed. The difference between $k_{\max}$=5 and $k_{\max} = 59$ is approximately 0.7 σ. For the following simulations, $k_{\max} = 59$ was used throughout, as large sample of angles in the $x-y$ plane is required in order to compare directly to measured data. This corresponds to a pair of particles tracked every 1.5 degrees in the $x-y$ plane. Although the difference between $k_{\max} = 30$ and $k_{\max} = 59$ is of the order of 0.02 σ for this simulation scenario shown in figure 6.6, including magnetic errors into the simulation model introduces significant non-linearities. Selecting a $k_{\max}$ value of 59 ensures that the minimum dynamic aperture is not missed, whilst retaining acceptable computational times [144].

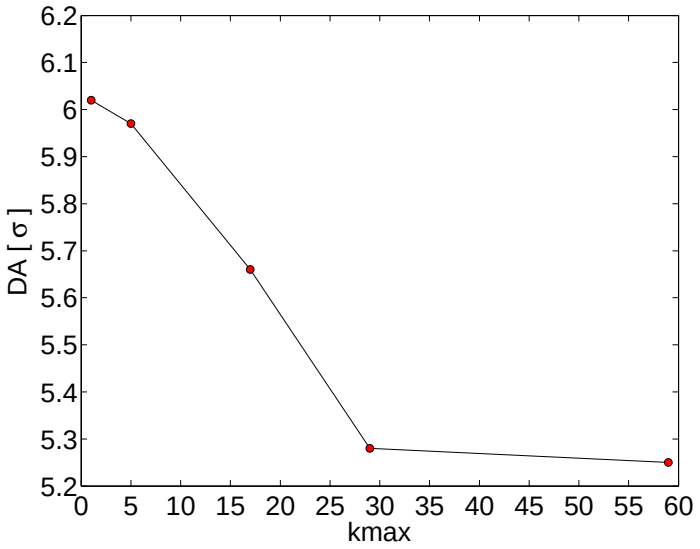

FIGURE 6.6: Minimum dynamic aperture as a function of $k_{\max}$. For $k_{\max} < 29$ the difference in the minimum dynamic aperture calculated is approximately $0.7\ \sigma$.

Similarly, in order to reduce the uncertainty in the minimum dynamic aperture calculation, particles were tracked over a large number of turns with the aim of minimising both the systematic errors from the simulations and the computational time required to perform the simulations. Therefore the particles were tracked over 1×10^6 turns.

In order to compare the results from simulation to measurement, the effect of proton burn-off on the bunches must also be considered. The dynamic aperture calculated in `Sixtrack` does not include particle losses due to head-on collisions with the counter rotating bunches, however these losses were present during the long-range beam-beam machine study. The losses due to proton-burn off can be calculated from the luminosity data and the effect of burn-off can be removed from the dynamic aperture calculation. An example calculation of the proton burn off is shown in figure 6.7 and is calculated using the simple formula

$$\mathcal{B}(t) = \mathcal{L}(t) \times \sigma_{in}, \tag{6.15}$$

where σ_{in} is the inelastic cross section for proton-proton collision and $\mathcal{L}$ is the bunch luminosity. In the LHC, the inelastic cross section is approximately $\sigma_{in} \approx$ 110 mb [146] and the luminosity during the long-range machine study was $\mathcal{L} \approx 6$ Hz per μb. Here the unit of "barn" is introduced, with 1 barn equal to 10^{-24} cm^2. From this, a burn-off rate of about 58 protons per turn per IP is obtained. The effect of burn off is removed by then adding the particles lost back to the fractional intensity in equation 6.7 such that,

$$\mathcal{D}(N) = \sqrt{-2\log(\Delta I + \delta I_{burnoff})}. \tag{6.16}$$

The particles lost from burn off after $1 \times 10^(6)$ turns will be approximately 1×10^8 protons. Including these lost protons back into the dynamic aperture calculation will increase the measured dynamic aperture marginally by approximately 4×10^{-4} σ. Proton burn-off is not the only source of difference between the measured

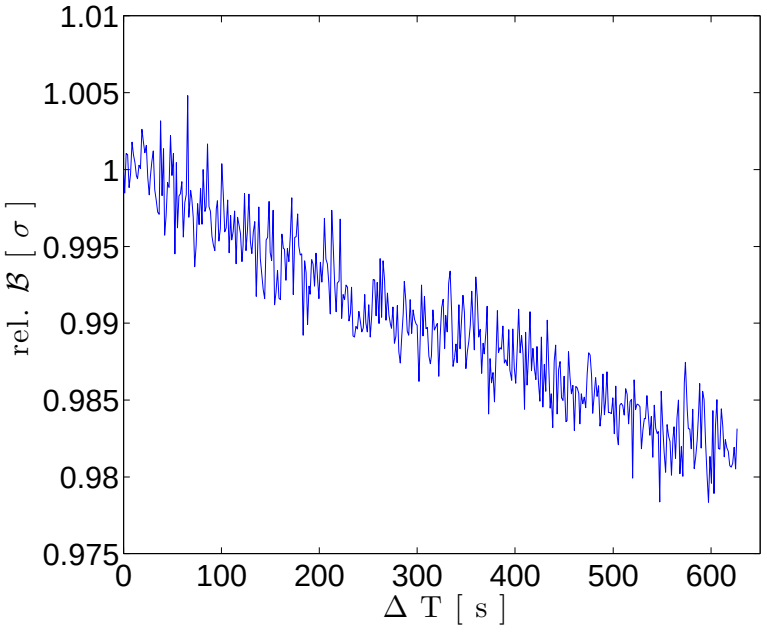

FIGURE 6.7: The relative proton burn off calculated for the nominal bunches over the crossing angle step $\alpha = 210$ μrad.

data and simulation model, as discussed in the next section.

6.5.1.1 Errors on Measured Data

In order to calculate the dynamic aperture using equation 6.7 and obtain a realistic calculation, the fractional intensity loss and emittance of the bunches are required. Details of the relevant LHC beam instrumentation can be found in chapter 3. In order to calculate the bunch intensity, FBCT data is used and is accurate to within approximately 1%. The error from the measured intensity will hence also impact the dynamic aperture calculation. An error of 1% on the bunch intensity corresponds to approximately 0.01 σ error in the dynamic aperture. In addition to the measured intensity, the emittance of the bunch is required to normalise the dynamic aperture to the emittance used in the simulations. The error from the BSRT is more substantial than the FBCT and corresponds to approximately $10\% - 20\%$ error [146]. As well as an error in the bunch emittance, an emittance asymmetry between the bunch planes was also present during the 2016 machine study. The error bars used throughout this analysis took into account this emittance asymmetry as well as the error from the BSRTs. The error from the measured bunch parameters were considered, however additional sources of error which are more difficult to measure should also be discussed briefly. Effects such as closed orbit drifts, transverse offsets between the colliding bunches and crossing angle error will all impact the dynamic aperture and the physical processes that the particles in the bunches experience. Closed orbit drifts will change the beam trajectory through the IP and may result in a smaller long-range beam-beam separation and hence a smaller dynamic aperture. Similarly, if the bunches collide with a transverse offset at the IP, the particles in the bunch may experience more of the non-linear force of the beam-beam interaction. These additional sources of non-linearities will all impact the dynamic aperture. These additional sources and the interplay with the beam-beam interaction is discussed in the next section.

6.5.2 Comparison to Tracking Simulations

In order to provide an accurate comparison between the measured dynamic aperture and simulated dynamic aperture, baseline simulations were performed at the same crossing angle steps as the 2016 machine study. The baseline simulations initially only included beam-beam interactions. Additional effects were then included in the simulation model to better model the accelerator dynamics. The measured dynamic aperture and dynamic aperture from tracking simulations is shown in figure 6.8, for the nominal colliding bunch. The measured dynamic aperture was computed at $N = 1 \times 10^6$ turns, in order to directly compare to the results from `Sixtrack`. In figure 6.8, the red, blue and green points correspond to the measured dynamic aperture normalised to the RMS value, the horizontal, and vertical bunch emittances. At small crossing angles below $\alpha = 260$ μrad,

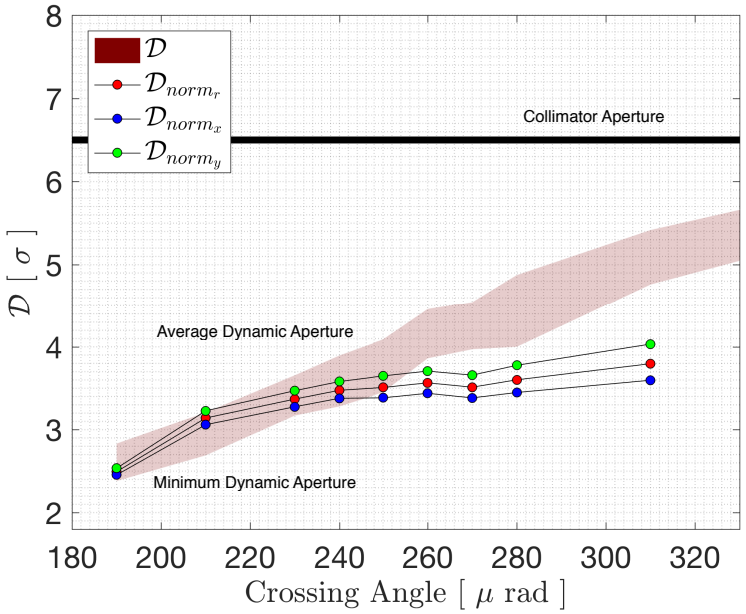

FIGURE 6.8: Comparison of tracking simulations (red shaded area) to the measured dynamic aperture (red, green, and blue points) at $N = 1 \times 10^6$ turns, for the nominal colliding bunch, including measured intensity and emittance

where the beam-beam separation is smaller than 8.5 σ, the dynamic aperture compares well for both measured and simulated results. The agreement between measurement and simulation occurs within the region in which the long-range

beam-beam interaction is strongest. At small beam-beam separations, the long-range beam-beam interaction dominates the particle losses and the dynamic aperture, corresponding to losses observed during the 2016 machine study. The small dynamic aperture causes particles to diffuse to larger amplitudes. These particles are then lost on the collimators . At crossing angles below $\alpha = 220$ μrad, the dynamic aperture is smaller than 3 σ. This corresponds to a beam-beam separation of ~ 7 σ. Here the dynamic aperture is significantly small enough as to cut into the core of the bunch. This provides a possible explanation as to the apparent loss of emittance measured by the BSRTs as observed in chapter 5. For dynamic aperture smaller than 3 σ, the long-range beam-beam interaction behaves like a collimator cutting into the core of the bunch. At crossing angles larger than $\alpha = 260$ μrad, when the beam-beam separation is larger than 8.5 σ, there is a clear discrepancy between the simulated and measured dynamic aperture that cannot be explained by the beam-beam interaction alone. The simulated dynamic aperture continues to increase towards larger crossing angles whereas the measured dynamic aperture appears to saturate at approximately 3.75 σ.

Previous studies [115, 116, 147] show that the Landau octupoles and chromaticity are known to limit the dynamic aperture towards large crossing angles. The impact of the parameters on the dynamic aperture whilst including long-range and head-on beam-beam effects is shown in figure 6.9 for various operational scenarios. The simulations presented in this chapter use the same operational settings as the long-range beam-beam machine study with chromaticity and Landau octupole currents set to $Q' = 16$ units and $J_{oct} = 476$ A. This octupole current gives the octupole strength as $k_{oct} = 16.27$ Tm^{-3}. These sources alone cannot account for the dynamic aperture difference between measurement and simulation shown in figure 6.8. Therefore additional physical effects, other than the beam-beam interaction, which limit the dynamic aperture will be considered, in order to better explain measured results.

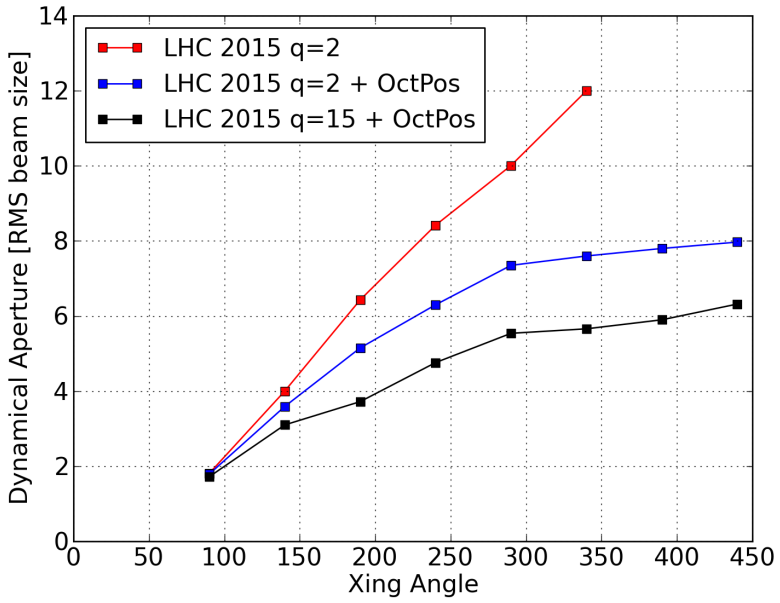

FIGURE 6.9: Dynamic aperture simulations for the 2015 LHC operational configuration, with $\beta^* = 0.8$ m, $n_p = 1.3 \times 10^{11}$ ppb, and $\epsilon_n = 3.75$ μm. For these operational settings, the chromaticity was varied from $Q' = 15$ units to $Q' = 2$ units and the impact of Landau octupoles on the dynamic aperture was also investigated [147].

Figure 6.10 shows the measured dynamic aperture for the head-on and nominal colliding bunches. For beam-beam separations larger than 8.5 σ, outside the long-range beam-beam dominated region, the head-on and nominal bunches have similar dynamic aperture and show no significant differences. The saturation of the dynamic aperture for these crossing angles is impacting bunches in the beam irrespective of whether the bunches collide head-on only or experience long-range interactions. In order to understand the effect limiting the dynamic aperture, the simplest beam-beam configuration of the head-on only colliding bunch is considered first.

A comparison between the measured dynamic aperture and the simulated dynamic aperture for the head-on only colliding bunch is shown in figure 6.11. In figure 6.11, the top boundary of the shaded area describes the average dynamic aperture obtained from tracking simulations. The averaged dynamic aperture is calculated by taking the mean dynamic aperture over all of the $x - y$ angles.

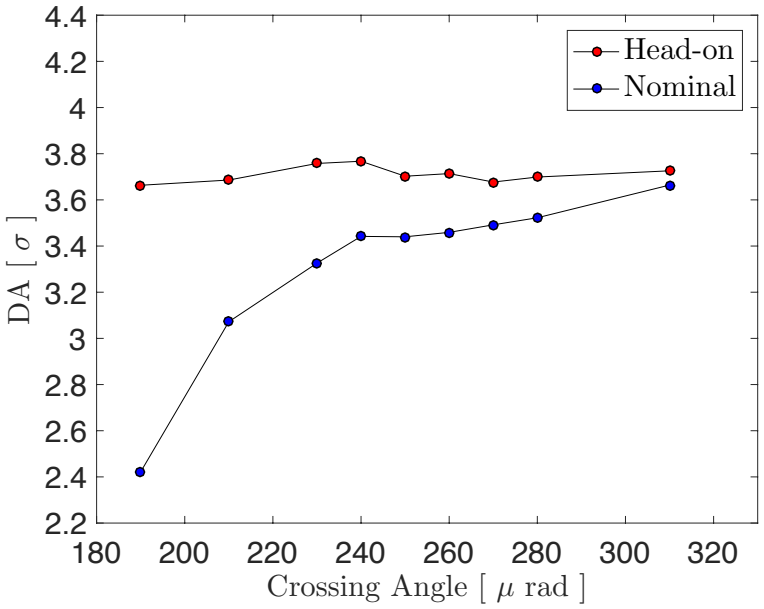

FIGURE 6.10: The measured DA calculated at $N = 1 \times 10^6$ turns, with emittance normalised to $\epsilon_n = 2.5\ \mu m$ for the HO colliding bunch and the mean DA for nominal bunches colliding at IP1 and IP5 with both HO and the maximum number of 34 LR beam-beam interactions.

The lower boundary of the shaded area corresponds to the minimum dynamic aperture. The minimum dynamic aperture is given by the smallest value of the dynamic aperture in the $x - y$ plane. The black line describes the collimator aperture at 6.5σ. The error bars are calculated by normalising the measured dynamic aperture at $N = 1 \times 10^6$ turns, to the horizontal and vertical emittances, whilst including a 20% error on the measured emittance.

The comparison shows a clear discrepancy between the dynamic aperture calculated from tracking simulations and measured data. The dynamic aperture from tracking simulations is within the range of $7-9\ \sigma$, whereas the measured dynamic aperture lies between 3.5 σ and 4 σ. In a real machine like the LHC, collimators are located around the ring in order to protect cold magnets and sensitive equipment from particle losses [148]. The physical aperture is set by the collimator openings and defines the maximum amplitude a particle can reach before being lost. For an emittance of $\epsilon = 2.5\ \mu$m, the collimator aperture is set at 6.5 σ. Particles at amplitudes larger than this will be lost onto the collimators. As seen

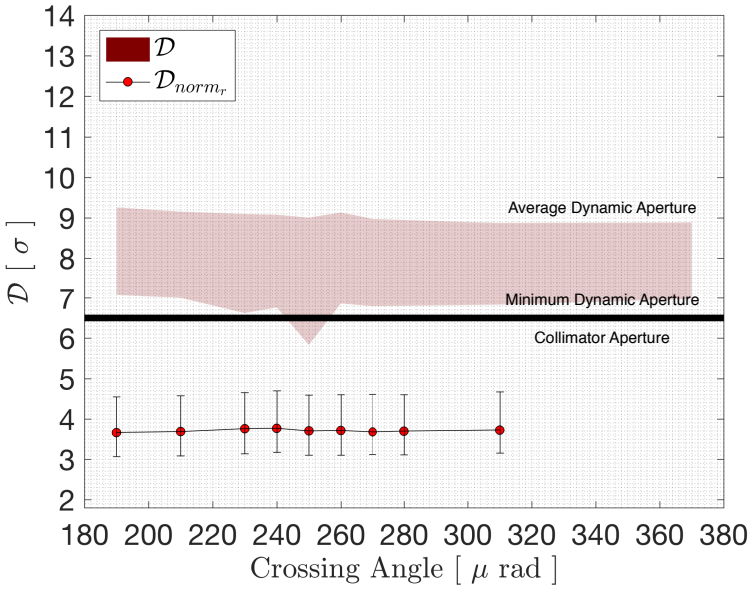

FIGURE 6.11: Comparison of simulation and measured dynamic aperture at $N = 1 \times 10^6$ turns for the head-on colliding bunch including measured intensity and emittance.

from figure 6.11, the dynamic aperture from simulations suggest that in the realistic machine the performance would be limited by the collimator aperture not by the head-on beam-beam interaction. This suggests that another beam dynamics process was limiting the measured dynamic aperture during the machine study.

The dynamic aperture as a function of $x-y$ plane is shown in figure 6.12 with the black line representing the collimator aperture. From figure 6.12 an asymmetry between the beam planes can be observed with the larger dynamic aperture found in the vertical plane. The reason for the asymmetry observed in figure 6.12 is unknown and warrants further investigation. Since the dynamic aperture can not be explained by the beam-beam interaction alone, additional effects which limit dynamic aperture are included in the simulation to better explain the discrepancy.

Linear coupling is one such effect that is known to impact the dynamic aperture [149]. In the LHC, the linear coupling is approximately $|\mathcal{C}^-| = 4 \times 10^{-3}$ during normal luminosity production [150]. Including this value into tracking

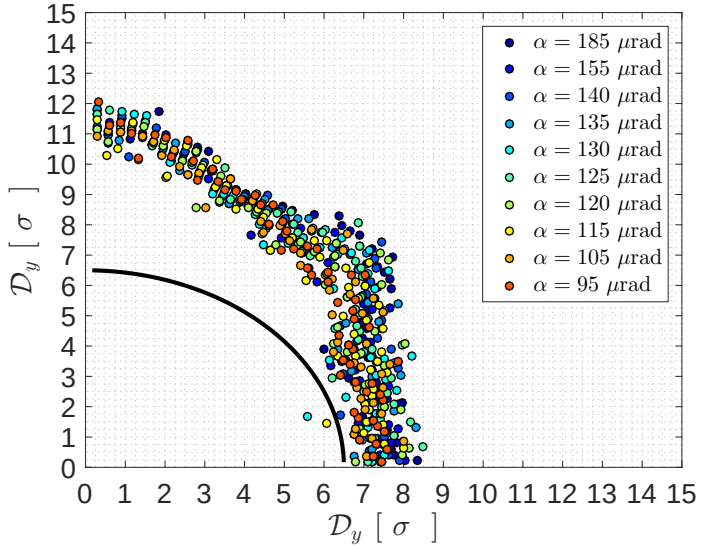

FIGURE 6.12: Dynamic aperture simulations as a function of $x - y$ plane for the head-on colliding bunch including measured intensity and emittance.

simulation reduces the dynamic aperture as seen in figure 6.13. The linear coupling introduces an interplay between the horizontal and vertical planes resulting in an additional degree of freedom. The additional degree of freedom introduced by linear coupling may reduce the stable region in phase space to zero and hence impact particle survivability, as described in ref [122]. The dynamic aperture obtained from tracking simulations show that the linear coupling reduces the dynamic aperture by ~ 1 σ over all crossing angle steps. The average dynamic aperture from simulation model still remains larger than the physical aperture defined by the collimators. The minimum dynamic aperture from the tracking simulations is within the collimator aperture but still differs from the measured dynamic aperture by ~ 2 σ. This suggests that linear coupling and the interplay with the head-on beam-beam is not solely responsible for the limited measured dynamic aperture that was observed during the long-range beam-beam machine study. The dynamic aperture as a function of the $x - y$ plane is shown in figure 6.14. The asymmetry between the planes is still present and does not change significantly when including the linear coupling. The linear coupling appears to reduce the dynamic aperture uniformly in the $x - y$ plane by about 1 σ. The

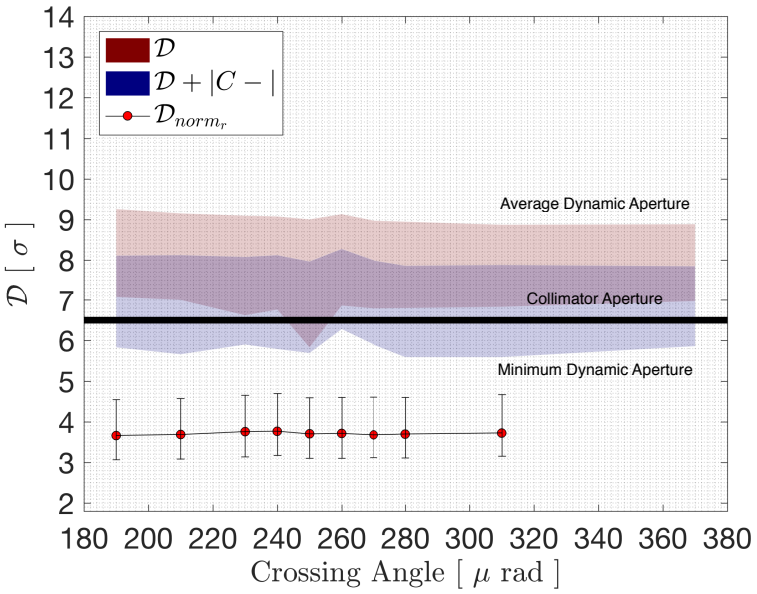

FIGURE 6.13: Comparison of simulation and measured DA for the HO only bunch including measured intensity, emittance, and linear coupling.

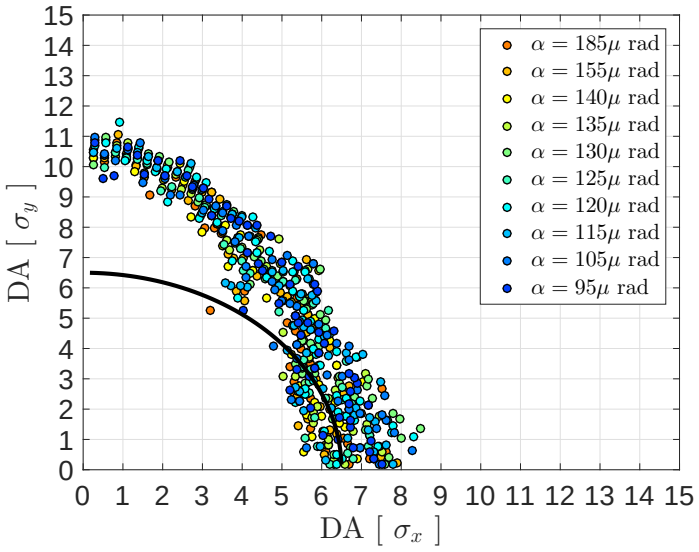

FIGURE 6.14: Dynamic aperture from tracking simulations for the head-on colliding bunch including measured intensity, emittance, and linear coupling as a function of the $x - y$ plane.

dynamic aperture in the x plane is slightly smaller and drops just below the collimator aperture, whereas the dynamic aperture in the y plane remains significantly above the 6.5 σ collimator aperture.

To further explain the discrepancy between the measured and simulated dynamic

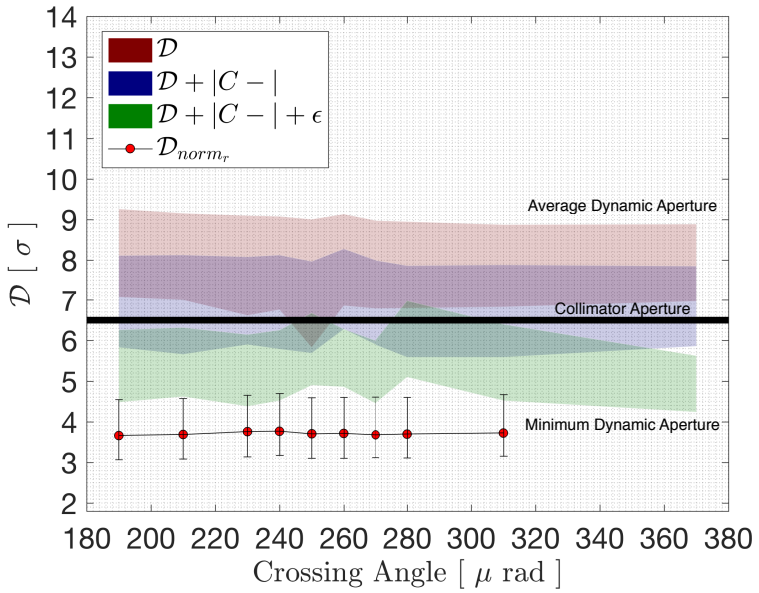

FIGURE 6.15: Dynamic aperture from measurement and tracking simulations for the head-on colliding bunch including multipolar errors, measured intensity, emittance, and linear coupling.

aperture, multipole errors in addition to linear coupling and the beam-beam interaction were included into the simulation model. Tracking simulations were performed using 60 realisations of the LHC lattice for each of crossing angle step. These simulations were computationally expensive, with each crossing angle producing approximately $50,000$ jobs. In order to compute such a large number of jobs the `Boinc` infrastructure was used for tracking simulations including magnetic errors [151].

The tracking simulations including magnetic errors and linear coupling are shown in figure 6.15. Including the magnetic errors in the simulation model further reduces the dynamic aperture by approximately $1-1.5\ \sigma$ and provides a reasonable comparison between simulation and measurement. There is still some discrepancy of approximately $0.5\ \sigma$ between the two models. There are a number of possibilities which could explain this. One explanation is the working point chosen for the simulations may not be quite the same as the measured data. During the long-range beam-beam machine study a tune drift was observed [152]. The tune

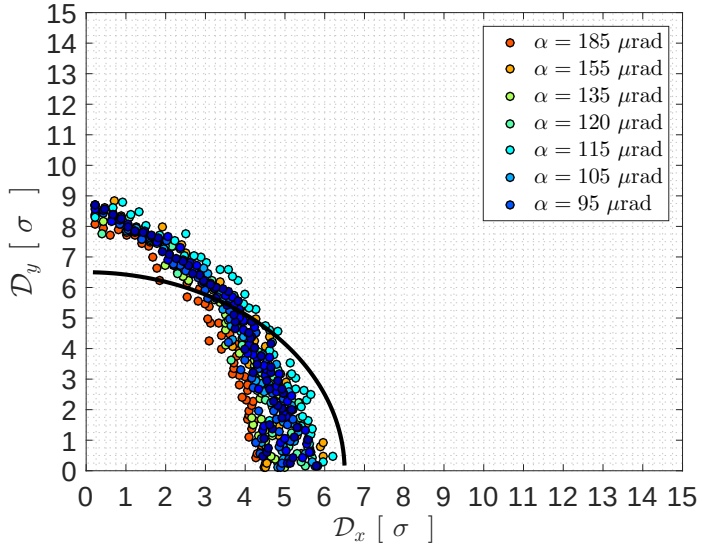

FIGURE 6.16: Dynamic aperture from tracking simulations in the $x - y$ for the head-on colliding bunch including multipolar errors, measured intensity, emittance, and linear coupling.

throughout the experiment drifted towards the third order resonance. If particles moved close to this resonance then they may be excited to larger amplitudes and then lost. An alternative scenario that causes a reduction in the dynamic aperture, arises due to a small transverse offset at the IP between the colliding bunches. In this case, the bunches are exposed to more of the beam-beam non-linearities, giving particles an amplitude dependent tune shift, which as a result could lead to particle losses. The transverse offset between the bunches is difficult to measure and can only be mitigated through luminosity optimisation.

The dynamic aperture in the $x - y$ plane from tracking simulations including magnetic errors and linear coupling is shown in Figure 6.16. Initial comparison between the measured and simulated dynamic aperture suggests that there is some interplay between the head-on beam-beam interaction, the non-linearities of the interaction region, and linear coupling that causes the dynamic aperture to saturate towards larger crossing angles. However this is not conclusive and some discrepancy between the model and the experimental data still exists, and this needs to be understood. In order to investigate further this interplay, additional

effects such as the transverse offset, tune drift, and closed orbit drift will be studied outside of this thesis.

The dynamic aperture for the nominal colliding bunch was also investigated as shown in figure 6.17. Here the error bars are calculated by normalising the measured dynamic aperture at $N = 1 \times 10^6$ turns, to the measured emittances in the x and y plane, plus a 10% error on the measured emittance. A similar saturation of the dynamic aperture was observed for crossing angles larger than $\alpha = 260$ μrad, corresponding to a beam-beam separation of 8.5 σ. Figure 6.17 shows the impact of both the head-on and long-range beam-beam interactions on the dynamic aperture of the nominal colliding bunch at the same crossing angle steps as the 2016 machine study. Below $\alpha = 260$ μrad, the dynamic aperture is well described by the tracking simulations. At these crossing angles the beam-beam separation is smaller than 8.5 σ and the losses are dominated by the long-range beam-beam interaction. As a result, the the dynamic aperture reduces following the crossing angle steps. Above $\alpha = 260$ μrad, outside of the long-range dominated region, the dynamic aperture from simulation continues to improve whereas the measured dynamic aperture becomes limited at approximately 3.75 σ. Although not conclusive, results from the head-on only case suggest that there may be an interplay between the beam-beam effects, the non-linearities of the machine, and the linear coupling, causing a saturation of the dynamic aperture towards larger crossing angles outside of the long-range beam-beam dominated region. These effects are then applied to the nominal colliding bunch in order to investigate the difference between the model and experimental data.

The dynamic aperture from simulation as a function of the $x - y$ plane is shown in figure 6.18, for a nominal colliding bunch. The dynamic aperture for the nominal colliding bunch in the $x - y$ plane appears to be uniformly distributed over the different angles and does not show the asymmetry observed for the head-on only bunch. The dynamic aperture over the different angles is almost

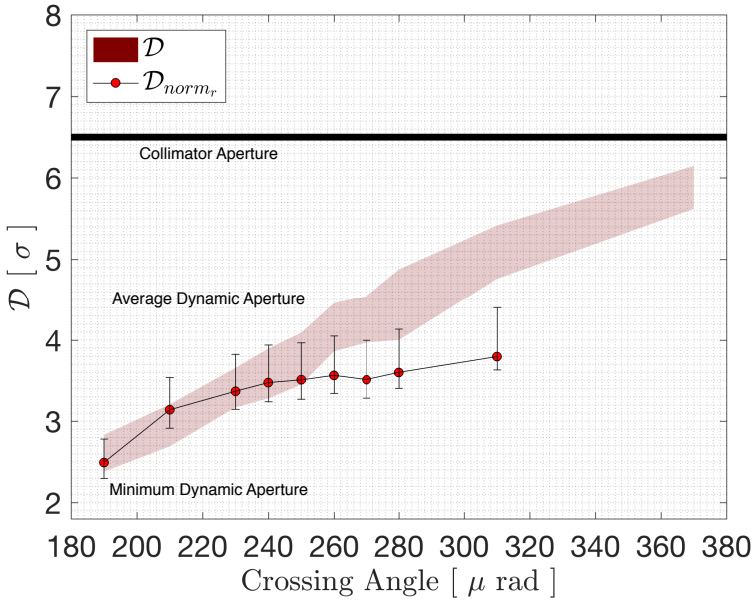

FIGURE 6.17: Dynamic aperture from tracking simulations for the nominal colliding bunch including measured bunch intensity, emittance, and long-range and head-on beam-beam effects.

entirely confined below the collimator aperture, and reduces successively with each crossing angle step. As previously observed for the head-on only bunch, the beam-beam interaction alone cannot account for the dynamic aperture for crossing angles above $\alpha = 260$ μrad.

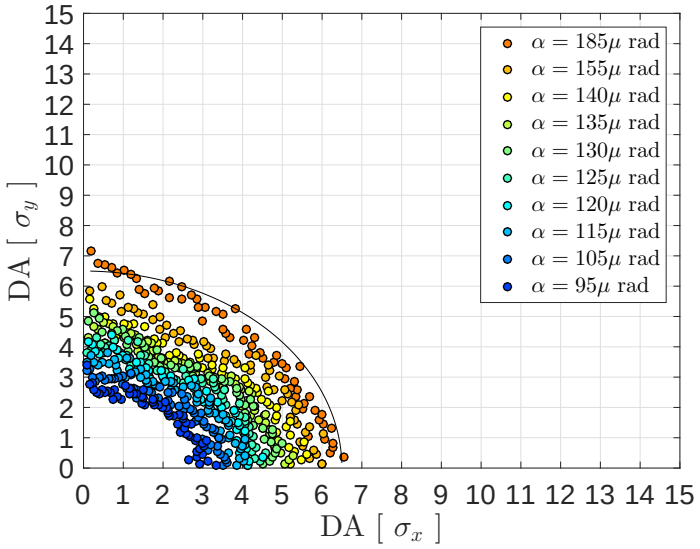

FIGURE 6.18: Dynamic aperture in the $x - y$ plane as a function of crossing angle for the nominal colliding bunch, including measured intensity and emittance

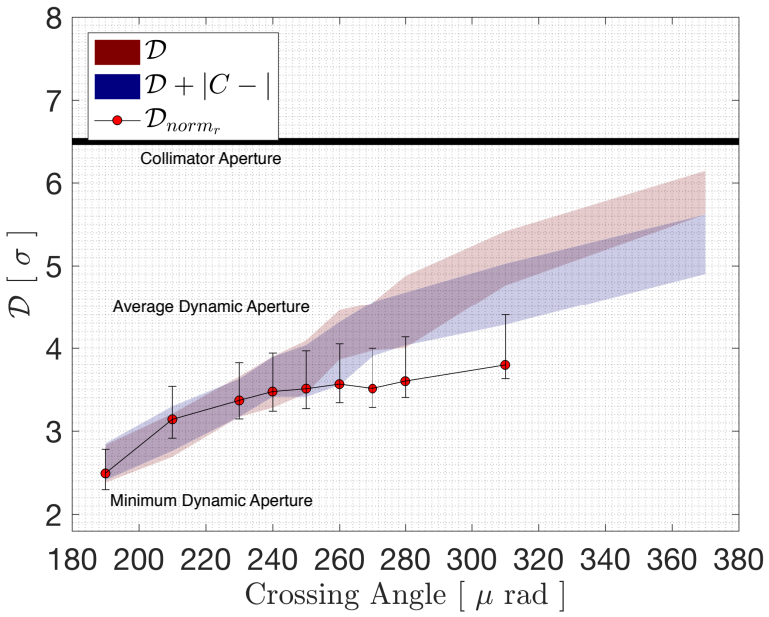

FIGURE 6.19: Dynamic aperture from tracking simulations for the nominal colliding bunch including measured intensity, emittance, and linear coupling.

Previous investigations including linear coupling for the head-on only colliding bunch shows that this effect reduces the dynamic aperture for $\alpha > 260$ μrad. In figure 6.19, linear coupling with a value of $|\mathcal{C}^- = 4 \times 10^{-3}|$ is included in the tracking simulations. Including linear coupling as shown in figure 6.19 limits the minimum and average dynamic aperture towards larger crossing angles by approximately 1 σ. This is comparable to the observations of the dynamic aperture reduction for the head-on colliding bunch. The dynamic aperture as a function of the $x - y$ plane including linear coupling is shown in figure 6.20. The linear coupling does not impact the smaller crossing angles, below $\alpha = 260$ μrad, with the losses continuing to be dominated by the long-range beam-beam interaction. For the larger crossing angle steps above $\alpha = 260$ μrad, the dynamic aperture is reduced and the difference between each crossing angle step is also reduced.

Finally magnetic errors were included in the simulations and were expected to impact the dynamic aperture outside of the long-range beam-beam dominated region. The tracking simulations including magnetic errors and linear coupling, compared to the measured dynamic aperture are shown in figure 6.21 and 6.22.

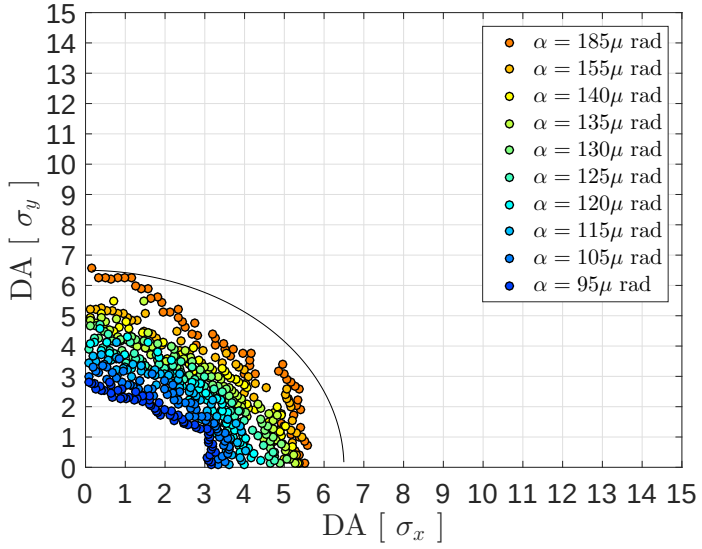

FIGURE 6.20: Dynamic aperture in the $x - y$ plane as a function of crossing angle for the nominal colliding bunch, including measured intensity, emittance and coupling

Including 60 realisations of the lattice provides a realistic estimate of the non-linearities of the machine [144]. The magnetic errors, in combinations with the beam-beam interaction and linear coupling, impact dynamic aperture for crossing angles above $\alpha = 260$ μrad. The magnetic errors act to further reduce the dynamic aperture for these angles. The dynamic aperture including these errors, well describes the measured dynamic aperture over all of the crossing angle steps. The possible interplay between the magnetic errors, linear coupling and the beam-beam interaction appears to saturate the dynamic aperture outside of the long-range beam-beam dominated region and may provide an explanation for the limited dynamic aperture observed during the 2016 machine study.

The magnetic errors and non-linearities in the IRs may be one source of the limited dynamic aperture for $\alpha > 260$ μrad and arises due to the crossing angle and the path of the beams through the triplet. For large crossing angles, the beams will travel off centre through the inner triplet quadrupoles. The field quality for these magnets is best towards the centre and hence, if the beams are offset, the bunches experience stronger non-linearities. These non-linearities can result in

chaotic particle motion or move particles onto resonant tunes which may cause particle losses and hence reduce the dynamic aperture. For large crossing angles and beam-beam separations above 8.5 σ, the dynamic aperture will saturate and may possibly become limited by the non-linearities of the triplets. For a crossing angle of $\alpha < 260$ μrad, the beams are no longer offset as much through the magnet centre, therefore the magnetic non-linearities of the triplet become have a smaller impact on the dynamic aperture. However, the beam-beam separation is smaller and the long-range beam-beam interaction will begin to dominate the losses instead.

The non-linearities will also further affect the dynamic aperture when β^* is small. In order to obtain tightly squeezed beams and a β-function at IP1 and IP5 of 0.4 m, the bunches have to be blown up through the triplet. The β-function through the IP is shown in figure 3.2 in chapter 3. As a result, the bunches again travel off centre through the triplet magnets causing a feed down effect of the non-linear magnet errors which scale approximately with $(\beta^*)^{-\frac{n}{2}}$, where n is the magnetic multipole order [4, 153]. However in order to conclusively determine whether it is the interplay between the beam-beam effects, linear coupling, and magnetic non-linearities, additional studies are required. Other effects should be considered that may impact the dynamic aperture at larger crossing angles such as a traverse offset between the colliding beams, closed orbit drift, larger values of linear coupling, and tune drift. These effects will be investigated further outside of this thesis and in addition the dynamic aperture model will then be compared to experimental data from the 2015 long-range beam-beam machine study.

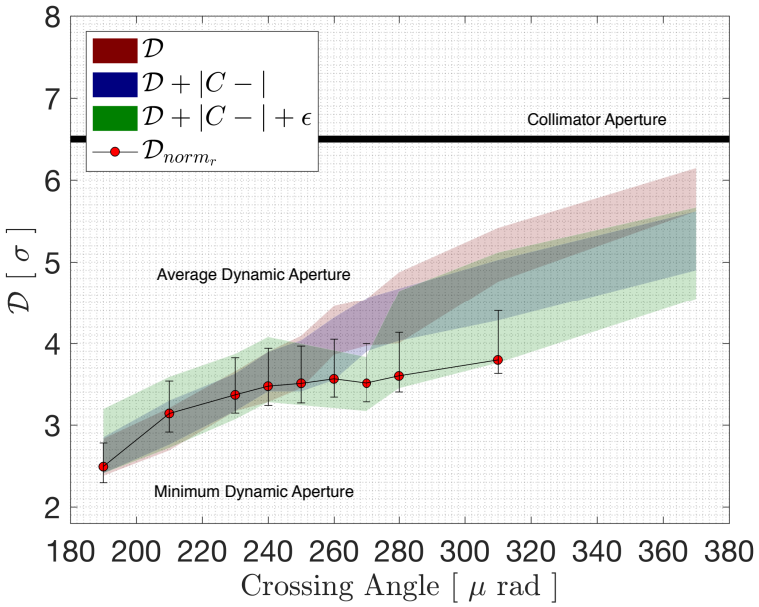

FIGURE 6.21: Dynamic aperture from tracking simulations for the nominal colliding bunch including multipolar errors, measured intensity, emittance, and linear coupling.

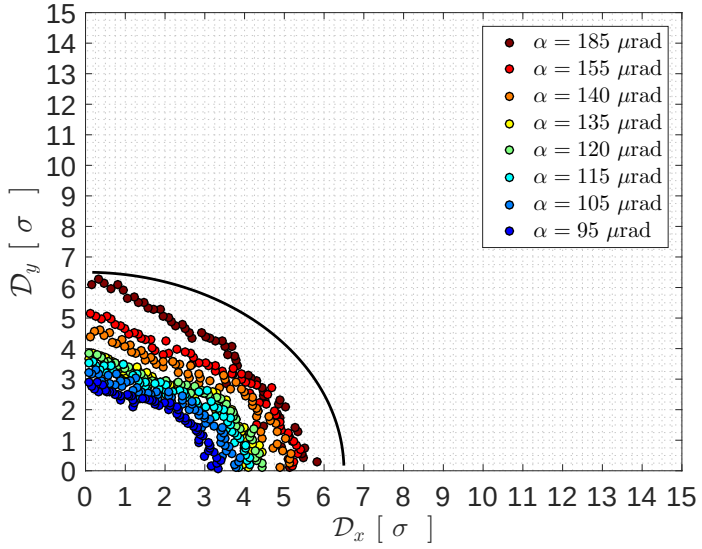

FIGURE 6.22: Dynamic aperture in the $x - y$ plane as a function of crossing angle for the nominal colliding bunch, including measured intensity, emittance, coupling and magnetic errors.

6.6 Conclusion

The aim of this chapter was to investigate and benchmark existing models in `Sixtrack`, to measured data obtained during the 2016 long-range beam-beam

machine study. In order to achieve this, the dynamic aperture from intensity loss was calculated. To provide a more accurate comparison to the simulation model, the effect of proton burn-off was removed and the dynamic aperture from measurement was normalised to the emittance of $\epsilon_n = 2.5$ μm. For the head-on only and nominal colliding bunches, a clear discrepancy was observed between measured dynamic aperture and the simulation model including only beam-beam effects. The simulation model predicted a continuous improvement of dynamic aperture for crossing angles larger than $\alpha = 260$ μrad. Instead however, the measured dynamic aperture saturates at approximately $\alpha = 260$ μrad and remains around 3.75 σ. In order to investigate a possible explanation, the simplest beam-beam configuration of the head-on only colliding bunch was considered first. Including only the head-on beam-beam interaction in the model predicts a dynamic aperture of $7.5 - 9.5$ σ, which lies outside of the collimator aperture at 6.5 σ. However the measured dynamic aperture remains at approximately 3.75 σ. This suggests that the head-on beam-beam interaction alone cannot account for the observations during the 2016 machine study. To improve the model, additional sources that impact the dynamic aperture were introduced. Firstly linear coupling, with typical values obtained during normal operation were included. Linear coupling was shown to reduce the dynamic aperture by approximately 1 σ. As a result, the minimum dynamic aperture from the model dropped below the collimator aperture, and remained around $\sim 5.8 - 6$ σ. The average dynamic aperture still remained above the collimator aperture however. This indicates that both linear coupling and the beam-beam interaction alone cannot account for the observed dynamic aperture. The LHC machine is complicated and contains multiple sources of magnetic errors and misalignments. In the previous simulation models, the non-linearities of the machine, such as magnetic errors and magnetic misalignments were not included. Finally the non-linearities of the machine were included into the simulation model and this was shown to

further reduce the dynamic aperture. Including these errors in the model reduces minimum and average dynamic aperture almost entirely below the collimator aperture. There is still approximately a 0.5 σ difference between the measured dynamic aperture and the dynamic aperture from models. This difference may be accountable due to a number of issues such as transverse offset or tune working point that is still to be investigated outside of this thesis. It appears as if the interplay between linear coupling, magnetic errors and the beam-beam interaction all impact and limit the dynamic aperture at $\sim 3.75\ \sigma$.

For the nominal colliding bunch, the model and measured dynamic aperture compares well below $\alpha = 260$ μrad. Within this region, the long-range beam-beam interaction is strong and is the main contribution to the particle losses. Outside of this region however, for $\alpha > 260$ μrad and beam-beam separations $> 8.5\,\sigma$, the model shows a continuous improvement in dynamic aperture, whereas the measured dynamic aperture saturates, in a similar way to the head-on bunch, at 3.75 σ. Linear coupling was then added to the simulation model. This reduced the dynamic aperture for crossing angles steps larger than $\alpha = 260$ μrad by approximately 1σ. In the same way as for the head-on bunch, this suggests that linear coupling in combination with the beam-beam interaction is not the sole source responsible for limiting the dynamic aperture. To further improve the model and hence compare to a more realistic scenario observed during the machine study, the non-linear errors of the machine were included. These again impacted the dynamic aperture for beam-beam separations larger than 8.5 σ, but did not impact separations smaller than this. Outside of the long-range beam-beam dominated region, the minimum dynamic aperture further reduced by approximately $0.5-1\ \sigma$. Including magnetic errors, linear coupling and beam-beam effects into the model appears to provides a sufficient explanation for the observed dynamic aperture obtained during the 2016 machine study, however this needs to be studied in more detail. The interplay between these effects appear

to saturate and limit the dynamic aperture for the nominal colliding bunch at $\alpha > 260$ μrad. This saturation likely arises due to the trajectory of the bunches through the inner triplet quadrupoles. At larger crossing angles, the bunches are off-centred through the inner triplet quadrupoles, resulting in a larger sampling of the magnetic field errors. This in combination with a small β^*, possibly causes the non-linearities of the magnets to induce chaotic motion or cause particles to cross resonant tunes. These mechanisms can result in particle losses and hence limit the dynamic aperture to 3.75 σ. However further work and additional mechanisms which limit the dynamic aperture need to be investigated further. Effects such as transverse offset between the colliding bunches, orbit drift, tune drift, and larger values of linear coupling can all impact the dynamic aperture. Further work is due to be conducted outside of this thesis and compared to other long-range beam-beam machine studies with different β^* and optics configurations. This will allow the dynamic aperture model to be improved and benchmarked against experimental data.

In the context of the LHC luminosity performance, these studies have shown that the combination of beam-beam effects and the non-linearities of the inner triplet can saturate the dynamic aperture for a particular machine configuration. Although the dynamic aperture may not necessarily correspond to particle losses, it implies that the particle motion may be chaotic for a signifiant proportion of the bunch. With regard to future performance, the non-linearities of the machine may further restrict the choice of operational parameters for β^* and crossing angle α and impact with luminosity reach.

Chapter 7

Summary and Conclusions

7.1 Summary

The LHC is an intricate and complicated machine that presents a number of challenges for accelerator physicists working within the field. In order to improve the machine performance and learn for future machines, a detailed understanding of the physical processes that the beams undergo is required. The aim of this thesis was to present some of the challenges from the perspective of the beam-beam interaction, overcome these challenges, and improve the machine performance.

In this thesis, the luminosity performance limitations due to beam-beam interaction have been investigated. The beam-beam interaction can significantly impact the machine performance. Understanding the beam-beam interaction and the limiting factors from this effect, allow the LHC luminosity performance to be improved, whilst simultaneously gaining experience for the operation of future machines like the HL-LHC. This understanding of beam-beam effects and other limiting factors in the LHC has allowed the luminosity reach to be increased each year, by pushing the optics to smaller β^* values whilst retaining luminosity lifetimes larger than 10 hours, ensuring long fill lengths.

Challenges in future machines will be different to that of the LHC, but gaining vital operational experience now will be invaluable for future colliders. The HL-LHC will push the luminosity reach even further by increasing the bunch intensity, reducing the bunch emittance and operating at a smaller β^*. One aspect that arises when operating at a small β^* is the hourglass effect. The hourglass effect will reduce the luminosity and hence impact the machine performance. In order to describe this effect, a new method was derived in chapter 4, which allowed analytic expressions to be obtained whilst the charge density distribution did not remain fixed throughout the interaction. This was applied to a number of non-Gaussian charge density distributions and where possible, the result was compared to literature. The standard 2-dimensional Gaussian electric field was re-derived to validate the theory. The method was then applied to describe the hourglass effect. An analytical expression in the rest frame of the bunch was obtained and compared to the standard fixed Gaussian bunch distribution. Although the method has been successful in allowing an analytical expression for the hourglass effect to be obtained, further work outside of this thesis is required to test and refine the calculation using a tracking code. To include the expression into a tracking code, the electric field should be boosted into the collision frame and the kick should be derived. This work is on-going outside of this thesis.

In addition to the theoretical work, experimental and simulation work was carried out, whilst based at CERN. The experimental and simulation work involved investigating the impact of the long-range beam-beam interactions on the luminosity performance and the β^* reach, during the 2015 and 2016 proton-proton run. The machine studies took place in order to identify the beam lifetime dependancy on the long-range beam-beam separation and to compare the measurements to predictions from models. In addition to this, these studies allowed the luminosity reach to be determined in the LHC, by reducing the crossing angle to the smallest

value, before additional losses occurred due to the long-range beam-beam interaction. The minimum crossing angle and beam-beam separation was identified for two different collision optics with $\beta^* = 0.8$ m and $\beta^* = 0.4$ m. During the 2016 proton-proton run, with bunch intensities and emittances of $n_p = 1.3 \times 10^{11}$ ppb and $\epsilon_n = 2.5$ μm, the minimum crossing angle was identified at $\alpha = 260$ μrad, which corresponds to a beam-beam separation of 7.5 σ. This allowed the crossing angle to be reduced from $\alpha = 370$ μrad to $\alpha = 280$ μrad during normal luminosity production fills. This lead to an increase in luminosity of approximately $10 - 15\%$, improving machine performance of 2016.

In order to understand the physics processes impacting the beam and luminosity lifetimes, a computational study was performed comparing measured data, discussed in chapter 5, to tracking simulations of the long-range beam-beam machine study. These studies are discussed in depth in chapter 6 and allowed measured data to be compared directly to predictions from models. Comparing the head-on colliding bunches to the simulation model showed that there was a significant disagreement between measurement and model, which could not be explained by the head-on beam-beam interaction alone. In order to better understand the discrepancy, additional processes that impact the dynamic aperture were included in the model. Firstly, linear coupling was included. This was shown to reduce the dynamic aperture by approximately 1 σ. However, this alone could not account for the dynamic aperture at crossing angles larger than $\alpha = 260$ μrad. Magnetic errors were also included in the simulation model and brings the dynamic aperture to within approximately 0.5 σ of the measured data. A number of possible explanations for the differences between the model and the measured data are discussed. The dynamic aperture for the nominal colliding bunch was also compared to the simulation model. For crossing angles and beam-beam separations smaller than $\alpha = 260$ μrad and 8.5 σ, the dynamic aperture is well described by the beam-beam interaction. Within this region, the long-range beam-beam

interaction is strong and dominates the particle losses. For crossing angles larger than $\alpha = 260$ μrad, the dynamic aperture predicted by the model continues to improve, whereas the measured dynamic aperture saturates to approximately 3.75 σ. Including both magnetic errors and linear coupling, provides a good comparison between the model and measured dynamic aperture for the nominal colliding bunch. This study suggests that the interplay between the beam-beam interaction, linear coupling, and the non-linearities of the machine have a significant impact on the dynamic aperture for crossing angles larger than $\alpha = 260$ μrad and beam-beam separations greater than 8.5 σ. The impact of magnetic errors on the dynamic aperture is not negligible, especially as the demand for smaller β^* increases. For a smaller β^* the bunches are blown up more in the triplet. As a result the beams experience more of the non-linearities of the triplet. These non-linearities can be strong and when combined with beam-beam effects and linear coupling, limit the dynamic aperture. These studies show that there is a complicated interplay between the non-linearities of the machine and the beam-beam interaction which significantly impact the dynamic aperture. The measured data does however, compare well to predictions from models. This allows accurate predications to be made for future machine configurations.

The research performed in this thesis has provided an improved understanding of beam-beam effects in the LHC and the impact of these effects on the luminosity performance for the LHC and the future HL-LHC. This research, collectively, will enable future machine performance to be pushed, allowing larger luminosity to be reached.

Appendix A

The Method of Characteristics

The subject of partial differential equations are of great interest to a number of different fields outside of mathematics, such as physics, financial economics, computational biology and chemistry among others. This appendix will provide a brief review of one particular method of solving partial differential equations.

A.1 Method of Characteristics

The method of characteristics is an approach that may allow solutions of partial differential equations to be obtained. Solutions can be found by reducing the equation to a family of ordinary differential equations using characteristic curves. The so called characteristic curves can then be integrated to find solutions to the original hyperbolic partial differential equation. This method is general for n-dimensions and can even be extended, under some circumstances to non-linear equation. Consider the 2-dimensional vector functions f_1 and f_3 related to one another through the homogenous partial differential equation,

$$f_3 \partial_x f_2 + f_1 \partial_y f_2 = 0, \tag{A.1}$$

where f_2 is some hyper-surface. The term hyper-surface in this instance corresponds to a plane or surface that can take any number of dimensions. To find the characteristic curves, the functions f_1 and f_3 must be orthogonal to the hyper-surface f_2. Hence, the functions f_1, f_3 and f_2 are related to one another through

$$(f_1 - f_3)\nabla f_2 = 0. \tag{A.2}$$

Equation A.2 can be expressed as equations,

$$f_1 \partial_y f_2 - f_3 \partial_x f_2 = 0, \tag{A.3}$$

Considering equation A.3 and rearranging for f_1/f_3 gives

$$\frac{f_1}{f_3} = \frac{\partial_x f_2}{\partial_y f_2}. \tag{A.4}$$

Treating the ordinary differential of the hyper-surface $\mathrm{d}f_2 = 0$ as constant, then the ordinary differentials are related to the partial differentials through

$$df_2 = \partial_x f_2 \mathrm{d}x + \partial_y f_2 \mathrm{d}y,$$

$$\partial_x f_2 \mathrm{d}x = -\partial_y f_2 \mathrm{d}y,$$

$$\frac{\partial_x f_2}{\partial_y f_2} = -\frac{\mathrm{d}y}{\mathrm{d}x}.$$

Substituting back into equation A.4 gives

$$f_1 \mathrm{d}x + f_3 \mathrm{d}y = 0. \tag{A.5}$$

Integrating this gives the equation gives the condition that characteristic curves must satisfy. Hence,

$$f_2 = f_2\left(\int f_1 \mathrm{d}x + \int f_3 \mathrm{d}y\right),$$

is true under the condition that f_1 and f_3 are functions of only x and y respectively. Briefly, some examples of the method of characteristics will be provided in the following sections.

A.1.1 Example 1:

Considering the homogenous partial differential equation

$$x^2 \partial_y g(x,y) - y \partial_x g(x,y) = 0, \tag{A.6}$$

where $g(x,y)$ is some arbitrary function. Applying the method of characteristics gives the ordinary differential equation as,

$$\frac{\mathrm{d}x}{y} + \frac{\mathrm{d}y}{x^2} = \frac{\mathrm{d}g}{0}. \tag{A.7}$$

Collecting functions that contain x and y only gives the ordinary differential equation under the condition that $dg = 0$, then the integral to evaluate is

$$\int x^2 \mathrm{d}x + \int y \mathrm{d}y = 0 \tag{A.8}$$

Hence the function g

$$g = g\left(\frac{x^3}{3} + \frac{y^2}{2}\right). \tag{A.9}$$

This gives the functional form of g, that solves equation A.6.

Bibliography

[1] J. D. Jackson. *Classical electrodynamics*. Wiley, 1999.

[2] J. C. Maxwell. A dynamical theory of the electromagnetic field. *Philosophical transactions of the Royal Society of London*, 155:459–512, 1865.

[3] K. Schindl. CAS-CERN accelerator school: Intermediate course on accelerator physics. *Zeuthen, Germany*, pages 305–320, 2003.

[4] H. Wiedemann. *Particle accelerator physics*. Springer, 2015.

[5] M. Livingston E. D. Courant et al. The strong-focusing synchroton¯a new high energy accelerator. *Phys. Rev.*, 88:1190–1196, Dec 1952. doi: 10.1103/PhysRev.88.1190. URL http://link.aps.org/doi/10.1103/PhysRev.88.1190.

[6] E. Todesco A. Bazzani. A normal form approach to the theory of nonlinear betatronic motion. *Unknown*, 1994.

[7] USPAS. USPAS lecture 6: Emittance in multi-particle beams. https://www.classe.cornell.edu/~dugan/USPAS/Lect6.pdf/.

[8] Y.S. Lee. *Accelerator physics*. World scientific, 2004.

[9] Klaus Wille. *The Physics of Particle Accelerators: An Introduction*. Clarendon Press, 2000.

[10] J. D. Meiss R. S. MacKay. *Hamiltonian Dynamical Systems: a reprint selection*. CRC Press, 1987.

[11] D. Hilbert R. Courant. *Methods of mathematical physics*, volume 1. CUP Archive, 1965.

[12] J. D. Finch L. N. Hand. *Analytical mechanics*. Cambridge University Press, 1998.

[13] E. H. Maclean. *Modelling and correction of the non-linear transverse dynamics of the LHC from beam-based measurements*. PhD thesis, University of Oxford, 2014.

[14] A. Chao et al. *Handbook of accelerator physics and engineering*. World scientific, 2013.

[15] J. Jones. *Design of a Novel Stacked Storage Ring for Low Emittance Light Sources*. PhD thesis, University of Manchester, 2015.

[16] W. Herr. Beam beam effects. *CERN Accelerator School: 5th Advanced Accelerator School*, 1995.

[17] K. Y. Ng. *Physics of intensity dependent beam instabilities*. World Scientific, 2006.

[18] W. Herr. Introduction to landau damping. *arXiv preprint arXiv:1601.05227*, 2016.

[19] B. D. Muratori. Luminosity and luminous region calculations for the LHC. Technical report, LHC Project Note 301, 2002.

[20] E. Metral et al. Summary of the half-day internal review of LHC performance limitations (linked to transverse collective effects) during run ii (CERN, 29/11/2016). Technical report, 2017.

[21] A. Apollonio. LHC report: Astounding availability. https://cds.cern.ch/record/2197580/files/lumi-proj-16-9July_image.png?subformat=.

[22] G. Erskine M. Bassetti. Closed expression for the electrical field of a two-dimensional Gaussian charge. Technical Report CERN-ISR-TH-80-06. ISR-TH-80-06, CERN, Geneva, 1980.

[23] R. D. Ryne J. Qiang, M. A Furman. Parallel particle-in-cell simulation of colliding beams in high energy accelerators. In *Supercomputing, 2003 ACM/IEEE Conference*, pages 29–29. IEEE, 2003.

[24] G. Green. *An essay on the application of mathematical analysis to the theories of electricity and magnetism*. author, 1828.

[25] R. Wanzenberg. *Nonlinear Motion of a Point Charge in the 3D Space Charge Field of a Gaussian Bunch*. Dt. Elektronen-Synchrotron DESY, 2010.

[26] D. J. Griffiths. Introduction to electrodynamics, 2005.

[27] R. Assmann et al. The beam-beam interaction in the presence of strong radiation damping. Technical report, 2000.

[28] K. Yokoya et al. Tune shift of coherent beam-beam oscillations. *Part. Accel.*, 27(KEK-89-14):181–186, 1989.

[29] X. Buffat. Coherent beam-beam effects. *CERN Yellow Reports: School Proceedings*, 3(0):391, 2017. ISSN 2519-805X. URL https://e-publishing.cern.ch/index.php/CYRSP/article/view/265.

[30] K. Yokoya. Limitations of the soft gaussian approximation. *Physical Review Special Topics-Accelerators and Beams*, 3, 2000.

[31] R. D. Ryne J. Qiang, M. Furman. Strong-strong beam-beam simulation using a green function approach. *Physical Review Special Topics-Accelerators and Beams*, 5(10):104402, 2002.

[32] T. Pieloni. *A study of beam-beam effects in hadron colliders with a large number of bunches*. PhD thesis, Ecole Polytechnique, Lausanne, 2008.

[33] C. Lefevre. The CERN accelerator complex. Technical report, 2008.

[34] C. Amsler D. E. Groom, M. Aguillar-Benitez. Review of particle physics. particle data group. *European Physical Journal. C*, 15(1-4):1–878, 2000.

[35] D. Brandt et al. Accelerator physics at lep. *Reports on Progress in Physics*, 63(6):939, 2000.

[36] Atlas Collaboration. The atlas experiment at the CERN large hadron collider. *Journal of instrumentation*, 3(8):S08003–S08003, 2008.

[37] CMS Collaboration. The cms experiment at the CERN LHC. 2008.

[38] K. Aamodt et al. The alice experiment at the CERN LHC. *Journal of Instrumentation*, 3(08):S08002, 2008.

[39] LHCb Collaboration. The LHCb detector at the LHC. *Journal of instrumentation*, 3(08):S08005, 2008.

[40] R. W. Assmann et al. The consequences of abnormal beam dump actions on the LHC collimation system. Technical report, CERN-LHC-Project-Note-293, 2002.

[41] A. Ijspeert et al. Principles developed for the construction of the high performance, low-cost superconducting LHC corrector magnets. *IEEE transactions on applied superconductivity*, 12(1):90–93, 2002.

[42] LHC design report v.1: the LHC main ring. 2004.

[43] CERN. Position and intensity monitors. https://espace.cern.ch/be-dep/BI/PI/FBCT/SitePages/Home.aspx.

[44] A. Rabiller F. Roncarolo et al. Can we get a reliable on-line measurements of the transverse beam size? 2010.

[45] A. Goldblatt et al. Design and performance of the upgraded LHC synchrotron light monitor. Technical report, 2013.

[46] M. Gasior et al. An overview of the LHC transverse diagnostics systems. *CERN-LHCPROJECT-Report-1166*, 2008.

[47] LHC Performance Note. First results from the LHC BBQ tune and chromaticity systems. 2009.

[48] ATLAS collaboration et al. Characterisation and mitigation of beam-induced backgrounds observed in the atlas detector during the 2011 proton-proton run. *arXiv preprint arXiv:1303.0223*, 2013.

[49] O. Brüning. *Large Hadron Collider Design Report*, volume 1. European Organization for Nuclear Research, 2004.

[50] S. Redaelli. Beam cleaning and collimation systems. *arXiv preprint arXiv:1608.03159*, 2016.

[51] W. Herr X. Buffat et al. Long range beam-beam effects in the LHC. (arXiv:1409.4942):6 p, 2014. URL http://cds.cern.ch/record/1953724. Presented at the ICFA Mini-Workshop on Beam-Beam in Hadron Colliders, CERN, Geneva, Switzerland, 18-22 March 2013.

[52] HiLumi LHC Collaboration et al. HL-LHC preliminary design report. Technical report, CERN-ACC-2014-0300, 2014.

[53] G. Apollinari et al. High-luminosity large hadron collider (HL-LHC): Preliminary design report. Technical report, Fermi National Accelerator Laboratory (FNAL), Batavia, IL (United States), 2015.

[54] R. Assmann Y. Sun et al. Beam dynamics aspects of crab cavities in the CERN large hadron collider. *Physical Review Special Topics-Accelerators and Beams*, 12(10):101002, 2009.

[55] L. Rossi. LHC upgrade plans: options and strategy. Technical report, 2011.

[56] T. Pieloni B. D. Muratori. Luminosity levelling techniques for the LHC. *arXiv preprint arXiv:1410.5646*, 2014.

[57] H. Koiso et al. Beam operation with crab cavities at KEKB. 2007.

[58] D. Amos et al. ILC crab cavity phase control system development and synchronisation testing in a vertical cryostat facility. *EuroTeV-Report-2008-073, Dec*, 2008.

[59] B. D. Muratori M.P. Crouch, R.B. Appleby. Strong-strong simulations of beta star levelling for flat and round beams. Technical report, 2015.

[60] D. Jacquet F. Follin. Implementation and experience with luminosity levelling with offset beam. *arXiv preprint arXiv:1410.3667*, 2014.

[61] B. D. Muratori W. Herr. Concept of luminosity. In *proceedings of CERN Accelerator School*, volume 361, 2003.

[62] R. Siemann S. Krishnagopal. Bunch-length effects in the beam-beam interaction. *Physical Review D*, 41(7):2312, 1990.

[63] E. Keil. Beam-beam dynamics. Technical report, CERN, 1994.

[64] K. Yokoya K. Oide. Beam-beam collision scheme for storage-ring colliders. *Physical Review A*, 40(1):315, 1989.

[65] F. Ruggiero K. Hirata, H. W. Moshammer. A symplectic beam-beam interaction with energy change. *Part. Accel.*, 40(KEK-92-117):205–228, 1992.

[66] A. Wolski B. D. Muratori, J. Jones. Analytical expressions for fringe fields in multipole magnets. *Phys. Rev. ST Accel. Beams*, 18:064001, Jun 2015. doi: 10.1103/PhysRevSTAB.18.064001.

[67] Z. Nehari. *Conformal mapping*. Courier Corporation, 1975.

[68] G. N. Watson E. T. Whittaker. *A course of modern analysis*. Cambridge university press, 1996.

[69] R. L. Walker J. Mathews. *Mathematical methods of physics*, volume 501. WA Benjamin New York, 1970.

[70] A. Sommerfeld. *Partial differential equations in physics*, volume 1. Academic press, 1949.

[71] P. W. Ketchum. Analytic functions of hypercomplex variables. *American Mathematical Society*, 30(4):641–667, 1928.

[72] P. W. Ketchum. A complete solution of laplace's equation by an infinite hypervariable. *American Journal of Mathematics*, 51(2):179–188, 1929.

[73] P. W. Ketchum. Solution of partial differential equations. *American Journal of Mathematics*, 54(2):253–264, 1932.

[74] T. Poston C. TJ. Dodson. *Tensor geometry: the geometric viewpoint and its uses*, volume 130. Springer Science & Business Media, 2013.

[75] G. C. Wick. Properties of bethe-salpeter wave functions. *Physical Review*, 96(4):1124, 1954.

[76] N. M. J. Woodhouse. Contour integrals for the ultrahyperbolic wave equation. In *Proceedings of the Royal Society of London A: Mathematical, Physical and Engineering Sciences*, volume 438, pages 197–206. The Royal Society, 1992.

[77] E. T. Whittaker. On the partial differential equations of mathematical physics. *Mathematische Annalen*, 57(3):333–355, 1903.

[78] H. Bateman. The solution of partial differential equations by means of definite integrals. *Proceedings of the London Mathematical Society*, 2(1): 451–458, 1904.

[79] H. Bateman. *The Mathematical Analysis of Electrical and Optical Wave-motion on the Basis of Maxwell's Equations*. University press, 1915.

[80] R. Penrose. The twistor programme. *Reports on Mathematical Physics*, 12 (1):65–76, 1977.

[81] M. Dunajski. Twistor theory and differential equations. *Journal of Physics A: Mathematical and Theoretical*, 42(40):404004, 2009.

[82] M. Dunajski. *Solitons, instantons, and twistors*, volume 19. Oxford University Press, 2010.

[83] R. Penrose. Solutions of the zero-rest-mass equations. *Journal of mathematical Physics*, 10(1):38–39, 1969.

[84] E. Witten. Perturbative gauge theory as a string theory in twistor space. *Communications in Mathematical Physics*, 252(1-3):189–258, 2004.

[85] W. T. Shaw. Complex variable methods for 3d applied mathematics: 3d twistors and the biharmonic equation. *arXiv preprint arXiv:1005.4184*, 2010.

[86] W. T. Shaw. Complex variable methods for 3d applied mathematics: 3d twistors and an application to stoke's flow.

[87] H. S. Ruse. Generalised solutions of laplace's equation. *Proceedings of the Edinburgh Mathematical Society*, 2(4):181–188, 1931.

[88] E. Stiefel. On cauchy-riemann equations in higher dimensions. *J. Res. Nat. Bureau Stand*, 48(5):395–398, 1952.

[89] T. Levi-Civita. *The absolute differential calculus (calculus of tensors)*. Courier Corporation, 1926.

[90] H. T. H. Piaggio. *An elementary treatise on differential equations and their applications*. Bell, 1952.

[91] K. Schindl. Space charge. In *Beam Measurement-Proceedings of the Joint US-CERN-Japan-Russia School on Particle Accelerators. Edited by TURNER STUART ET AL. Published by World Scientific Publishing Co. Pte. Ltd., 1999. ISBN# 9789812818003, pp. 127-151*, pages 127–151, 1999.

[92] C. Prior. Dynamics of non-linear beams with space-charge. http://cas.web.cern.ch/cas/Bilbao-2011/Lectures/PriorbeamDynamics2.pdf.

[93] L. J. Laslett. On intensity limitations imposed by transverse space-charge effects in circular particle accelerators. *Summer Study on Storage Rings, BNL Report*, 7534:325–367, 1963.

[94] M.K. Murray. Twistor theory. *Geometric Approaches to Differential Equations*, 15:201, 2000.

[95] E. Hughes. *Twistor Transform*. PhD thesis, Queens' College, University of Cambridge, 2013.

[96] L. F. Shampine. Vectorized adaptive quadrature in matlab. *Journal of Computational and Applied Mathematics*, 211(2):131–140, 2008.

[97] Matlab: Numerical integration. https://uk.mathworks.com/help/matlab/ref/integral.html.

[98] G. Papotti W. Herr. *Proceedings of the ICFA Mini-Workshop on Beam-Beam Effects in Hadron Colliders (BB2013), CERN, Geneva, Switzerland, 18-22 Mar 2013*. Number CERN-2014-004. CERN, 2014.

[99] T. Pieloni et al. Two beam effects. In *Proceedings of the 5th Evian Workshop, Evian, France*, 2014.

[100] T. Pieloni. Long-range beam-beam studies and possible reduction of the crossing angles in the LHC. *Presentation*, 2016.

[101] W. Herr R. Assmann et al. Results of long-range beam-beam studies-scaling with beam separation and intensity. Technical report, 2012.

[102] W. Herr R. Alemany et al. Results of long range beam-beam studies and observations during operation in the LHC. Technical report, 2011.

[103] T. Pieloni M. Albert et al. Head-on beam-beam collisions with high intensities and long range beam-beam studies in the LHC. Technical report, 2011.

[104] A. Esmail-Yakas. *Effects of the beam-beam interactions on luminosity decay rates in the LHC 2012*. PhD thesis, Imperial College London, 2015.

[105] Y. Li T. F. Coleman. An interior trust region approach for nonlinear minimization subject to bounds. *SIAM Journal on optimization*, 6(2):418–445, 1996.

[106] R. E. Walsh J. E. Dennis, D. M. Gay. An adaptive nonlinear least-squares algorithm. *ACM Transactions on Mathematical Software (TOMS)*, 7(3): 348–368, 1981.

[107] E. McCrory et al. Fitting the luminosity decay in the tevatron. In *Proceedings of the 2005 Particle Accelerator C onference*, pages 2434–2436. IEEE, 2005.

[108] T. Pieloni M. P. Crouch et al. Long range beam-beam interaction and the effect on the beam and luminosity lifetimes. Jan 2016. URL https://cds.cern.ch/record/2124748. Research supported by the High luminosity LHC project.

[109] T. Pieloni M. P. Crouch et al. Impact of long range beam-beam effects on intensity and luminosity lifetimes from the 2015 LHC run. In *7th International Particle Accelerator Conference (IPAC'16), Busan, Korea, May 8-13, 2016*, pages 1422–1425. JACOW, Geneva, Switzerland, 2016.

[110] T. Pieloni J .Barranco Garcia et al. Md 400: LHC emittance growth in presence of an external source of noise during collision. Technical report, 2016.

[111] R et al Steinhagen. Results of the LHC prototype chromaticity measurement system studies in the CERN-SPS. (LHC-PROJECT-Report-1159. CERN-LHC-PROJECT-Report-1159):4 p, Sep 2008.

[112] T. Pieloni. Private Communication, .

[113] L.R. Carver. Instabilities at flat top and mid-squeeze. https://indico.cern.ch/event/440271/contributions/1096273/attachments/1147739/1646145/LBOC_LCarver_Instabilities.pdf.

[114] T. Pieloni M.P. Crouch et al. Long-range beam-beam limit in the LHC. https://indico.cern.ch/event/576908/contributions/2335642/attachments/1354494/2046286/LR_limit_HL-LHC_meeting.pdf.

[115] T. Pieloni M. P. Crouch et al. Long range beam-beam interaction and the effect on the beam and luminosity lifetimes. Technical report, 2016.

[116] T. Pieloni M. P. Crouch et al. Md 385: Long range beam-beam interaction and the effect on the beam and luminosity lifetimes.

[117] Dynamic aperture. *CERN Accelerator School: 3rd Advanced Accelerator School*, 1995.

[118] Dynamic aperture. *CERN Accelerator School: 5th Advanced Accelerator School*, 1995.

[119] M. Giovannozzi. Proposed scaling law for intensity evolution in hadron storage rings based on dynamic aperture variation with time. *Physical Review Special Topics-Accelerators and Beams*, 15(2):024001, 2012.

[120] V. I. Arnol'd. *Mathematical methods of classical mechanics*, volume 60. Springer Science & Business Media, 2013.

[121] V. I. Arnold. Instability of dynamical systems with several degrees of freedom. *Collected Works: Representations of Functions, Celestial Mechanics and KAM Theory, 1957–1965*, pages 423–427, 2009.

[122] E. Todesco M. Giovannozzi, W. Scandale. Prediction of long-term stability in large hadron colliders. *Part. Accel.*, 56(LHC-Project-Report-45):195–225, 1996.

[123] E. Todesco M. Giovannozzi, W. Scandale. Dynamic aperture extrapolation in the presence of tune modulation. *Physical Review E*, 57(3):3432, 1998.

[124] J. K. Moser. Lectures on celestial mechanics, 1971.

[125] L. Michelotti. *Intermediate Classical Dynamics with Applications to Beam Physics*. Wiley, 1995.

[126] N. N. Nekhoroshev. An exponential estimate of the time of stability of nearly-integrable hamiltonian systems. *Russian Mathematical Surveys*, 32 (6):1–65, 1977.

[127] G. Turchetti A. Bazzani, S. Marmi. Nekhoroshev estimate for isochronous non resonant symplectic maps. *Celestial Mechanics and Dynamical Astronomy*, 47(4):333–359, 1989.

[128] G. Turchetti. Number theory and physics berlin–heidelberg, 1990.

[129] E. Todesco M. Giovannozzi, W. Scandale. Dynamic aperture extrapolation in the presence of tune modulation. *Phys. Rev. E*, 57:3432–3443, Mar 1998. doi: 10.1103/PhysRevE.57.3432. URL http://link.aps.org/doi/10.1103/PhysRevE.57.3432.

[130] F. Schmidt. Sixtrack: a single particle tracking code. Technical report, CM-P00061013, 1990.

[131] R. De Maria E. McIntosh. The sixdesk run environment for sixtrack. *CERN-ATS-Note-2012-089 TECH*, 2012.

[132] M. Fjellstrom R. De Maria. Sixtrack physics manual (draft), 2015.

[133] F. Schmidt H. Grote. Mad-x-an upgrade from mad8. In *Particle Accelerator Conference, 2003. PAC 2003. Proceedings of the*, volume 5, pages 3497–3499. IEEE, 2003.

[134] A. Wolf et al. Quantifying chaos with lyapunov exponents. *Chaos*, 16: 285–317, 1986.

[135] G. Boeing. Visual analysis of nonlinear dynamical systems: Chaos, fractals, self-similarity and the limits of prediction. *Systems*, 4(4):37, 2016.

[136] F. Schmidt M. Böge. Estimates for long-term stability for the LHC. In *AIP Conference Proceedings*, volume 405, pages 201–210. AIP, 1997.

[137] M. Javed and R. De Maria. Sixdesk library. https://indico.cern.ch/event/327359/contributions/762039/attachments/635939/875447/Moonis_gsoc14.pdf.

[138] E. H. Maclean. Private Communication, .

[139] L. Vos. Ground motion in LEP and LHC. In *Particle Accelerator Conference, 1995., Proceedings of the 1995*, volume 5, pages 3367–3369. IEEE, 1995.

[140] M. Giovannozzi P. Hagen et al. Wise: A simulation of the LHC optics including magnet geometrical data. Technical report, 2008.

[141] R. Tomás et al. CERN large hadron collider optics model, measurements, and corrections. *Physical Review Special Topics-Accelerators And Beams*, 13(12):121004, 2010.

[142] D. Richter J. Buckley et al. Dynamic magnetic measurements of superconducting magnets for the LHC. *IEEE Transactions on Applied Superconductivity*, 5(2):1024–1027, 1995.

[143] M. Giovannozzi et al. Dynamical aperture studies for the CERN LHC: Comparison between statistical assignment of magnetic field errors and actual measured field errors. *Proceedings of EPAC 2006, Edinburgh, Scotland*, 2006.

[144] E. McIntosh M. Giovannozzi. Parameter scans and accuracy estimates of the dynamical aperture of the CERN LHC. Technical report, 2006.

[145] G. Ripken L. H. A. Leunissen, F. Schmidt. Six-dimensional beam-beam kick including coupled motion. *Physical Review Special Topics-Accelerators and Beams*, 3(12):124002, 2000.

[146] T. Pieloni. Private Communication, .

[147] T. Pieloni et al. Beam-beam effects: long range and head-on. In *Proceedings of the 6th Evian Workshop, Evian, France*, 2015.

[148] R. Assmann et al. The final collimation system for the LHC. Technical report, 2006.

[149] G. Parzen. Dynamic aperture effects due to linear coupling. In *1991 IEEE Particle Accelerator Conference (APS Beam Physics)*, page 1875, 1991.

[150] R. Tomas. Private Communication.

[151] D. P. Anderson. Boinc: A system for public-resource computing and storage. In *Grid Computing, 2004. Proceedings. Fifth IEEE/ACM International Workshop on*, pages 4–10. IEEE, 2004.

[152] J. Barranco García B. Salvachua et al. Observations of beam losses at the LHC during reduction of crossing angle. In *8th Int. Particle Accelerator Conf.(IPAC'17), Copenhagen, Denmark, 14â 19 May, 2017*, pages 2105–2108. JACOW, Geneva, Switzerland, 2017.

[153] E. Maclean. Tune-footprint through the LHC cycle. https://indico.cern.ch/event/672805/contributions/2752715/attachments/1540407/2415341/2017-10-17_Qspread.pdf, .